Understanding High-Pressure Induced Solid State Polymorphism

RIDOUT, JOSEPH

Understanding High-Pressure Induced Solid State Polymorphism

Joe Ridout

Thesis submitted in part fulfilment of the requirements for the degree of

Doctor of Philosophy

at the

University of Durham

Department of Chemistry

September 2014

Understanding High-Pressure Induced Solid State Polymorphism

Thesis submitted in part fulfilment of the requirements for the degree of
Doctor of Philosophy at the University of Durham

Joe Ridout

Department of Chemistry
Durham University
September 2014

Abstract

This research investigates the effect of high-pressure on the solid-state with a particular focus on the crystallisation of liquids using high-pressure.

Chapter 1 gives an introduction into the theory underpinning the cryo- and high-pressure crystallisation processes as well as details of X-ray high-pressure diffraction experiments. Chapter 2 outlines the theory behind intermolecular interactions and polymorphism.

Chapter 3 details the analysis of two series of simple fluoroaromatics that have been crystallised at both high-pressure and low-temperature, exploring how these forms differ. Chapter 4 examines how the varying the rate of compression in the high-pressure crystallisation of 2-fluorophenylacetylene results in the formation of different polymorphs. Attempts to use high-pressure crystallisation to form different low-melting molecular complexes to those generated through cryo-crystallisation are outlined in chapter 5. Chapter 6 explores the cryo- and high-pressure crystallisation products of isopropyl alcohol, diethyl ether, anisole, dimethylacetylene and acetic anhydride through examination of the intermolecular interactions and crystal packing. The very different molecular geometry of acetic anhydride in the low-temperature and high-pressure forms is discussed. Chapter 7 outlines how the use of different pressure-transmitting media resulting in a metal organic framework behaving differently under the application of pressure.

Table Of Contents

Note that in this thesis, the following colour scheme has been adopted:

Atom	Colour
Carbon	Grey
Hydrogen	White
Fluorine	Light Green
Chlorine	Dark Green
Bromine	Dark Red
Iodine	Purple
Oxygen	Light Red
Nitrogen	Light Blue
Silver	Dark Blue

The work described herein was performed in the Department of Chemistry at the University of Durham between October 2011 and September 2014, under the supervision of Dr. Ehmke Pohl, Dr. Mike Probert and Prof. Jon Steed. All the work described in this thesis is my own, unless clearly stated otherwise.

Joe Ridout

Acknowledgements

I would like to thank everyone who has helped me in the last three years, in no particular order:

Judith Howard for helping securing my funding, running the crystallography lab, and having an incredible, infectious amount of energy and enthusiasm.

The late Andres Goeta, for accepting me to be his PhD student. I regard it as a great shame that I never really got to know Andres, as everybody has extremely kind words for him, both professionally and personally.

Ehmke Pohl, for picking up the formal supervisory reins and mentoring me throughout my time in Durham, and for being extremely kind and friendly.

Jon Steed (and group), for being generous in allowing me to speak on several occasions at his group meetings and for invaluable scientific advice.

Dima Yufit, for putting up with me breaking his stuff constantly and generally being a pain!

Andrei Batsanov, Oleg Dolomanov, and Horst Puschmann for being there to answer various scientific queries.

Sally Price and Louise Price for welcoming me to London and for advice and help running crystal energy landscape calculations.

Everyone at Newcastle Chemistry Department – notably Dr. Paul Waddell (for his dry sense of humour and encyclopaedic knowledge), Dr. Andrew Houlton, Chris and Glenn.

Finally, Mike Probert for his extreme patience and goodwill and excellent choice of PhD area. I am really indebted to you.

I would like to dedicate this thesis, to my wife, Lizzy. Thanks so much for supporting me these last five years, I adore you.

Chapter 1: Introduction to High-Pressure Crystallisation and Diffraction Experiments

1.1 High-Pressure Crystallography

Many scientific fields were revolutionised by the discovery that crystals diffract X-rays.[1] This phenomenon makes it possible to study the structure of crystals, giving detailed molecular information with extreme precision. Indeed, much of our knowledge of structure and bonding in materials is derived from crystallographic experiments. For example, the Braggs showed that the structure of NaCl comprises of Na and Cl ions rather than Na-Cl molecules.[2] Lonsdale was able to give the first definitive proof of the atomic arrangement in benzene, which had previously been argued to have alternative molecular structures.[3] The crystallographic study of molecular compounds under pressure has a long history, and various methods have been developed to apply elevated pressures to a single-crystal sample. The most commonly used of these is the anvil cell, where opposing anvils apply pressure to the sample, as shown below in figure 1.1. Opposed anvil devices made of tungsten carbide[4,5] based on the principle of massive support[6,7,8] were developed in the early 1950s by Percy Bridgman, who won the Nobel prize in physics for his work in high pressure physics, and have since been developed to use several anvil types.

Introduction of diamond as the anvil material[9,10] allowed X-rays access to the sample and increased the range of accessible pressures by an order of magnitude. A diamond anvil cell (DAC) comprises two diamonds oriented in opposing directions, with the sample between them, held in place by a small piece of metal commonly known as the gasket. To complete the sample chamber, gaskets used in this work were prepared by indenting a sheet (typically made of stainless steel or tungsten) from an initial thickness of approximately 0.25 mm to approximately 0.10 mm by the diamond anvils. A hole of typical diameter 0.3 mm was then drilled through the centre of the indentation to form a cylindrical sample chamber.

A schematic of a typical DAC is shown below in figure 1.1.

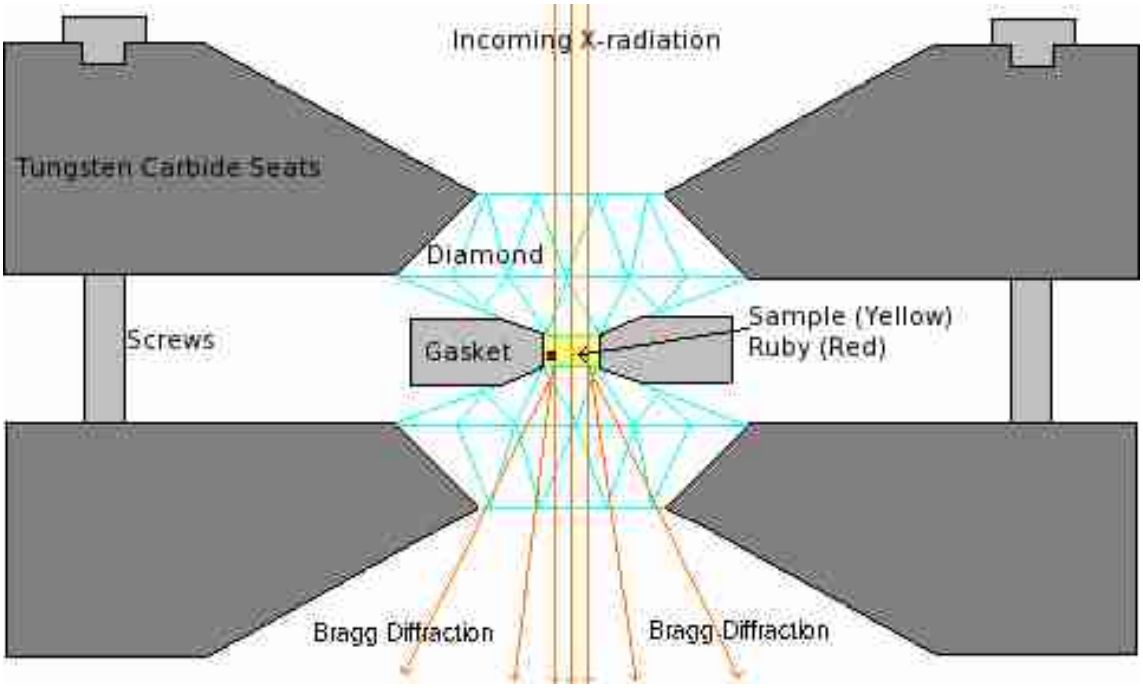

Figure 1.1 Components in a typical diamond anvil cell designed for single-crystal X-ray diffraction.

To provide a hydrostatic environment, samples which are solids under ambient conditions must be suspended in a fluid in the sample chamber. A wide range of materials can be used to transmit pressure, these include methanol/ethanol mixtures, alkane mixtures such as paraffin and liquefied gases such as nitrogen, argon and helium.[11]

Pressure can also be used to induce the crystallisation of liquids. This is achieved through increasing the pressure until nucleation occurs, leading to a multi-crystalline phase. The smaller crystallites are then melted until only one remains. This is achieved by either increasing the temperature through use of an IR laser or by decreasing the pressure. The remaining crystallite is then grown to fill the sample chamber either by decreasing the temperature back to ambient or by increasing the pressure. All high-pressure experiments involving the crystallisation of liquids described in this thesis are mediated through variation in pressure alone unless stated otherwise.

The pressure inside the sample chamber cannot be directly calculated from the force applied to the diamonds because of the difficulty in predicting the plastic and elastic deformations in the gasket and components of the DAC.[12] As a result, methods had to be developed to measure the pressure inside the sample chamber. The most common method now employed is through adding a chip of ruby to the sample chamber and measuring its fluorescence spectrum. At ambient conditions ruby

produces a strong doublet at 692.7 and 694.2 nm. Up to 19.5 GPa the wavelength of the doublet wavelength increases linearly with increasing pressure:

$$\Delta p = 0.2740(16) \times \Delta\lambda \, GPa \quad (\Delta\lambda \text{ in Å}).^{13}$$

The collection of diffraction images from samples enclosed in a DAC is hampered by its limited opening angle, a typical half-opening angle of a diamond anvil cell being around 40°. This results in only a dumbbell-shaped section of a given sphere of reciprocal space being accessible. A schematic showing the area of reciprocal space in which reflections that may be collected and a diagram showing reflections collected in a typical high-pressure diffraction experiment are shown in figure 1.2 below.

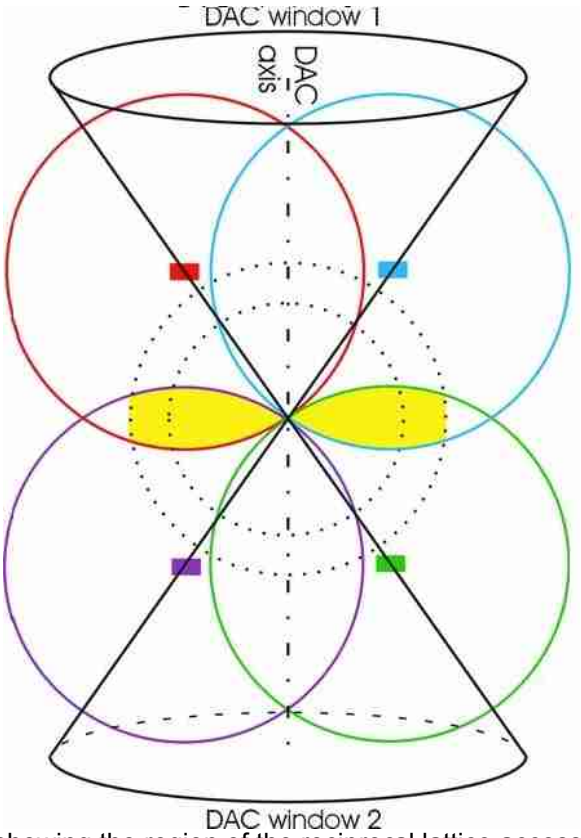

Figure 1.2 Construct showing the region of the reciprocal lattice accessible in a high-pressure diffraction experiment (highlighted in yellow).The four Ewald spheres correspond to the the edges of the windows. Reprinted with permission from Ref. 12 © IUCr

Figure 1.3, shown below, illustrates the reflections in the reciprocal lattice that were collected in a typical high-pressure diffraction experiment. This figure demonstrates the biconcave volume of reciprocal space (shown in yellow in figure 1.2) experimentally accessible.

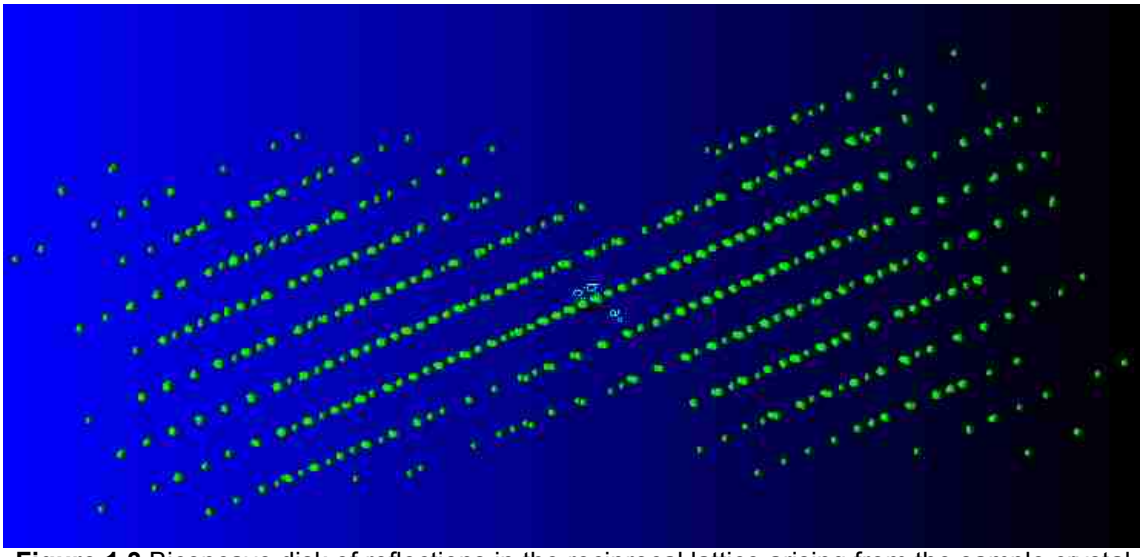

Figure 1.3 Biconcave disk of reflections in the reciprocal lattice arising from the sample crystal that were collected in a typical high-pressure diffraction experiment. (Image created using APEX2).[14]

The orientation, symmetry and unit cell dimensions of the crystal all influence how problematic the restricted geometrical access to the sample is. If the crystal is in a low symmetry space group then the data completeness to a given resolution will be low. As shown in figure 1.2, access to the sample is most restricted in the axis along the X-ray beam. Therefore, if the crystal is orientated such that a short unit cell axis is aligned along the direction of the beam then few reflections will be observed along that axis.

Early high-pressure crystal structures determinations included water ice (1965),[15] chloroform (1968),[16] and benzene (1971).[17] Water ice and benzene were both found to adopt a different polymorph to that seen at ambient-pressure and low-temperature, while high-pressure chloroform was found to be isostructural with its low-temperature form. However, due to the difficulty in collecting data of sufficient quality and completeness to solve the phase problem, structural study at high-pressure was relatively rare before the turn of the millennium. This is highlighted by the fact that in 2000, there were only 123 CCDC entries at high-pressure,[12] a figure that has risen tenfold to 1217 as of August 2014. The sharp upturn in high-pressure diffraction research may be principally attributed to the use of CCD detectors. Previously, most diffraction studies had been carried out using a point detector. Data collection times using point detector often took several weeks for samples in low symmetry space groups and/or with a large unit cell.[18]

1.1.1 Experimental Techniques

1.1.1.1 Crystal Centering

For any single crystal X-ray diffraction experiment, the crystal must be centred in the X-ray beam, a process normally achieved by placing the crystal at the optical centre of the instrument. Sample centring is more challenging in high-pressure diffraction studies as the sample may only be viewed through the diamond windows. An additional problem is that the refractive index of diamond (2.419) is very different to that of air.[19] This means that the apparent crystal position on the camera is different for samples mounted in a diamond anvil cell and those mounted in air.

The process used to centre the sample in thesis utilises a camera mounted on a movable platform that may be adjusted by a micrometer. Having the camera mounted in this way makes centering samples less difficult because it is possible to accurately and precisely record the magnitude of a change in the focal point of the camera (x in figure 1.5). The experimental setup in the centring protocol is shown in figure 1.4. The centring process is illustrated below in a flowchart in figure 1.5.

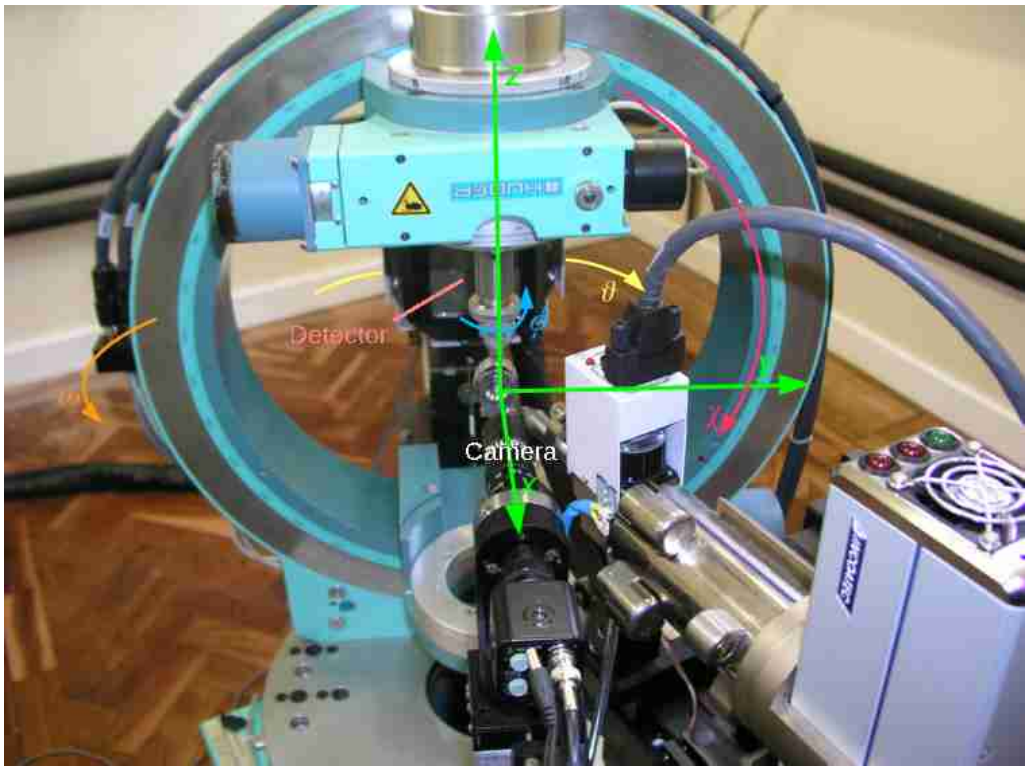

Figure 1.4 Photograph showing the experimental setup at the start of the centring procedure, with the window of the diamond anvil cell facing the camera. The three Cartesian axes; x, y and z are shown in green. Movement of the ϕ, ω, χ and ϑ circles is shown in blue, orange, red and yellow respectively.

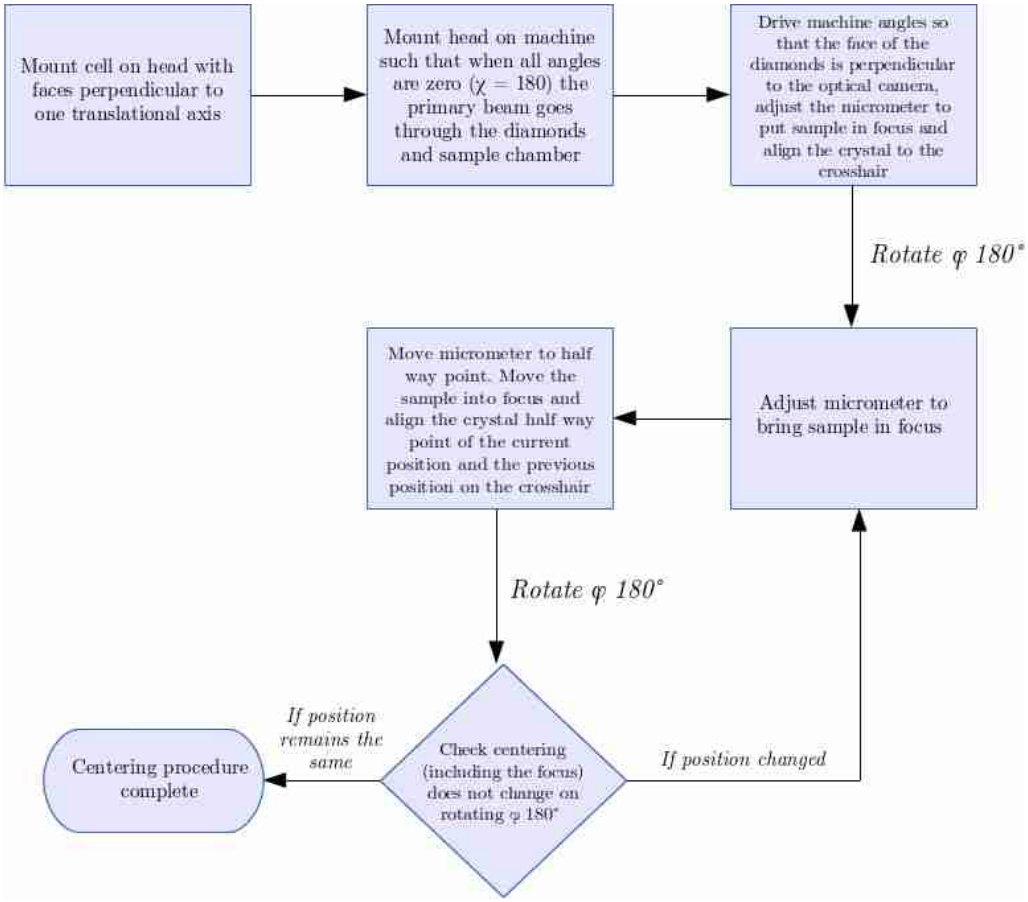

Figure 1.5 Flowchart showing a method of centring a single crystal held in a diamond anvil cell.

For very small samples centring by diffraction may be required.[20] This was not needed for much of the work carried out in this thesis, as crystals grown from the liquid grow to fill the gasket and as such are relatively large in comparison to the beam.

1.1.1.2 Data Collection Strategy

Due to the body of the DAC eclipsing incoming and outgoing X-radiation, data can only be collected at certain combinations of χ, ω, ψ and θ. These correspond to the orientations of the cell that allow diffraction events to occurs and be recorded on the detector.

Diffraction images collected from the middle of the DAC's opening window contain higher quality data as there is no shading of the detector by the DAC, and there is less scatter from the gasket and backing plates. Given that during data integration a model profile is generated using reflections observed from the first few diffraction images, collecting data from the open to eclipsed orientation is desirable. Therefore, two sister scans are used to cover the opening window at a given orientation. Both scans cover

slightly more than half of the opening window in order that reflections towards the middle of the window are fully observed in one or both scans.

Table 1.1 shows a typical data collection strategy employed in high-pressure single-crystal diffraction experiments carried out in this thesis.

Scan Type	Distance / mm	2θ	ω	ψ	χ	Sweep Length / °	Sweep Direction
Phi	60	-10	0	-10	180	50	Positive
Phi	60	-10	0	10	180	50	Negative
Phi	60	-10	0	170	180	50	Positive
Phi	60	-10	0	-170	180	50	Negative
Phi	60	-10	-10	160	135	60	Positive
Phi	60	-10	-10	-160	135	60	Negative
Phi	60	-10	-10	-20	135	60	Positive
Phi	60	-10	-10	20	135	60	Negative
Phi	60	10	10	-10	180	50	Positive
Phi	60	10	10	10	180	50	Negative
Phi	60	10	10	170	180	50	Positive
Phi	60	10	10	-170	180	50	Negative

Table 1.1 Typical data collection strategy used in high-pressure single-crystal diffraction experiments carried out in this thesis.

1.1.1.3 Masking Occluded Regions of the Diffraction Pattern

Regions of the detector in certain diffraction images cannot collect useful diffraction data as the path from the crystal to the detector is occluded by the DAC. These regions are often described as shaded. Since no diffraction data can be collected from these regions they should be removed before the integration stage of the data processing. This can be achieved by creating mask files that remove these areas of the diffraction pattern from the data integration process. (For example, by using the program ECLIPSE[21].)

1.1.1.4 XIPHOS II Diffractometer

High-pressure data described in this thesis were collected on XIPHOS II,[22] a four-circle diffractometer custom-built for high-pressure studies at the XIPHOS diffraction facility[23] (initially at Durham University, now at Newcastle University). XIPHOS II uses an Incoatec Ag IμS[24] system (λ = 0.5609 Å) for generating X-radiation. Ag radiation is ideal for high-pressure studies, despite the decrease in scattered intensity, as more

data can be collected within the geometrical constraints of the DAC. Additionally, due to its lower wavelength than Cu (λ = 1.5418 Å) or Mo (λ = 0.7107 Å), Ag radiation is less strongly absorbed by the diamond anvils than more conventional longer wavelength radiation.

1.1.2 Diffraction Theory and Analysis

1.1.2.1 The Bragg Condition

W. L. Bragg showed that any diffraction event can be treated as if it were a reflection from sets of parallel lattice planes in the crystal structure. A diffraction event may only observed when the interference between the beams is constructive, i.e. the path length difference between the two beams must be a equal to a integer number of wavelengths. This is visualised below in figure 1.6.

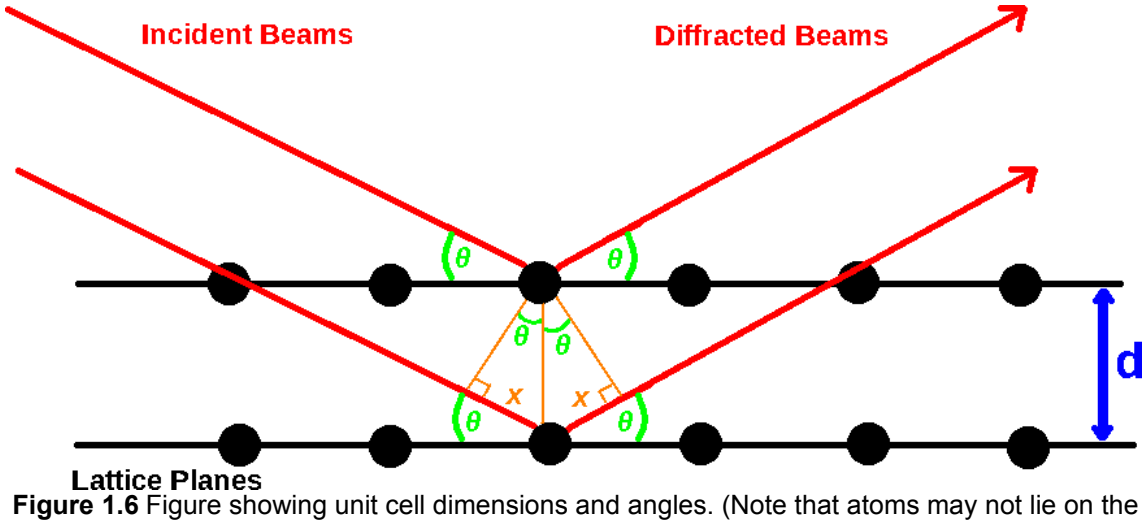

Figure 1.6 Figure showing unit cell dimensions and angles. (Note that atoms may not lie on the lattice planes)

For the interference to be constructive, nλ = 2*x*. Using trigonometry it is clear that *x* = d sin *θ*, thus the Bragg Condition is met when nλ = 2d sin *θ* .

1.1.2.2 Unit-Cell Determination

In an ideal crystallographic experiment, all of the reflections collected in a set of images result from scatter from the sample. Those reflections with a I/σI (where I is the intensity and σI represents the error in the intensity measurement) value ≥ a particular value may then be used to calculate the unit cell dimensions and orientation matrix of the sample. This is done by calculating the vectors between reflections and selecting the three shortest non-coplanar vectors. A unit cell is a parallelepiped that when reproduced through translational symmetry alone reproduces the crystal structure in

three dimensions. The unit cell may be defined by a combination of three unit cell dimensions, a, b and c and three angles, α, β and γ as shown below in figure 1.7.

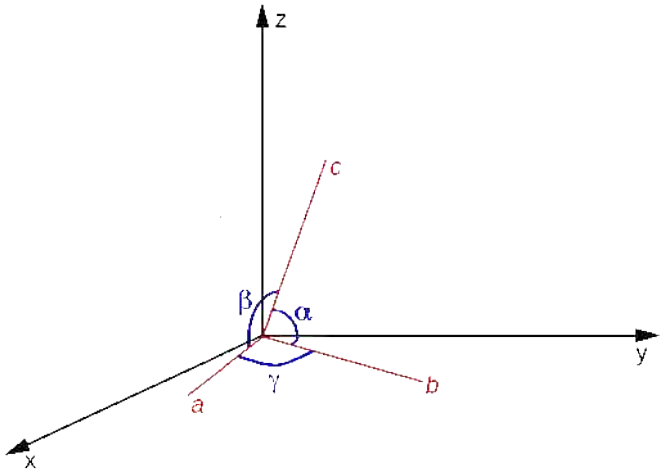

Figure 1.7 Figure showing unit cell dimensions and angles

Unit cells may be categorised into one of seven lattice systems dependant on the point group of the diffraction pattern. Combination of the lattice system with lattice centring results in the formation of fourteen symmetrically distinct lattices (known as *Bravais Lattices*), as shown in table 1.2.[25]

Lattice system	**Laue Class**	**Centring Allowed**	**Essential Symmetry**	**Restrictions on unit cell**
Triclinic	-1	*P*	None	None
Monoclinic	2/*m*	*P C*	1 x 2-fold rotation (parallel to b)	α = γ = 90°
Orthorhombic	*mmm*	*P C I F*	3 x perpendicular 2-fold rotations	α = β = γ = 90°
Tetragonal	4/*m*, 4/*mmm*	*P I*	1 x 4-fold rotation (parallel to c)	a = b, α = β = γ = 90°
Rhombohedral	-3, -3*m*	*P*	1 x 3-fold rotation	a = b = c, α = β = γ ≠ 90°
Hexagonal	6/*m*, 6/*mmm*	*P*	1 x 6-fold rotation (parallel to c)	a = b, α = β = 90°, γ = 120°
Cubic	*M*3, *m*-3*m*	*P I F*	4 x 3-fold rotations (along body diagonals)	a = b = c, α = β = γ = 90°

Table 1.2 Table showing crystal systems, Laue Class (point group of the diffraction pattern) centring allowed, the essential symmetry, and the restrictions on the unit cell.

In high-pressure diffraction experiments, collecting all reflections with a value of I/σI over a given value (typically around 3) leads to harvesting diffraction spots arising from the gasket, backing plate, both diamonds, ruby and sample. As such, some automated indexing programs may not be able to determine the unit-cell of the sample. This may be overcome by using Sheldrick's CELL NOW program[26] or by manually removing diffraction spots not arising from the sample using a reciprocal lattice viewer[27] before using an automated indexing program.

1.1.2.3 Data Reduction

In the data reduction process, the intensity of each reflection in a dataset is converted into structure factor amplitudes. Some corrections to the intensity data need to be made in this process. The relationship between the intensity data and the structure factors is given by:

$$|F_{hkl}| = K\sqrt{\frac{I_{hkl}}{Lp.Abs}}$$

Here, *K* is simply a scale factor, relating to the crystal and radiation wavelength in question.

The need for a Lorentz correction, *L*, arises from the fact that some reciprocal lattice points pass through the Ewald sphere more rapidly than others. Those that pass through more quickly will give rise to an anomalously low intensity reflection. The Lorentz correction thus applies a scaling factor to the raw intensity data based on the speed at which it passes through the Ewald sphere. The need for a polarisation correction, *p*, arises from the partial polarisation of the beam by a crystal monochromator. The intensity of diffracted intensity is proportional to the root of the sine between the incident and scattering vectors and therefore diffracted intensity varies with 2*θ*. The Lorentz and polarisation corrections can be applied with no knowledge of the crystal structure, and thus may be automatically applied within data reduction programs. Absorption corrections are applied to correct for the loss of diffracted intensity due to the crystal absorbing incoming X-radiation. The magnitude of the absorption of X-radiation by crystals is highly dependant on the composition of the crystal, with heavy atoms absorbing more strongly than lighter atoms.

SADABS[28] is a program used throughout this work to scale diffraction data. It exploits the high redundancy of data in datasets collected by area detectors to correct for systematic errors such as absorption. The program operates by correcting reflections to have a similar intensity to symmetrically equivalent reflections using the formula $I_c = I_o . S_n . P_{uvw}$ where *S* and *P* are refined such that $\sum w(\langle I_c \rangle - I_c)^2$ is minimised. (Here, S_n is the scale factor relating to diffraction image *n* and P_{uvw} is the absorption factor).[29]

The scale factor correctors for various errors such as:[29]

- Absorption of X-radiation by the crystal
- Changes of the volume of crystal in the beam
- Decomposition of the crystal
- Variation in intensity of the primary beam

The weight of outliers is downgraded by calculating an error model for the reflections. The error model is given by $\sigma^2_{abs} = k[\sigma^2_{raw} + g\langle I \rangle^2]$. *k* and *g* are refined such that a bin of reflections of similar intensity has a normal distribution of intensities by minimising the function $\chi^2 - 1$.[29]

1.1.2.4 Space Group Determination

Once the unit cell has been determined and assigned to one of the fourteen Bravais lattices and the diffraction data has been collected then the space group may be determined. This is achieved through examination of systematically absent reflections. Translational symmetry elements in the crystal structure result in groups of lattice planes that diffract X-radiation out of phase. This causes destructive interference and thus the reflection is not observed.

For example, a N_M screw axis is a rotation of $\frac{360}{N}$ degrees about a line, followed by a translation of $\frac{M}{N}$ along that line. If there is a 2_1 screw axis parallel to **a**, then the position (*x*, *y*, *z*) is equivalent to the position (*x* + 0.5, -*y*, -*z*). This causes reflections to be systematically absent if *k* and *l* are both 0 and *h* is odd. This is explained through analysis of the structure factors.

$$F_{hkl}=\sum_j f_j[\exp[2\pi i(hx_j+ky_j+lz_j)]+\exp[2\pi i(h(x_j+\frac{1}{2})-ky_j-lz_j)]]$$

$$F_{h00}=\sum_j f_j[\exp(2\pi ihx_j)+\exp(2\pi ih[x_j+\frac{1}{2}])]$$

As $e^{n+m} = e^n \cdot e^m$: $F_{h00}=\sum_j f_j[\exp(2\pi ihx_j)+\exp(\pi ih).\exp(2\pi ihx_j)]$

$$F_{h..}=\sum_j f_j\exp(2\pi ihx_j)[1+\exp(\pi ih)]$$

As $e^{i\pi} = -1$: $F_{h00}=\sum_j f_j\exp(2\pi ihx_j)[1+(-1^h)]$

Thus if *h* is odd, F_{h00} is equal to zero, and therefore systematically absent. It is possible to derive the systematic absences relating to glide planes and lattice centring in a similar manner. These are shown below in table 1.3.

Symmetry Element		**Absence Conditions**
A centring		*k* + *l* = 2n + 1
B centring		*h* + *l* = 2n + 1
C centring		*h* + *k* = 2n + 1
F centring		*h, k, l* all even or all odd
I centring		*h* + *k* + *l* = 2n + 1
R (obverse)		-*h* + *k* + *l* = 3n
R (reverse)		*h* – *k* – *l* = 3n
2_1, 4_2, 6_3 screw axes || *a*, *b*, *c*		*h*00: *h* = 2n, 0*k*0: *k* = 2n, 00*l*: *l* = 2n
3_1, 3_2, 6_2, 6_4 screw axes || a, *b*, *c*		*h*00: *h* = 3n, 0*k*0: *k* = 3n, 00*l*: *l* = 3n
4_1, 4_3 screw axes || *a*, *b*, *c*		*h*00: *h* = 4n, 0*k*0: *k* = 4n, 00*l*: *l* = 4n
6_1, 6_5 screw axes || *a*, *b*, *c*		*h*00: *h* = 6n, 0*k*0: *k* = 6n, 00*l*: *l* = 6n
glide plane ⊥ *a*	translation *b*/2 (b)	0*kl*: *k* = 2n
	translation *c*/2 (*c*)	0*kl*: *l* = 2n
	translation *b*/2 + *c*/2 (n)	0*kl*: *k* + *l* = 2n + 1
	translation *b*/4 + *c*/4 (d)	0*kl*: *k* + *l* = 4n + 1
glide plane ⊥ *b*	translation *a*/2 (a)	*h*0*l*: *h* = 2n
	translation *c*/2 (b)	*h*0*l*: *l* = 2n
	translation *a*/2 + *c*/2 (n)	*h*0*l*: *h* + *l* = 2n + 1
	translation *a*/4 + *c*/4 (d)	*h*0*l*: *h* + *l* = 4n + 1
glide plane ⊥ *c*	translation *a*/2 (a)	*hk*0: *h* = 2n
	translation *b*/2 (b)	*hk*0: *k* = 2n
	translation *a*/2 + *b*/2 (n)	*hk*0: *h* + *k* = 2n + 1
	translation *a*/4 + *b*/4 (d)	*hk*0: *h* + *k* = 4n + 1

Table 1.3 Table showing conditions for systematic absences

Analysis of systematic absences does not distinguish between some pairs of space groups, for example where one space group is centrosymmetric and the other is its acentric (e.g. *P*1 and *P*-1). Determining which of the pair of space groups a crystal structure is in may be achieved by examination of the average values of the normalised structure factors, $\langle E \rangle$ and $\langle E^2 - 1 \rangle$, as shown in table 1.4. These values should not be dependant on the composition of the crystal.

Space Group	$\langle E \rangle$	$\langle E^2 - 1 \rangle$
centrosymmetric	0.798	0.968
acentric	0.886	0.736

Table 1.4 Table showing $\langle E \rangle$ and $\langle E^2 - 1 \rangle$ values for centrosymmetric and acentric crystals,

1.1.2.5 An Introduction to the Solution of the Phase Problem

Any wave diffracted by a crystal has a given phase and amplitude. The combination of these two variables is known as the structure factor, F_{hkl}. The phase of an X-ray beam, α_{hkl} is not easily measured experimentally. α_{hkl} can be thought of as the phase difference between a wave scattered at the origin of a unitcell and that scattered by the plane *hkl*.[30] However, the intensity of the beam, which is directly proportional to the square of the amplitude of the structure factor, $|F_{hkl}|^2$, can be more readily measured.

The structure factor for a given diffracted beam may be defined as:

$$F_{hkl} = \sum_j f_j \exp[2\pi i(hx_j + ky_j + lz_j)]$$

Here, the sum considers all the atoms present in the unit cell. (x_j , y_j, z_j) represent the co-ordinates of the j^{th} atom and f_j represents the atomic scattering factor of the j^{th} atom. The atomic scattering factor simply represents how strongly the atom in question scatters X-rays. The form factor is proportional to the number of electrons in the atom (i.e. the atomic number). At sin $\theta/\lambda = 0$, the form factor is maximal, and decreases as sin θ/λ increases.

The electron density at any location (*x*, *y*, *z*) in a unit cell of volume *V* is given by[31]

$$\rho_{xyz} = \frac{1}{V} \sum_{all hkl} \sum |F_{hkl}| \exp[-2\pi i(hx + ky + lz)]$$

Direct methods are the most commonly used method for retrieving phase information in crystallography. These methods determine the phases using only measured intensities. The fact that electron density must be non-zero throughout the crystal with positive peaks at atomic locations is used to derive equations relating the relationships between phases. A further restriction is that in centrosymmetric structures the phase angle must be 0 or 180°, meaning that cos α = +/- 1.). Electron density waves in a centrosymmetric 1-dimensional cell are shown in figure 1.8 below.

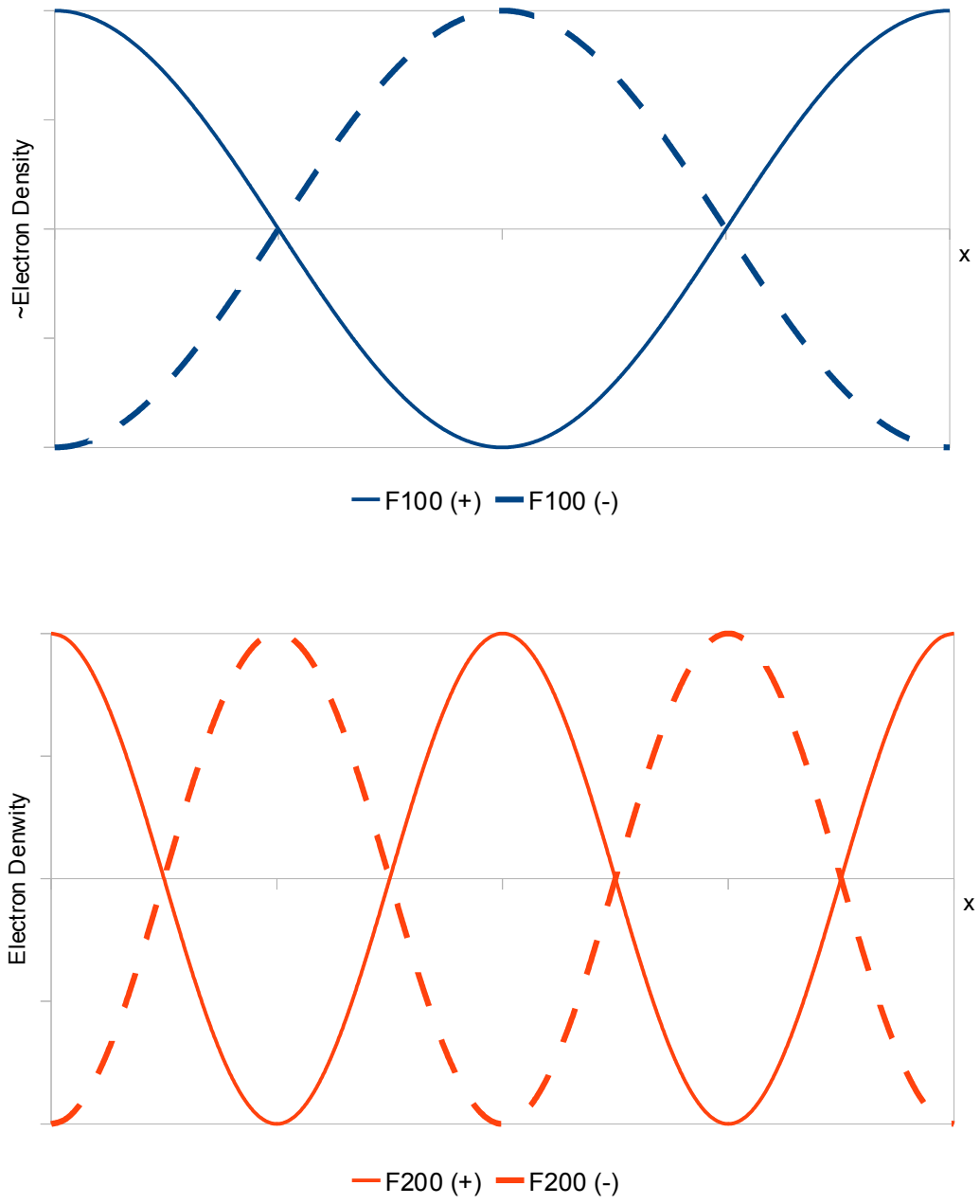

Figure 1.8 One dimensional electron density maps derived solely from structure factors (**Top**) *F*(100) and (**Bottom**) (200) [(+) and (-) refer to phase angles of 0 and 180° respectively]

If *F*(1 0 0) is strong, then it can be shown that the phase of *F*(2 0 0) is likely to be 0° regardless of the phase of *F*(1 0 0) in a centrosymmetric structure. This principle can be extended to three dimensional centrosymmetric structures:

$$S(h_h, k_h, l_h) \approx S(h_{h'}, k_{h'}, l_{h'}).S(h_{h-h'}, k_{h-h'}, l_{h-h'})$$

(Here *S* refers to the sign of the phase angle, 0° being positive, 180° being negative)

This can be expressed in more concise notation as $S_H \approx S_{H'}.S_{H-H'}$

Here S refers to the sign and $\approx$ means probably equal to. This relationship is known as the triplet equation.[32] The probability, *P*, of the triplet equation being correct is given by

$$P = \frac{1}{2} + \frac{1}{2}\tanh\left(N^{\frac{-1}{2}}|E_H.E_{H'}.E_{H-H'}|\right)$$

Here, *N* refers to the number of atoms in the unit cell and *E* refers to the structure factor, *F*, normalised to take into account the decrease in the magnitude of the scattering factor with increasing scattering angle, $E^2_{hkl} = \frac{F^2_{hkl}}{\langle F^2_{hkl} \rangle}$, where $\langle F_{hkl}^2 \rangle$ refers to the average value of F_{hkl}^2 at a given resolution.[33]

If the structure is non-centrosymmetric, the tangent formula may be used to determine the relationship between sets of phases:[34]

$$\tan\varphi_H \approx \frac{\sum_{H'} |E_{H'}||E_{H-H'}||\sin(\varphi_{H'} + \varphi_{H-H'})}{\sum_{H'} |E_{H'}||E_{H-H'}||\cos(\varphi_{H'} + \varphi_{H-H'})}$$

These equations give only the relationship between the phase angles rather than giving absolute values for the phase angles. In direct method programs, the phases are initially given random values and the phases of all structure factors are then generated from these randomly generated phases. The procedure is then repeated using different randomly generated sets of phases until the program finds a set where the initial phasing was found to be correct, thus solving the phase problem.

1.1.2.6 Structure Refinement

After the determination of a model which successfully determines the position of most of the atoms in the structure, the model is improved through refinement in order to better match the diffraction data. Least squares refinement is the most commonly used method to fit the model to the data. In least squares refinement, the square of the difference between the square of the experimentally determined structure factors (*Fo*) and the square of those calculated from the model (*Fc*) is the typical function minimised:

$$Q = \sum w \left| F_o^2 - F_c^2 \right|^2$$

w represents a weighting scheme.(Some prefer to refine the data using ΔF rather than ΔF^2)

The model should be refined such that the residual electron density is minimised in a chemically reasonable manner. The correctness of the model can be calculated using several functions. The most often used are the residual and weighted *R*-factors:

$$R = \frac{\sum \left| |F_o^2| - |F_c^2| \right|}{\sum |F_o^2|} \qquad wR = \sqrt{\frac{\sum |w\,|F_o^2 - F_c^2|^2|}{\sum |w\,F_o^2|}}$$

Residual R Factor (Left) and Weighted R Factor (Right)

A low *R*-factor does not necessarily mean that the refinement is of a high-quality, merely that the model matches the data well. It is quite possible that a poor quality refinement may match poor quality data well, thus giving a sub-optimal structure with a low *R*-factor. Care should thus be taken that the model is chemically reasonable and has reasonable anisotropic parameters as well as merely having acceptable (typically < 0.075 for a small molecule structure) *R*-factors.

1.1.2.7 Programs used to Analyse Diffraction Data

In both high-pressure and low-temperature experiments, SAINT[35] and SADABS were used for data reduction within the Bruker APEX2 GUI.[14] The SHELX suite of programs was used for structural solutions and least squares refinement[36] within the Olex 2 GUI.[37,38]

1.1.2.8 Position of Hydrogen Atoms

Given that hydrogen bonding is highly important when considering intermolecular interactions, it is important to briefly consider the role played by hydrogen atoms in single-crystal X-ray diffraction experiments. X-rays are scattered by electrons, of which hydrogen atoms only have one. The true position of hydrogen atoms therefore cannot always be observed from an electron density difference map following elucidation and refinement of heavier atom positions and displacement parameters. As the associated electron of all hydrogen atoms is held in a bond, the position of the atom is systematically incorrect and therefore the length of all H-X bonds are underestimated by X-ray diffraction.

Hydrogen atoms may be accurately and precisely located using neutron diffraction, as neutrons are diffracted mostly by the nuclei of the atoms and as such the scattering length does not depend on the number of electrons that an atom has. Neutron scattering lengths do not vary systematically according to the atomic mass of the atom involved. This is shown in figure 1.9 below.

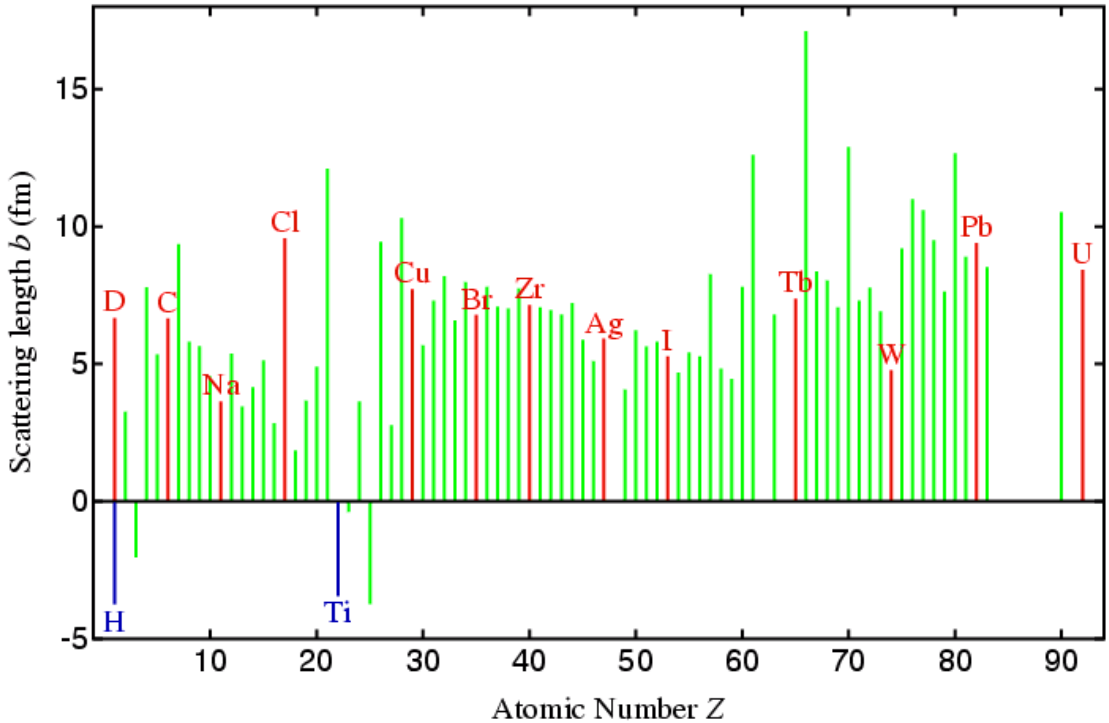

Figure 1.9 Scattering length of elements in the periodic table. A positive scattering length means that the neutron is repulsed by the nucleus, a negative scattering length means that the neutron is attracted by the nucleus. Reproduced with permission from Jeremy Karl Cockroft (pd.chem.ucl.ac.uk)

Unfortunately, single-crystal neutron diffraction cannot be widely used due to the very high running costs of neutron sources and requirement for large crystals (of the order of 1 mm^3 or greater).

1.2 Cryo-Crystallisation

In-situ cryo-crystallisation (used herewithin for comparative purposes with high-pressure crystallisation) has been employed for many decades to probe the structure and intermolecular interactions of materials that are liquids under ambient conditions.[39] The standard technique used to obtain crystals by cryo-crystallisation suitable for single crystal X-ray diffraction, is as follows: a thin (c.10 μm) walled borosilicate glass capillary (known as a Lindemann tube) of typical diameter 0.3 – 0.5 mm is filled with the sample. The capillary is then sealed at both ends by suspending the end of the capillary in a flame. Borosilicate glass tubes are normally used in cryo-crystallisation experiments for two principal reasons. Firstly, they are very resistant to thermal stress and to attack from most laboratory chemicals except very strong alkalis and acids. Secondly, borosilicate glass produces less background scatter, as it may be made thinner than most other glasses due to its high surface strength.

After the sample is loaded, the temperature is lowered until crystallisation occurs through homogeneous nucleation. This is typically some 10's of degrees below the melting point. For example, water is known to homogeneously nucleate at -48 °C.[40] Cooling a liquid to below its melting point with no subsequent phase change is possible, because in the absence of a seed crystal / nucleus, (homogenous) nucleation requires the unfavourable formation of an interface at the boundary of the nucleus and the surrounding phase. The formation of the bulk solid, however, remains favourable. These two factors are in direct competition. When the radius of the nucleus is low, the unfavourable interface energy is larger than the favourable bulk free energy. However, the bulk free energy increases more rapidly than that of the interface energy with the increasing radius of the nuclei. This is because the bulk free energy scales with r^3, whereas the interface term is dependant on the surface area, and hence scales with r^2.

It therefore follows that a critical size of nuclei is required for the crystal to be stable with respect to the liquid phase and to allow growth to the solid phase. This is demonstrated in figure 1.10.

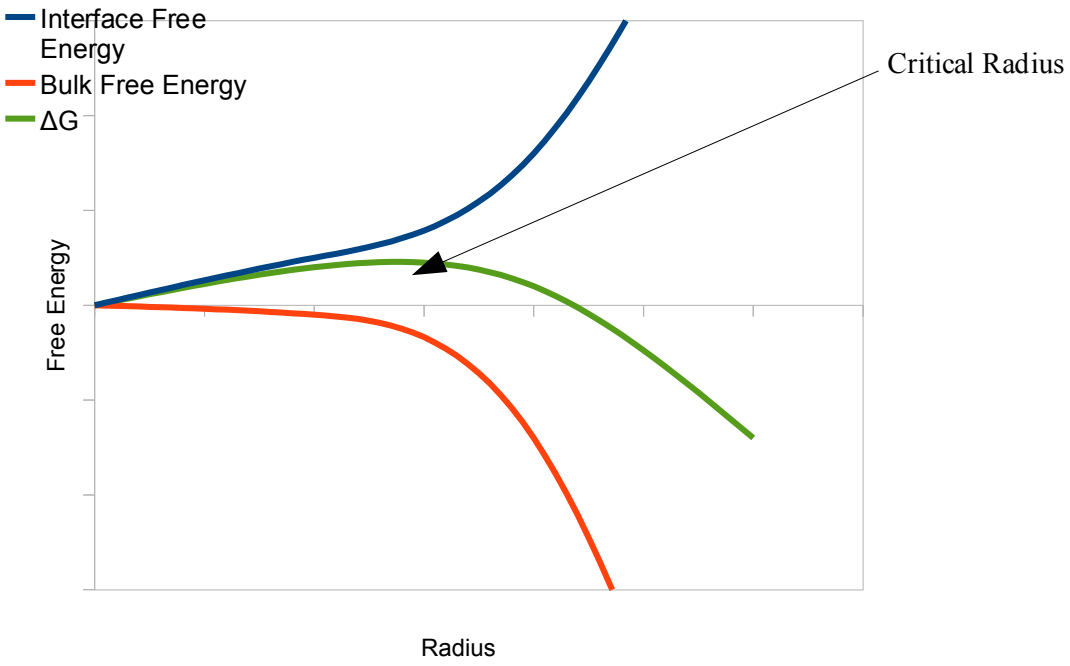

Figure 1.10 Schematic of contributions to the free energy in homogeneous nucleation

As the temperature is lowered, the difference in the Gibbs free energy between the liquid and solid phase increases, as the entropic term decreases in magnitude. This increases the bulk free energy term, decreasing the required size of the critical radius of the nucleus. Therefore, on cooling, the critical radius is eventually sufficiently small that crystallisation may spontaneously occur, forming a polycrystalline phase.

Following crystallisation, the temperature is then raised to just below the melting point. There are several different methods to grow single crystals from this point: One common method is to use an IR-laser (with a typical power of 25 W) to melt the sample in a localized zone (typically smaller than 0.1 mm). Local temperatures in the beam may exceed 1000°C.[41] Scanning the laser up and down the length of the capillary causes the melting of smaller satellite crystals and growth of the larger crystals to a size suitable for single crystal X-ray diffraction experiments.[41] Another method used is to gently touch the capillary to melt a localized section of crystals, before letting the remaining crystallites grow to a sufficient size for study through single-crystal X-ray diffraction experiments. The second method was employed throughout this thesis.

Examples of phenomena studied using cryo-crystallisation include the alternation in melting points and densities with increasing number of carbons in alkanediols, diamines,[42] and alkanedithols;[43] and study of electron density of distribution in boranes,[44] ethylene glycol,[45] and ammonia.[46] Study of low-temperature / high-pressure

polymorphism in liquids, as studied herein, has previously been examined in fluoro and chlorophenols using cryo-crystallisation.[47,48]

Data obtained in cryo-crystallisation experiments can be complimentary to the high-pressure diffraction data, providing an ambient-pressure benchmark against which the high-pressure data can be compared.

Chapter 2: Introduction to Polymorphism and Intermolecular Interactions

2.1 Polymorphism

The best definition of polymorphism is given by Dunitz, who described it as the existence of different crystal structures that melt to give identical liquid and vapour states.[49] Polymorphism is of critical importance in fields such as materials science, biosciences and pharmaceuticals because different polymorphs may have very different properties. For example, the bioavailablity of different polymorphs of drug molecules may be substantially different.[50]

To give well known example, a cursory examination of the polymorphic structures of carbon; graphite and diamond, is more than sufficient to understand why diamond is an extremely hard, high melting point solid, while graphite is a brittle solid that exhibits anisotropic behaviours (such as anisotropic thermal expansion and thermal conductivity)[51]. Obviously the dissimilarity in the structure of these materials leads to very different functionality and exemplifies why the study of polymorphism is of wider interest than a mere esoteric examination of structural change.

Given the importance of polymorphism, a deep understanding of when, how and why it occurs is highly desirable. It has been recognised that the observation of multiple polymorphs of a material should be expected; McCrone famously wrote "*every compound has different polymorphic forms … in general, the number of forms known for a given compound is proportional to the time and energy spent in research on that compound.*"[52] Indeed, Buerger and Bloom stated as far back as the 1930's that "*polymorphism is an inherent property of the solid state and it fails to appear only under special conditions.*"[53] However, theoretical calculations usually find more thermodynamically competitive crystal structures than are observed through experiment, indicating that, for one reason or another, some polymorphs may be difficult or impossible to crystallise.[54]

For one possible explanation why more than one polymorph occurs, one should examine the Gibbs equation: $G = U - TS + PV$. At a temperature of absolute zero $G = U$ and this would suggest that the most stable polymorph should be that with the lowest internal energy. However, in reality entropy also plays a role, and it may be that this explains phase transformations or a change in the stability ordering at variable

temperatures.

Kinetic factors may also be important. Specifically, if the formation of one crystal form has a lower activation energy than another, that crystal structure may form under kinetic control even if it is less thermodynamically favourable. This is illustrated below in figure 2.1.

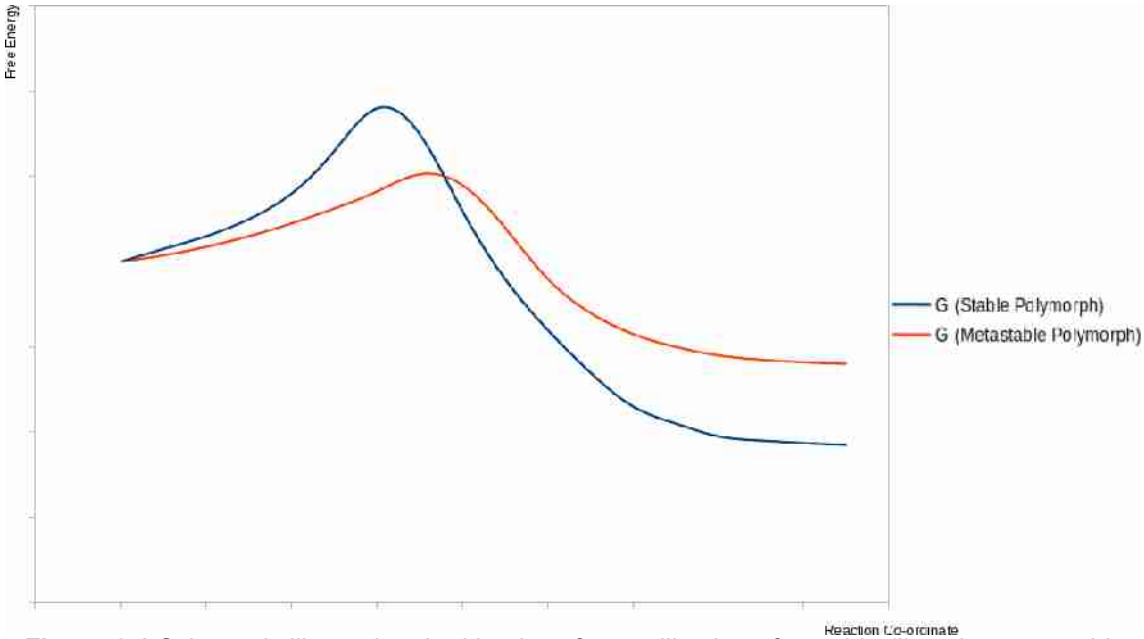

Figure 2.1 Schematic illustrating the kinetics of crystallisation of a stable (I) and a metastable (II) polymorph.

Clearly, the activation energy of the thermodynamically stable polymorph in the above figure is higher than that of the metastable polymorph. This issue was originally addressed by Ostwald. He stated that it was the least stable polymorph that crystallised first from the melt, going through any possible intermediates to the most stable polymorph.[55]

One explanation for Ostwald's empirical observation is that the least stable of a set of observed polymorphs at low-temperature is actually the most stable polymorph at the melting point. This is known as an enantiotropic system. In such a system, the system will go through a series of changes that correspond to the inverse order of stability at low-temperature as one crystallises from the melt. This is demonstrated in figure 2.2.

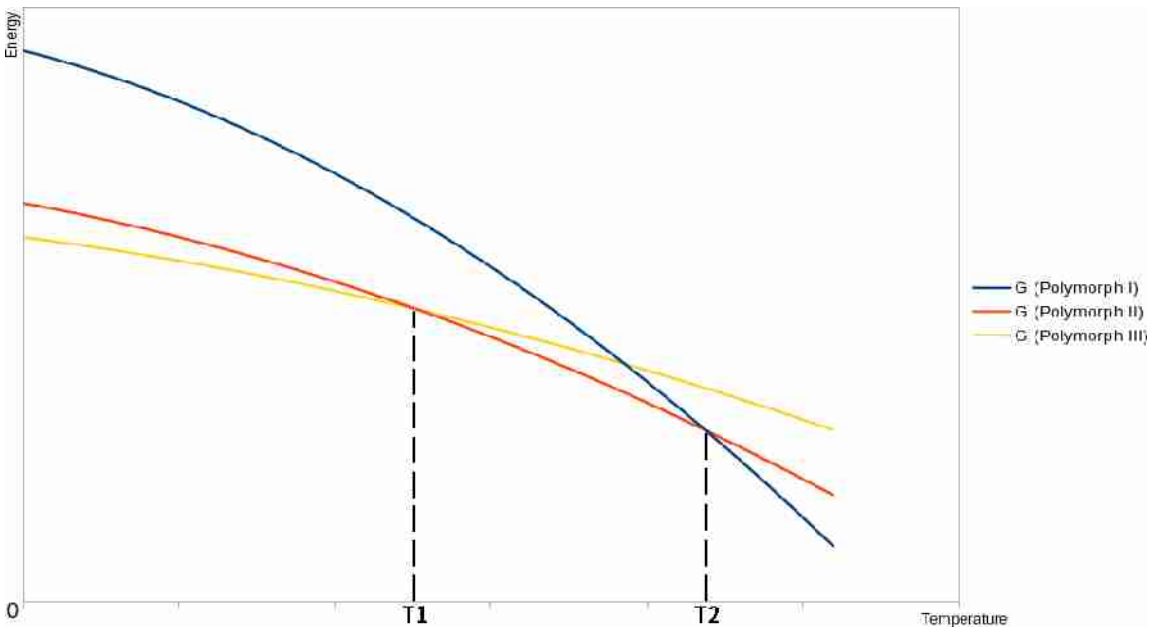

Figure 2.2 Schematic illustrating the free energy as a function of temperature for a set of three enantiotropic polymorphs

In this scheme, polymorph III is the lowest in energy and polymorph I the highest in energy at low-temperature (<T1). At high-temperatures, (>T2) polymorph I is the lowest in energy and polymorph III the highest. At intermediate temperatures (between T1 and T2), polymorph II is the lowest in energy.

Therefore, when the liquid is cooled below the melting point, it will crystallise, forming polymorph I. When the temperature is lowered below T2, a phase transition from polymorph I to polymorph II is thermodynamically favourable. When the temperature is further lowered below T1, a phase transition from polymorph II to polymorph III is thermodynamically favourable.

2.1.1 High-Pressure / Ambient-Pressure Polymorphism

2.1.1.1 Polymorph Stability Under Pressure

Ostwald's observation presumes that the pressure is low and constant throughout the crystallisation experiment. If high-pressure is applied to the sample, more factors must be considered.

The thermodynamic relationship between two structures at a given temperature and pressure are represented by the equation.

$$\Delta G = \Delta U - T\Delta S + P\Delta V$$

U, the internal energy, represents the energy of interactions within the crystal structure. The *TΔS* term represents the entropic term, and *PΔV* the contribution of pressure and volume.

At ambient pressure, the *PΔV* term is negligible and thus the order of stability follows the order given by *U* – *TΔS*. However, on increasing the pressure to the magnitudes created in a diamond anvil cell the *PΔV* term becomes increasingly relevant. Clearly, structures with a smaller volume will have a less unfavourable *PΔV* term and thus will be less destabilised with increasing pressure.

Many high-pressure polymorphs have significant structural similarity to ambient-pressure polymorphs, these may have the same space group symmetry and may even be almost isostructural.[56] Indeed, in many cases close examination of whether the unit-cell parameters change continuously or abruptly is necessary to determine whether a phase transition has taken place or if the unit-cell transformation is as a result of a highly anisotropic response to the application of pressure.[57,58.59,60]

2.1.1.2 High-Pressure Solid to Solid Phase Transformation Behaviour

Phase transformations under the application of high-pressure commonly give rise to metastable polymorphs. Perhaps the best example of this is glycine,[56] which has three polymorphs at ambient pressure, α, β and γ. These are very close in energy and may be formed concomitantly.[61,62,63,64] The α polymorph is stable to increasing pressure and no phase transformations are observed below 23 GPa.[65] The β polymorph undergoes a single crystal to single crystal transformation at 0.76 GPa,[66,67] to a related structure, β'. The γ polymorph undergoes a destructive phase transition at 3.5 GPa to a δ polymorph.[65-70] On decompression the δ polymorph does not transform back to the γ polymorph, but rather to a new polymorph, ζ.[71] The pressure induced phase transitions that have been found to occur in glycine are shown in figure 2.3.[56]

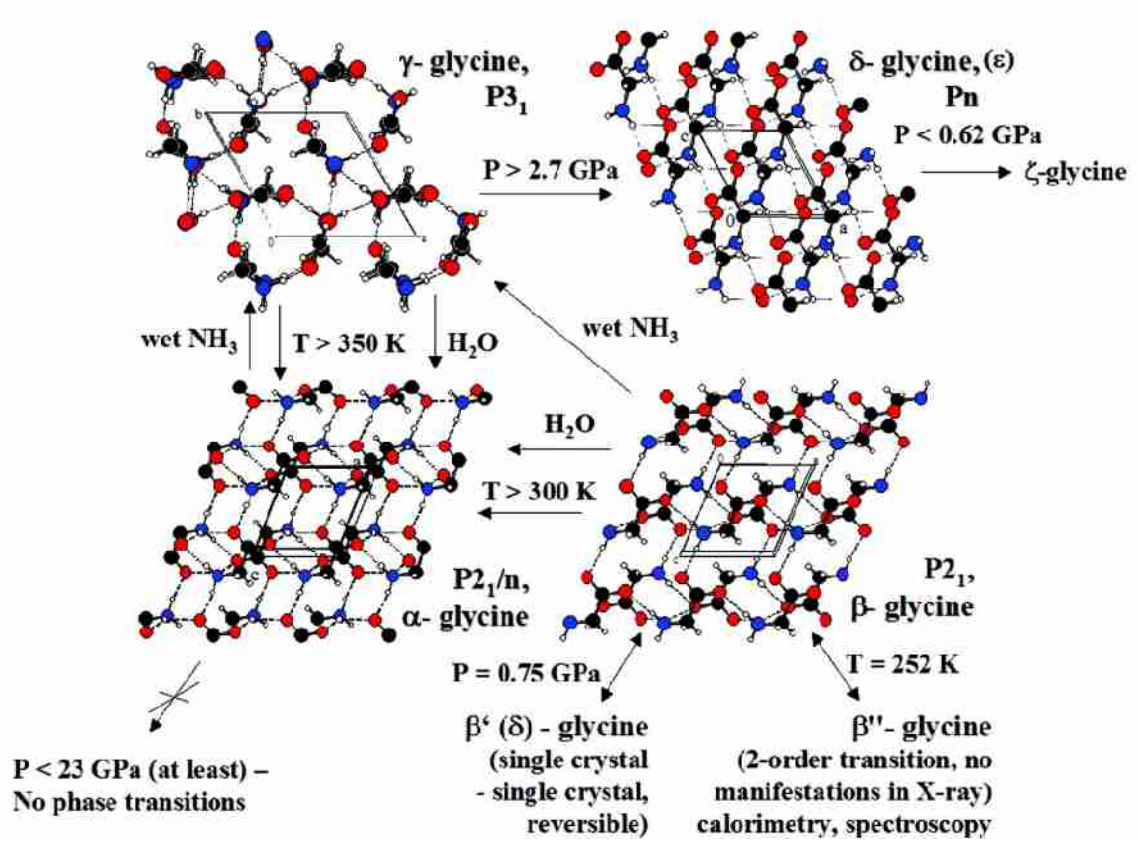

Figure 2.3 Schematic showing solid-to-solid phase transitions in glycine. Reprinted with permission from Ref. 56 © 2008, American Chemical Society

Furthermore, different phase-transformation behaviour has been observed for single crystals and powder samples. A good example of this is paracetamol. Compression of a single-crystal of polymorph I of paracetamol does not result in a phase transformation up to 5 GPa or on subsequent decompression.[72] Compression of paracetamol polymorph I powder does not result in a transformation. However, on subsequent decompression of the powder partial transformation to polymorph II has been observed.[73]

Different rates of compression and the use of different pressure transmitting media are also known to give rise to different phase transformations or alter the pressure at which phase transformations take place.[56] Two polymorphs of $[Co(NH_3)_5(NO)_2]I_2$ can easily be obtained. Transformation of polymorph I to II was not observed in poly-(chlor-tri-fluor-ethylen)-oil, but occurred at 0.5 GPa in a methanol/ethanol mix.[74]

One can see that high-pressure phase changes are difficult to predict and that several variables may effect whether a phase change occurs or not. Significant further investigation may therefore be required to fully characterise all high-pressure polymorphs.

2.1.1.3 Compression of Liquids

There has been significant interest in crystallisation of liquids under high-pressure, both in the examination of intermolecular interactions and the observations of new polymorphs.

There are many examples where the same polymorph is generated as through cryo-crystallisation, for example dichloromethane,[75] and 1,2-dichlorobenzene.[76] However, it is also common for cryo- and high-pressure crystallisation procedures to yield different polymorphs.[77] Examples include acetone,[78] phenol,[79] 1,2-dichloroethane,[80] chlorotrimethylsilane,[81] 1-bromo-2,4,6-trimethylsilane,[82] and 4-fluorophenol.[83]

The formation of distinct polymorphs through cryo- and high-pressure crystallisation may be due to thermodynamics, i.e. a different structure represents the thermodynamic minima at high-pressure to that of ambient-pressure.

However, as rates of compression in high-pressure experiments are typically much greater than the rate of cooling in low-temperature experiments, it can be assumed that the phase barrier is crossed more quickly. This may lead to greater kinetic control in high-pressure crystallisation experiments than in cryo-crystallisation. Furthermore, it has been previously suggested that the presence of impurities in the sample chamber, such as the ruby or metal fragments from the gasket may be able to template the formation of polymorphs that are not observed through homogeneous nucleation in cryo-crystallisation experiments, thus inducing polymorphism.[77]

2.1.2 Polymorphism in terms of Intermolecular Interactions

Polymorphism can be considered as a discrete variation in the distance and orientation of the intermolecular contacts between molecules within a crystal. It is these interactions that drive the packing of molecules to form a particular structure. It is therefore vital to understand the interactions between molecules in order to understand what drives the formation of one polymorph over another.

2.2 Intermolecular Interactions

A crystal structure consists of a perpetual array of molecular subunits, held in place by an intricate, interconnecting, web of intermolecular interactions in an a near infinite repeating pattern that leads to a minimisation of the free energy. Indeed, a crystalline phase may be best understood through examination of the links between molecules as the reason each molecule orients itself at a particular displacement and angle to neighbouring molecules is that this particular orientation represents a maxima (local or global) in the difference between attractive and repulsive intermolecular interactions in the structure. As a crystal consists of an infinite array of these interactions, crystals have been described as "*the ultimate supermolecule*" by Desiraju.[84] Indeed, one could say that the role of the intermolecular interactions in crystal packing is similar to the role of covalent interactions in organic chemistry. Furthering this analogy; organic chemistry has long worked on the principle of retrosynthesis, i.e. breaking down a target molecule into a number of smaller sub-units known as synthons. These are defined by Corey as "*structural units within molecules which can be formed and/or assembled by known or conceivable synthetic operations.*"[85] In his seminal 1995 paper Desiraju extends the principle to supramolecular chemistry, stating that "*if crystals are the supramolecular equivalents of molecules, crystal engineering is the supramolecular equivalent of organic synthesis.*"[34] Likewise, he defined supramolecular synthons as "*structural units within supermolecules which can be formed and/or assembled by known or conceivable synthetic operations involving intermolecular interactions*."[84]

Examples of supramolecular synthons are shown in Figure 2.4 below.

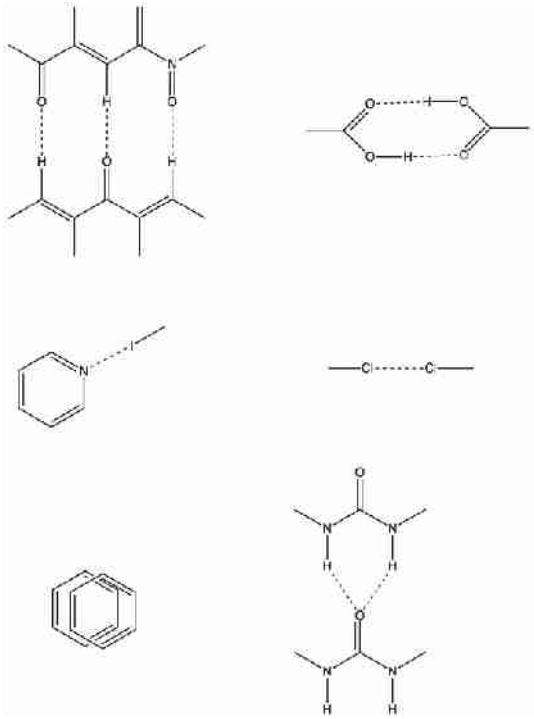

Figure 2.4 Examples of various supramolecular synthons. Origins of the attractive intermolecular forces (shown by a dotted lines) involved in these synthons will be discussed in the upcoming sections.

It should be remembered, that supramolecular synthons such as those shown in figure 1.6 can be incorporated into many different possible space groups and crystal structures. As a result, one cannot design a crystal structure merely through simple incorporation of one or more synthons. This is because the concept of a supramolecular synthon relies on intermolecular bonding arising between two or more distinct covalently bonded systems. The fact that such units have been selected as synthons implies that such a bond is near-universally observed if both units are present in a structure. However, there are a plethora of weaker intermolecular interactions that are not sufficiently strong to be universally observed, and so tend not to be defined as synthons, but still contribute to the lattice energy and thus packing arrangement of the crystal. Although these weak interactions do not individually contribute significantly to the overall energy, the summation of many these makes it is clear that the nature of these weak intermolecular interactions and their role in crystal packing and polymorphic behaviour merits investigation.

2.2.1 Hydrogen Bonds

The formal status of the hydrogen bond has recently been clarified by the IUPAC definition, which concludes, "*The hydrogen bond is an attractive interaction between a hydrogen atom from a molecule or a molecular fragment X–H in which X is more electronegative than H, and an atom or a group of atoms in the same or a different molecule, in which there is evidence of bond formation.*"[86] It further states that to be classified as a hydrogen bond the interaction must be dominated by electrostatic forces. Given this definition, the strength of the hydrogen bond varies from around a few $kJmol^{-1}$ in the C-H· · ·Cl-C synthon[87] to 165 $kJmol^{-1}$ in the case of HF_2^-.[88]

The five most significant energetic terms in intermolecular contacts may be described as:[89]

1) Permanent electrostatic interactions: the interactions between the undistorted electron distribution of the two monomers, i.e. dipole-dipole, dipole-quadrupole etc.

2) Polarization interactions: the effect of distortion of the electron distribution of A by B and B by A and of higher order coupling resulting from such a distortion. i.e. dipole-induced dipole, quadrupole-induced dipole etc.

3) Exchange repulsion: the repulsion caused by the overlap in electron density between A and B.

4) Charge transfer: the interaction caused by the movement of electrons from the molecular orbitals of A to B or from B to A.

5) Dispersion forces, i.e. the instantaneous and simultaneous polarization of A and B.

A convenient system classifying hydrogen bonds by strength is described by Desijraju.[90] Very strong hydrogen bonds are defined as having a stabilisation of 60 $kJmol^{-1}$ or more,[90] typically they involve a member with a formal charge. Strong hydrogen bonds are defined as ranging in strength from around 20 - 60 $kJmol^{-1}$.[90] In this range the dominant forces are electrostatic and if the molecule can arrange itself in such a way as to achieve the formation of such a bond it will do so unless the steric penalty is considerable. The forces involved in both strong and very strong hydrogen bonds are dominated by electrostatics and the bond distance is lower than the sum of the Van der Waal's radii.

Weak hydrogen bonds (typically < 20 $kJmol^{-1}$) arguably represent the more interesting end of the hydrogen bond spectrum. Electrostatic forces are present in these interactions, but of an order not overwhelmingly greater than that of dispersive forces. Obviously, weak hydrogen bonds occur when H is bonded to an atom that is only weakly electronegative, such as C in organic structures. Giving solid boundaries defining the weakest end of the hydrogen-bonding spectrum is a matter of semantics rather than science, however a good starting point seems to be examining whether the majority of the interaction energy arises from electrostatics.

An early example of the weak hydrogen bond was discovered by Pauling,[91] who noticed that the boiling point of acyl chloride is 51 °C higher than that of trifluoroacyl chloride. This he attributed to the formation of hydrogen bonds.

There is significant spectroscopic evidence for the weak hydrogen bond.[90] For example, the υ_{CH} of 1,3,5-trichlorobenzene in the presence of pyridine is lowered by 35 cm^{-1}.[92] Desiraju notes this as the first reported evidence of hydrogen bond formation by aromatic H atoms.

The strongest evidence for the phenomenon can be seen in crystallography. Sutor[93,94] observed short hydrogen bond like C-H· · ·O contacts in caffeine, with a distance of 2.12 Å (as compared to the combined Van der Waal's radius of 2.60 Å), as well as similar contacts in theophylline and uracil. Donohue[95] criticised this work, incorrectly, as being statistically irrelevant and for several years the topic was largely ignored. However, Taylor and Kennard[96] challenged Donohue's view using the then embryonic Cambridge Structural Database (CSD).[97,98] They based their study on 113 crystals structures, all elucidated using neutron diffraction (in order that the hydrogen atom location was accurate). They searched this set of structures for contacts that were shorter than the sum of the Van der Waal's radii of the proton and the acceptor atom. They found that the C-H proton had a statistically significant tendency to form intermolecular contacts to oxygen atoms over hydrogen or carbon. Furthermore they noticed that these bonds were highly directional. There were insufficient C-H· · ·N and C-H· · ·Cl contacts to have a statistically significant sample, but they concluded that if oxygen were sufficiently electronegative to cause such an interaction, it was likely that nitrogen and chlorine would also be.

Aakeroy *et al* [99] noted that identifying weak hydrogen bonding purely on the basis

of the bond length is not sufficient because hydrogen bonds are, by definition, at least moderately electrostatic, and as such are not as highly dependant on displacement as other forces and therefore the use of a hard displacement limit is not satisfactory. An angular dependence is a far more satisfactory method ($\alpha_{C-H\cdots X} >> 90^{o}$) of identifying the bond, as an electrostatic interaction should be relatively linear, (although weak hydrogen bonds can obviously be significantly bent due to being out-competed by stronger directional interactions in driving a given structure).

Aakeroy *et al* therefore searched the CSD for data to confirm this hypothesis. They found that in O-H· · ·Cl interactions, the contacts are clustered around a small range of distances within the sum of the Van der Waal's radii, and at angles approaching linearity – clear evidence for a strong hydrogen-bonding interaction. In the case of C-H· · ·Cl^{-} contacts there is still a marked distance dependency, although considerably less than in O-H· · ·Cl interactions. Although the maxima (2.95 Å) is within the sum of the Van der Waal's radii (3 Å), many of the C-H· · ·Cl^{-} contacts are found beyond this value. The data showed that the smaller the displacement the closer the angle was to linearity – as would be expected for an electrostatic force of attraction. In the case of C-H· · ·Cl^{0} contacts, the maxima was at a similar value to the sum of the Van der Waal's radii, with the majority of contacts being beyond this value. As expected the maxima is the least well defined with the least strong relationship between displacement and angle - indicating a weaker, yet still significant electrostatic force of attraction.

Clearly, the strength of a hydrogen bond C-H· · ·X should depend on the basicity of X. For example, one would expect that as the oxygen in C=O is more electronegative than that in C-O-C, hydrogen bonds to a carbonyl would be stronger than those to an ether. Steiner's study[100] into the mean H· · ·O and D· · ·O bond distances in hydrogen bonds with H_2O and C-NH_3^{+} donors yields conclusive results that this is the case. Table 2.1 shows typical H· · ·O bond distances for various acceptors with an H_2O donor.[100]

Acceptor	Mean H· · ·O Bond Distance / Å
P=O	1.871 (7)
H_2O	1.903 (3)
C=O	1.903 (3)
S=O	1.906 (7)
C(sp^3)-OH	1.921 (5)
C-O-C	2.018 (11)
C-NO_2	2.158 (12)

Table 2.1 Mean Distances *d*(H· · ·O) in hydrogen bonds of H_2O donors with various O atom acceptors. Adapted from Ref. 100 with permission from the Centre National de la Recherché Scientifique (CNRS) and The Royal Society of Chemistry.

Hydrogen bond lengths decrease in length with increasing basicity of the acceptor. Similarly, the strength of hydrogen bonds should also depend on the electron withdrawing properties of the donor group. If C in a weak C-H· · ·X hydrogen bond is bonded to electron withdrawing groups (O, N, Cl etc.) then the hydrogen should have a greater partial positive charge and as such the electrostatic force between H and electronegative X should be greater. Likewise, the donor strength of H should also depend on the hybridization of C - sp^3 C < sp^2 C < *sp* C.

A good illustration of the relative directionality of hydrogen bonds of varying strengths can be seen in the work of Steiner and Desiraju,[101] who clearly show that the directionality of the C-H· · ·O interaction decreases as the C-H acidity increases. (See Figure 2.5 below)

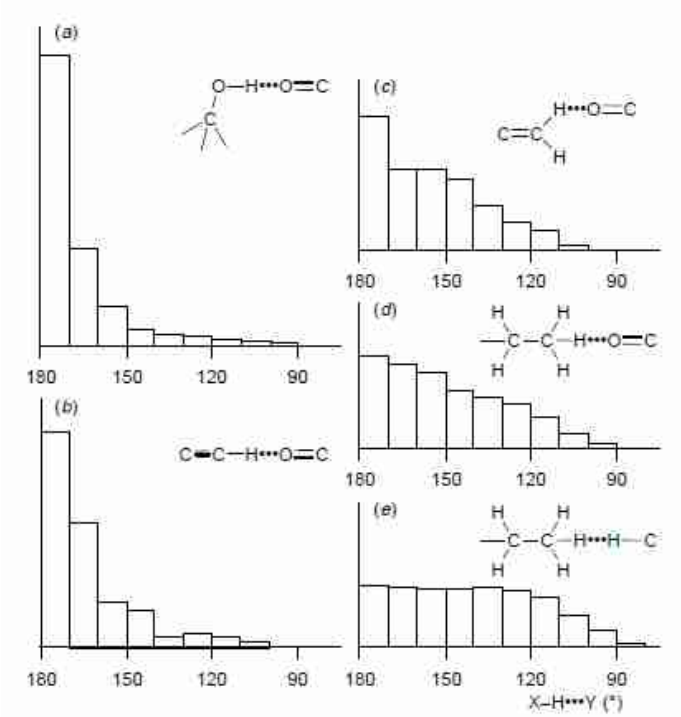

Figure 2.5 Directionality of C-H· · ·O hydrogen bonds formed by C-H groups of different acidity. For comparison the strong hydrogen bond C(sp^3)-O-H· · ·O=C and the Van der Waal's' contact H_2C-H_2C-H· · ·H-C are shown. Reproduced from Ref. 101 with permission from The Royal Society of Chemistry.

Hydrogen bonds are co-operative, that is to say that arrays of hydrogen bond networks are stronger than the sum of an equivalent number of isolated bonds. This is because on formation of a hydrogen bond between two molecules, the hydrogen atom has increased electron density whereas the donor atom has decreased electron density. This increases the ability of the donor atom to engage in further hydrogen bonding.

A good example of co-operative hydrogen bonding can be seen in the crystal structure of 2-ethynyladamantan-2-ol.[102] Here, there are co-operative C-H· · ·O and O-H· · ·O hydrogen bonds which drive the formation of a *Z'* = 2 structure where one ethnyl proton forms a C-H· · ·O bond and the other one does not. (See figure 2.6 below)

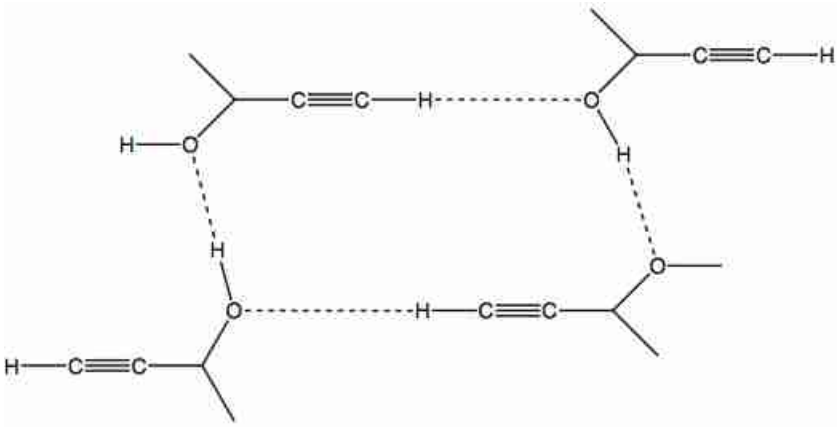

Figure 2.6 The co-operative hydrogen bonding in 2-ethynyladamantan-2-ol. Adapted with permission from Ref. 102 © 1996, American Chemical Society

A ramification of the electrostatic nature of the hydrogen bond, and thus the relative lack of importance of the bond's displacement requirements is that long range *bifurcated* hydrogen bonds can be formed, where there are either two acceptors (*bifurcated acceptors*) or two donors (*bifurcated donors*). Such interactions are rather common and, indeed, even trifurcated hydrogen bonds can occasionally be seen. Bifurcated hydrogen bonds (shown in figure 2.7 below) are typically rather longer than regular hydrogen bonds, and the electrostatic nature of the bond results in a predisposition towards planarity in a manner similar to the linearity observed in regular hydrogen bonding.

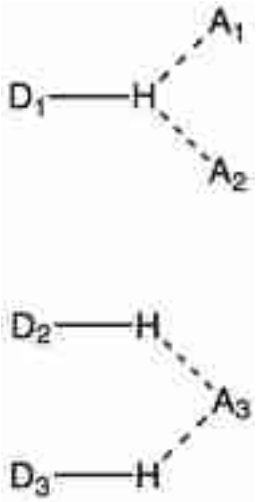

Figure 2.7 Top, a bifurcated acceptor complex, below a bifurcated donor complex

In summary, there is convincing evidence for the presence of a spectrum of “hydrogen bonding” from a powerful electrostatic force that has highly defined angular and displacement requirements to cases where the force acting on the atoms involved is only a little more attractive than that observed in a purely dispersive case.

2.2.2 Halogen Bonding

The donation of electron density from electron rich to electron poor sites does not necessarily have to be mediated through hydrogen. Although halogens as a group are considered to be, broadly speaking, electronegative they can act analogously to electropositive hydrogen in their intermolecular interactions. I.e. D-Hal···A rather than D-H···A. The angle D-Hal-A in halogen bonds, as in strong hydrogen bonds, usually approaches 180°. These initially surprising findings were based on analysis of the CSD,[103,104,105] where it was found that close contacts with electrophiles occurred at low angles (typically 90 - 120°), whereas with nucleophiles the angle was typically close to 180° (See figure 2.8 below).[106]

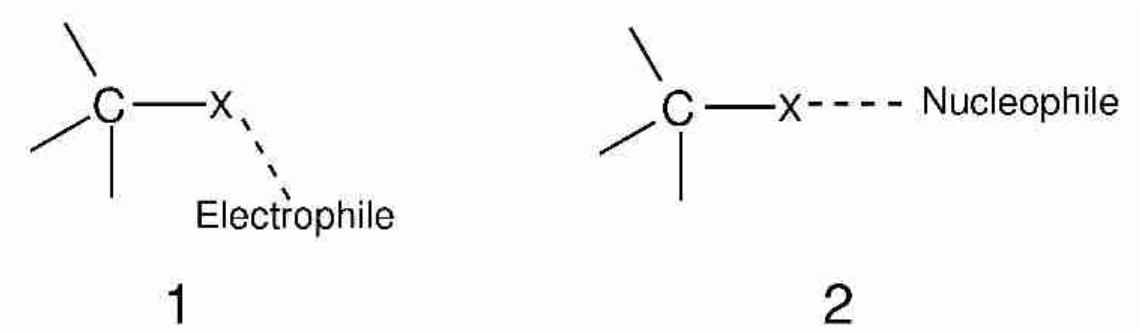

Figure 2.8 Diagram showing typical angle of approach of halogen atoms (X) to electrophiles (1) and nucleophiles (2) Reproduced from Ref. 106 with kind permission from Springer Science and Business Media

An early example of halogen bonding observed crystallographically was seen in the work of Hassel and Rømming, who observed that 1,4-dioxane forms complexes with Chlorine, Bromine and Iodine (but not Fluorine).[107] In this structure there are infinite chains comprising of alternating 1,4-dioxane and dihalogen molecules (see figure 2.9 below).

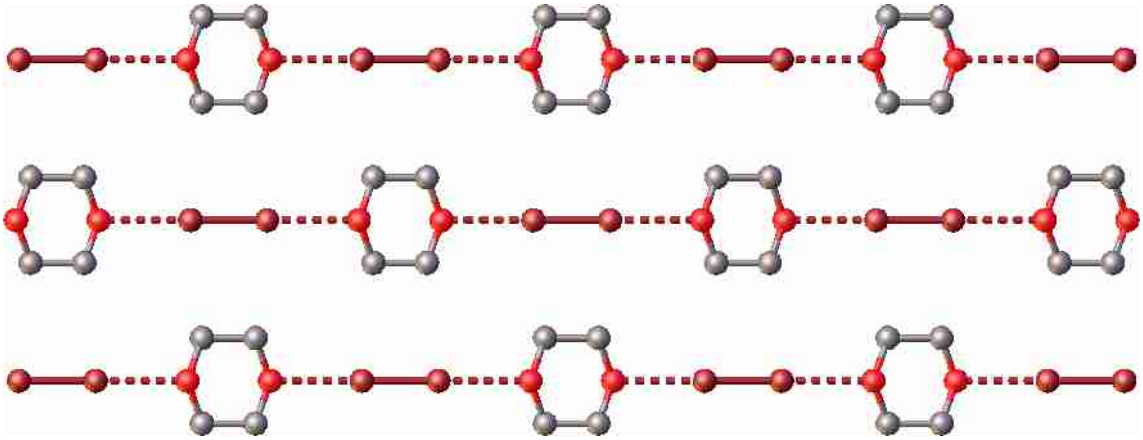

Figure 2.9 Halogen bonding in the 1:1 1,4-dioxane : dihalogen complex.

Most halogens in organic systems have a region of positive electrostatic potential, known as a σ-hole.[106] The origin of the σ-hole derives from covalent bonding. A free atom in the ground state has a spherically symmetrical charge distribution. When this atom forms a covalent bond, electron density is polarized towards the bond, making the side of the atom away from the bond electron-poor.[108] This can only occur if there is little *sp* hybridization present. As the *sp* hybridization in F is considerable, this (combined with the electronegativity of F) means that fluorine does not usually have a σ-hole and as such the bonding of fluorine with a nucelophile is either extremely weak or repulsive.

The strength of the interaction increases from Cl (which may require adjacent electron donors) to Br to I. This is due to a combination of decreasing electronegativity of the element increasing the size and strength of the hole and increasing polarizability increasing the strength of the dispersion component of the interaction.

For example, calculated electrostatic potentials show that CH_3F and CH_3Cl do not have a σ-hole and thus are unsuitable as a candidate for halogen bonding, whereas the Cl in CF_3Cl and CH_3Br both have an area of positive electrostatic potential and as such have electrostatically favourable interactions with nucleophiles.[106] Figure 2.10, below, shows the electrostatic potentials for these compounds.[106]

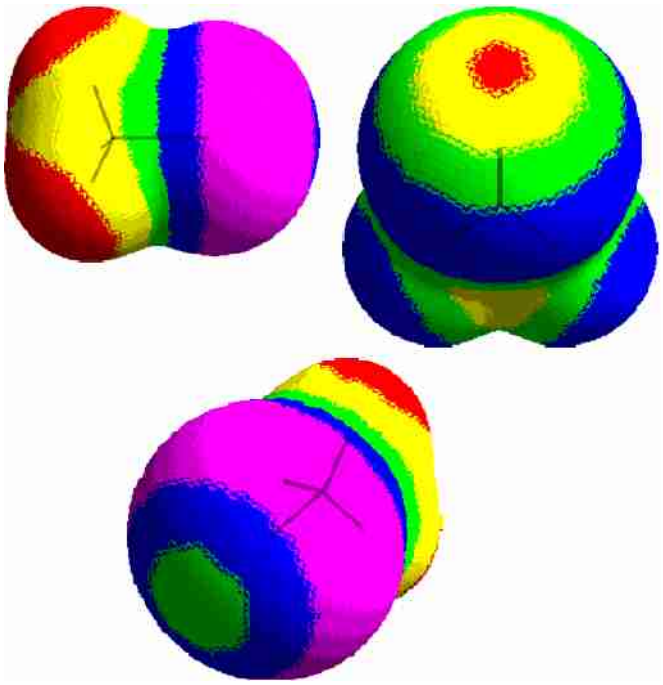

Figure 2.10 Computed B3PW91/6-31G(d.p.) electrostatic potential (in kcal mol^{-1}) of (in clockwise order from top left) CH_3Cl, CF_3Cl and CH_3Br. The relevant halogen atom is at the right, top and left of the page respectively. The colour ranges are: *red*, more positive than 15; *yellow*, between 7 and 15; *green*, between 0 and 7; *blue*, between 0 and -10; and *purple*, more negative than -10. Reproduced from Ref. 106 with kind permission from Springer Science and Business Media.

Typical interaction energies range from near zero, e.g. $F_2\cdots NH_3$ to around 84 kJ mol^{-1} in $(CH_3)_3N\cdots BrF$,[109] equivalent in energy to a very strong hydrogen bond.

2.2.3 Cl···Cl Interactions

There has been considerable debate about the existence of attractive intermolecular forces between chlorine atoms. Given that it is well established that, in general, the structure of organic crystals widely follows the principle of close packing,[110] one would not expect the substitution of Me (24 $Å^3$) for Cl (20 $Å^3$) to alter the crystal structure. However, this is not the case, especially in the case of aromatic compounds. For example, C_6Me_6 and C_6Cl_6 have unrelated crystal structures, due to Cl· · · Cl interactions, while C_6Br_6 (Br = 26 $Å^3$) is isostructural to C_6Cl_6.[111] Further evidence for an attractive Cl· · · Cl intermolecular force is to be found in the solid-state structure of Cl_2, where there is a short Cl· · · Cl contact of 3.294 Å.[112]

Price *et al*,[116] searched the CSD for high quality structures containing only carbon, chlorine and optionally hydrogen, and collected all intermolecular Cl· · · Cl contacts where the contact distance was shorter than 3.52 Å. They found almost 200 unique contacts in 154 compounds. However, they found that the majority of these contacts occur in the structures of totally or heavily chlorinated molecules, with less than 20% of the close contacts occurring in crystal structures which have more hydrogen than chlorine atoms, despite these comprising over half of the compounds analysed.[116]

There are two distinct geometries adopted by Cl· · · Cl contacts. If one defines θ_1 = C_1-Cl_1· · · Cl_2 and likewise θ_2 = Cl_1· · · C_2-Cl_2 then the type I structure is defined by $\theta_1 \approx \theta_2$ while the type II structure is defined by $\theta_1 \approx 180°$ and $\theta_2 \approx 90°$ as shown in Figure 2.11 below.[113]

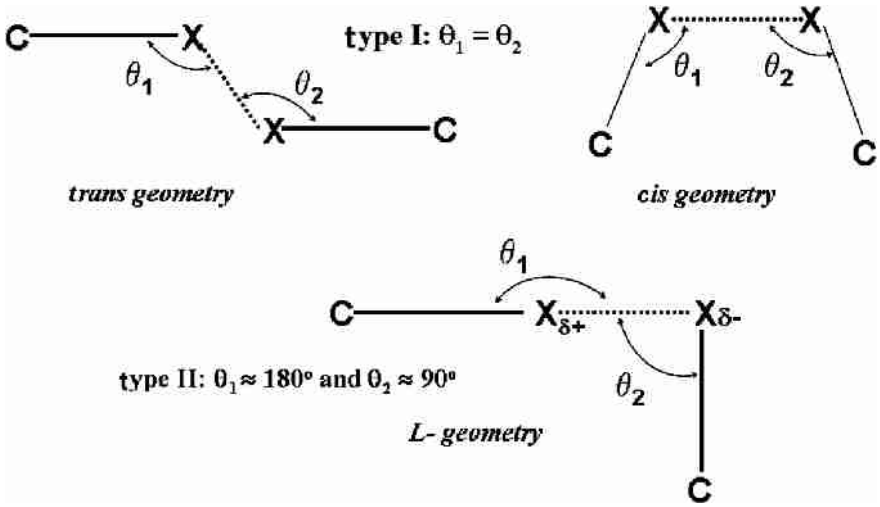

Figure 2.11 Possible geometries of Cl· · · Cl intermolecular bonding. Adapted with permission from Ref. 113 © 2010, American Chemical Society

The driving force behind these interactions is not yet fully understood. Two distinct models have attempted to explain Cl· · · Cl intermolecular bonding based on the simplest case in point, solid dichlorine:

The Williams Model[114] claims that the Cl atoms participating in intermolecular bonding experience a degree of polarization, resulting in an attractive electrostatic force of interaction between the two atoms. A permanent polarization of dichlorine does not fit the observed lattice energies or geometrical constraints.[115,116] However, recent charge-density studies on type II interactions do indicate the bonding arises from an attractive force rather than a decrease in repulsion.[117,118] This would seem to place Cl· · · Cl interactions as a typical example of halogen bonding, described above.

Another possible driving force for Cl· · · Cl intermolecular forces, the Nyburg Model[119,120] states that the interactions arises from the anisotropy in the Van der Waal's radii of Cl atoms. This model proposes that Cl atoms have an effective elliptical shape, with a minor radius of 1.58 Å for head-on approach (θ = 180°) and a major radius of 1.78 Å for a side-on approach (θ = 90°), this would result in Cl· · · Cl interactions arising from a decreasing repulsion between the two atoms.

Analysis of structures in the CSD containing Cl· · · Cl by Price *et al*[116] suggests that most of the close Cl· · · Cl contacts occur due to the requirement for crystals to pack efficiently rather than a specific non-dispersive driving force. They found that the angle of type I contacts was more commonly near 165º than 180º, which implies that electrostatic forces, if present, are of minor importance.[116] They also found good agreement between the proposed elliptical atom shape model and contact distances found using the CSD.[116]

Hal· · · Hal contacts are also found in the heavier halogens (although not typically in fluorine). There is crystallographic and theoretical evidence that the strength of the contacts increases from Cl to I due to increasing polarizability,[121] and that the dependency on hybridisation follows the order $sp^2 > sp > sp^3$.[118] The strength of the interaction is also dependant on the electronegativity of the associated carbon.[122] In unsymmetrical type II contacts (i.e. I· · · Br, I· · · Cl and Br· · · Cl) the θ_2 angle has been shown to occur more often at the lighter of the two halogen atoms, indicating that the heavier atom has a partial positive charge, and the lighter a partial negative charge.[118,121]

2.2.4 π-π Stacking Interactions

π-π interactions are attractive intermolecular forces that exist between two or more discreet aromatic systems. There are three distinct ways in which two aromatic systems can interact.[123]

1) Sandwich or face-to-face stacking: This is generally relatively rarely observed as it involves a maximisation in the repulsive overlap of the two π-systems. However, due to its simplicity it has been used as the basis of several theoretical studies.

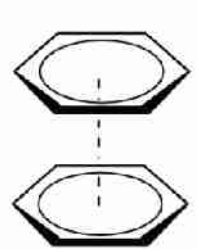

2) Face-to-face offset stacking: The offset minimises π-π repulsion, stabilising this geometry relative to the sandwich type complex shown above.

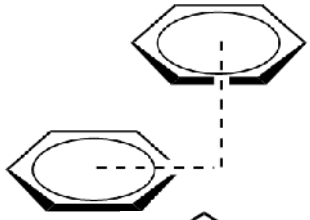

3) T- shaped or edge-to-face stacking: Here, an electropositive ring substituent, typically H forms a favourable interaction with the electronegative π-system of the other phenyl ring. (This is a C-H· · · π interaction rather than a true π · · · π interaction.)

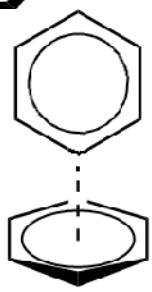

The nature of π-π interactions has been hotly debated over the last few decades. The classical understanding was that the net attractive force arises from the intermolecular overlap of π-orbitals between two conjugated aromatic systems. This view was challenged by Hunter and Sanders in 1990.[124] They claimed that the net favourable stacking interaction arises from an attractive π-σ force that overcomes π-π repulsions.

Hunter and Sanders modelled a π system as two negatively charged π-electron clouds (of charge –½ each) situated above and below the positively charged σ-framework (of charge +1). They concluded that it was these electrostatic effects which determine the geometry of interaction, with dispersion forces affecting only the magnitude of the interactions.

The Hunters-Sanders model was found to successfully predict experimental

geometries, such as parallel offset geometry between porphyrin rings, minimising the π-π repulsion while maximising the attraction between the σ-framework of the inner ring of one porphyrin with the π-electrons of its pair.

Several high-level theoretical studies, such as those by Tsuzuki *et al* [125,126] show, however, that the π-π binding energy in simple aromatic systems is largely a result of dispersion forces (rather than electrostatics as stated by the Hunter-Sanders model), although they concede that as the electrostatic interaction term is highly orientation dependant it is important in determining the directionality in π-π interactions.[125]

Wheeler and Houk[127] showed that substituent effects in face-to-face PhX · · · PhH complexes are near-identical to those observed in the equivalent HX· · · PhH complexes. This indicates that the effect of substituents on the binding energies arise from direct substituent-π interactions rather than through the substituent altering the π-π binding energy of the arene system.

For a series of substituents there was a strong correlation between the stabilization provided by the substituent and its Hammett parameter, σ_m. (although this breaks down for multiply-substituted dimers).[128] This implies although dispersion remains the largest component of the π-π binding energy it is the differential electrostatic effects that causes the ordering of the *relative* binding energy of the substituents.

It was recently determined using theoretical studies that Lewis *et al* [129] and Sherill *et al* [130] for face-to-face arenes and Seo *et al* [132] for offset systems that there is a larger π-π binding energy for both electron-withdrawing and electron-donating substituents as opposed to unsubstituted benzene. In recent work, Sherill *et al* [131] determined that the cause of the enhancement of π-π binding energy arises from charge penetration in face-to-face substituted benzene dimers.

Typical interaction energies from work by Seo *et al* are given below for offset complexes. (See figure 2.12 and table 2.2 below).[132]

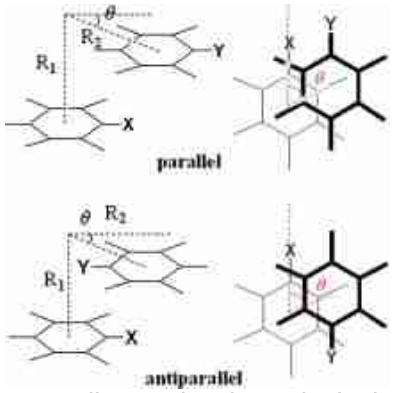

Figure 2.12 Substituted benzene dimers showing substitution in parallel and antiparallel configurations, showing intermolecular distances R_1 and R_2 and angle θ. Reprinted from Ref. 132 © 2009, with permission from Elsevier.

X	**Y**	**Parallel (KJ mol^{-1})**	**Anti-Parallel (KJ mol^{-1})**
H	H	-9.62	-9.62
OH	OH	-12.43	-17.74
F	F	-10.79	-14.14
CN	CN	-12.55	-22.51
NO_2	NO_2	-15.73	-25.23
OH	H	-13.10	-13.10
OH	F	-13.97	-14.48
OH	CN	-17.15	-19.16
OH	NO_2	-17.91	-19.58

Table 2.2 Calculated Interaction Energies at optimal values of R_1, R_2, and θ.[132]

2.2.5 C-H · · · π Interactions

The C-H · · · π interaction is a weak intermolecular interaction with stabilisation energies weaker than even the weakest hydrogen bonds. The recent IUPAC definition[86] on hydrogen bonding formally excludes C-H · · · π interactions on the basis that the interaction is primarily dispersive in nature.

It is clear that these interactions are not *purely* dispersive in nature as they are highly directional, indicating a sizeable electrostatic and charge-transfer component. It is widely accepted that such interactions play an important role in the conformation and crystal packing of the huge variety of compounds that contain aromatic systems, such as supramolecular and biological materials. All manner of C-H units can act as donors (sp^3, sp^2 or *sp*) and likewise any manner of π-system can act as the acceptor (e.g. benzene moieties, heteroaromatics, double and triple bonds).

The first experimental evidence for the presence of C-H · · · π interactions was found by Tamres, who observed that mixing chloroform and benzene in a 1:1 ratio was exothermic.[133] C-H · · · π interactions have also been implicated in the ligand-recognition function of carbohydrate-binding proteins[134] and as an important driving force of host-guest complexation in apolar media.[135]

A typical example of the importance of C-H · · · π interactions in the conformation of organic compounds is observed in the case of benzyl t-butyl sulphoxides.[136] Using the standard model of steric repulsion dominating conformation, conformer (a) (See Fig 2.13 below) would be expected to dominate.[136,137,138]

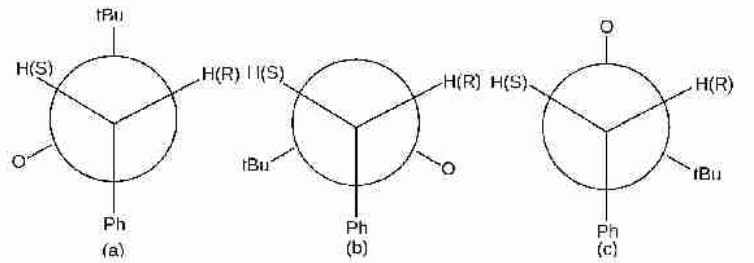

Figure 2.13 The 3 conformers of benzyl t-butyl sulphoxide. Reprinted from Ref. 138 © 1977, with permission from Elsevier

However, conformer (c) is observed experimentally. Similar observations can also be seen in the dominant conformations of 1-phenylethyl sulphide (1 in figure 2.14 below), sulphoxides (2) and (3) and sulphone (4). In all these cases the t-butyl group was found to be gauche to the phenyl group.[138]

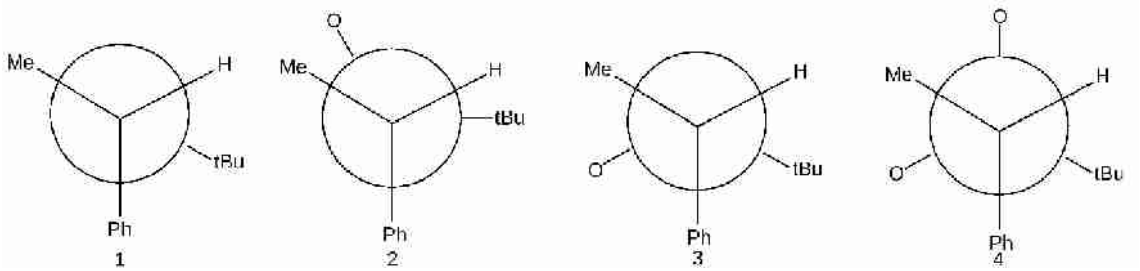

Figure 2.14 The 4 dominating gauche conformers. Reprinted from Ref. 138 © 1977, with permission from Elsevier

The reason for this observation was clear under X-ray analysis. In all cases a C atom in the ^{t}Bu group was found to be very close (3.3 Å) to a C in the phenyl ring, forming a C-H · · · π interaction. The stabilisation energy was calculated to be 4.8 kJ mol^{-1}.[138]

Nishio found that the proportion of the total energetic term in alkane-benzene C-H · · · π interactions arising from the electrostatic component increases on going from CH_4 (c. 17%) to *sp*^{2}-CH (16–32%) to *sp*-CH (c. 71%). The range of stabilisation energies of C-H · · · π interactions typically observed is in the range of 6-10 kJ mol^{-1}. Database studies[139,140] analysing C-H · · · π interactions in the CSD showed that of the 19,921 organic compounds found in the CSD that contain at least one RCH_3 group, and an Ar group, 54% had a RCH_3-Ar interaction present within the combined Van der Waal's radii (+5%). This obviously implies an energetic stabilisation. However, this does not necessarily imply that the C-H · · · π interactions are necessarily responsible for the formation of a specific crystal structure, rather that they make an energetic contribution in combination with hydrogen bonding and other types of intermolecular bonds towards the packing structure in question representing an energy minima.

It is clear that although C-H · · · π interactions individually make comparatively small energetic contributions, they can drive significant changes to both the conformation and packing of molecules.

2.2.6 Dispersion

Dispersion is an entirely non-classical phenomenon first characterized by Fritz London.[141] Dispersion alone explains why noble gas atoms are attracted to one-another and can form condensed matter phases at low temperatures.

Representing each atom as a one-dimensional harmonic oscillator, it is possible to derive the zero-point energy of two coupled oscillators relative to that of two independent oscillators as:[142]

$$U_{disp} = \frac{-h}{2\pi}\omega_o\left(\frac{1}{8}c^2 + \frac{5}{128}c^4 + \ldots\right)$$

Here, c refers to the coupling constant and ω_0 the frequency of an isolated harmonic oscillator. For interacting dipoles, the coupling constant is proportional to R^{-3}. As such, the attractive term is roughly proportional to R^{-6}. Dispersion increases with the sizes of the atoms involved; this is due to increased polarizability of the electron clouds.

This coupling causes (even in non-polar molecules), electron density to redistribute when the molecule comes into close contact with a neighbour, forming a temporary dipole. The interaction energy profile of an argon dimer with varying interatomic displacement is shown in figure 2.15.

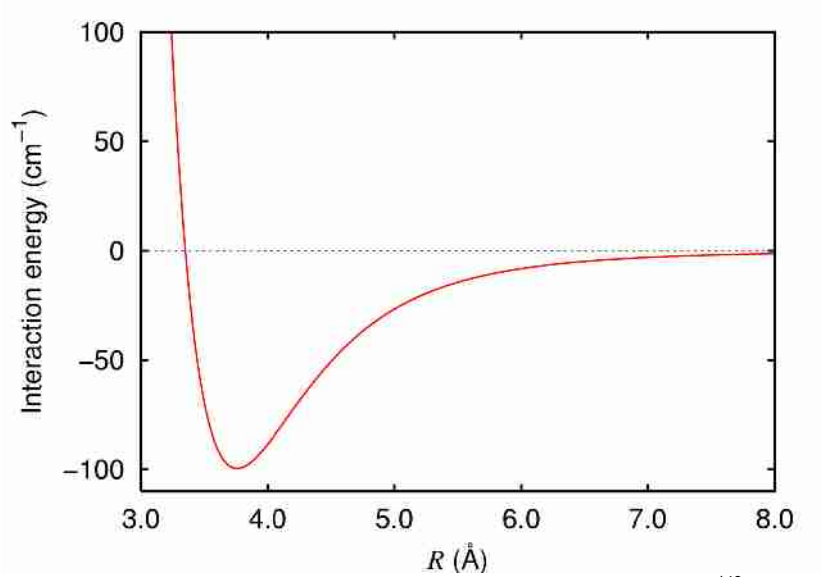

Figure 2.15 The interaction energy of an argon dimer.[143]

At close intermolecular distances, electron-electron repulsion dominates the energetic term (which is roughly proportional to R^{-12}). However, as separation increases up to the combined Van der Waal's radii, the interaction becomes increasingly

favourable due to the unfavourable repulsion term decreasing in magnitude more rapidly than the favourable dispersion term. At the combined Van der Waal's radii the sum of the repulsive and attractive dispersion term is at its most energetically favourable. As the interaction distance increases beyond the combined Van der Waal's radii the magnitude of the attraction decreases with increasing *R* as dispersion decreases in magnitude more rapidly than repulsion.

In most organic systems, the dominant force of interaction in terms of absolute energetic interaction arises from dispersion forces, the only exception being in highly polar species such as H_2O. Isrealachvili lists the theoretically derived contribution of dispersion to the energy contribution to the total for several homo- and hetero- dimers. These are shown below in Table 2.3.[144]

Interacting Molecules	**% Contribution From Dispersion to Total Energetic Term**
Ne-Ne	100
CH_4-CH_4	100
HI-HI	99
HBr-HBr	96
HCl-HCl	86
CH_3Cl-CH_3Cl	68
NH_3-NH_3	57
H_2O-H_2O	24
Ne-CH_4	100
HCl-HI	96
H_2O-Ne	92
H_2O-CH_4	87

Table 2.3 The contribution from dispersion to the total energetic term for various homo- and hetero- dimers. Adapted from Ref. 144 © 2011, with permission from Elsevier

It is worth mentioning that unlike other intermolecular forces there is no angular dependence for London dispersion forces. As a result, one may consider that although London dispersion forces may contribute most to the energetic term in weakly bonded systems, they may be less structurally directing, as the only variable in the term is the displacement, rather than the displacement and bond angle. However, dispersive forces are very important in driving the close packing of molecules within a crystal structure and as such are a very important factor in the way molecules are arranged in a crystal structure.

2.2.7 Hirshfeld Surfaces

A Hirshfeld Surface[145,146] is a graphical representation that shows where electron density in a crystal structure originates. The Hirshfeld surface is defined as the area around a given molecule where half of the electron density arises from that molecule and half from the sum of the remaining molecules in the crystal. This is more formally defined as a region in a crystal around a molecule where w(r) ≥ 0.5 where w(r) is defined as:

$$w(r) = \frac{\rho_{promolecule}(r)}{\rho_{procrystal}(r)}$$

In this thesis, d_{norm}[147] , is plotted onto the surface of the Hirshfeld Surface. d_{norm} is defined through the relationship:

$$d_{norm} = \frac{d_i - r_i^{VdW}}{r_i^{VdW}} + \frac{d_e - r_e^{VdW}}{r_e^{VdW}}$$

Here, d_e represents the distance from the surface to the nearest atomic nucleus exterior to the surface. Likewise d_i represents the distance from the surface to the nearest atomic nucleus inside the surface.[148] d_{norm} thus samples the length of intermolecular contacts at each point on the surface. Relatively close contacts are highlighted in red, with intermediate distance contacts in white and relatively long separations in blue.

Fingerprint plots[149] provide a unique way to break down the interactions on the Hirshfeld Surface to show the proportion of the surface corresponding to different kinds of interaction. Fingerprint plots are generated by sampling each point on the Hirshfeld surface, recording d_e and d_i values. The fingerprint plot plots d_e against d_i values. The graph is pixelated and the colour of each pixel corresponds to the frequency of occurrence. White corresponds to no contacts, blue to a small number, red to a large number.

Fingerprint plots have diagonal pseudo-symmetry as nearly all of the total volume of the crystal is within a surface, with small void spaces where no one molecule contributes the majority of the total electron density. Intermolecular interactions result in the formation of “wings” in fingerprint plots, with stronger interactions resulting in the wings being more sharply spiked.[149]

The numerical range that a given colour relates to can be altered within CrystalExplorer (in both the surfaces and plots).[150]

As an example, figure 2.16 shows the fingerprint plots of formamide and naphthalene.[149]

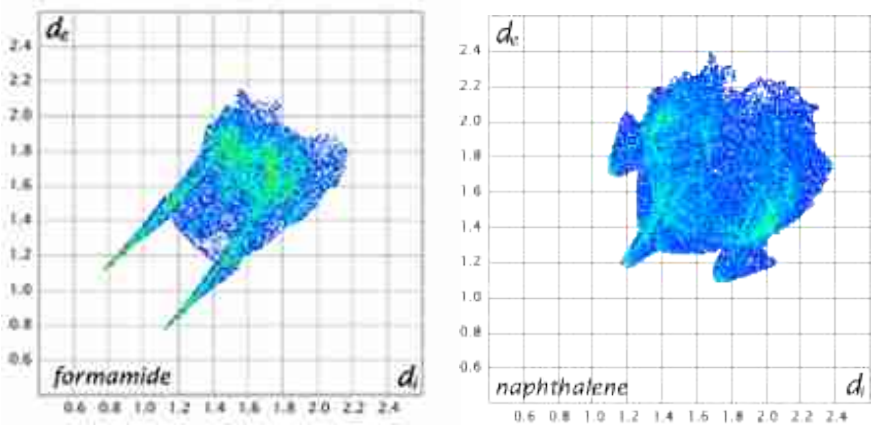

Figure 2.16 Fingerprint plots of formamide and naphthalene. Reproduced from Ref. 149 with permission from The Royal Society of Chemistry.

The pair of spikes in the formamide plot arise from N-H· · ·O hydrogen bonds. The spike in the diagonal in the naphthalene plot arises from H· · ·H contacts, with the outer "wings" arising from C-H· · ·π interactions.

Chapter 3: Cryo- and High-Pressure Crystallisation of Fluoroaromatics

3.1 Introduction

Despite the high electronegativity of fluorine, it has been apparent for many years that the C-F unit (*organic fluorine*) is a very poor hydrogen bond acceptor. As an example, the interaction energy of the C-F· · ·H-C hydrogen bond in 1,3,5-trifluorobenzene has been calculated at -4.5 kJmol^{-1} [151] (as a comparison, the strength of the O· · ·H-O hydrogen bond in water is -19.7[152] kJmol^{-1}).

This may initially seem to contradict the much-accepted statement by Pauling that "*only the most electronegative atoms should form hydrogen bonds, and the strength of the bond should increase with an increase in the electronegativity of the two bonded atoms.*" Given this, we would expect C-F to be a better acceptor than C-OH or C=O. However, it is in fact a substantially weaker acceptor than either. Indeed, this finding is striking when compared to the extremely strong hydrogen bonds formed by F^- ions (the $[F\text{-}H\text{-}F]^-$ interaction energy being calculated at -163 kJmol^{-1}).[153] The weakness of the C-H· · ·F-C interaction has been attributed to the low polarizability of the fluorine atom, its heavily contracted lone pairs, and the energy mismatch of the donor hydrogen atom with the fluorine 2*p* orbital.[154] The 2*p* in fluorine is lower in energy than that of nitrogen or oxygen due to the increased nuclear charge of fluorine, as shown in table 3.1.

Element	**1st Ionization Energy (kJmol^{-1})**	**Difference to 1st Ionization Energy of Hydrogen (kJmol^{-1})**
Hydrogen	1312.0	-
Nitrogen	1402.3	90.3
Oxygen	1313.9	1.9
Fluorine	1681.0	369.0

Table 3.1 First Ionization Energies of Hydrogen, Nitrogen, Oxygen and Fluorine[155]

Despite the inherent weakness of the C-H· · ·F-C hydrogen bond, fluorine and its intermolecular interactions are becoming increasingly important tools in driving the structure and selectivity of pharmaceuticals, as the presence of fluorine (when replacing hydrogen) can enhance selectivity and protein-ligand binding strength through C-F· · ·H and C-F· · ·C=O interactions.[156]

In an attempt to quantify the ability of the C-F unit to act as a hydrogen bond

acceptor (in terms of the length of interactions), Howard *et al*[157] reviewed short contacts from all organofluorine compounds in the CSD. They found that of 1163 unique C-F bonds only 166 of the fluorine atoms contained a C-F· · ·H-X contact below 2.35 Å (c.f. the combined Van der Waal's radii of 2.67 Å.)

In a similar study,[154] Dunitz and Taylor searched the CSD within crystal structures containing at least one C-F bond and at least one potential H-bond donor group, looking for contacts under 2.3 Å (their rationale being that nearly all O· · ·H and N· · ·H contacts are shorter than 2.2 Å), with the additional constraint that the F· · ·H-X angle should be greater than 90°. They found that out of 5947 C-F bonds only 37 (0.6%) (c.f. 42% and 32% for C=O and N(Ar) were involved in possible C-F· · ·H-X hydrogen bonds. Additionally, many of these 37 candidates for hydrogen bonding were rejected, some for having a closer O· · ·H-X than C-H· · ·F-C contact, others for occurring in organometallic systems.

The length of C-H· · ·F-C interactions decreases significantly with increasing *s* hybridisation of the carbon donor. A good example of this being the relatively short hydrogen bond of 2.26 Å observed by Boese *et al* for the *sp* hybridised C-H group in 4-fluoroethynylbenzene.[158] The C-H· · ·F-C hydrogen bond is sufficiently weak that it may even be out-competed by very weak C-H· · ·π interactions. For example, in one of the two polymorphs of each of 2-and 3- fluorophenylacetylene, C-H· · ·π interactions form in preference to C−H···F−C hydrogen bonds.[159]

Thalladi *et al* thought that to examine the likelihood of the C−H···F−C hydrogen bond forming, one should study model compounds that only contain C, H and F, in order to avoid these very weak interactions being overpowered by stronger intermolecular forces.[160] They found that the hydrogen bond lengths in a series of fluorobenzenes are typically high compared those in traditional hydrogen bond, usually in the range 2.5 - 2.7 Å. However, they did occur throughout the range of compounds studied, indicating that despite the weakness of the interaction, they are important in crystal packing, at least in the absence of stronger interactions. More recent crystal structures of compounds containing only C, H and F seem to have similar C−H···F−C hydrogen bond lengths.[161,162,163]

We noted that despite a large amount of experimental and theoretical work on C-H· · ·F-C interactions, examination of the role of the interaction plays at high-pressure is currently sparse. As of September 2014, there are only 113 structures in the CSD

that contain fluorine and the “pressure” field. Furthermore, many of these datapoints are redundant, representing the same structure at different pressures, and thus in total there are only 51 independent structures (different compounds or polymorphs). In 33 of these cases, the fluorine present is inorganic fluorine rather than organic or there is only one or a couple of fluorine atoms in a relatively large molecule, and as such the role of fluorine in driving structural formation would be expected to be limited. Removing these removes the number of structures down to 18. None of these 18 contain only C, H and F. Studying these interactions under pressure is interesting and worthwhile as the weaker the interaction binding molecules, the more easily the interaction can be distorted through extreme conditions, possibly leading to a greater chance of a different polymorph being crystallised.

A series of fluorobenzenes previously studied at low temperature by Thalladi *et al*[160] were selected for study at high-pressure in this thesis. All are liquids and contain only C, H, F atoms. To further increase the sample size, 2-, 3- and 4-fluorotoluene were also crystallised, using both cryo- and high-pressure crystallisation.[164] 1,4-dihalobenzenes involving F with either Cl, Br or I were studied for the purpose of comparison of the influence of different halogens on the packing of molecules and on the C−H···F−C hydrogen bonds. Figure 3.1 shows the full selection of compounds studied in this thesis.

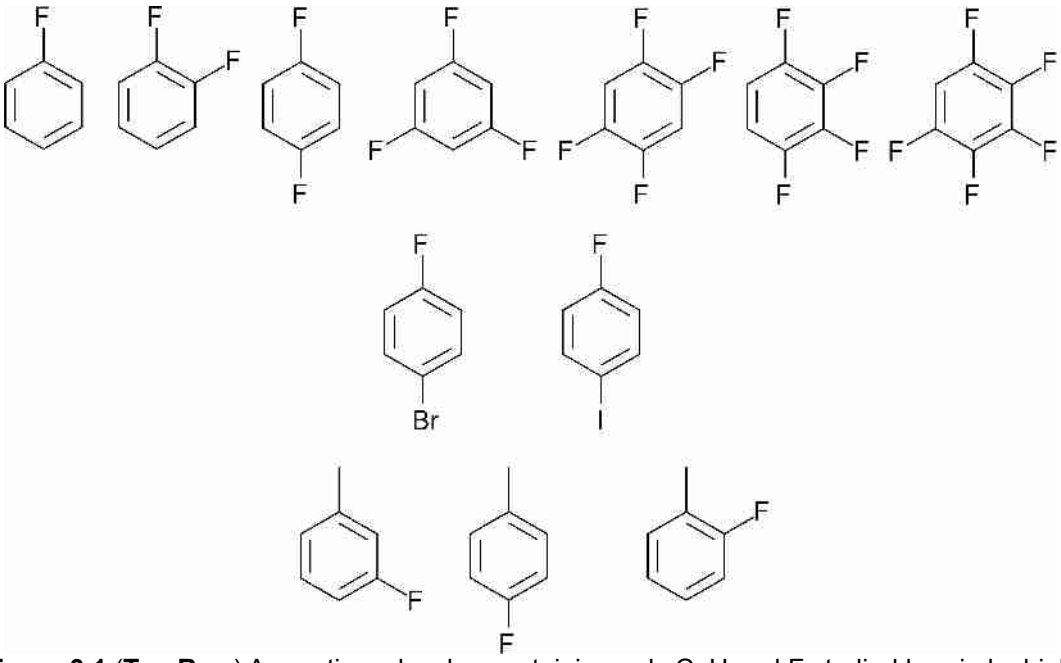

Figure 3.1 (**Top Row**) Aromatic molecules containing only C, H and F studied herein by high-pressure crystallisation (previously cryo-crystallised by Thalladi *et al* [160]) (**Middle Row**) 1,4-dihalobenzenes studied herein by high-pressure crystallisation (previously cryo-crystallised by Thalladi *et al* [160]) 4-fluorochlorobenzene was not studied under pressure as this work has been previously carried out by Masters *et al*.[165] (**Bottom Row**) Fluorinated aromatic molecules containing only C, H and F studied herein by both cryo- and high-pressure crystallisation.

3.2 Experimental Details

The standard cryo-crystallisation procedure, as described in section 1.2, was used to isolate and grow single-crystals of 2-, 3- and 4-fluorotoluene at low-temperature. All compounds except 3-fluorotoluene and 1,2,3,4-tetrafluorobenzene were crystallised using high-pressure using the standard procedure, detailed in section 1.1. 3-Fluorotoluene did not crystallise using compression alone, increasing the pressure lead to the formation of a glass. As a result an alternative high-pressure crystallisation strategy was employed for this compound. The liquid was compressed to approximately 2 GPa and the cell then placed in liquid nitrogen. The cell was then left to warm in air to room-temperature, the pressure was then decreased slightly and the cell placed back into the liquid nitrogen. This process was repeated until the formation of a multi-crystalline phase was observed. Following this, the standard pressure-cycling procedure was used to grow a single-crystal. The temperatures and pressures employed in data collection are shown below in table 3.2. One can see that the pressures and temperatures required for the monofluorotoluenes to crystallise are inversely proportional.

Compound	**Low-Temperature (K)**	**High-Pressure (kbar)**
2-Fluorotoluene	207 (2)	5.3 (2)
3-Fluorotoluene	179 (2)	10.0 (2)
4-Fluorotoluene	217 (2)	5.0 (2)
	High-Pressure (kbar)	
Fluorobenzene	3.6 (2)	
1,2-difluorobenzene	1.3 (2)	
1,4-difluorobenzene	0.9 (2)	
1,3,5-trifluorobenzene	1.3 (2)	
1,2,4,5-tetrafluorobenzene	1.9 (2)	
Pentafluorobenzene	1.5 (2)	
4-fluorobromobenzene	1.4 (2)	
4-fluoroiodobenzene	1.9 (2)	

Table 3.2 Thermodynamic conditions employed during data collection

3.3 Results

3.3.1 Crystal Structure of 2-Fluorotoluene

Cryo- and high-pressure crystallisation of the pure liquid yielded the same polymorph (polymorph I, *Pbc*a). The structure of this polymorph is shown below in figure 3.2.

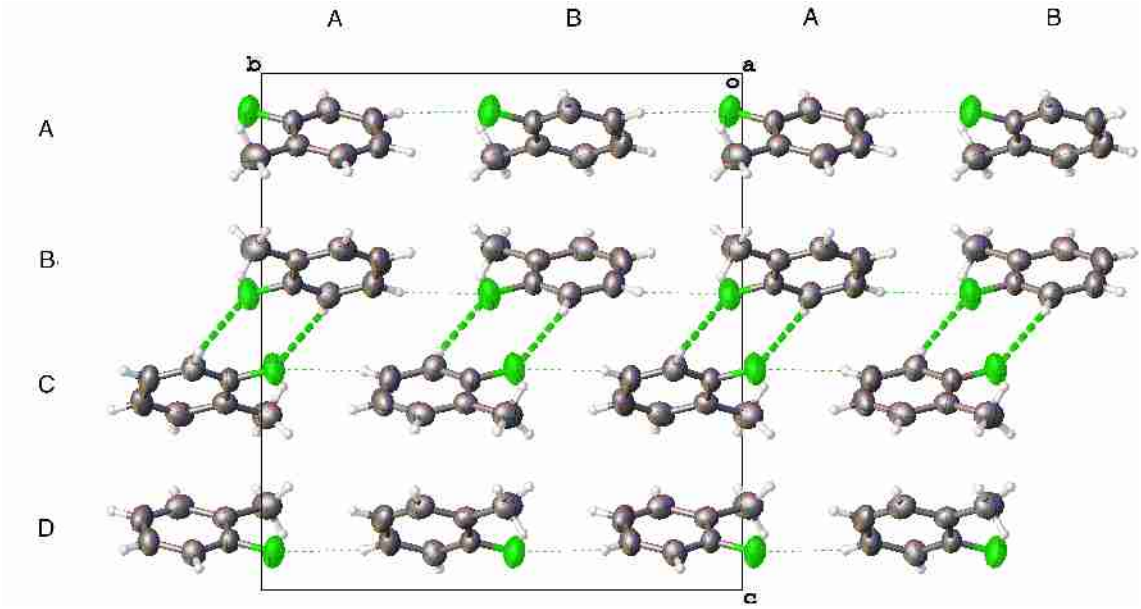

Figure 3.2 Structure of 2-fluorotoluene (polymorph I). The more linear C−H···F−C interactions are shown by an emboldened dashed line. The less linear C−H···F−C interactions are shown by a lighter dashed line.

There are two distinct hydrogen bonds present in this structure, one down the *b* axis, the other across the *bc* plane. Together these interactions form 2D sheets. The ordering follows an ABCDABCD motif down the *c* axis and ABAB down both the *a* and *b* axes (See figure 3.2). The principal hydrogen bonds are shown below in table 3.3.

Hydrogen-Bond		**Low-Temperature**		**High-Pressure**	
C-F· · ·H-C	Distance / Å	2.71 (3)	2.71 (3)	2.716 (13)	2.743 (7)
	Angle / deg	124 (2)	154 (2)	128.2 (8)	152.6 (10)

Table 3.3 Intermolecular interaction distances and angles in polymorph I of 2-fluorotoluene. The first hydrogen bond listed is that down the *b*-axis, the second is that which runs across the *bc* plane.

In an attempt to form a 1:1 co-crystal of 2- and 3-fluorotoluenes a novel phase of 2-fluorotoluene (2-fluorotoluene polymorph II) was generated through high-pressure crystallisation. The pressure at which this crystal formed was 5.5 (2) kbar, within the combined experimental error of that of polymorph I [5.5 (2) kbar]. However, the density of polymorph II was found to be considerably higher (see table 3.6 below). Neither

polymorph I nor II transformed into the other polymorph following an increase in pressure to 11.6 (2) kbar. In contrast, the attempted cryo-crystallisation of the 1:1 mixture of 2-fluorotoluene and 3-fluorotoluene yielded polymorph I of 2-fluorotoluene.

The crystal structure of 2-fluorotoluene polymorph II ($P2_1/c$) is shown below in figure 3.3.

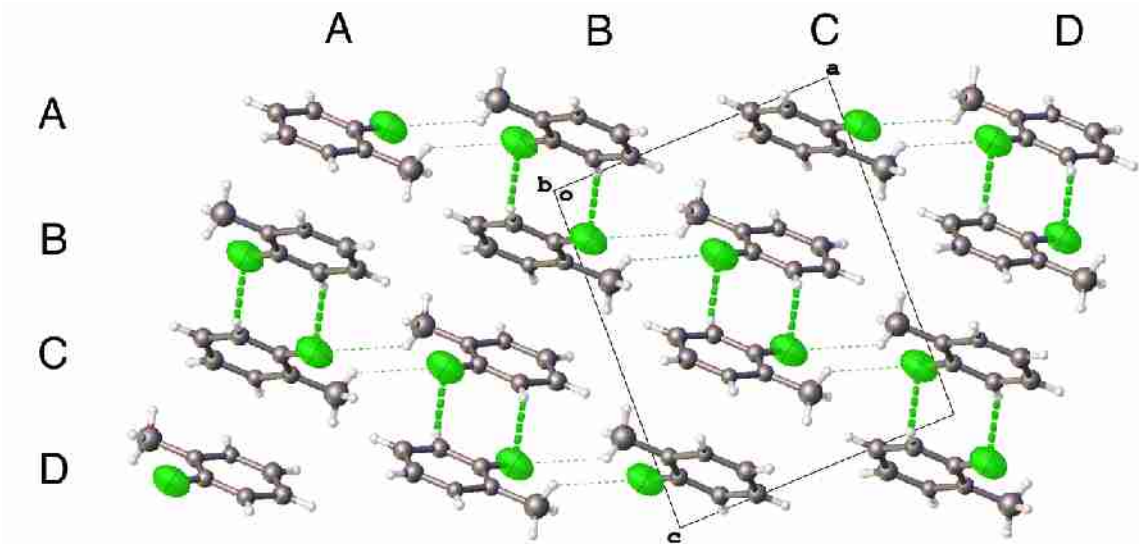

Figure 3.3 Crystal structure of 2-fluorotoluene polymorph II. The more linear C−H···F−C interactions are shown by an emboldened dashed line. The less linear C−H···F−C interactions are shown by a lighter dashed line.

Polymorph II also exhibits two hydrogen bonds per molecule. These are slightly shorter than for polymorph I [2.617 (14) Å] than those seen in polymorph I [2.71 (2) Å]. The primary difference between the two structures lies in the unit cell volumes of the two polymorphs. *V*/*Z* for the two polymorphs are I = 140.4 (1) Å^3, II = 137.5 (13) Å^3.

3.3.2 Crystal Structure of 3-Fluorotoluene

3-fluorotoluene crystallised into two different forms: polymorph I at low-temperature ($P2_1/n$) and polymorph II at high-pressure (*Pbca*). The high-pressure polymorph was grown using a modified crystallisation protocol as described in section 3.2. This involved pressurizing the liquid and then suspending the diamond anvil cell in liquid nitrogen. The crystal structure of the two polymorphs of 3-fluorotoluene are shown below in figures 3.4 and 3.5.

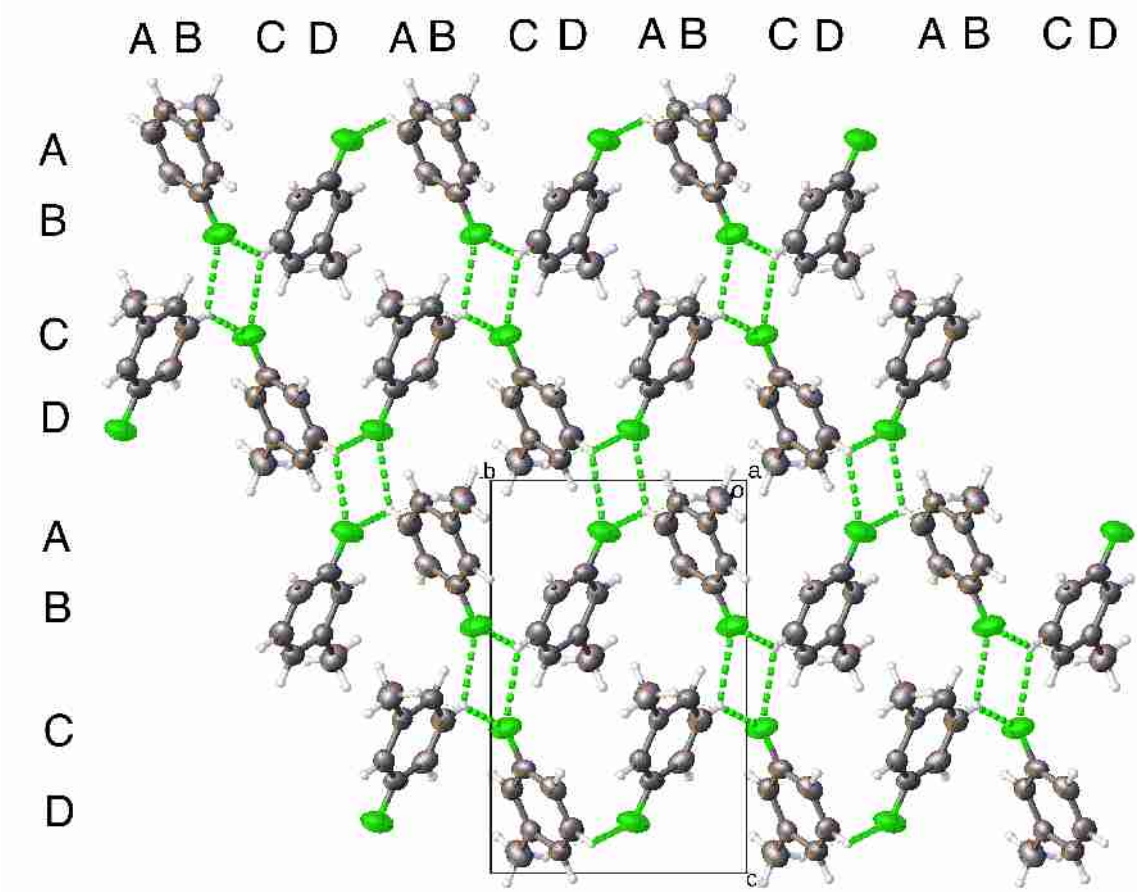

Figure 3.4 Structure of low-temperature polymorph (I) of 3-fluorotoluene

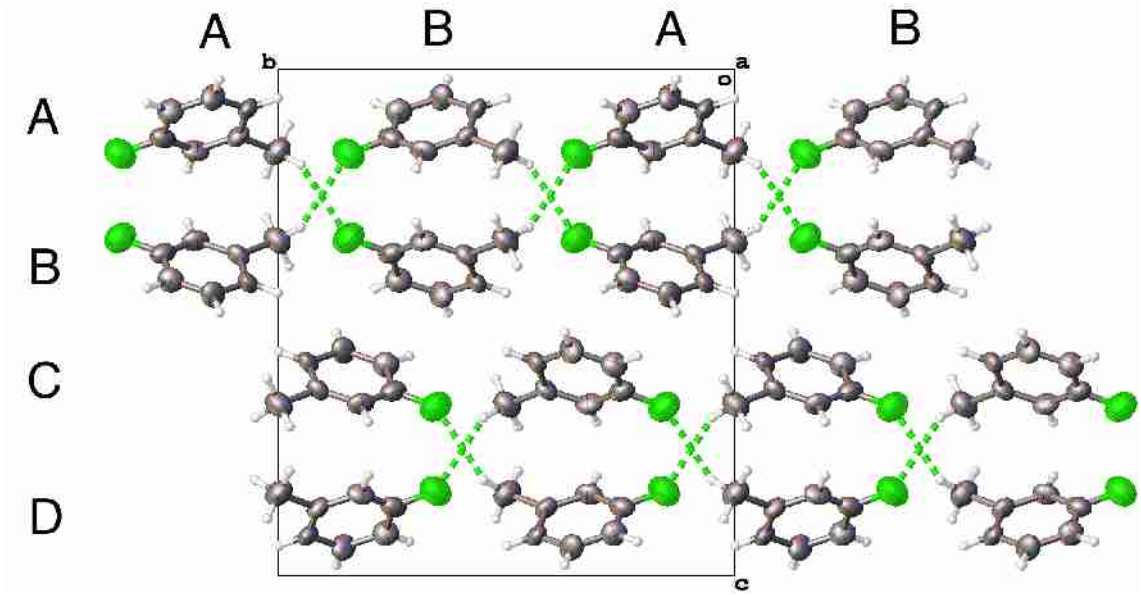

Figure 3.5 Structure of the high-pressure polymorph (II) of 3-fluorotoluene

The low-temperature structure of 3-fluorotoluene is surprisingly complicated for such a simple molecule, ordering ABCDABCD in two dimensions, forming hydrogen-bonded quadrilaterals. The high-pressure structure orders ABCDABCD along the *c* axis and ABAB along the *a* and *b* axes, forming 1D hydrogen-bonded chains. The density is significantly higher in the high-pressure polymorph (1.330 g cm^{-3}) than the low-temperature polymorph (1.140 g cm^{-3}).

The hydrogen bond lengths and angles are shown below in table 3.4

Contact		**Low-Temperature**		**High-Pressure (two equivs.)**
C-F· · ·H-C	Distance / Å	2.651 (3)	2.682 (3)	2.441 (3)
	Angle / deg	138.61 (16)	136.9 (2)	150.6 (2)

Table 3.4 Intermolecular interaction distances and angles in polymorphs I and II of 3-fluorotoluene.

It is apparent that as expected the hydrogen bonds are considerably shorter and more linear in the high-pressure polymorph.

3.3.3 Crystal Structure of 4-Fluorotoluene

4-fluorotoluene formed two distinct polymorphs: polymorph I ($P2_1/c$) from cryo-crystallisation and polymorph II (*Pnma*) from isothermal compression. Figures 3.6 and 3.7 below show the structure of polymorphs I and II of 4-fluorotoluene.

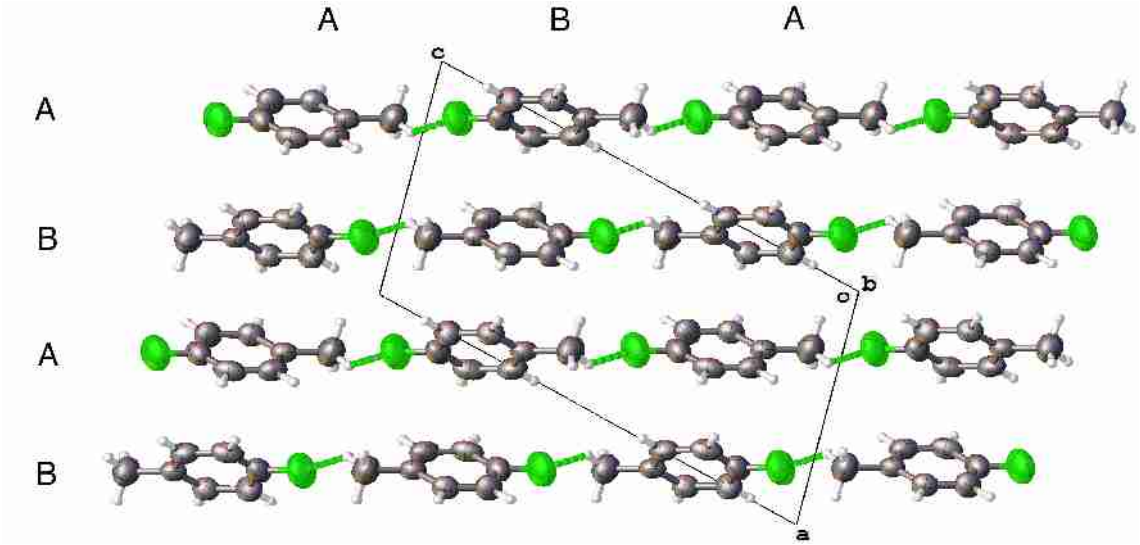

Figure 3.6 Structure of the low-temperature polymorph (I) of 4-fluorotoluene

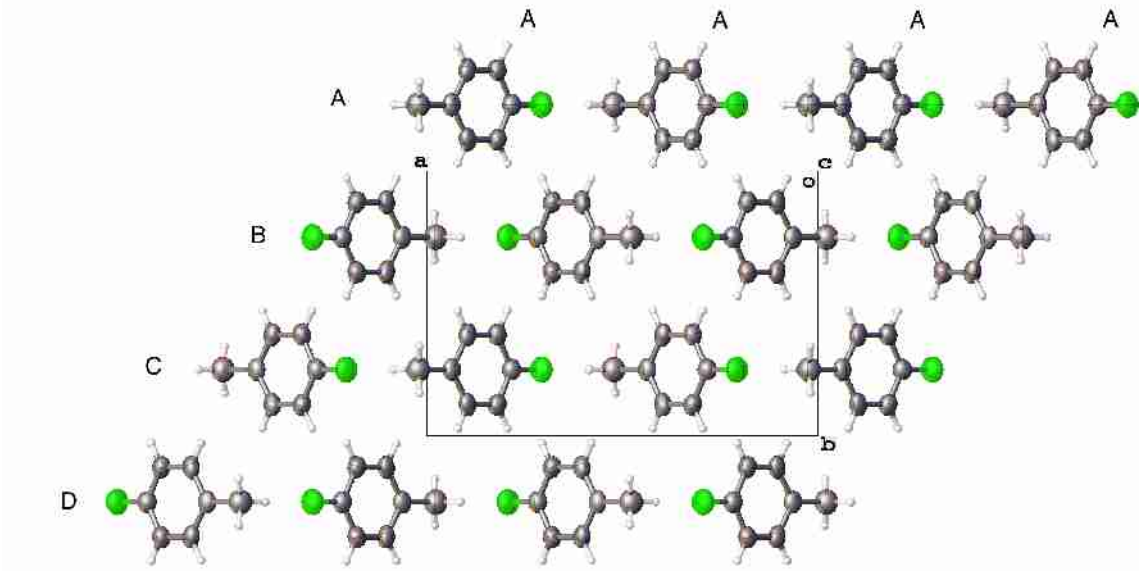

Figure 3.7 Structure of the high-pressure polymorph (II) 4-fluorotoluene

The two polymorphs have some apparent structural similarities. Both have head-to-tail organisation within each layer, with head-to-head layers perpendicular to this. The densities of the low-temperature and high-pressure polymorphs are once again rather different, with the high-pressure phase being denser [1.290 g cm^{-3}, cf. 1.150 g cm^{-3}]. Despite the lower density, the C−H···F−C contacts are considerably shorter (and more linear) in the low-temperature form (see table 3.5 below).

Contact		Low-Temperature	High-Pressure
C-F· · ·H-C	Distance / Å	2.589 (3)	2.832 (2)
	Angle / deg	173.8 (3)	126.54 (6)

Table 3.5 Length and directionality of C-F· · ·H-C intermolecular interactions in the two polymorphs of 4-fluorotoluene

The crystal structure of the two polymorphs of 4-fluorotoluene show that although high-pressure does not often disrupt the formation of a C-F· · ·H-C hydrogen bonded networks, it may do so on occasion if a particular packing provides the most effective way to increase the density, and hence the C-F· · ·H-C interaction can in these occasions cease to be structurally directing at high-pressure. The crystallographic data for the low-temperature and high-pressure crystal structures of 2-, 3- and 4-fluorotoluene are shown below in table 3.6.

compound	**2-fluorotoluene (LT)**	**2-fluorotoluene (HP polymorph 1)**	**2-fluorotoluene (HP polymorph 2)**	**3-fluorotoluene (LT)**	**3-fluorotoluene (HP)**	**4-fluorotoluene (LT)**	**4-fluorotoluene (HP)**
empirical formula				C_7H_7F			
formula weight				110.13			
T/K	207(2)	ambient	ambient	179(2)	ambient	217(2)	ambient
P/kbar	ambient	5.3(2)	5.5(2)	ambient	10.0(2)	ambient	5.0(2)
crystal system	orthorhombic	orthorhombic	monoclinic	monoclinic	orthorhombic	monoclinic	orthorhombic
space group	*Pbca*	*Pbca*	$P2_1/c$	$P2_1/n$	*Pbca*	$P2_1/c$	*Pnma*
a (Å)	5.960(3)	5.807(2)	8.773(13)	7.223(9)	5.4526(12)	7.452(6)	13.215(4)
b (Å)	14.019(9)	13.549(8)	5.838(8)	7.623(10)	13.538(3)	5.987(6)	4.7872(8)
c (Å)	15.021(11)	14.280(6)	10.740(15)	12.098(16)	14.735(4)	14.396(17)	8.9622(19)
β (°)	90	90	91.45(4)	105.67(3)	90	104.00(3)	90
Z	8	8	4	4	8	4	4
V/Å^3	1255.1(14)	1123.5(9)	549.9(13)	641.4(14)	1087.7(5)	636.1(11)	567.0(2)
*D*calc/g cm^{-3}	1.166	1.302	1.330	1.140	1.345	1.150	1.290
μ/mm^{-1}	0.087	0.060	0.061	0.085	0.062	0.086	0.059
unique reflns	1064	755	494	1051	833	724	540
observed reflns	870	347	236	747	593	534	369
θ_{max}	24.70	17.74	15.77	24.35	17.72	21.34	18.57
completeness/%	81.77	45.96	47.77	71.08	71.19	73.76	68.33
R_1 [I > 2σ]	0.0477	0.0430	0.0747	0.0489	0.0558	0.0474	0.0499
wR_2 [all]	0.1348	0.1316	0.2191	0.1520	0.1549	0.1384	0.1692
goodness-of-fit	1.080	1.113	1.056	1.121	1.093	1.031	1.050

Table 3.6 Crystallographic data for the three regioisomers of monofluorotoluene.

3.3.4 High-Pressure Crystal Structures of a Series of Fluorobenzenes

High-pressure crystallisation resulted in the formation of the same polymorphs as observed through cryo-crystallisation for fluorobenzene, 1,2-difluorobenzene, 1,4-difluorobenzene, 1,3,5-trifluorobenzene, 1,2,4,5-tetrafluorobenzene, pentafluorobenzene The structures obtained through high-pressure crystallisation are shown below in figures 3.8-3.13.

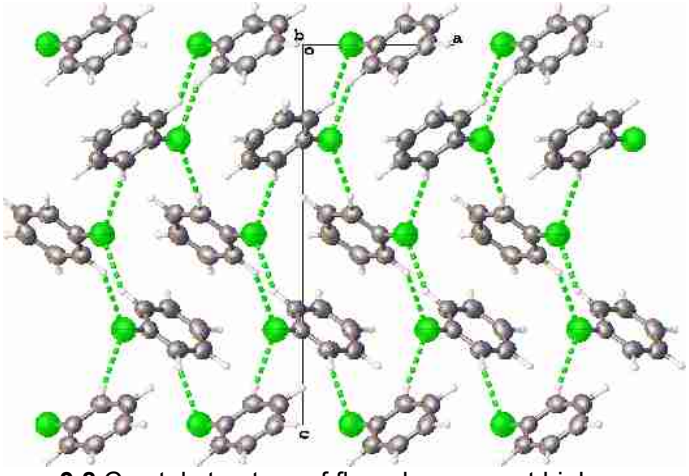

Figure 3.8 Crystal structure of fluorobenzene at high-pressure.

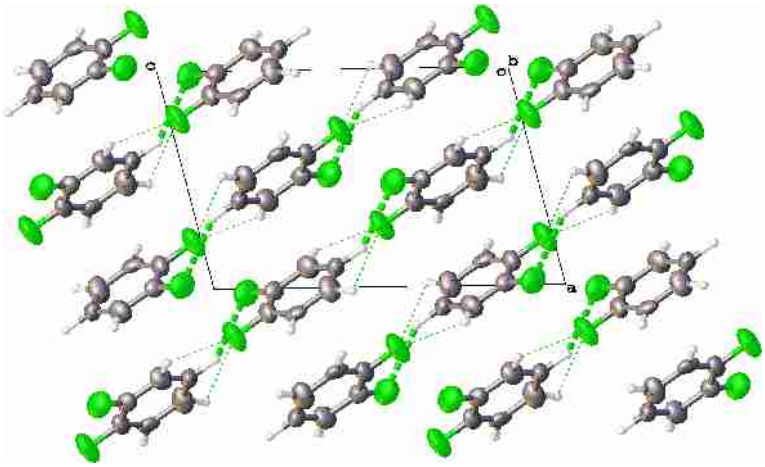

Figure 3.9 Crystal structure of 1,2-difluorobenzene at high-pressure. The more linear C−H···F−C interactions are shown by an emboldened dashed line. The less linear C−H···F−C interactions are shown by a lighter dashed line.

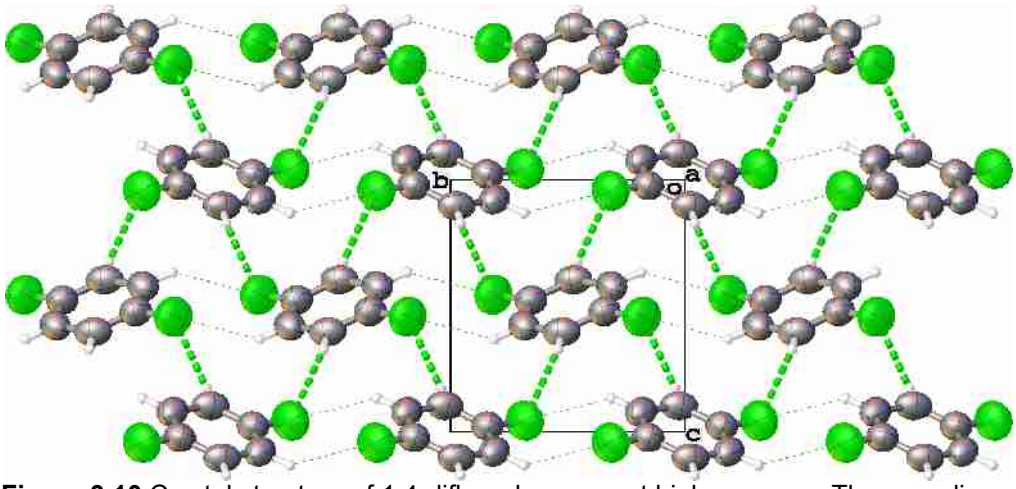

Figure 3.10 Crystal structure of 1,4-difluorobenzene at high-pressure. The more linear C−H···F−C interactions are shown by an emboldened dashed line. The less linear C−H···F−C interactions are shown by a lighter dashed line.

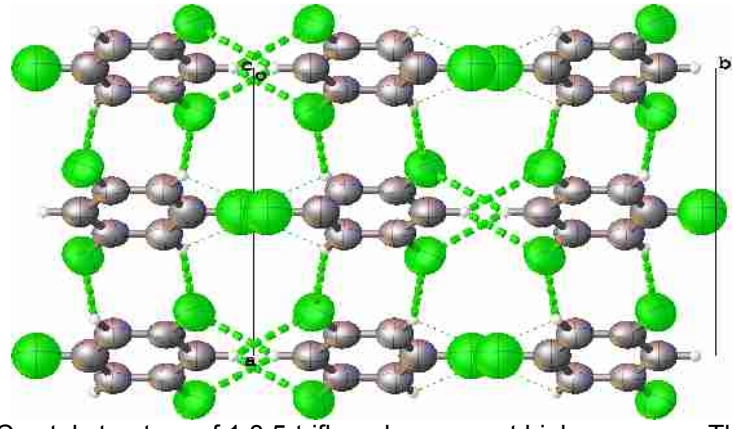

Figure 3.11 Crystal structure of 1,3,5-trifluorobenzene at high-pressure.. The more linear C−H···F−C interactions are shown by an emboldened dashed line. The less linear C−H···F−C interactions are shown by a lighter dashed line.

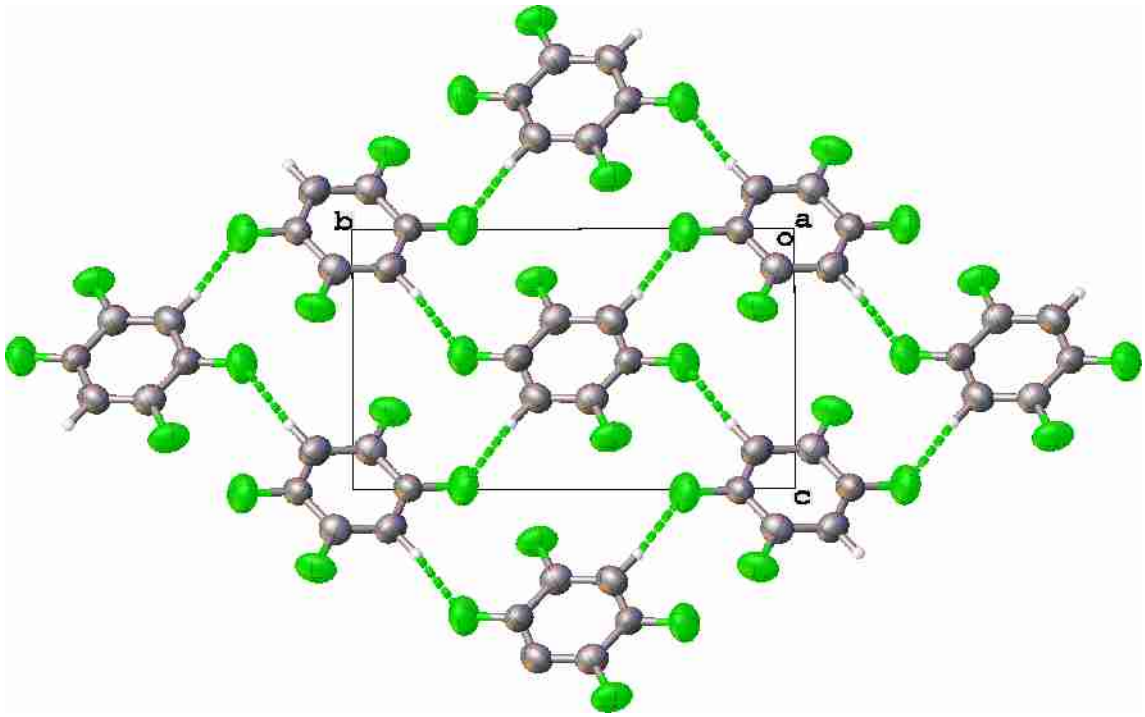

Figure 3.12 Crystal structure of 1,2,4,5-tetrafluorobenzene at high-pressure.

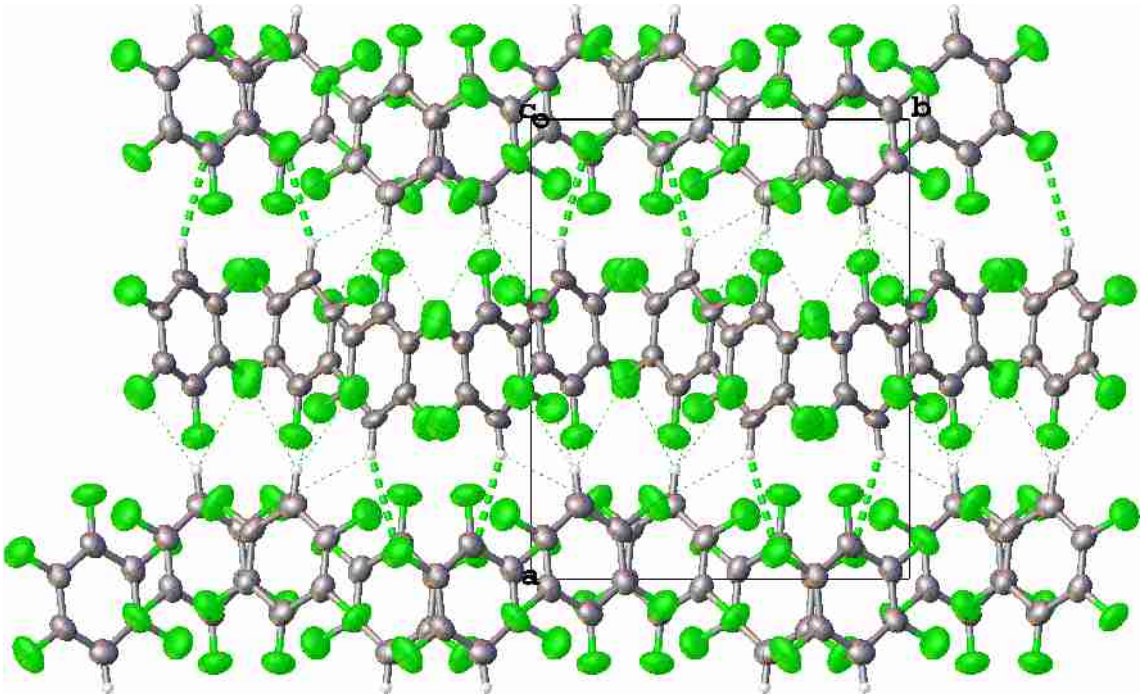

Figure 3.13 Crystal structure of pentafluorobenzene at high-pressure.

The high-pressure structures shown in figures 3.8 – 3.13 closely match those seen at low-temperature.

The crystallographic data are shown above in table 3.4. The lengths and angles of the C-H···F-C interactions in the structures shown in figures 3.8 - 3.13 are listed below in table 3.7.

Compound	**H···F / Å (LT | HP)**		**C-H···F / ° (LT | HP)**	
Fluorobenzene	2.47	2.4609 (8)	140.3	146.068 (6)
1,2-difluorobenzene	2.58	2.5362 (8)	145.0	148.293 (17)
	(2.64)	2.6083 (7)	(122.0)	130.360 (6)
1,4-difluorobenzene	2.49	2.4218 (3)	148.4	153.759 (4)
1,3,5-trifluorobenzene	2.45	2.439 (14)	151.3	150.1 (19)
	2.50	2.467 (7)	142.7	141.54 (14)
1,2,4,5-tetrafluorobenzene	2.36	2.436 (11)	156.8	155.8 (18)
Pentafluorobenzene	2.63	2.52 (2)	155.5	155.0 (19)
	2.64	2.600 (18)	143.5	143.7 (16)
	2.73	2.69 (1)	143.4	139.7 (5)

Table 3.7 Length of hydrogen bonds in a series of fluoroaromatics studied by Thalladi *et al* at low temperature[160] and by JR at high-pressure. Data collection temperatures for low-temperature work (K): Fluorobenzene=123 (2); 1,2-difluorobenzene=123 (2); 1,4-difluorobenzene=215 (2); 1,3,5-trifluorobenzene=130 (2); 1,2,4,5-tetrafluorobenzene=135 (2); Pentafluorobenzene= 200 (2); 4-fluorobromobenzene=125 (2)[160]

The hydrogen-bonding interactions are very similar in length at low-temperature and high-pressure, indicating that the C-H···F-C interaction is relatively unperturbed by high-pressure in these structures.

Compression of 1,2,3,4-tetrafluorobenzene yielded a multi-crystalline phase, however a destructive phase transition occurred during crystal growth, meaning that a suitable single-crystal could not be isolated. As this compound has two polymorphs that can be generated through cryo-crystallisation, it is possible that the phase transition observed at high-pressure corresponds to a transition between these two phases.

High-pressure crystallisation also resulted in the formation of the same polymorph as observed through cryo-crystallisation for 4-fluorobromobenzene. The high-pressure structure of 4-fluorobromobenzene is shown below in figure 3.14.

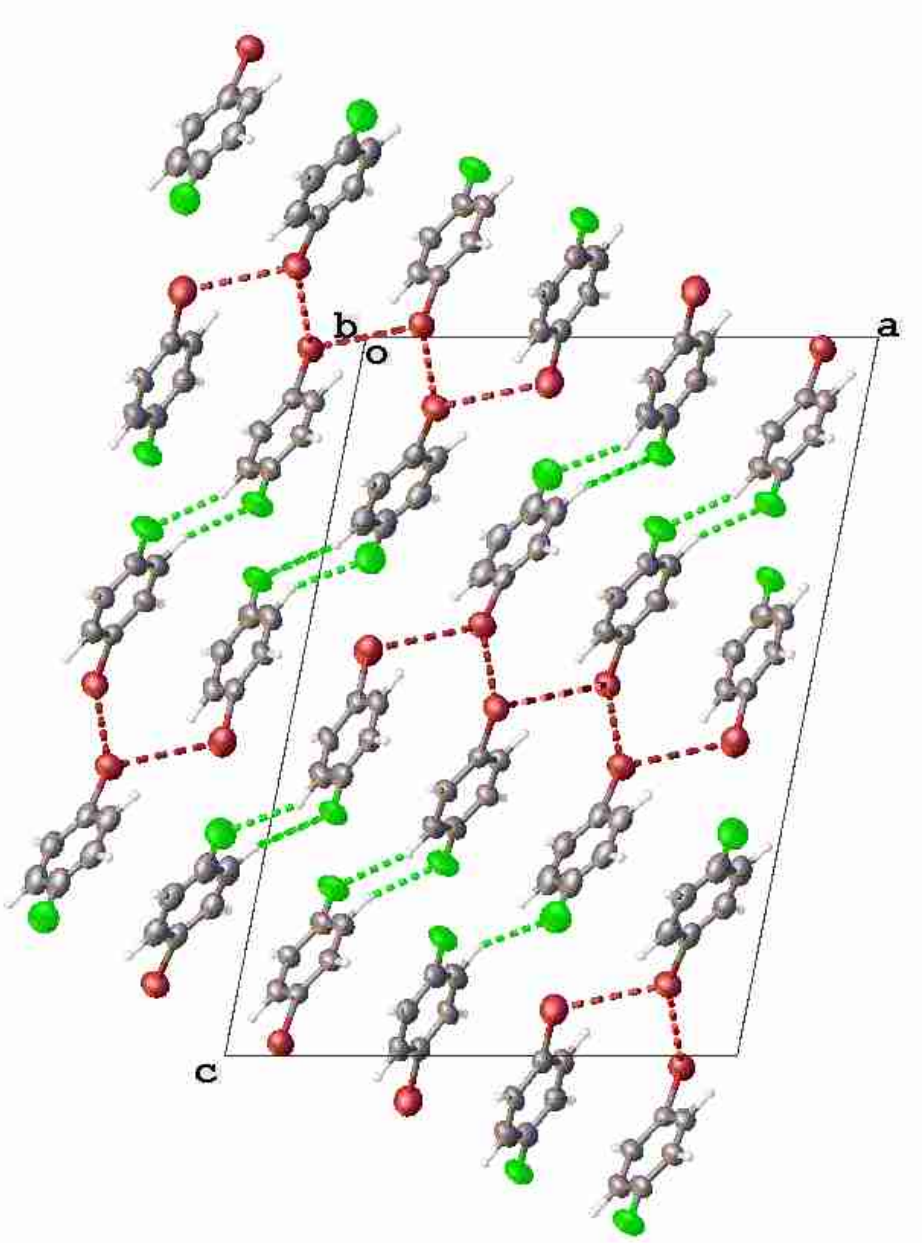

Figures 3.14 Crystal structure of 4-fluorobromobenzene at high-pressure.

The lengths and angles of the C-H···F-C interactions in 4-fluorobromobenzene are listed below in table 3.7.

	H···F / Å (LT | HP)		**C-H···F / ° (LT | HP)**	
4-fluorobromobenzene	2.42	2.505(16)	151.9	148.8 (8)
	2.50	2.555 (13)	161.3	162.8 (7)

The structure of 4-fluorobromobenzene is interesting, with a *Z′* value of 3 and a curious chequerboard motif of groups of 6 (3x2) bromine atoms forming a weakly Br···Br interacting block surrounded on all sides in two dimensions by groups of 6 (3x2)

of fluorine atoms involved in weak C-H···F-C interactions, themselves surrounded on all sides in 2 dimensions by the Br···Br interacting blocks.

The structures of the low-temperature and high-pressure polymorphs of 4-fluoroiodobenzene are shown below in figures 3.15 and 3.16 respectively.

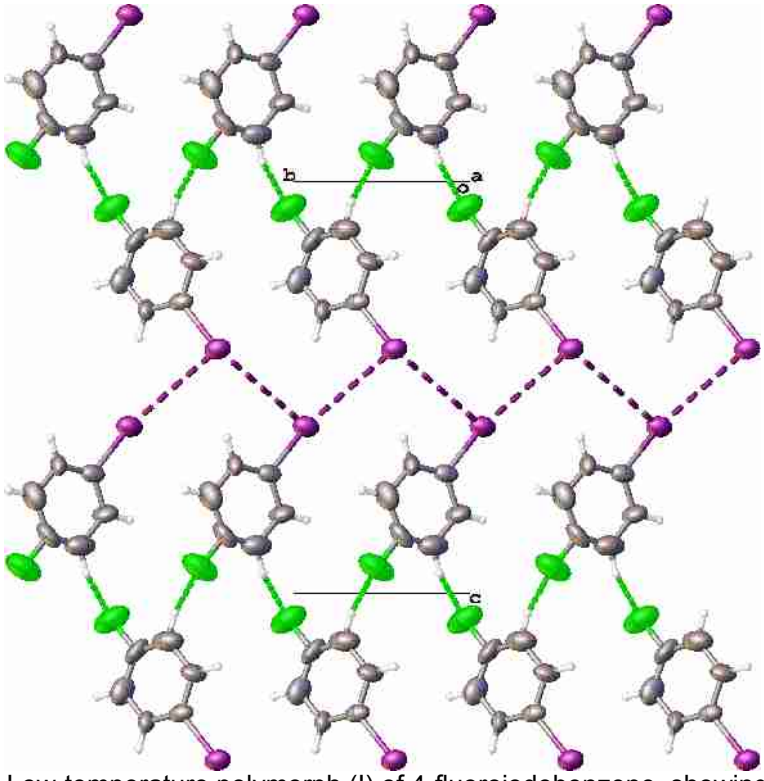

Figure 3.15 Low-temperature polymorph (I) of 4-fluoroiodobenzene, showing C-F· · ·H-C hydrogen bonds and type II I· · ·I interactions.

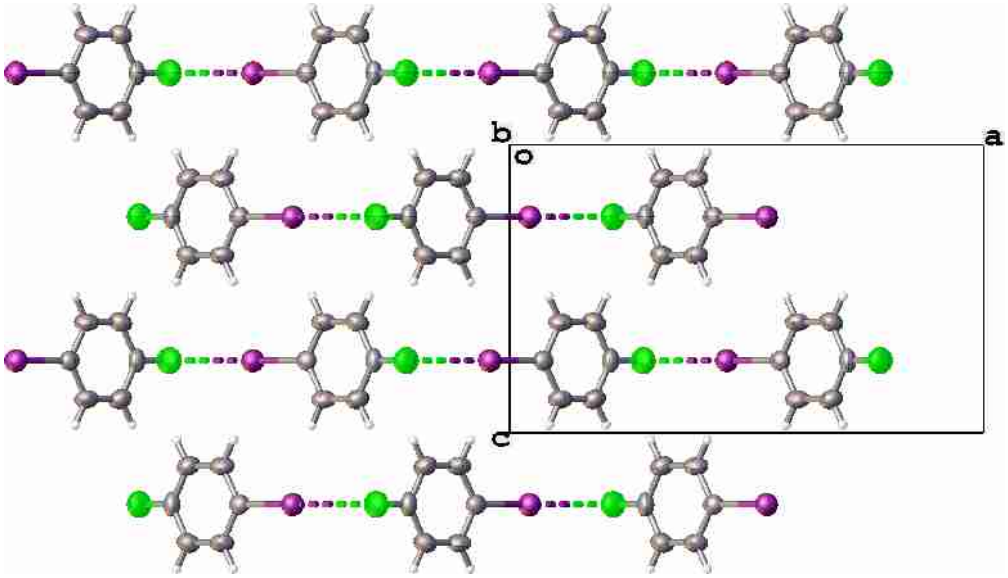

Figure 3.16 High-pressure polymorph (II) of 4-fluoroiodobenzene, showing type I I· · ·F interactions.

The length and directionality of the intermolecular interactions in the two polymorphs of 4-fluoroiodobenzene are shown below in table 3.8.

	Polymorph I (Low-Temperature) [243 (2) K]		**Polymorph II (High-Pressure) [1.9 (2) kbar]**	
V/*Z* / Å^3	166.12 (6)		160.03 (2)	
Intermolecular Interaction	Distance / Å	Angle / deg	Distance / Å	Angle / deg
C-H· · ·F-C	2.6220 (7)	135.930 (18)	-	-
I· · ·F (Type I)	-	-	3.383 (6)	177.45 (19)
I· · ·I (Type II)	3.9794 (7)	168.1683 (8), 98.89	-	-

Table 3.8 Distances and angles of principal intermolecular interactions in 4-fluoroiodobenzene polymorphs I and II.

It is clear that the two forms of 4-fluoroiodobenzene have a very different structure and intermolecular motifs. Type II I···I interhalogen interactions and C-H···F-C hydrogen bonds link layers of molecules together to form 2D sheets in polymorph I. Polymorph II has neither of these interactions present, instead having type I I···F halogen bonds forming 1D chains. The high-pressure structure was found to be only slightly (3.8 %) denser than the low-temperature structure.

The crystallographic data obtained for the crystal structures described in sections 3.3 are shown below in table 3.9.

Compound	**Fluorobenzene**	**1,2-diflurobenzene**	**1,4-difluorobenzene**	**1,3,5-trifluorobenzene**	**1,2,4,5-tetrafluorobenzene**	**Pentafluorobenzene**	**4-fluorobromobenzene**	**4-fluoroiodobenzene**
empirical formula	C_6H_5F	$C_6H_4F_2$	$C_6H_4F_2$	$C_6H_3F_3$	$C_6H_2F_4$	C_6HF_5	C_6H_4FBr	C_6H_4FI
formula weight	96.1	114.09	114.09	132.08	150.08	168.07	174.99	221.99
T (K)	ambient							
P (kbar)	3.6 (2)	1.3 (2)	0.9 (2)	1.3 (2)	1.9 (2)	1.5 (2)	1.4 (2)	1.9 (2)
crystal system	tetragonal	monoclinic	monoclinic	monoclinic	monoclinic	monoclinic	monoclinic	orthorhombic
space group	$P4_12_12$	$P2_1/n$	$P2_1/c$	C_2/c	$P2_1/c$	$P2_1/c$	$P2_1/n$	Pnam
a (Å)	5.772 (2)	7.472 (3)	5.7100 (9)	9.157 (2)	4.4620 (16)	12.252 (4)	14.709 (8)	14.7048 (11)
b (Å)	5.772 (2)	5.9424 (16)	6.5300 (5)	11.819 (5)	10.453 (3)	9.834 (2)	6.230 (3)	4.8543 (2)
c (Å)	14.698 (6)	11.602 (4)	7.2070 (7)	6.188 (3)	6.514 (3)	9.733 (2)	21.024 (13)	8.9676 (5)
β (deg)	90	103.778 (14)	101.911 (10)	125.793 (6)	109.082 (11)	102.725 (9)	101.11 (3)	90
Z	4	4	2	4	2	4	12	4
V (Å^3)	489.7 (4)	500.3 (3)	262.94 (5)	543.2 (4)	287.13 (19)	1143.9 (5)	1890.5 (18)	640.12 (7)
D_{calc} (g cm^{-3})	1.304	1.515	1.441	1.615	1.736	1.952	1.844	2.303
μ (mm^{-1})	0.062	0.082	0.078	0.095	0.109	0.129	3.443	2.603
unique reflns	344	740	414	395	471	1656	4011	1030
observed reflns	298	315	188	149	225	679	1755	560
θ_{max}	17.990	18.320	18.790	18.130	19.000	18.190	20.790	23.600
completeness %	86.6	42.6	45.4	37.7	47.8	41	43.8	37.7
R_1 [$I > 2\sigma$]	0.0605	0.0495	0.0394	0.0288	0.0364	0.0463	0.0402	0.0288
wR_2 [all]	0.1597	0.1474	0.1241	0.0561	0.0859	0.1278	0.1219	0.0561
goodness-of-fit	1.127	1.155	1.087	1.158	1.169	1.132	1.017	1.158

Table 3.9 Crystallographic data for high-pressure crystallised fluorobenzene, 1.2-difluorobenzene, 1,4-difluorobenzene, 1,3,5-trifluorobenzene, 1,2,4,5-tetrafluorobenzene, 4-fluorobromobenzene and 4-fluoroiodobenzene

3.4 Discussions and Conclusion

All three monofluorotoluenes have polymorphs that have only been observed at high-pressure. The C-F· · ·H-C hydrogen bonds in the two polymorphs of 2-fluorotoluene are similar in length to those at ambient-pressure, those in 3-fluorotoluene are considerably shorter, and those in 4-fluorotoluene are considerably longer.

Polymorph II of 2-fluorotoluene could only be obtained through high-pressure crystallisation of a 1:1 mixture of 2-fluorotoluene and 3-fluorotoluene: This is the first report of a liquid being found to crystallise into two different polymorph from the isothermal application of pressure to the liquid. A cryo-crystallographic study of liquid-mixtures involving norbornadiene previously showed that particular phases can only be grown from liquid mixtures.[166] Additionally, a report where different polymorphs were produced through isothermal compression and a procedure involving a laser to generate heat in combination with high-pressure to grow crystals has been published.)[167]

It was particularly interesting that neither the fact that crystallisation occurred from the mixture, nor the application of pressure alone resulted in the crystallisation of a new polymorph, but that in combination a new polymorph was formed. A possible explanation for this is that polymorph II is thermodynamically favoured at high-pressure (due to its higher density) whereas polymorph I is kinetically favoured. The addition of the second component may inhibit nucleation, leading to thermodynamic control of crystallisation from the liquid-mixture, but kinetic control of crystallisation for the pure sample.

All members of the set of fluorobenzenes studied through cryo-crystallisation by Thalladi *et al* [160] with the exception of 4-fluoroiodobenzene crystallised into the same form at high-pressure as observed at low-temperature. The low-temperature and high-pressure polymorphs of 4-fluoroiodobenzene were found to be remarkably distinct, and contain totally different supramolecular synthons, I· · ·I and C-F· · ·H-C interactions at low-temperature and I· · ·F interactions at high-pressure.

Given that it has previously been shown that high-pressure polymorphs can exhibit weaker intermolecular interactions in order to pack with a lower volume,[168] it is rather surprising that C-H···F-C interactions, representing the weakest end of the hydrogen bond spectrum, are present throughout the range of high-pressure crystal structures in this chapter. C-H···F-C bonds with lengths of approximately the combined Van der Waal's radii or lower are present in all but one of the compounds (4-fluorotoluene) crystallised using high-pressure in this investigation that contain only C, H and F. C-H···F-C interactions thus appear to be resistant to high-pressure and the requirement for close packing of molecules. Therefore, in the absence of stronger competing interactions one should expect to observe the near-ubiquitous presence of C-H···F-C hydrogen bonds at high-pressure.

Chapter 4: Kinetic Control of Polymorphism in the High-Pressure Crystallisation of Liquids

4.1 Introduction

Comprehending and being able to control which polymorph of a material is crystallised is highly important in many fields, particularly in the pharmaceutical industry. The most common ways to alter a crystallisation experiment to produce a desired polymorph include changing the experimental setup, (from melt, from solution etc.), the choice of solvent, the rate of solvent evaporation or the temperature.

Understanding how one can alter a high-pressure crystallisation experiment to produce different polymorphs is still limited. Examples of kinetic control of high-pressure crystallisation experiments leading to metastable polymorphs are currently sparse. These include acetamide,[169] parabanic acid,[170] and piracetam, which crystallises into form III from methanol and IV from water.[171,172]

Several factors in the high-pressure crystallisation process have been suggested as having the potential to alter the polymorph crystallised from the liquid, namely:[56]

- Procedures involving temperature variation, as compared to those where only pressure is varied, which has been substantiated in recent work.[173]
- The rate of compression.
- The presence of impurities in the starting materials.

The only prior empirical evidence of different polymorphs being produced when crystallising liquids using high-pressure involves CH_2ClI.[173] This is a special case, as it involves the high-temperature mediated decomposition of a crystal into a new high-pressure polymorph of a different compound ($2CH_2ClI \rightarrow CH_2Cl_2 + CH_2I_2$), and as such represents a solid-to-solid transformation rather than a liquid-to-solid transformation.

In addition, we have demonstrated in chapter 3 the role impurities can play in the high-pressure crystallisation process, with 2-fluorotoluene crystallising into a new polymorph when crystallised from a 1:1 mixture of 2-fluorotoluene and 3-fluorotoluene

at high-pressure.

Given that it has been known for decades that altering the rate of cooling when crystallising from the melt may cause a different polymorph to form,[174,175,176] and that this observation has also been noted more recently in the cryo-crystallisation of liquids,[159,160,177] we tested the hypothesis that altering the rate of compression can result in the formation of different polymorphs in high-pressure crystallisation experiments.

It has previously been reported that altering the cooling rate in the cryo-crystallisation of 2-fluorophenylacetylene (**2FPA**) results in the formation of different polymorphs.[159] Polymorph I was crystallised through quenching of the hot liquid (353 K) in liquid nitrogen. Molecules in this polymorph are linked through C-H···π and π···π interactions. Polymorph II was crystallised through cooling rates of 1000 Kh^{-1} from ambient conditions, with packing mediated through C-H···F and C-H···π interactions. Given that altering the rate of cooling results in polymorphism in **2FPA**, this compound represents a good opportunity tor studying polymorphism through altering the rate of compression.

4.2 Experimental Details

In order to isolate the effect of varying the rate of compression, crystals were grown through variation in pressure alone. The standard high-pressure crystallisation technique, described in section 1.1 was used in all experiments in this chapter. The pressures used in the high-pressure crystallisation experiments in the experiments in this chapter are listed in table 4.1 below. The rates of application of pressure varied, as described herein in section 4.3.

4.3 Results and Discussion

On initial crystallisation of **2FPA** it was clear from unit-cell measurements that a weakly diffracting sample of polymorph I had been formed. However, further attempts to repeat the procedure yielded polymorph II, and a new form, polymorph III that had not previously been reported.

Table 4.1 lists the crystallographic data obtained for these three polymorphs.[178]

	Polymorph I	**Polymorph II**	**Polymorph III**
empirical formula	C_7H_5F		
formula weight	120.13		
T (K)	ambient		
P (kbar)	5.7 (2)	5.3 (2)	5.7 (2)
crystal system	orthorhombic	monoclinic	monoclinic
space group	$Pna2_1$	$P2_1$	$P2_1$
a (Å)	7.578 (6)	7.031 (4)	3.9343 (7)
b (Å)	13.024 (14)	5.924 (4)	5.9336 (10)
c (Å)	6.171 (5)	7.441 (5)	12.962 (4)
β (deg)	90	103.563 (17)	98.467 (9)
Z	4	2	2
V (Å^3)	609.1 (10)	301.3 (3)	299.29 (12)
D_{calc} (g cm^{-3})	1.310	1.324	1.333
μ (mm^{-1})	0.059	0.060	0.059
reflns collected	1591	1372	686
unique reflns	446	1021	846
observed reflns	253	566	472
θ_{max}	14.33	19.18	17.99
completeness %	56.73	55.44	55.79
R_1 [$I > 2\sigma$]	0.0426	0.0424	0.0346
wR_2 [all]	0.1033	0.0895	0.0630
goodness-of-fit	1.1196	1.1550	1.1810

Table 4.1 Crystallographic data from the three polymorphs of **2FPA** obtained at high-pressure.

The crystal structure of the three polymorphs is shown below in figures 4.1-3. Polymorphs I and III were found to have disorder of the fluorine atom position. (Polymorph I has previously been shown to exhibit this disorder at low-temperature).

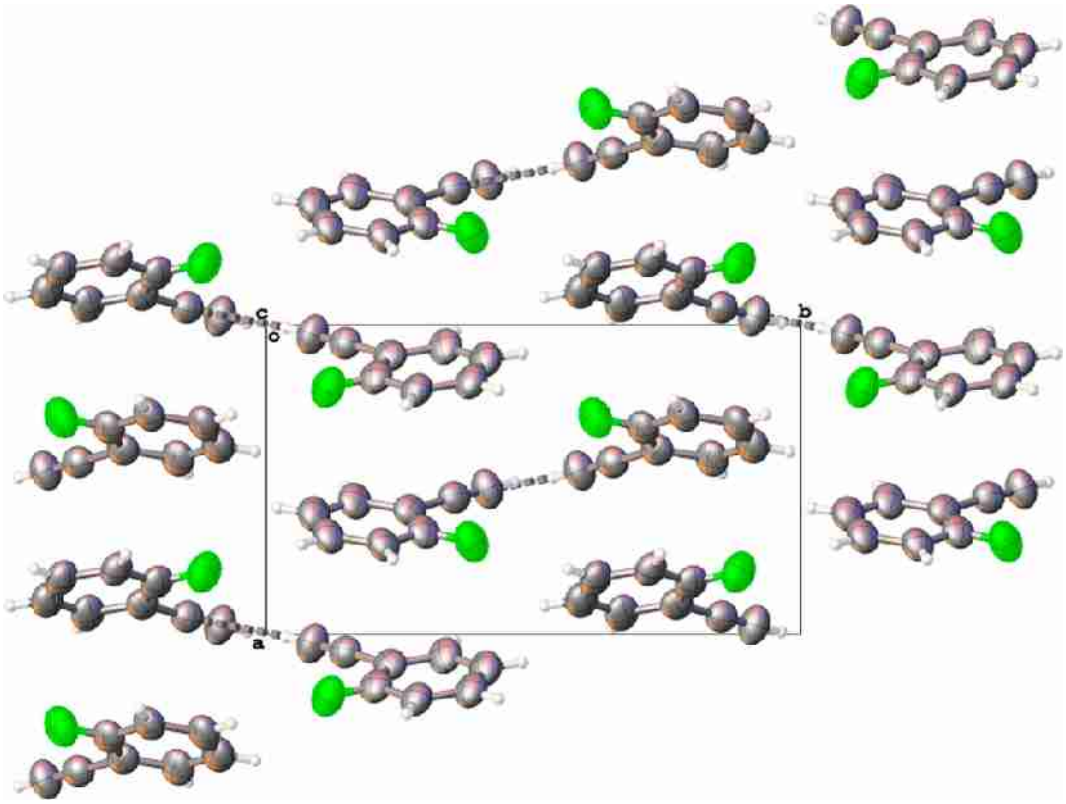

Figure 4.1 Crystal structure of polymorph I of **2FPA**. Gray dashed bonds represent CH···π interactions. Fluorine is disordered across two positions in the ratio 0.773 (17) : 0.237 (17), with only the major component shown above.

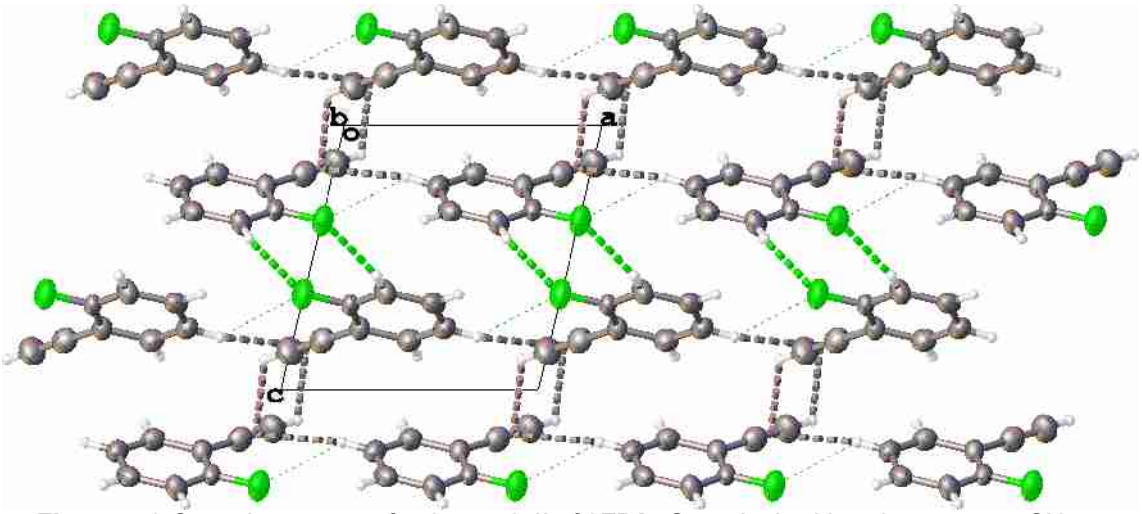

Figure 4.2 Crystal structure of polymorph II of **2FPA**. Grey dashed bonds represent CH···π chains. Green dashed lines represent CH···F interactions. (The heavier and lighter dashed lines refer to shorter and longer CH···F interactions respectively).

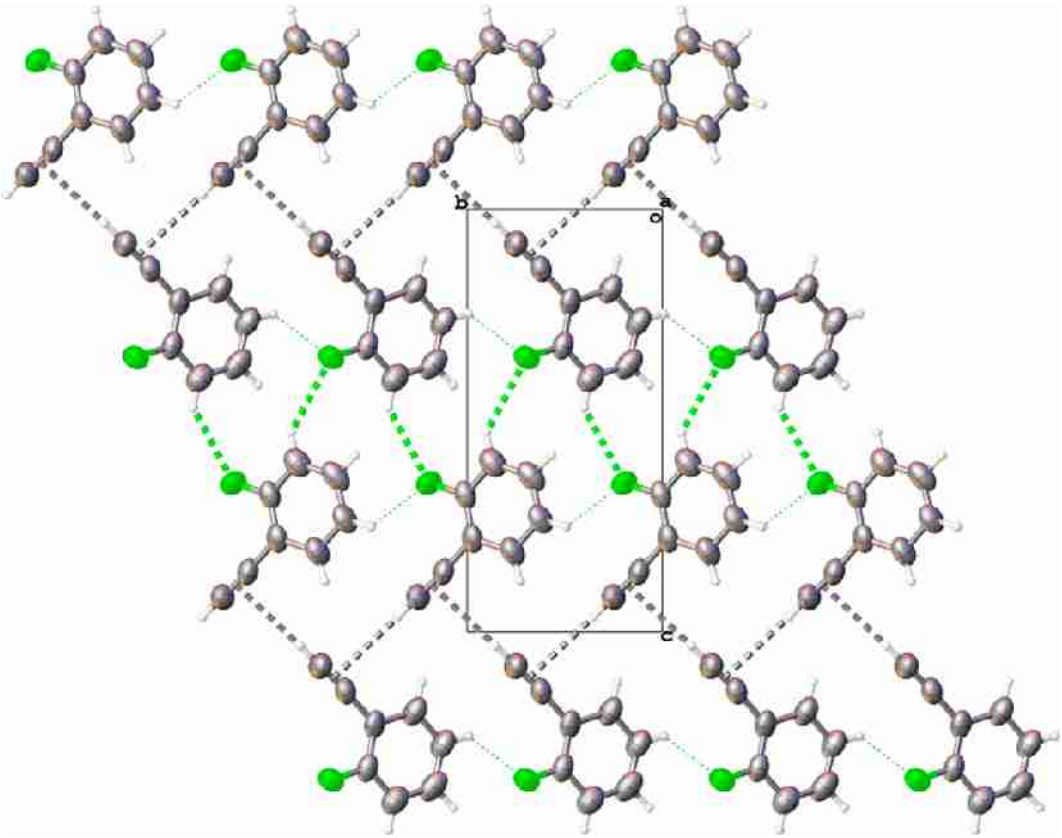

Figure 4.3 (a) Crystal structure of polymorph III of **2FPA**. Gray dashed lines represent CH···π chains. Green dashed lines represent CH···F interactions. (The heavier and lighter dashed lines refer to shorter and longer CH···F interactions respectively). Fluorine is disordered across two positions in the ratio 0.852 (6) : 0.148 (6).

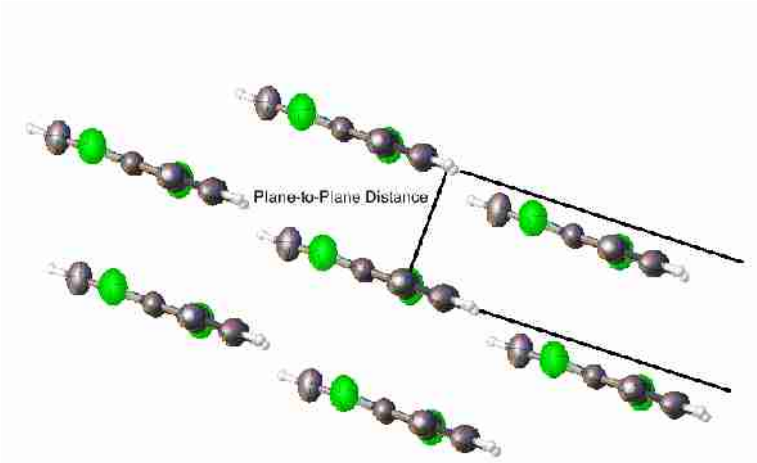

Figure 4.3 (b) Diagram showing π···π interactions in polymorph III of **2FPA**.

The different packing motifs in the three structures are probed through examination of the intermolecular interactions in the three polymorphs. Tables 4.2-4.4 lists the relevant distances and angles for CH···F, CH···π and π···π interactions.

Polymorph I (*Pna*2$_1$)		
Interaction	d (H···A)/Å	∠(D-H---A)/°
CH(*sp*)···π	2.896 (2)	176.9 (8)

Table 4.2 Intermolecular interactions in polymorph I of **2FPA** at high-pressure. Only interactions involving the major position of F are shown. C-H bonds have been constrained in length to 0.93 Å.

Polymorph II (*P*2$_1$)		
Interaction	d (H···A)/Å	∠(D-H---A)/°
CH(*sp*)···π	2.871 (1)	132.4 (4)
CH(sp^3)···π	2.971 (1)	151.9 (5)
CH(sp^2)···F	2.605 (3)	156.3 (4)
CH(sp^2)···F	2.740 (4)	127.6 (5)

Table 4.3 Intermolecular interactions in polymorph II of **2FPA** at high-pressure. Only interactions involving the major position of F are shown. C-H bonds have been constrained in length to 0.93 Å.

Polymorph III (*P*2$_1$)		
Interaction	d (H···A)/Å	∠(D-H---A)/°
CH(*sp*)···π	2.7732 (4)	171.4 (4)
CH(sp^2)···F	2.598 (6)	138.8 (4)
CH(sp^2)···F	2.713 (6)	134.7 (8)
π···π	Plane to Plane Distance/Å	
	3.467 (3)	

Table 4.4 Intermolecular interactions in polymorph III of **2FPA** at high-pressure. Only interactions involving the major position of F are shown. C-H bonds have been constrained in length to 0.93 Å.

After data collection, the pressure applied to crystals of each of the three polymorphs was further increased in order to see if there were any solid-to-solid phase transformations. No phase transformations were observed at pressures of up to 35 kbar. The unit cell volumes of each of the three polymorphs collected at various pressures are shown below in figure 4.4.

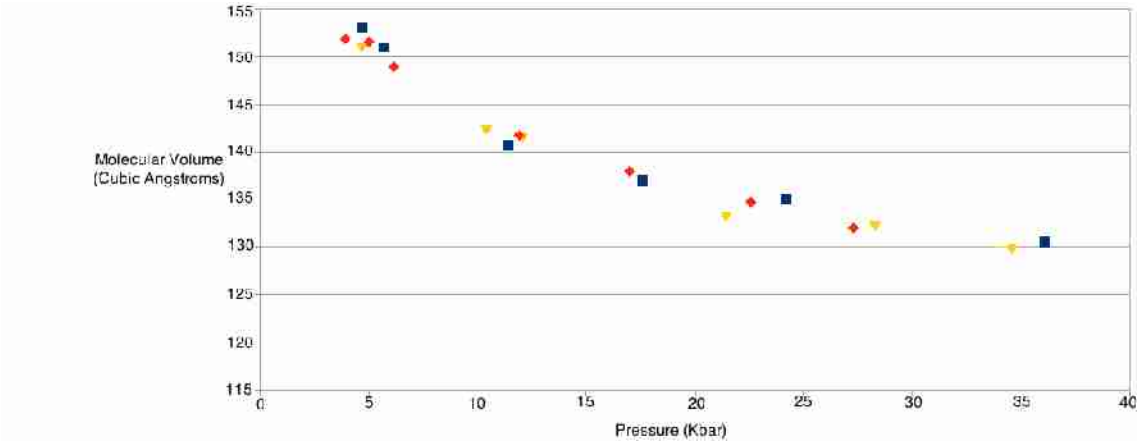

Figure 4.4 Graph showing the volume occupied by one molecule in each of the three polymorphs of **2FPA** at variable pressure. Polymorph I is represented by blue squares, polymorph II by red diamonds, polymorph III by yellow triangles.

The densities of the three polymorphs are clearly quite similar at all pressures. As such, increasing the pressure is unlikely to significantly destabilise one polymorph in relative terms.

On obtaining the structure of the three polymorphs, repeated crystallisation experiments were carried out to better understand the system. It was found that Polymorph II forms through slow compression. Near the liquid-crystalline phase boundary a minor increase in pressure was applied every 15 minutes until crystallisation occurred. Polymorphs I and III were both crystallised by rapid compression (<2s) from ambient pressure to the crystallisation pressure. The presence (or not) of ruby and other impurities in the sample chamber did not appear to alter the outcome in these experiments. Immersion of the DAC in liquid nitrogen and subsequent pressurisation (as described in the crystallisation of 3-fluorotoluene in section 2.2) led to the formation of polymorph II.

There are several obvious differences in the intermolecular interactions of **2FPA** in the three polymorphs. Polymorphs II and III have CH···F interactions, while polymorph I only has CH···F interactions involving the less occupied position of disordered **2FPA**. Polymorphs I and III have π···π stacking forces between layers. These are not observed in polymorph II. All three polymorphs have significant CH···π interactions, however polymorphs I and III have one relatively linear interaction from the alkynyl proton to the centre of the C≡C bond, whereas polymorph II has a bifurcated donor (with one of the two donors being the alkynyl proton).

We have shown these intermolecular interactions in a Hirshfeld Surface in order to visualise the differences in packing between the three polymorphs. d_{norm} is mapped onto the surface.

Figures 4.5, 4.6, and 4.7 show the Hirshfeld Surfaces and fingerprint diagrams for the three polymorphs.

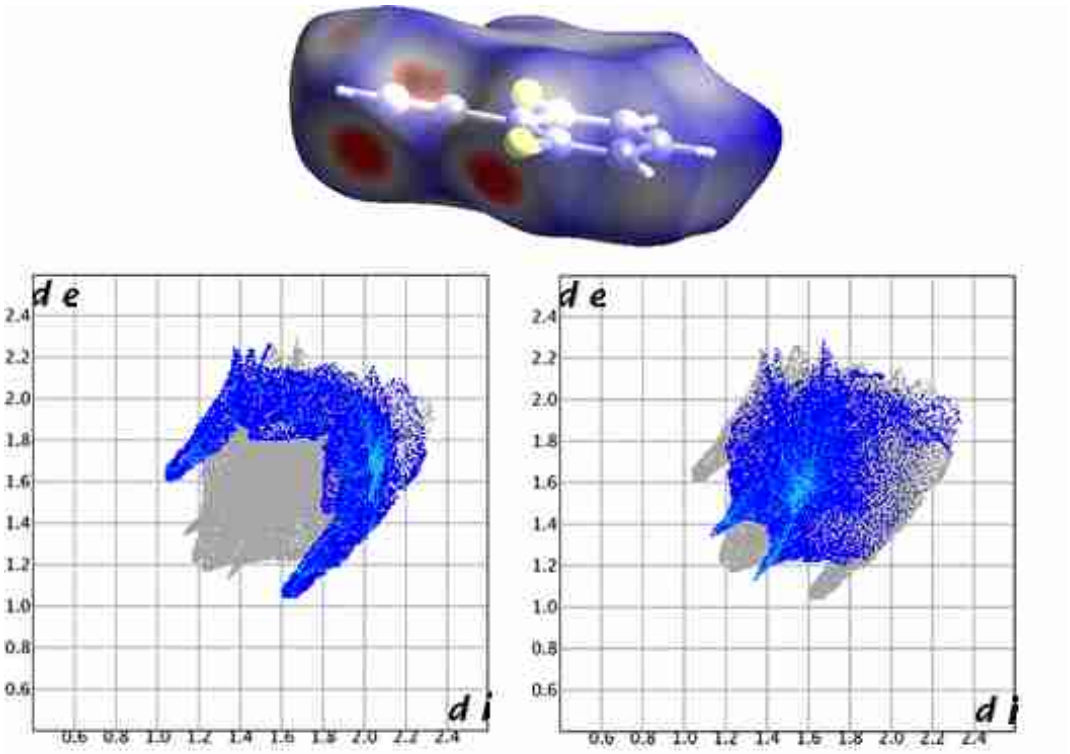

Figure 4.5 Hirshfeld and fingerprint plots for **2FPA** polymorph I, with the CH···C (left) and CH···F (right) interactions highlighted.

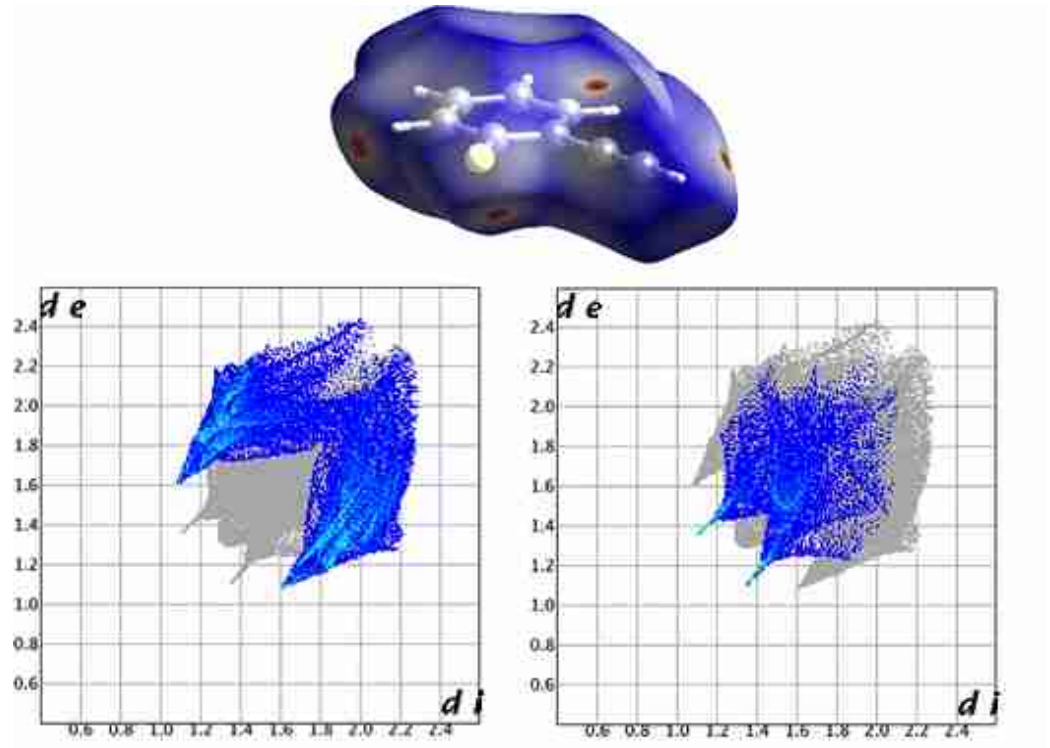

Figure 4.6 Hirshfeld and fingerprint plots for **2FPA** polymorph II, with the CH···C (left) and CH···F (right) interactions highlighted.

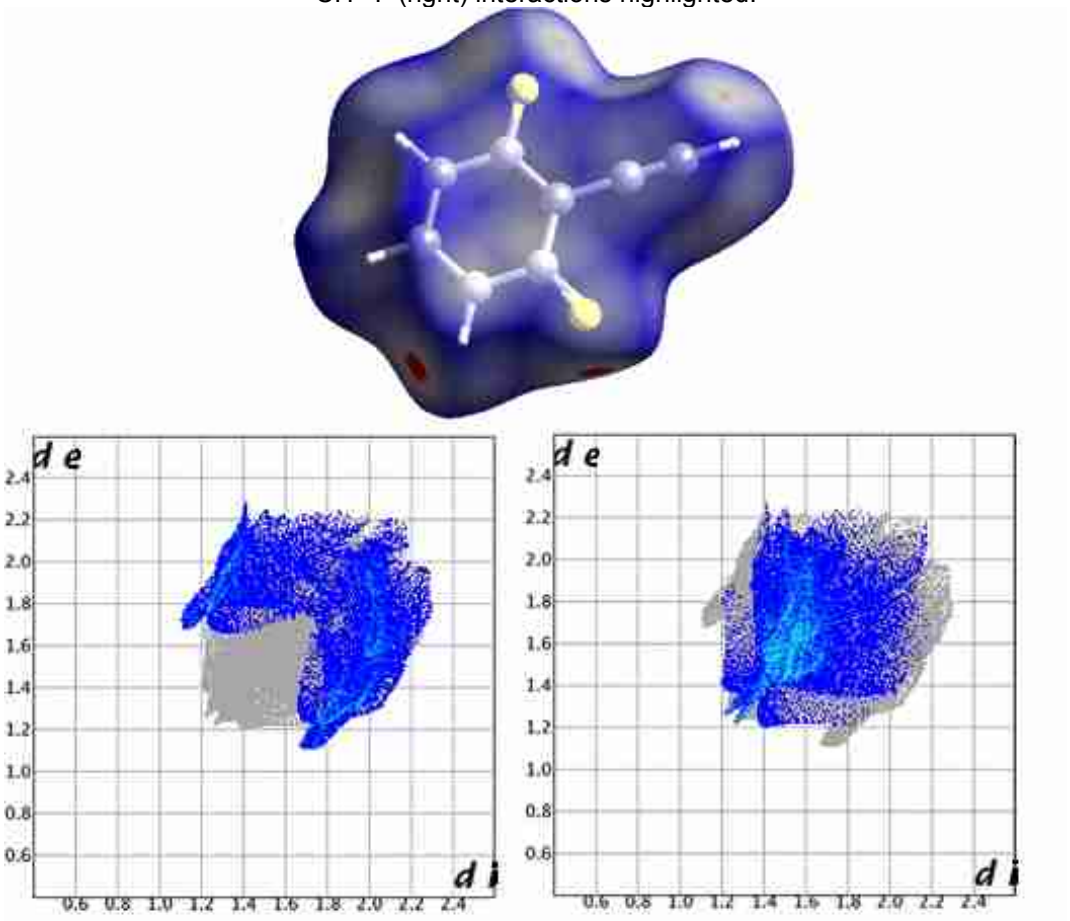

Figure 4.7 Hirshfeld and fingerprint plots for **2FPA** polymorph III, with the CH···C (left) and CH···F (right) interactions highlighted.

The data from the Hirshfeld Surface and attached fingerprint plots suggest that CH···F interactions are weakest in polymorph I and CH···π interactions are rather stronger in III than in I and II.

4.4 Complementary Computational Calculations

4.4.1 Introduction

Crystal energy landscapes have proven to have some success in the prediction of the crystal structure of molecular systems, particularly where the molecule in question is small and rigid, although techniques for flexible molecules have been improved in recent years.[177-187] However, the computational power required to model subtle intermolecular interactions sufficiently accurately that the true thermodynamic ordering of polymorphs is reproduced is vast, and as such this method is still in its infancy. Although one cannot presume that the calculations reproduce the exact thermodynamic ordering of polymorphs, it possible to examine a set of several low-energy polymorphs in order to make sensible conclusions.[54]

The electrostatic term typically dominates the order of thermodynamic stability of different polymorphs of a material. Rayleigh–Schrödinger perturbation theory can be used in principle to calculate the electrostatic term, U_{est}, between two molecules, *A* and *B*.[142,190]

$$U_{est} = \frac{\int \rho^{A}(r)\,\rho^{B}(r')}{4\pi\epsilon_0 \|r - r'\|}\,dr dr'$$

Here $\rho^{A}(\mathbf{r}) = \Psi^{A} * \Psi^{A}$ represents the ground state charge density of an isolated molecule *A*. The integration is over the coordinates of the charge density in molecules *A* and *B*. However, Rayleigh–Schrödinger perturbation theory is far too computationally expensive for use in crystal structure prediction. As such, the molecular charge density is assigned to individual atoms within the molecule. (This is done using Stone's Distributed Multipole Analysis (DMA) which represents the *ab initio* charge density matrix as sets of multipoles.)[191]

$$E_{electrostatic} = \frac{1}{2}\sum_{A}\sum_{B} Q_t^a T_{tu}^{ab} Q_u^b$$

Here the summation is over molecules A and B. Q_t^a refers to the atomic sites *a*, in molecule A with multipole components, *t*. *T* refers to the interaction function between

two molecules.[191]

Crystal structure prediction[192] has been used to supplement the experimental results described in this chapter by calculating the lattice energy of the three polymorphs of **2FPA**, and putting these energies into context through comparison with hypothetical, computationally generated structures. Given the highly interesting kinetic control of the crystallisation of **2FPA**, we were interested in the thermodynamic characterisation of the three polymorphs in order to better understand the system. Calculations were carried out with assistance from Professor S. L. Price and Dr. L. S. Price at University College London. Intermolecular interactions are modelled in these calculations using several components, namely electrostatics, induction, electron-electron repulsion and charge transfer.[193]

4.4.2 Computational Methods

The molecular geometry of **2FPA** was calculated using an *ab initio* optimisation of the HF/6-31G(d,p) wave function using GAUSSIAN 03.[194] MOLPAK[195] was used to produce densely packed crystal structures in a number of common space groups with $Z' = 1$. (This procedure uses a totally rigid body model to build potential packing arrangements and a very simple repulsion-only model to roughly calculate the packing energy.)[195]

A set of the most energetically favourable crystal structures are then ran through DMACRYS[196] to minimise the lattice energy, generating the crystal energy landscape. DMACRYS calculates the electrostatic contribution to the lattice energy using Stone's Distributed Multipole Analysis (DMA) (see above) of the HF/6-31G(d,p) charge density using the program GDMA.[197] An isotropic atom-atom potential was used to calculate the repulsion-dispersion contribution to the lattice energy. In this potential, repulsion-dispersion term between atom *i* of type ι in molecule M and atom *k* of type κ in molecule N separated by distance R_{ik} is given by

$$U_{rep-disp}^{MN} = \sum_{i \in M,\, k \in N} A_{ik} \exp\left(-B_{ik} - R_{ik}\right) - \frac{C_{ik}}{R_{ik}}$$

(*A*, *B* and *C* are parameters relating to the atom types ι and κ),[198] These parameters for all atomic types were taken from the work of Williams *et al*.[199,200] The input files for DMACRYS are generated using NEIGHCRYS,[201] which turns the crystallographic data (.res files) into the Cartesian co-ordinate format.

4.4.3 Computational Results and Discussion

The lattice energies and densities of theoretically generated structures using an SCF optimised input generated using MOLPAK[195] and DMACRYS[196] are shown below in figure 4.8.

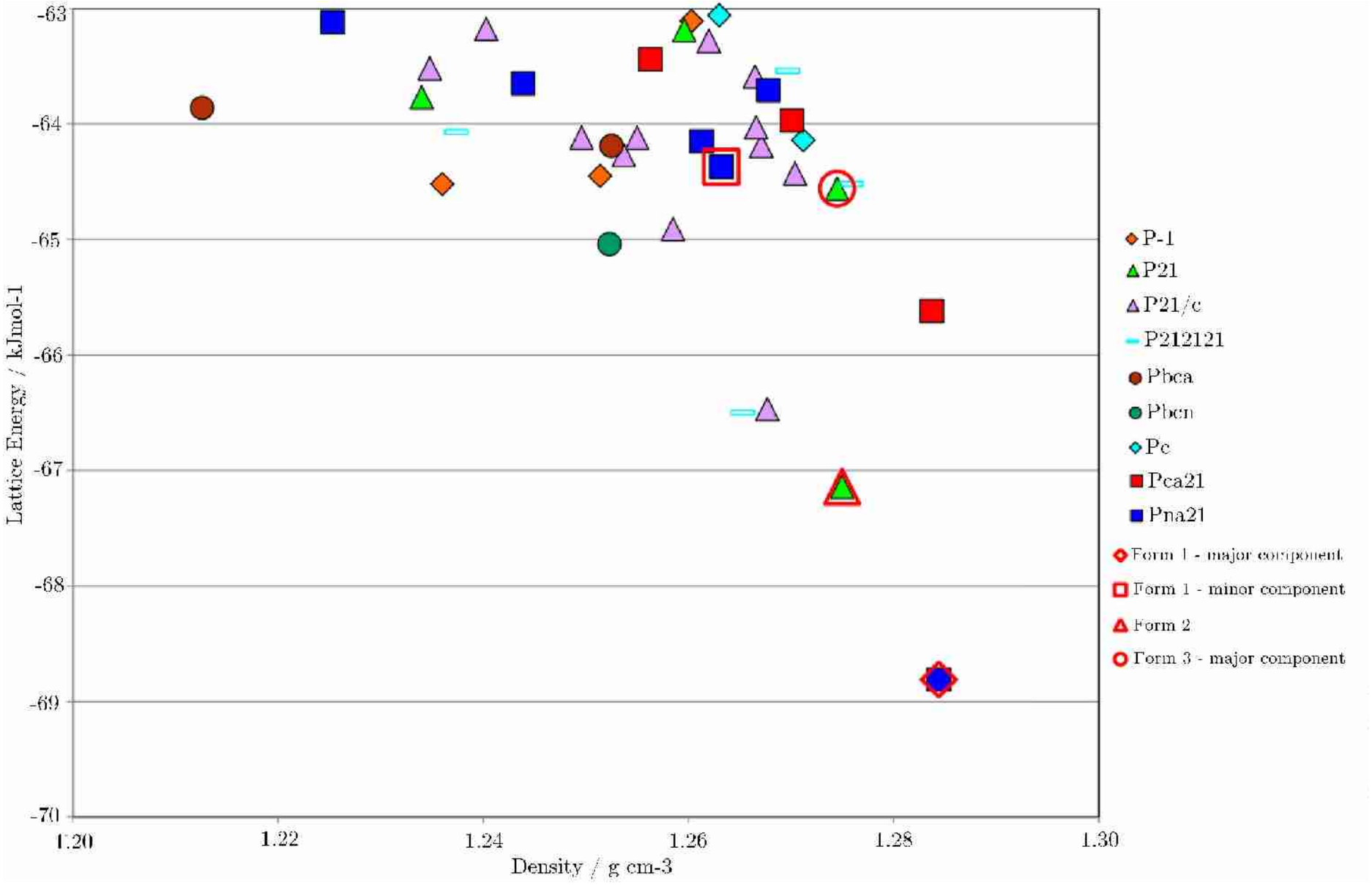

Figure 4.8 Lattice energies and densities of theoretically generated structures of **2FPA**, with structures that match the experimentally observed polymorphs highlighted.[178]

Polymorph II and the higher occupied of the two positions of disordered polymorph (hereafter known as the major component) were found to be the two most energetically favourable structures. The major component of polymorph III was found to be the 6th lowest energy structure.

We were interested why the hypothetical polymorphs ranked 3rd – 5th were not observed, while the 6th ranked theoretical polymorph corresponds to the experimental polymorph III. Clearly, it is possible that the crystallisation of polymorph III is kinetically favoured. However, another possible explanation for the experimental observation of this polymorph but not those ranked 3rd – 5th is that the latter three structures all display very significant structural similarities to either polymorph I or II, and as such transformation to these polymorphs early in the nucleation process may be possible.

Figures 4.9-11 show the extent of structural similarity between each of the three potential low energy polymorphs with one of the existing polymorphs. (Images generated using Mercury[202] and Olex2.[37])

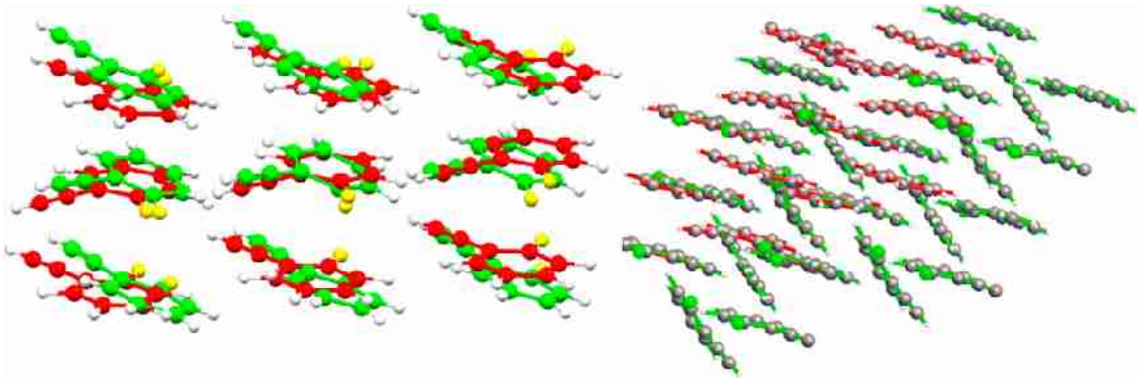

Figure 4.9 Left: Structural similarity between am34 (green) and the major component ofpolymorph I (red). Right: Overlay of the two structures, showing packing differences.

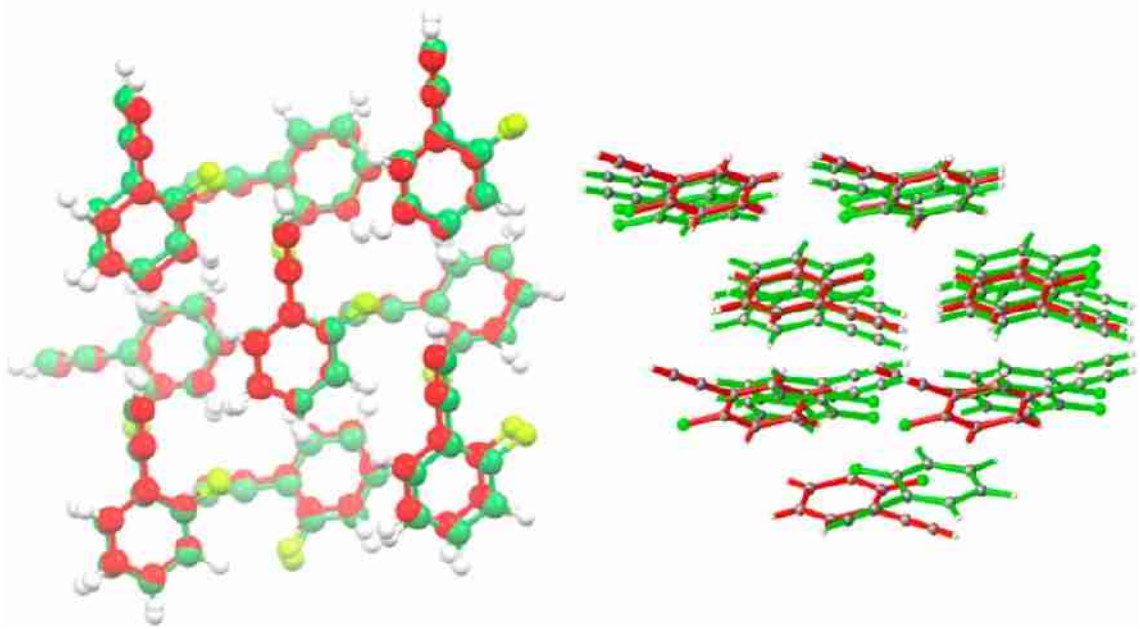

Figure 4.10 Left: Structural similarity between bh82 (green) and polymorph II (red). Right: Overlay of the two structures, showing packing differences.

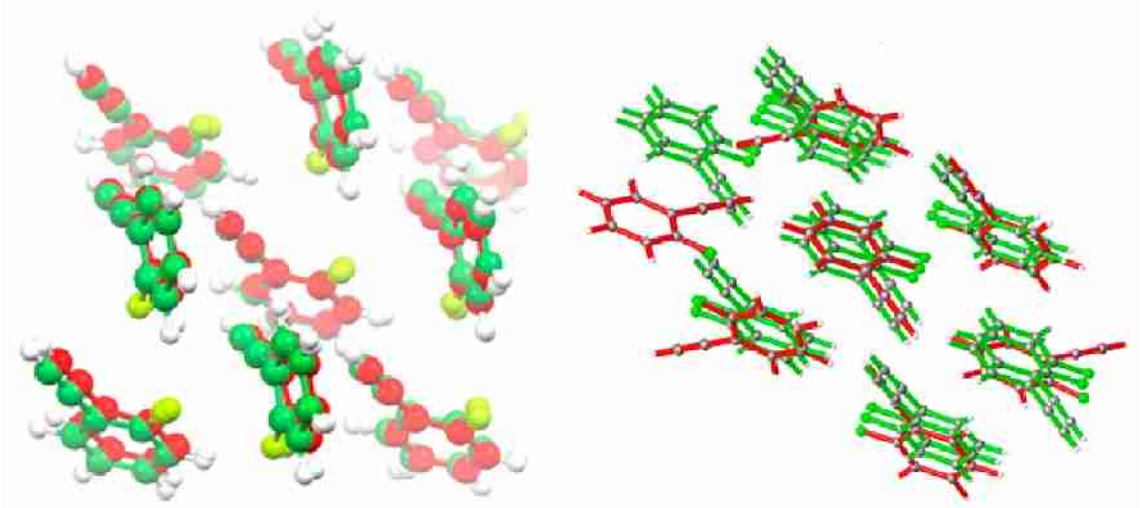

Figure 4.11 Left: Structural similarity between aq9 (green) and polymorph II (red). Right: Overlay of the two structures, showing packing differences.

The experimentally observed polymorphs and the hypothetical polymorphs ranked 3rd – 5th in energy were then re-minimised at higher levels of theory by Prof. Chris Pickard (UCL) using the CASTEP software package.[203] The results are shown below in table 4.5.

Polymorph	Energy Relative to Form I (Major) / kJ mol^{-1}
III (major component)	-4.05
II	-1.64
bh82	-0.77
I (major component)	0.00
aq9	0.48
III (minor component)	0.58
I (minor component)	1.25
am34	6.18

Table 4.5 Relative energies at the PBE and PBE + TS theory levels.

Table 4.6 shows the weighted relative energies of the polymorphs taking account of the disorder in polymorphs I and III.

Polymorph	Energy Relative to Form III / kJ mol^{-1}
III	0
II	1.72
bh82	2.59
I	3.67
aq9	3.84
am34	9.54

Table 4.6 Weighted relative energies at the PBE and PBE + TS theory levels.[178]

The results above show that the calculated energies of the three hypothetical polymorphs are all less favourable than those of the structurally related experimentally observed polymorphs (as shown in figures 4.9-11).

It is clear that both thermodynamics and kinetics are important in the high-pressure crystallisation of **2FPA**. Thermodynamics selects a small group of viable polymorphs. Kinetics, (in this case through varying the rate of compression), then determines which one of this set is crystallised from the liquid.

4.5 Conclusions

In summary, it has been shown that a subtle variation in the high-pressure crystallisation method, namely varying the rate of compression, results in the formation of distinct polymorphs of **2FPA**.

Potential supramolecular synthons in **2FPA** include CH···F, CH···π and π···π interactions. The three experimentally observed polymorphs have very different interactions to one-another, suggesting that these weak intermolecular interactions are in close competition, resulting in very different structures of **2FPA** having similar lattice energies - thus driving polymorphism in this system. The similar lattice energies go some way to explaining why the three polymorphs form under only slightly different experimental conditions, namely the rate of compression of the liquid.

It is interesting to compare the observed polymorphs of **2FPA** to its parent compound, phenylacetylene (**PA**).[178] Both compounds are liquids under ambient conditions, and three polymorphs of each compound have been isolated and characterised. In each compound, one polymorph can be obtained through slow cryo-crystallisation, one through rapid cryo-crystallisation, and one through high-pressure crystallisation. Furthermore, **3FPA** has two polymorphs. One that may be grown through slow cryo-crystallisation and the other through rapid cryo-crystallisation. Observing multiple forms at the same thermodynamic conditions is quite rare for compounds that are liquids at ambient conditions, so it seems rather interesting that this family of compounds seems to be so polymorphically rich. Despite the method of crystallising each of the three polymorphs being similar in **PA** and **2FPA**, the structures are very different. All three polymorphs of **2FPA** are relatively simple structures with $Z' = 1$, whereas the three polymorphs of **PA** are relatively complicated, with $Z' = 2.5$, 3 and 6.[204,205,206] In this chapter it has been demonstrated for the first time that the rate of compression is very important in high-pressure crystallisation experiments.

Chapter 5: High-pressure Crystallisation of Low-Melting Molecular Complexes

5.1 Introduction

The design of co-crystals - crystals combining two or more neutral components, is becoming an increasingly important research theme in crystal engineering and the formation of pharmaceuticals.[205-209] Research into multi-component systems where the mixture is a liquid under ambient conditions has been limited so far,[210-219] due to the difficulty in crystallising the liquid mixture. We are interested if compression of a liquid mixture might give rise to different structures to those seen through cryo-crystallisation.

Different terms have been used in the past to describe these low-melting multi-component systems, including “molecular complexes”, “co-crystals”, “co-liquids”, “co-solvents” and “solvent-solvates”. The terms solvent-solvate and co-liquids/co-solvents are inappropriate as, in this work, these materials are being studied in the solid state. The term co-crystal is typically used to describe materials that are solid under ambient conditions. Therefore we shall use the term *Low-melting Molecular Complex* (LmMC), as used by Yufit and Howard.[212]

There are several potential differences in the product of crystallisation experiments of liquid mixtures. Firstly, different polymorphs or ratios of components in the LmMC could crystallise at low-temperature and high-pressure. Secondly, it is possible for a single-component of the mixture to crystallise from the liquid under high-pressure, and a multi-component system at low-temperature, or vice versa. Thirdly, there is also the potential to crystallise new polymorphs of one of the single components from the mixture.

In order to see if the two crystallisation methods form different products, we determined the crystal structures of a wide range of liquid mixtures crystallised through cryo- and high-pressure. The systems studied are listed in sections 5.2 and 5.3 below.

5.2 Weakly Interacting Liquid Mixtures

5.2.1 Introduction

The first eight liquid mixtures studied were a selection of weakly interacting systems, listed in table 5.1, that had previously been shown to form LmMCs through cryo-crystallisation.[212,213,214,217]

Experiment Number	Liquid Mixture
I	Chloroform 1 : 1 Cyclohexane
II	1,4-Dioxane 1 : 1 Chloroform
III	Cyclohexanone 1 : 1 DCM
IV	1,4-Dioxane 1 : 1 DCM
V	DMSO 1 : 3 Chloroform
VI	DCM 4 : 1 DMSO
VII	1,4-Dioxane 1 : 1 Bromoform
VIII	DMSO 1 : 1 Bromoform

Table 5.1 Weakly interacting liquid mixtures studied by high-pressure crystallisation

5.2.2 Experimental Details

The liquid mixtures listed in table 5.1 were crystallised using the standard high-pressure crystallisation procedure described in section 1.1.

5.2.3 Results and Discussion

High-pressure crystallisation of the weakly interacting liquid mixtures listed in table 5.1 resulted in the formation of a LmMC in three cases (I,V,VII), with each LmMC crystallising into the same polymorph that was observed through cryo-crystallisation. In the remainder of the experiments, a known polymorph of a single component was crystallised from the liquid mixture. The results obtained from these high-pressure crystallisation experiments are summarised below in table 5.2.

Experiment	High-Pressure Unit-Cell Dimensions		Crystallisation Product	Ambient-pressure Unit Cell Dimensions of Crystallisation Product	
	Length / Å	Angle / °		Length / Å	Angle / °
I (Chloroform 1 : 1 Cyclohexane)	a=5.951 (3)	α=98.63 (6)	LmMC (isomorphous to cryo-crystallised LmMC)[222]	a=6.044 (1)	α=98.82 (1)
	b=8.923 (3)	b=100.18 (7)		b=9.099 (2)	β=100.43(1)
	c=9.431 (19)	γ=98.19 (2)°		c=9.596 (2)	γ=97.22 (1)°
II (1,4-Dioxane 1 : 1 Chloroform)	a=5.7333	β=100.40 (2)°	1,4-Dioxane (High-pressure polymorph)[241]	a=5.659 (1)	β=98.36 (3)
	b=6.438 (3)			b=6.410 (1)	
	c=6.167 (2)			c=5.892 (1)	
III (Cyclohexanone 1 : 1 DCM)	a=5.686 (10)	β=100.7 (1)	1,4-Dioxane (High-pressure polymorph)[241]	a=5.659 (1)	β=98.36 (3)
	b=6.368 (15)			b=6.410 (1)	
	c=6.113 (19)			c=5.892 (1)	
IV (1,4-Dioxane 1 : 1 DCM)	a=5.2902	β=90°	polymorphs produced at ambient pressure)[223]	a=5.374 (1)	β=90°
	b=6.891 (7)			b=7.039 (1)	
	c=14.977 (6)			c=15.191 (1)	
V (DMSO 1 : 3 Chloroform)	a=5.883 (3)	β=91.88 (7)	LmMC (isomorphous to cryo-crystallised LmMC)[212]	a=5.9679 (3)	β=91.63 (1)
	b=8.881 (6)			b=9.0041 (6)	
	c=22.74 (3)			c=23.142 (2)	
VI (DCM 4 : 1 DMSO)	a=5.181 (5)	α=72.81 (9)	DMSO[224]	a=5.308 (3)	α=72.56 (5)
	b=5.720 (19)	β=83.85 (6)		b=5.914 (4)	β=84.35 (4)
	c=6.992 (4)	γ=63.13 (11)		c=7.243 (2)	γ=63.66 (6)
VII (1,4-Dioxane 1 : 1 Bromoform)	a=4.060 (6)	β=107.30 (3)	LmMC (isomorphous to cryo-crystallised LmMC)[213]	a=4.1771 (3)	β=106.73 (1)
	b=19.160 (5)			b=19.300 (2)	
	c=5.909 (2)			c=6.0082 (5)	
VIII (DMSO 1 : 1 Bromoform)	a=6.213 (11)	α=90	Bromoform[225]	a=6.312 (1)	α=90
	b=6.213 (11)	β=90		b=6.312 (1)	β=90
	c=7.49 (2)	γ=120		c=7.151 (16)	γ=120

Table 5.2 Results of co-crystallisation attempts I – VIII.

It is notable that the application of pressure often fails to generate LmMCs that may be crystallised using low-temperature. This however, is not altogether surprising when one considers that the application of high-pressure alone can fail to crystallise single component liquids (such as 3-fluorotoluene), instead producing a glass.[164]

5.3 Liquid Mixtures of Carboxylic Acids and Basic Aromatic Rings

5.3.1 Introduction

Ten liquid mixtures of various carboxylic acids with aromatic bases (pyridine / pyrimidine / pyrazine) were studied. Five of these systems had previously been studied at low-temperature, while the remainder are unstudied. The systems studied are listed below in table 5.3.

Experiment Number	Liquid Mixture
IX*	Pyrazine 1 : 2 Acetic Acid
X*	Pyrazine 1 : 2 Propionic acid
XI*	Pyrazine 1 : 2 Butanoic acid
XII*	Pyridine 1 : 4 Formic Acid
XIII*	Pyridine 1 : 1 Formic Acid
XIV	Pyrimidine 1 : 2 Formic Acid
XV	Pyridine 1 : 2 Glutaric Acid
XVI	Pyridine 2 : 1 Pimelic Acid
XVII	Pyridine 2 : 1 Suberic Acid
XVIII	Pyridine 2 : 1 Azelaic Acid

Table 5.3 Liquid mixtures of aromatic nitrogen bases with carboxylic acids. Those systems marked with a star had previously been studied through cryo-crystallisation[212,213,214,217]

It was thought that these systems should readily form LmMCs due to the O-H···N interactions being stronger than any of the interactions possible between two molecules of either of the single components.

5.3.2 Experimental Details

The liquid mixtures that had not previously been investigated at low temperature were studied herein using the standard cryo- and high-pressure crystallisation techniques detailed in sections 1.2 and 1.1 respectively. Those liquid mixtures that had been previously studied through cryo-crystallisation were studied herein using the standard high-pressure crystallisation procedure detailed in section 1.1.

5.3.3 Results and Discussion

We found that attempts to form LmMCs comprising carboxylic acids and basic aromatic rings were almost always successful, both in cryo- and high-pressure

crystallisation experiments. This is due to the strong hydrogen-bonding between the two components.

Table 5.4 shows the unit-cell dimensions of the product of the high-pressure crystallisation experiments for those co-crystals which have been previously crystallised through cryo-crystallisation.

Experiment	**High-Pressure Unit-Cell Dimensions**		**Crystallisation Product**	**Ambient-pressure Unit Cell Dimensions of Crystallisation Product**	
	Length / Å	Angle / °		Length / Å	Angle / °
IX (Pyrazine 1 : 2 Acetic Acid)	a=5.500 (9)	α=71.31	Co-crystal (isomorphous to cryo-crystallisation)[215]	a=5.4869 (2)	α=70.076 (1)
	b=8.15 (3)	β=86.94 (6)		b=8.1885 (2)	β=86.667 (1)
	c=11.762 (10)	γ=89.07 (2)		c=11.9960 (4)	γ=89.925 (2)
X (Pyrazine 1 : 2 Propionic acid)	a=4.881 (8)	β=93.08 (5)	Co-crystal (isomorphous to cryo-crystallisation)[215]	a=4.8735 (2)	β=93.197 (1)
	b=5.375 (6)			b=5.4384 (2)	
	c=23.090 (18)			c=23.243 (10)	
XI (Pyrazine 1 : 2 Butanoic acid)	a=4.0602 (19)	β=91.43 (2)	Co-crystal: New polymorph[215]	a=9.8544 (7)	β=109.736 (3)
	b=28.73 (2)			b=5.7127 (4)	
	c=6.022 (4)			c=13.534 (2)	
XII (Pyridine 1 : 4 Formic Acid)	a=3.5788 (5)	β=93.875 (6)	Co-crystal: New polymorph[217]	a=16.35 (1)	β=90°
	b=16.598 (4)			b=3.702 (3)	
	c= 9.8456 (13)			c=20.23 (1)	
XIII (Pyridine 1 : 1 Formic Acid)	a=10.836 (4)	β=104.24 (4)	Co-crystal (isomorphous to cryo-crystallisation)[217]	a=10.954 (6)	β=104.96 (4)
	b=3.697 (4)			b=3.817 (3)	
	c=15.691 (9)			c=15.842 (7)	

Table 5.4 Results of high-pressure co-crystallisation attempts IX – XIII.

The crystal structures of two polymorphs of XI (pyrazine 1 : 2 butanoic acid) are shown below in figures 5.1 and 5.2.

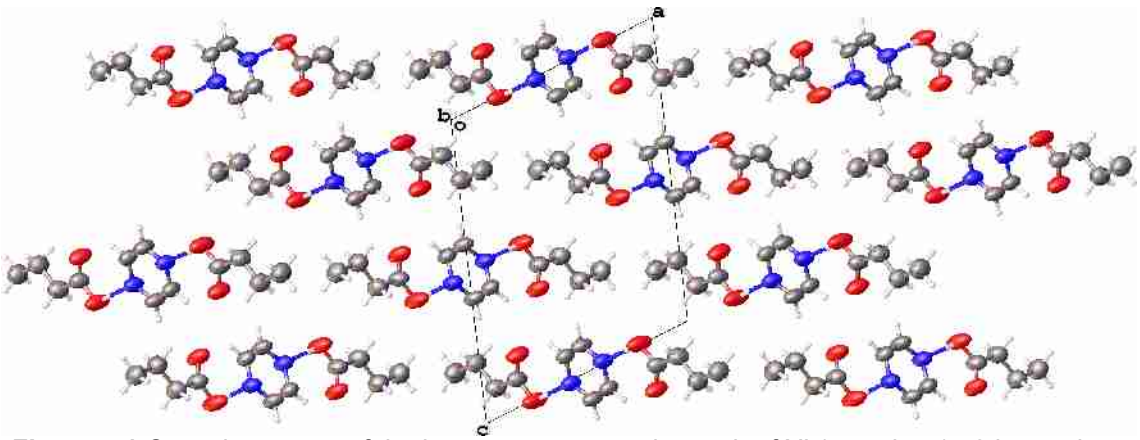

Figure 5.1 Crystal structure of the low-temperature polymorph of XI (pyrazine 1 : 2 butanoic acid).

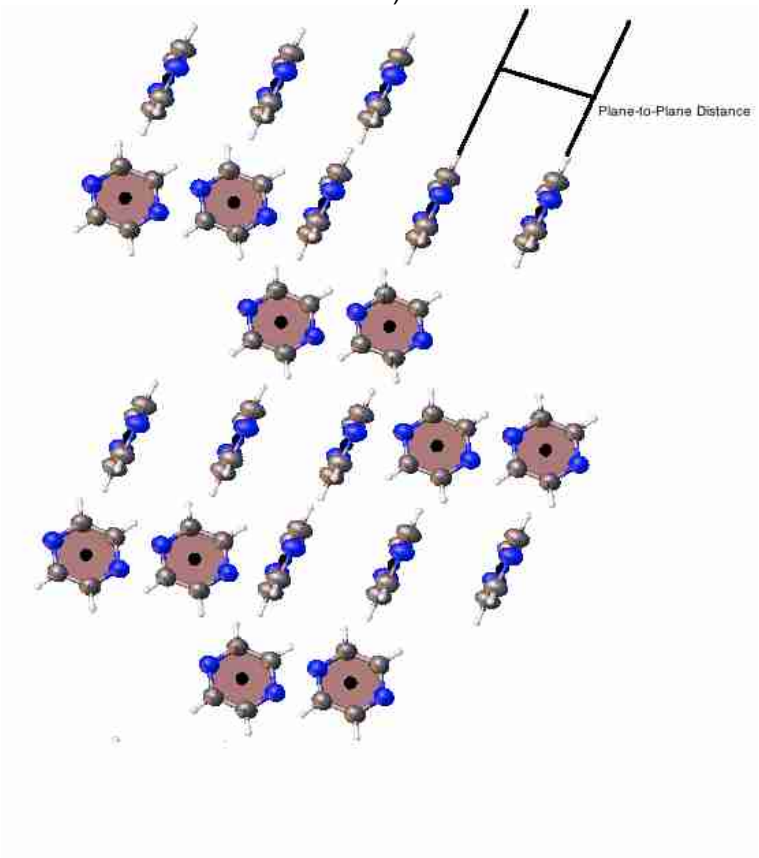

Figure 5.1 (b) Diagram showing only the pyrazine molecules in the low-temperature polymorph of XI (pyrazine 1 : 2 butanoic acid) showing the plane-to-plane distance between pyridine molecules.

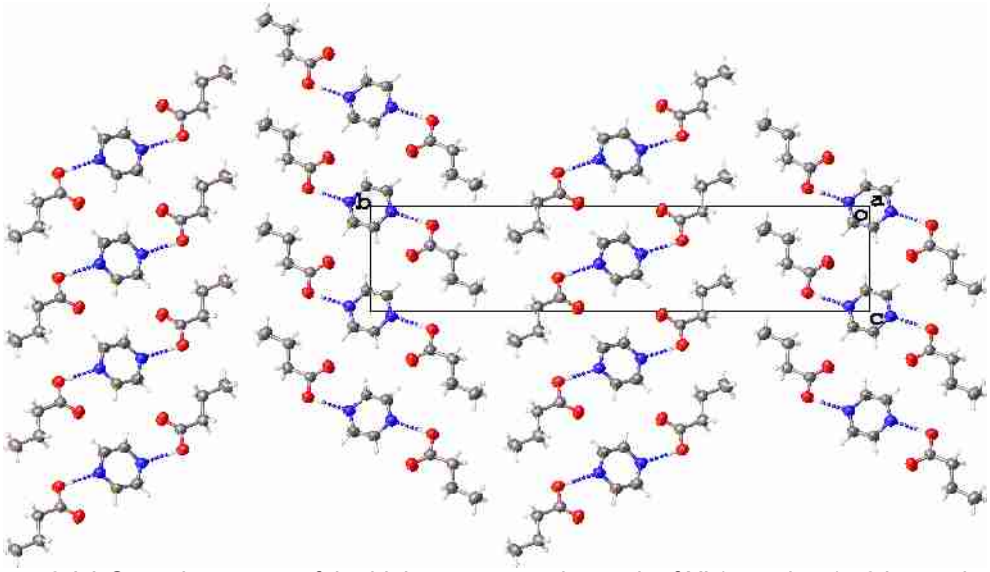

Figure 5.2 (a) Crystal structure of the high-pressure polymorph of XI (pyrazine 1 : 2 butanoic acid).

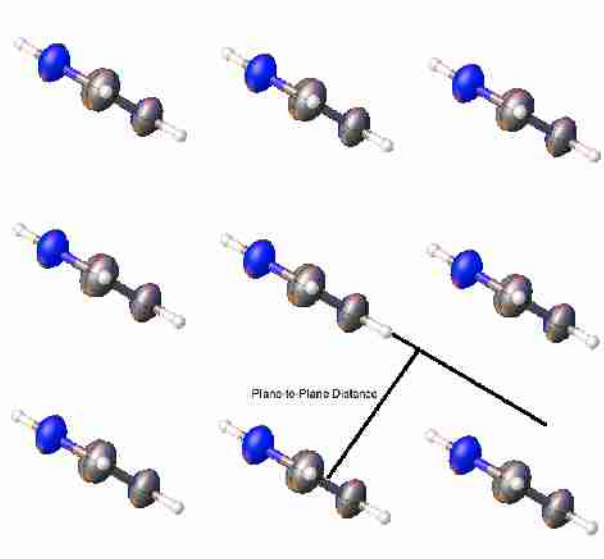

Figure 5.2 (b) Diagram showing only the pyrazine molecules in the high-pressure polymorph of XI (pyrazine 1 : 2 butanoic acid) showing the plane-to-plane distance between pyridine molecules.

The unit-cell volumes and the length of the hydrogen bonds and π-π plane-to-plane distances in the two polymorphs of pyrazine 1 : 2 butanoic acid (XI) are listed below in table 5.5.

Structure	**O···N**	**π-π Plane to Plane**	**Density**/ gcm^{-3}
	Length / Å	Length / Å	
High-pressure XI (pyrazine 1 : 2 butanoic acid)	2.7303 (13)	3.5156 (14)	1.218 (1)
Low-temperature XI (pyrazine 1 : 2 butanoic acid)	2.7216 (13)	3.5508 (18)	1.159 (1)

Table 5.5 Unit-cell volumes and the length of hydrogen bonds and π-π plane to plane distances in the two polymorphs of XI (pyrazine 1 : 2 butanoic acid).

One can see that the trimeric moiety is almost identical in the two structures, with just a slight compression of the π-π stacking distances and a very marginal increase in the O···N distance at high-pressure. The differences between the two structures arise from the packing of these trimers. The high-pressure polymorph is 4.6% more dense than the low-temperature polymorph.

The structures of the two polymorphs of XII (pyridine 1 : 4 formic acid) are shown below in figures 5.3 and 5.4.

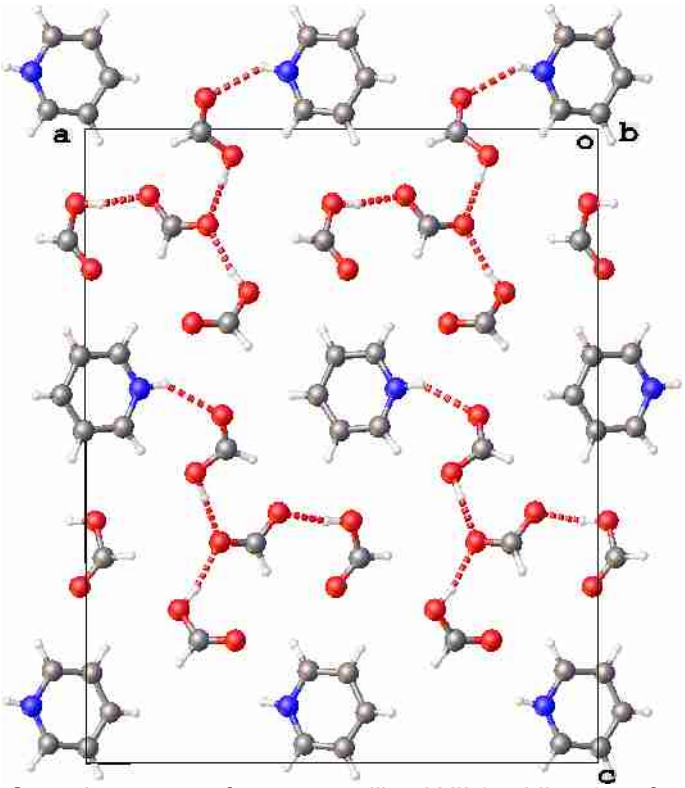

Figure 5.3 Crystal structure of cryo-crystallised XII (pyridine 1 : 4 formic acid)[217]

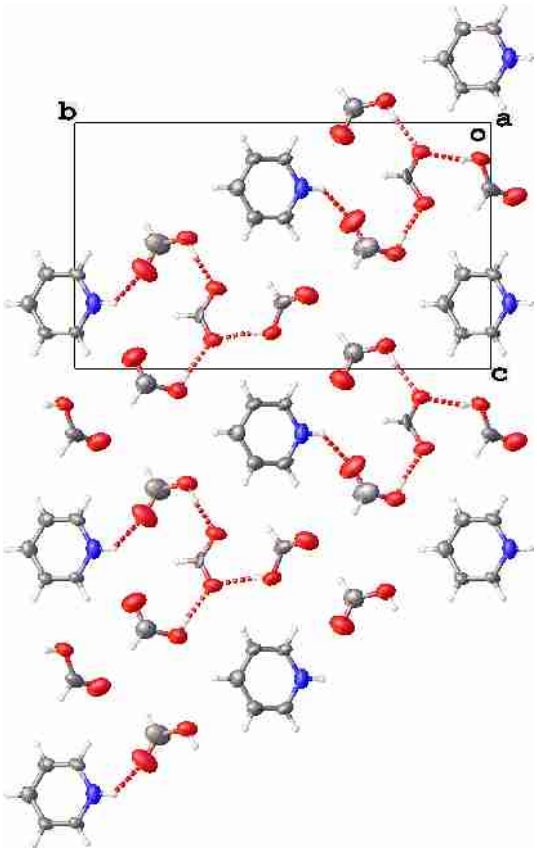

Figure 5.4 Crystal structure of high-pressure crystallised XII (pyridine 1 : 4 formic acid)

The **O-H···O, N-H···O and C-H···O** interactions in the two polymorphs of XII are listed below in table 5.6.

Structure	**O-H···O**		**N-H···O**		**C-H···O**	
	Length / Å	Angle / °	Length / Å	Angle / °	Length / Å	Angle / °
Low-Temperature XII (Pyridine 1 : 4 Formic Acid)[217]	1.5826 (7)	168.893 (7)	2.1392 (10)	141.27 (3)	2.449 (1)	144.098 (10)
	1.7289 (7)	168.059 (4)			2.455 (1)	158.226 (5)
	1.7574 (9)	167.237 (7)			2.471 (1)	121.40 (4)
High-Pressure XII	1.7557 (2)	169.157 (1)	2.2184 (2)	136.784 (4)	2.3191 (3)	131.02 (1)
					2.3859 (4)	154.125 (1)
					2.4187 (3)	148.055 (5)
	1.7838 (2)	166.010 (2)			2.4216 (3)	162.701 (3)
					2.4304 (4)	123.934 (6)
					2.4540 (2)	155.363 (4)
	1.7954 (3)	161.006 (4)			2.4949 (3)	169.278 (2)

Table 5.6 Table showing length and directionality of hydrogen bonds in the two polymorphs of XII (pyridine 1 : 4 formic acid).

Table 5.7 shows the unit-cell data collected in co-crystallisation experiments XIV – XVIII.

Experiment	Low-Temperature Unit-Cell Dimensions		High-Pressure Unit-Cell Dimensions	
	Length / Å	Angle / °	Length / Å	Angle / °
XIV (Pyrimidine 1:2 Formic Acid)	a=3.7878 (17)	β=91.747 (17)	a=3.7549 (7)	β=92.099 (13)
	b=12.397 (7)		b=12.365 (4)	
	c=17.981 (5)		c=17.962 (5)	
XV (Pyridine 1 : 2 Glutaric Acid)	Crystallisation did not occur on cooling nor on compression.			
XVI (Pyridine 2:1 Pimelic Acid)	a=23.4 (3)	β=90	a= 21.39 (3)	β=90
	b=5.56 (4)		b=5.348 (5)	
	c=30.5 (4)		c= 29.89 (3)	
XVII (Pyridine 2:1 Suberic Acid)	a=5.7644 (13)	β=95.920 (11)	a=7.262 (4)	α=98.64 (3)
	b=14.547 (6)		b=8.790 (5)	β=98.47 (3)
	c=10.955 (4)		c=20.564 (18)	γ=95.582 (13)
XVIII (Pyridine 2:1 Azelaic Acid)	a=9.403 (6)	α=105.551 (14)	a=9.376 (18)	α=105.53 (12)
	b=10.028 (6)	β=92.180 (16)	b=10.01 (2)	β=92.86 (12)
	c=11.484 (6)	γ=108.257 (13)	c=11.16 (3)	γ=108.99 (9)

Table 5.7 Unit-cell dimensions of cryo- and high-pressure products from experiments XIV-XVIII.
* - Very high errors due to highly twinned crystals with very similar orientations.

All LmMCs XVI-XVIII were formed in the expected ratio, with one acid unit for every two of pyridine - forming trimers. XIV was found to crystallise in the ratio pyrimidine 1 : 2 formic acid (from an input ratio of pyrimidine 2 : 1 formic acid).

The asymmetric unit and crystal structure of XIV (pyrimidine 1 : 2 formic acid), is shown below in figure 5.5.

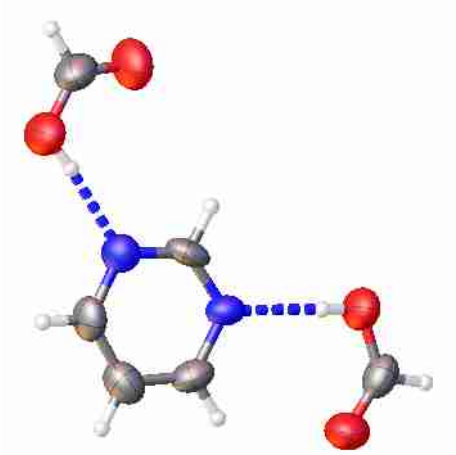

Figure 5.5 (**a**) Asymmetric unit of XIV (pyrimidine 1 : 2 formic acid).

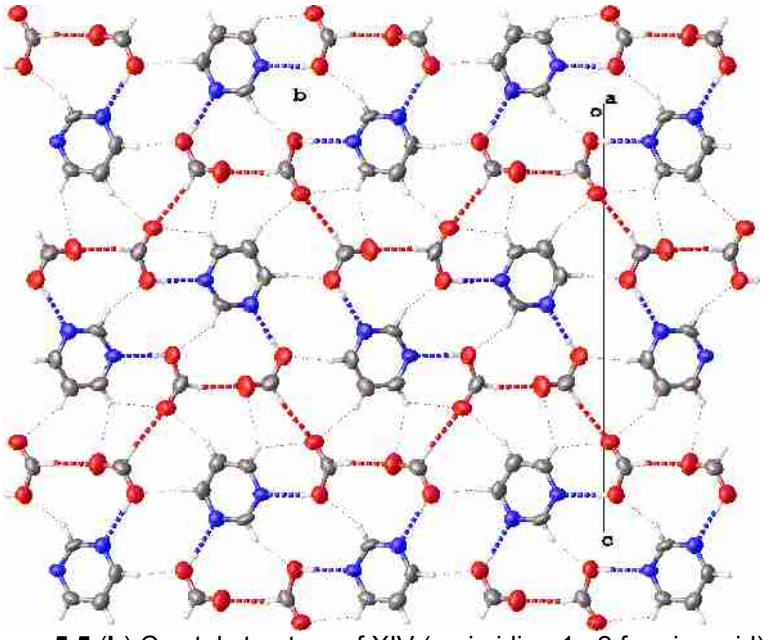

Figure 5.5 (**b**) Crystal structure of XIV (pyrimidine 1 : 2 formic acid).

The LmMC XIV (pyrimidine 1 : 2 formic acid) forms a 2D layered structure, with O-H···N, O-H···O and C-H···O hydrogen bonds linking molecules in each layer together. π···π stacking of pyrimidine rings links each layer to its neighbours.

The asymmetric unit and crystal structure of XVI (pyridine 2 : 1 pimelic acid), is shown below in figure 5.6.

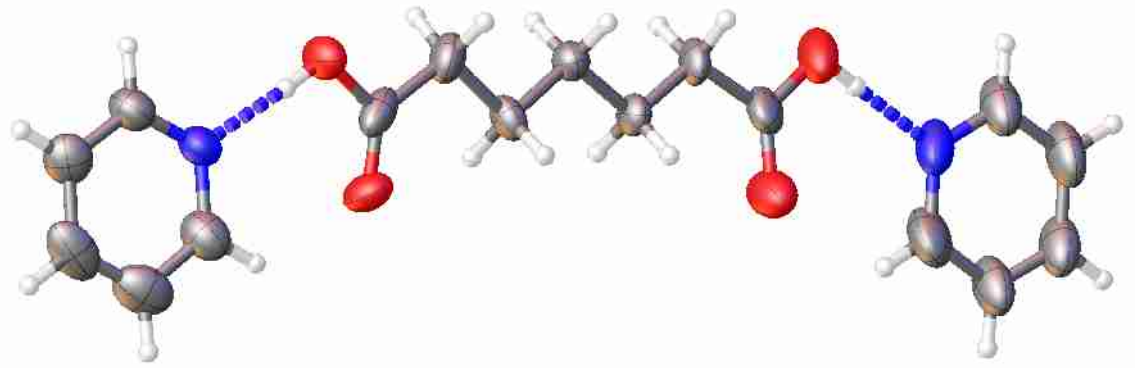

Figure 5.6 (**a**) Asymmetric unit of XVI (pyridine 2 : 1 pimelic acid).

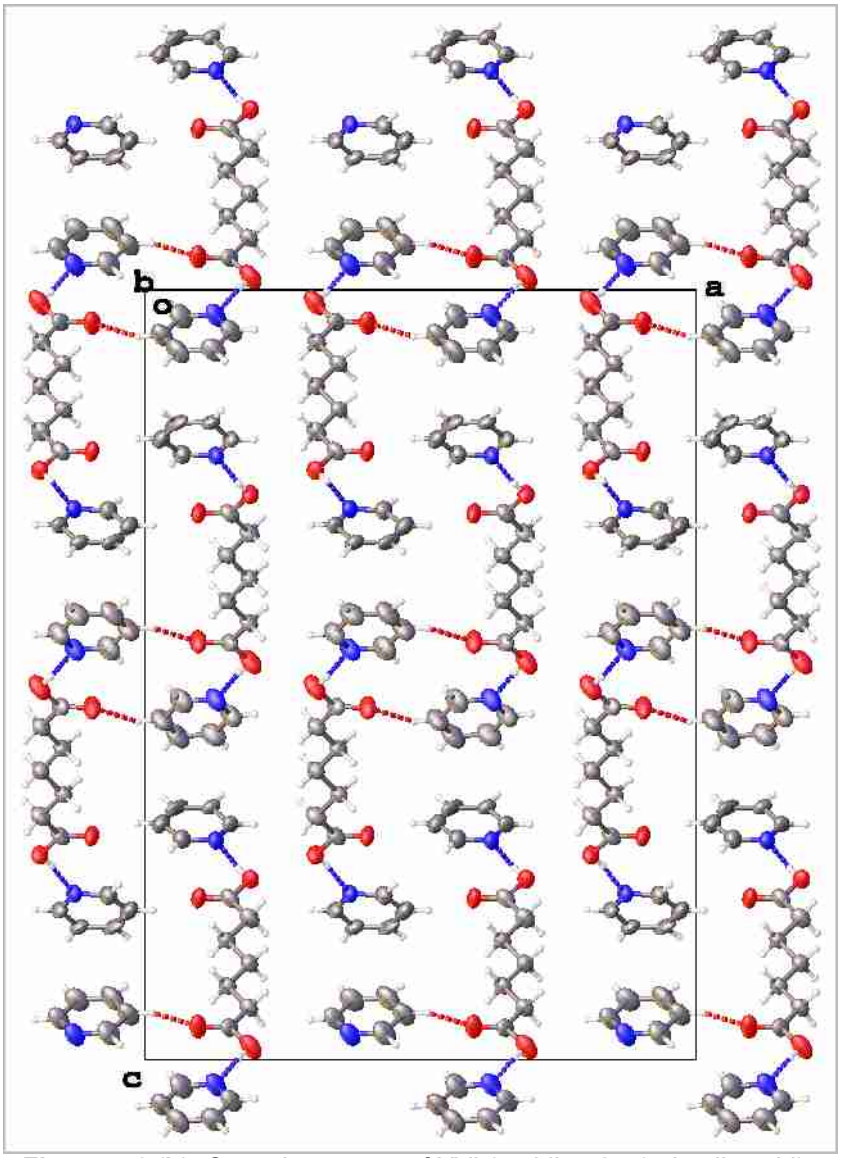

Figure 5.6 (**b**) Crystal structure of XVI (pyridine 2 : 1 pimelic acid).

XVI (pyridine 2 : 1 pimelic acid) also has a layered structure, with O-H···N and C-H···O hydrogen bonds linking molecules in each layer and stacking of pyridine molecules linking adjacent layers. The acid molecule adopts a straight-chain conformation.

The asymmetric unit, molecular and crystal structures of the low-temperature polymorph of XVII (pyridine 2 : 1 suberic acid), are shown below in figure 5.7.

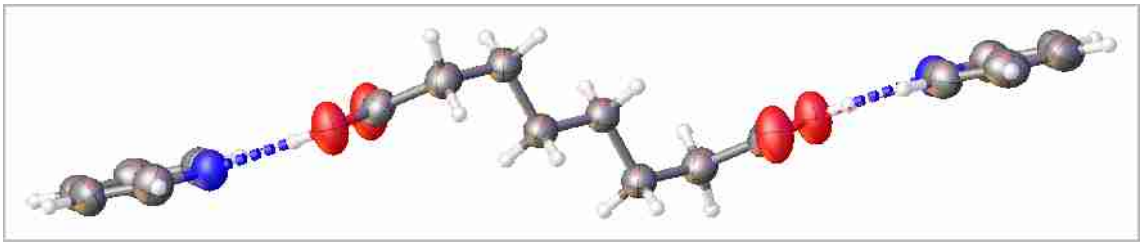

Figure 5.7 (**a**) Asymmetric unit of the low-temperature polymorph of XVII (pyridine 2 : 1 suberic acid).

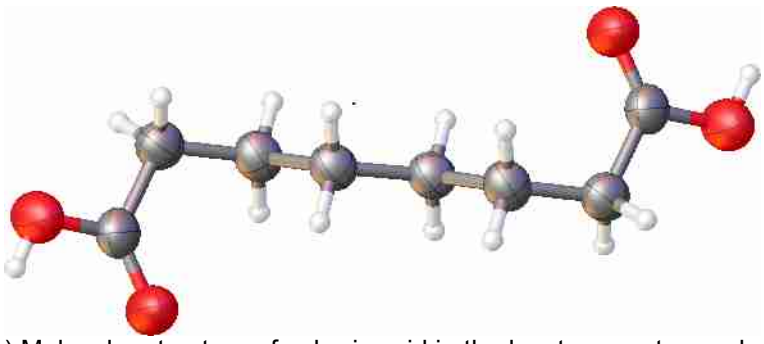

Figure 5.7 (**b**) Molecular structure of suberic acid in the low-temperature polymorph of XVII (pyridine 2 : 1 suberic acid)

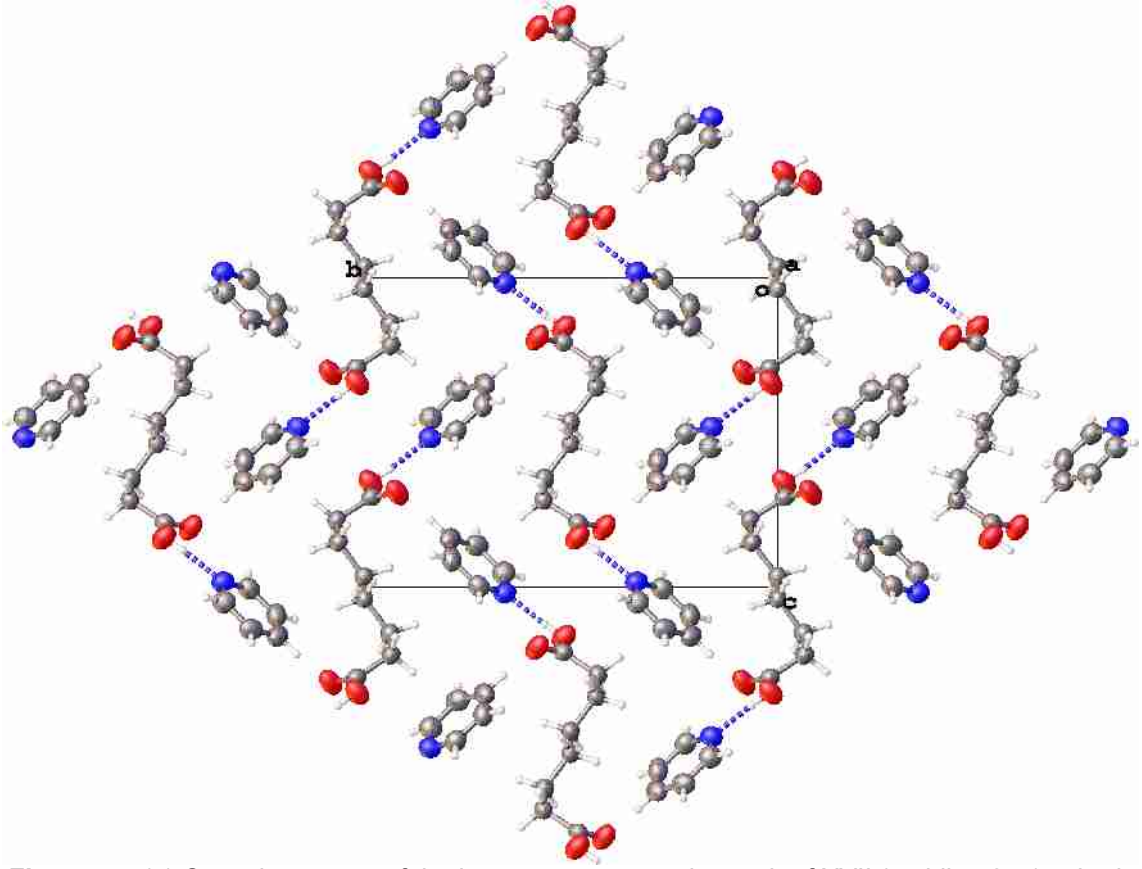

Figure 5.7 (**c**) Crystal structure of the low-temperature polymorph of XVII (pyridine 2 : 1 suberic acid).

The low-temperature polymorph of XVII (pyridine 2 : 1 suberic acid) adopts a Z' = 0.5 structure. Unlike XVI (pyridine 2 : 1 pimelic acid), the suberic acid molecule does not adopt a linear conformation. Both tails of the molecule are held out of the plane of the carbon chain, as shown in figure 5.7. The pyridine molecules are arranged in layers, and the suberic acid molecules link pyridine molecules in adjacent layers through O-H···N hydrogen bonds.

The asymmetric unit, molecular and crystal structures of the high-pressure polymorph of XVII (pyridine 2 : 1 suberic acid), are shown below in figure 5.8.

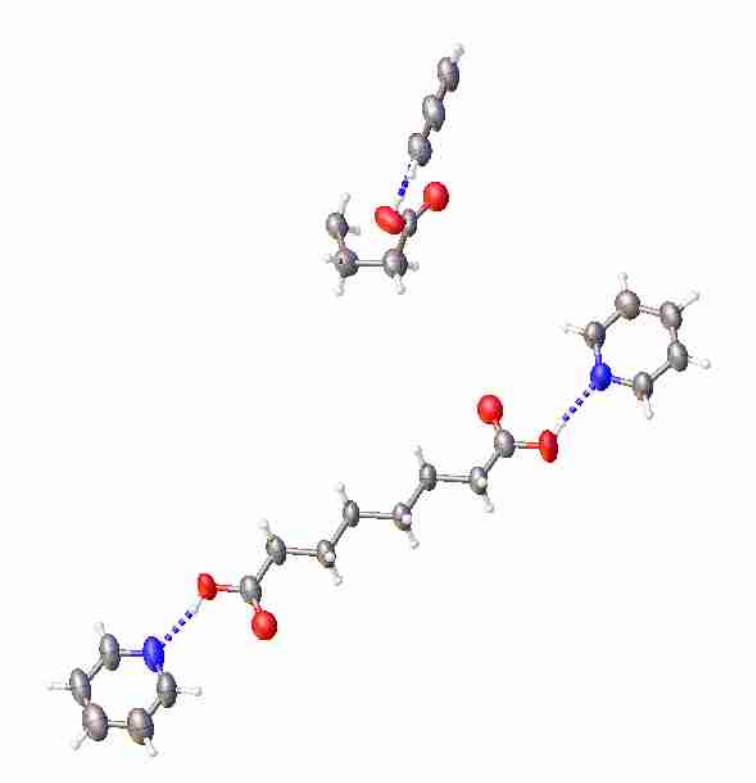

Figure 5.8 (**a**) Asymmetric unit of the high-pressure polymorph of XVII (pyridine 2 : 1 suberic acid).

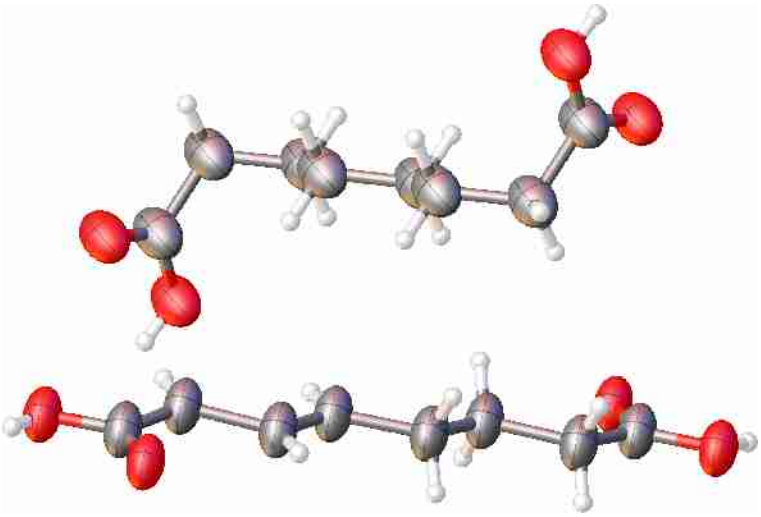

Figure 5.8 (**b**) Molecular structure of suberic acid in the high-pressure polymorph of XVII (pyridine 2 : 1 suberic acid).

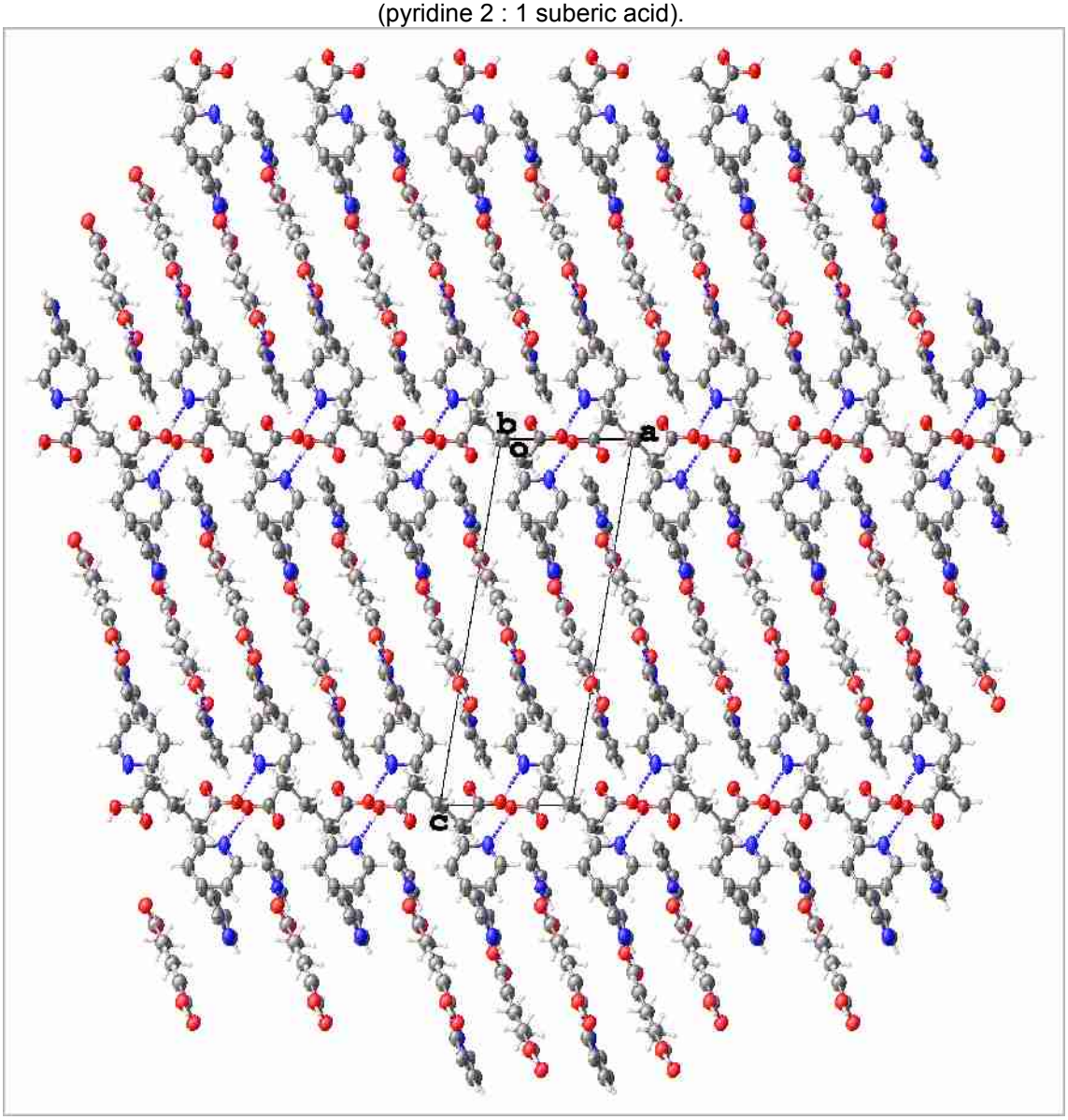

Figure 5.8 (**c**) Crystal structure of the high-pressure polymorph of XVII (pyridine 2 : 1 suberic acid).

The high-pressure polymorph of XVII (pyridine 2 : 1 suberic acid) adopts a rather complicated structure with Z' = 1.5, with three pyridine molecules and one and a half suberic acid molecules in the asymetric unit. The two symmetrically independent acid molecules have different molecular geometries, with one having a linear chain and the other being bent at both ends (as seen in the low-temperature polymorph). The linear suberic acid molecules are orientated perpendicularly to the bent suberic acid molecules. The two pyridine molecules in the asymmetric unit also perpendicular to one another.

The asymmetric unit and crystal structures of XVIII, (pyridine 2 : 1 azelaic acid) are shown below in figure 5.9.

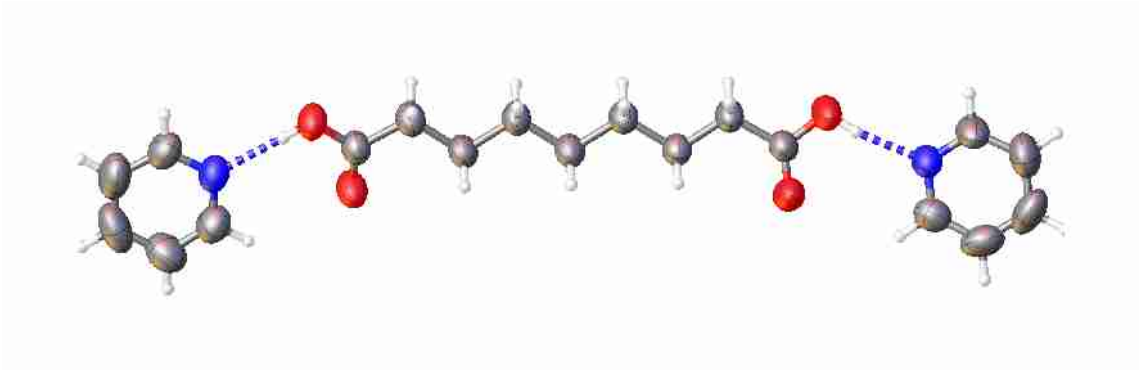

Figure 5.9 (**a**) Asymmetric unit of XVIII (pyridine 2 : 1 azelaic acid).

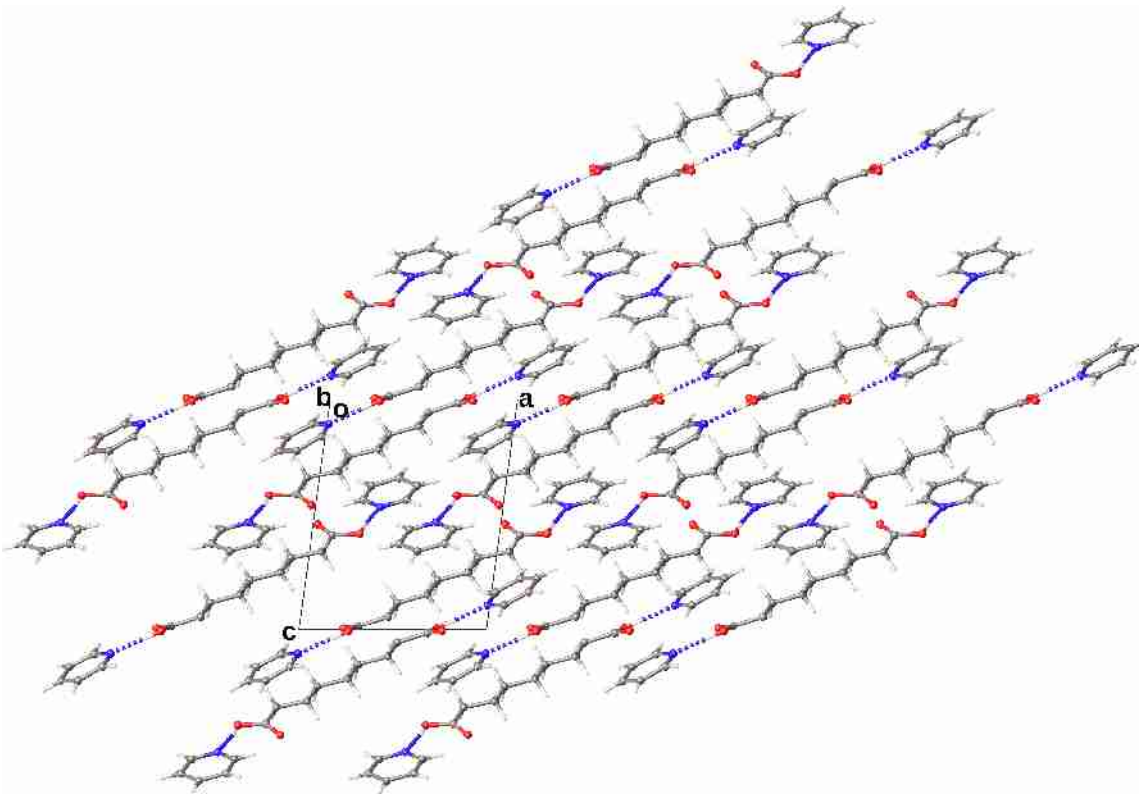

Figure 5.9 (**b**) Crystal structure of XVIII (pyridine 2 : 1 azelaic acid).

XVIII (pyridine 2 : 1 azelaic acid) adopts a simple layered structure with $Z' = 1$ and a linear azelaic acid molecule. π···π stacking of pyridine molecules links adjacent layers. Table 5.8 shows the shortest hydrogen-bond (N-H···O and C-H···O) lengths and angles (using a cut-off of length < 2.8 Å and X-H···O angle > 120°) in XIV and XVI-XVIII.

Structure		**O-H···N**		**C-H···O**	
		Length / Å	Angle / °	Length / Å	Angle / °
XIV (Pyrimidine 1:2 Formic Acid)		1.8633 (4)	174.263 (1)	2.4760 (5)	168.876 (3)
				2.4826 (4)	165.905 (3)
				2.5478 (5)	163.551 (3)
		1.9265 (5)	175.026 (1)	2.5789 (7)	129.581 (8)
				2.5948 (5)	148.810 (5)
				2.7143 (5)	138.665 (8)
				2.7302 (7)	127.225 (14)
XVI (Pyridine 2:1 Pimelic Acid)		1.8416 (11)	174.461 (3)	2.7251 (18)	126.99 (6)
		1.9097 (12)	173.176 (4)	2.7379 (18)	127.95 (6)
Low-temperature XVII (Pyridine 2:1 Suberic Acid)		1.8305 (5)	174.0116 (14)	2.7053 (5)	132.966 (8)
				2.7312 (7)	125.252 (11)
High-pressure XVII (Pyridine 2:1 Suberic Acid)	Straight Chain	1.83411 (11) 1.8900 (12)	169.444 (6) 164.327 (11)	2.4454 (19)	160.079 (18)
				2.6482 (15)	167.38 (1)
				2.6864 (14)	156.255 (15)
				2.7565 (19)	120.75 (5)
	Bent Chain	1.8083 (11)	175.259 (3)	2.6225 (14)	126.48 (4)
				2.6933 (14)	125.12 (3)
				2.723 (2)	121.88 (3)
				2.7700 (18)	120.45 (4)
XVIII (Pyridine 2:1 Azelaic Acid)		1.8274 (9)	169.196 (7)	2.6677 (11)	155.375 (16)
				2.7310 (11)	126.71 (3)
		1.8488 (8)	170.175 (5)	2.7462 (11)	135.567 (18)
				2.7598 (14)	128.14 (4)

Table 5.8 Table showing length and directionality of hydrogen bonds in XIV - XVIII.

The polymorphism in XVII, (pyridine 2 : 1 suberic acid), appears to arise through competition between the most favourable hydrogen-bonding interactions and packing

efficiency. The short O-H···N hydrogen bonds are on average more linear in the low-temperature form than in the straight-chain component of the high-pressure form. The high-pressure form of XVII is considerably more closely-packed. The volume required for each [pyridine 2 : 1 suberic acid] unit is 456.8 (3) $Å^3$ in the low-temperature form, and only 424.7 (1) $Å^3$ in the high-pressure form, a substantial increase in density of 7.6%.

5.4 Co-crystals of Di-Carboxylic Acids and Basic Aromatic Rings

In addition to the LmMCs listed above in sections 5.2 and 5.3, three new co-crystals containing di-carboxylic acids and pyridine, solid at ambient conditions, were crystallised. Succinic acid combined with pyridine (in the input ratio pyridine 2 : 1 succinic acid) was found to form a 1 : 1 co-crystal. The structure is shown below in figure 5.10.

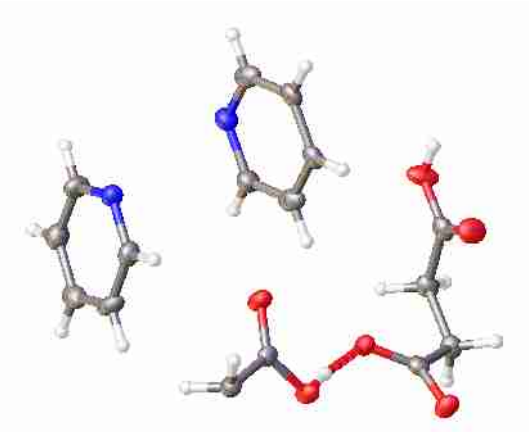

Figure 5.10 (**a**) Asymmetric unit of pyridine 1 : 1 succinic acid.

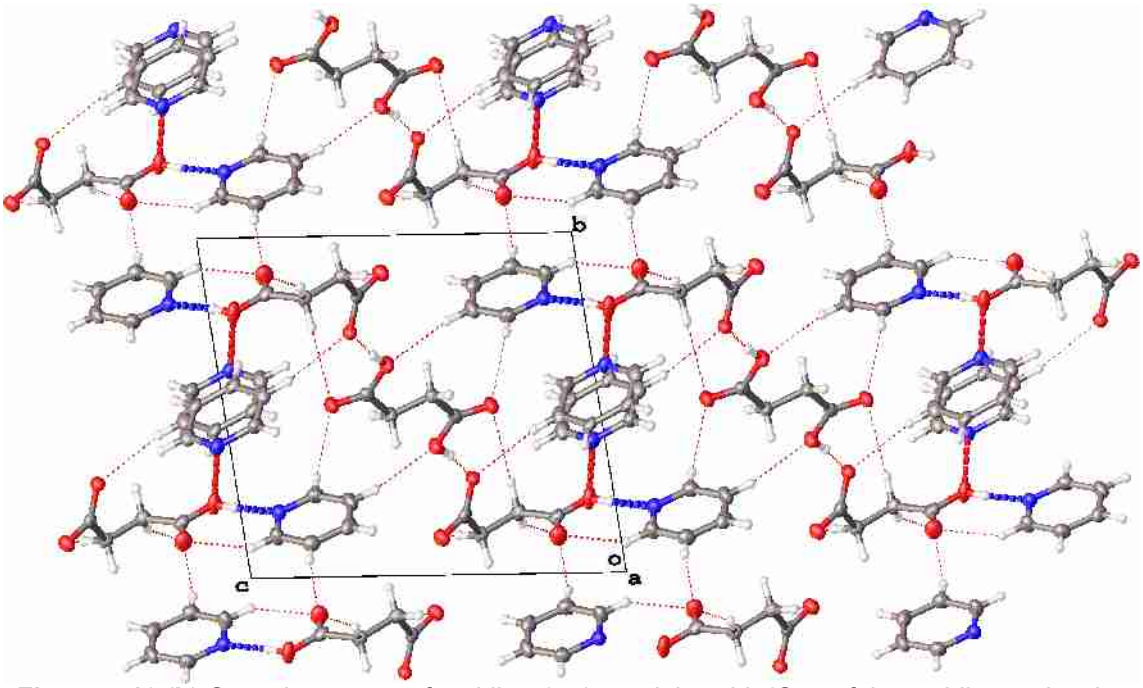

Figure 5.10 (**b**) Crystal structure of pyridine 1 : 1 succinic acid. (One of the pyridine molecules in the asymmetric unit has an occupancy of 0.5).

The LmMC pyridine 1 : 1 succinic acid co-crystal has an unusual structure, with *Z*′ = 1.5. One molecule of pyridine was found to be disordered over two sites and is only weakly bound to the rest of the structure. The rest of the structure is linked together by short O-H···O and O-H···N hydrogen bonds.

Terepthalic acid and adipic acid were both found to form co-crystals with pyridine in the ratio pyridine 2 : 1 di-carboxylic acid. The asymmetric unit and structure of pyridine 2 : 1 terepthalic acid is shown below in figure 5.11.

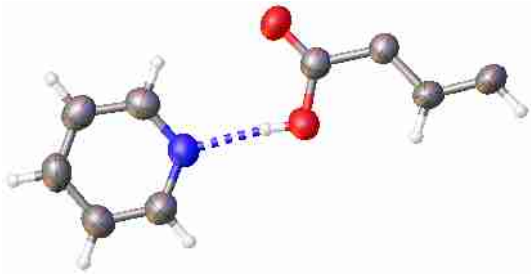

Figure 5.11 (**a**) Asymmetric unit of pyridine 2 : 1 terepthalic acid.

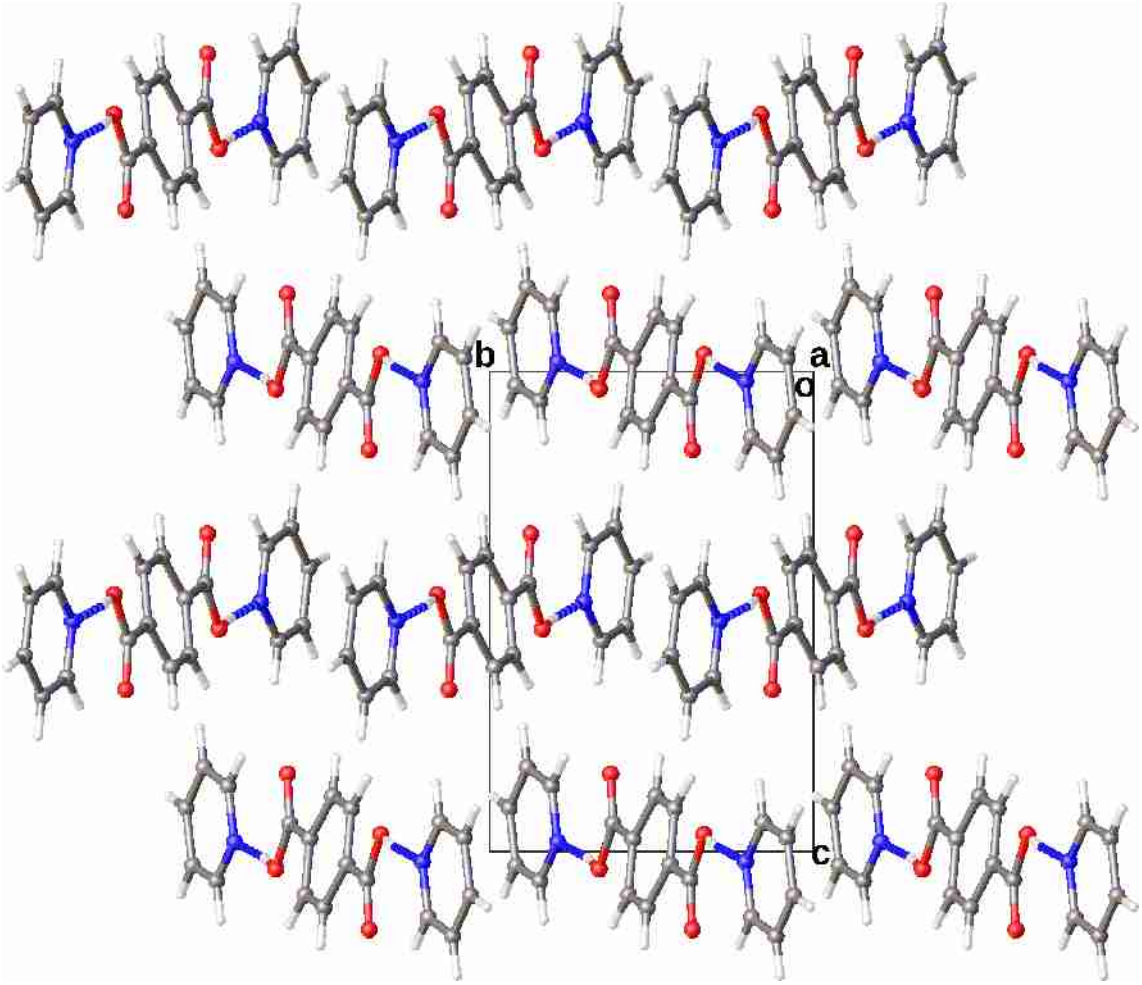

Figure 5.11 (**b**) Crystal structure of pyridine 2 : 1 terepthalic acid.

Pyridine 2 : 1 terepthalic acid has a *Z′* value of 0.5. The crystal structure contains isolated trimers comprising two molecules of pyridine and one of terepthalic acid linked by strong O-H···N hydrogen bonds.

The asymmetric unit and structure of pyridine 2 : 1 adipic acid is shown below in figure 5.12.

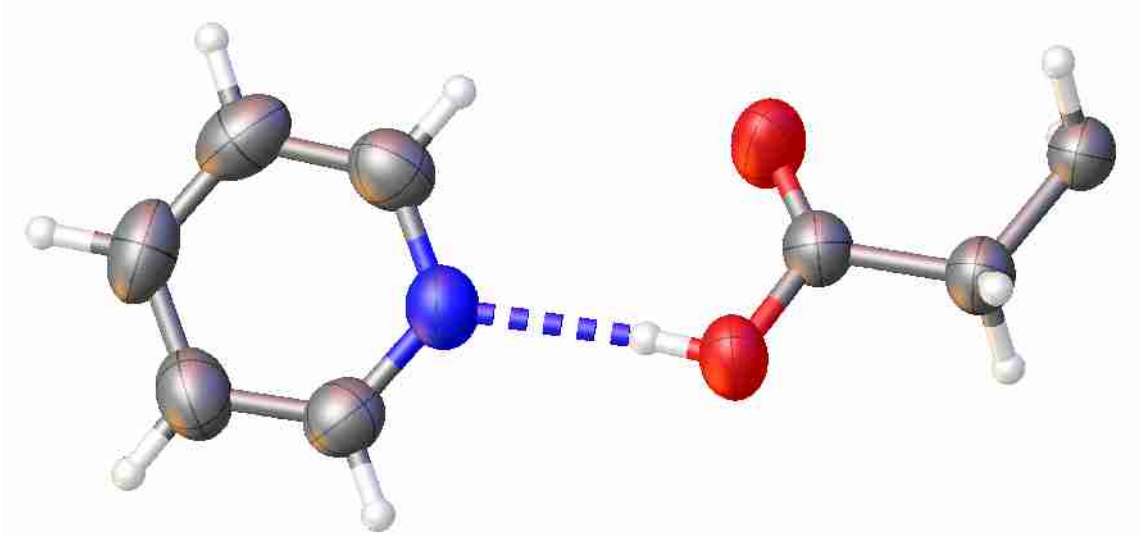

Figure 5.12 (**a**) Asymmetric unit of pyridine 2 : 1 adipic acid.

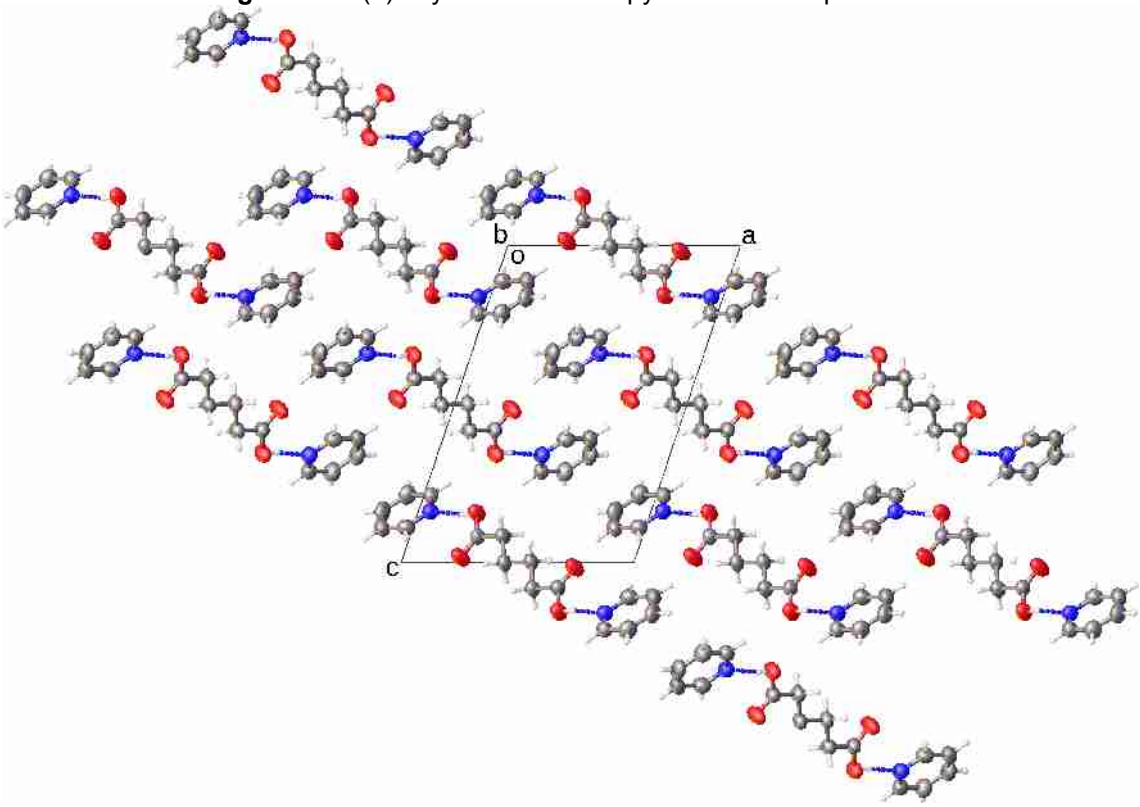

Figure 5.12 (**b**) Crystal structure of pyridine 2 : 1 adipic acid.

Pyridine 2 : 1 adipic acid forms a structure with $Z' = 0.5$. The adipic acid molecule has a straight chain conformation and forms a trimer with two molecules of pyridine linked through O-H···N hydrogen bonds.

Table 5.9 gives an overview of the crystallisation products of di-carboxylic acids of varying length carbon chains mixed with pyridine in an input ratio of pyridine 2 : 1 di-carboxylic acid.

Di-Carboxylic Acid	No. of Carbons in Di-Carboxylic Acid	State of Matter at Ambient Conditions	Pyridine:Di-Carboxylic Acid Ratio
Oxalic	2	Solid	1 : 1
Malonic	3	Solid	1 : 2
Succinic	4	Solid	1 : 1
Glutaric	5	Liquid	No crystal formed through cryo-crystallisation or compression
Adipic	6	Solid	2 : 1
Pimelic	7	Liquid	2 : 1
Suberic	8	Liquid	2 : 1
Azelaic	9	Liquid	2 : 1

Table 5.9 Table showing the ratio of co-crystals comprising linear dicarboxylic acids and pyridine mixed with the input ratio of pyridine 2 : 1 di-carboxylic acid.

That the mixture of glutaric acid (C5) and pyridine is liquid at ambient conditions, despite the succinic acid (C4) and adipic acid (C6) mixtures with pyridine both being solid is rather surprising. Furthermore, finding that the glutaric acid and pyridine mixture does not even crystallise under cooling or compression indicates that there may be no way to pack the two components in an energetically satisfying manner. A further indication of the difficulty of packing pyridine with di-carboxylic acid molecules of these lengths is given by the fact succinic acid (C4) and pyridine co-crystal has a weakly bound disordered pyridine molecule.

Table 5.10 shows the crystallographic data obtained for all previously unreported LmMC structures described in this chapter.

compound	**Pyrazine 1:2 Butanoic Acid High-Pressure**	**Pyridine 1:4 Formic Acid High-Pressure**	**Pyridine 2:1 Pimelic Acid**	**Pyridine 2:1 Suberic Acid Cryo-crystallised**	**Pyridine 2:1 Suberic Acid High-Pressure**	**Pyridine 2:1 Azelaic Acid**	**Pyridine 2:1 Terepthalic Acid**	**Pyridine 2:1 Adipic Acid**
empirical formula	$C_4H_8O_2$, 0.5($C_4H_4N_2$)	C_5H_5N, 3(CH_2O_2), CHO_2	2(C_5H_5N), $C_7H_{12}O_4$	2(C_5H_5N), $C_8H_{14}O_4$	2(C_5H_5N), $C_8H_{14}O_4$	2(C_5H_5N), $C_9H_{16}O_4$	2(C_5H_5N), $C_8H_6O_4$	2(C_5H_5N), $C_6H_{10}O_4$
formula weight	128.15	263.20	318.37	332.39	332.39	346.42	324.33	304.34
T/K	ambient	ambient	ambient	258 (2)	ambient	255 (2)	120 (2)	120 (2)
P/kbar	3.3 (2)	1.2 (2)	0.6 (2)	ambient	0.8 (2)	ambient	ambient	ambient
crystal system	monoclinic	monoclinic	monoclinic	monoclinic	triclinic	triclinic	monoclinic	monoclinic
space group	$P2_1/n$	$P2_1$	$C2/C$	$P2_1/c$	P-1	P-1	$P2_1/n$	$P2_1/n$
a (Å)	4.0602 (19)	3.5788 (5)	21.316(4)	5.7644 (13)	7.261 (4)	9.403 (6)	9.966 (2)	10.411 (3)
b (Å)	28.73 (2)	16.598 (4)	5.3319 (6)	14.547 (6)	8.790 (5)	10.029 (6)	7.4298 (15)	5.5604 (11)
c (Å)	6.022 (4)	9.8456	29.817 (4)	10.955 (4)	20.564 (18)	11.484 (6)	11.972 (2)	14.942 (3)
α (°)	90	90	90	90	98.64 (3)	105.551 (14)	90	90
β (°)	91.43 (2)	93.875 (6)	90	95.920 (11)	98.47 (3)	92.180 (16)	112.769 (5)	108.555 (5)
γ (°)	90	90	90	90	95.582 (13)	108.257 (13)	90	90
Z	4	2	8	2	3	2	2	2
V/Å^3	702.2 (8)	583.50 (18)	3388.8 (9)	913.7 (5)	1273.8 (15)	982.0 (10)	817.4 (3)	820.0 (3)
D_{calc}/g cm^{-3}	1.212	1.498	1.248	1.208	1.300	1.172	1.318	1.233
μ/mm^{-1}	0.056	0.080	0.055	0.086	0.058	0.082	0.094	0.089
unique reflns	1008	1559	1433	1504	2663	2098	1550	578
observed reflns	509	611	642	1305	965	1986	1550	578
θ_{max}	18.130	17.74	15.17	24.40	16.28	20.960	25.68	18.14
completeness/%	50.5	39.2	44.8	86.8	36.2	94.7	100.00	100.00
R_1 [I > 2σ]	0.0339	0.0305	0.0605	0.0370	0.0530	0.0468	0.0464	0.0452
*w*R2 [all]	0.0837	0.0669	0.1480	0.1030	0.1510	0.1327	0.1404	0.1237
goodness-of-fit	1.081	1.115	1.161	1.031	1.130	1.020	1.025	1.070

Table 5.10 Crystallographic data of previously unreported LmMCs described in chapter 5.

5.5 Conclusions

It was hypothesised that the requirement for close packing at high-pressure could result in the crystallisation of different ratios of LmMCs through high-pressure to those seen through cryo-crystallisation. This hypothesis was not realised in the LmMCs studied in this thesis. Despite this, it is not unreasonable to expect that this behaviour would be seen if crystallisation of more systems were to be carried out. However, due to time constraints, only a limited number of co-crystallisation attempts could be made.

Nonetheless, some LmMCs were found to crystallise in different forms through cryo- and high-pressure crystallisation, namely pyridine 1 : 2 butanoic acid and pyridine 2 : 1 suberic acid. The apparent reason for the polymorphism is the increased packing efficiency of the high-pressure phase, in a similar manner to the polymorphism seen in single-component systems. In pyridine 1 : 2 butanoic acid this was achieved through hydrogen-bonded trimers packing in a herringbone rather than layered motif. In pyridine 2 : 1 suberic acid, the molecular geometry of the acid molecules in the two polymorphs is different. The suberic acid molecule in the cryo-crystallised polymorph has a bent chain. The high-pressure polymorph has two acid molecules in the asymmetric unit, one being bent and the other straight chained.

It was interesting to see that LmMCs that form under cryo-crystallisation with weak intermolecular interactions linking the two components do not always form under compression. Of course, some single-component systems do not crystallise under compression alone (e.g. 3-fluorotoluene),[164] presumably due to kinetic effects. It is therefore possible that the difference in energy between the single-component phase and the LmMC is sufficiently low due to the weakness of the interactions involved that the the single-component phase is formed as a kinetic product.

The observation that glutaric acid (C5) did not form a LmMC with pyridine either through cryo-crystallisation or high-pressure crystallisation, despite all other carboxylic acids in this work doing so was also intriguing. It is believed that this is due to difficulty in packing the two molecules in an efficient manner. Succinic acid (C4) also appears to have difficulty packing in an efficient manner. One would expect that strong O-H···N hydrogen bonds would form, resulting in a fully ordered structure based on isolated trimers. However, the structure actually contains O-H···O interactions formed at the

expense of stronger O-H···N interactions and has a disordered weakly bound pyridine molecule in the crystal structure.

Chapter 6: Crystallisation of Solvents

6.1 Introduction

There is substantial interest in the structural determination of compounds that are liquid under ambient conditions. This is because probing individual intermolecular interactions may be more easily achieved through cryo-crystallisation of these small and simple molecules than compounds which are solid at ambient conditions.[177,226,227] The determination of a crystal structure may also help to solve problems that are otherwise only accessible through difficult to interpret spectroscopic data, such as the molecular conformation.[228,229]

6.2 Isopropyl Alcohol

6.2.1 Introduction

Isopropyl alcohol is a very commonly used solvent for non-polar solvates. A previous report gives the unit cell dimensions of the low-temperature polymorph, but not the atomic positions.[230] The melting point of isopropyl alcohol is 184 K, therefore ambient-pressure crystallisation can only be readily achieved through the cryo-crystallisation technique described in section 1.2.

6.2.2 Crystallisation Procedure

Isopropyl alcohol did not crystallise on cooling to 85 K. However, on warming back up to 180 K, crystallisation occurred. This was unsurprising, as simple monoalcohols are known to have high viscosity and a tendency to form amorphous phases at low-temperatures.[231]

Neither compression alone, nor compression followed by decompression resulted in the crystallisation of isopropyl alcohol. However, immersing the diamond anvil cell in liquid nitrogen with no pressure applied to the sample, removing the cell from the nitrogen and increasing the pressure as the temperature increased resulted in crystallisation. The sample was found to be crystalline at 11.2 (2) kbar at ambient temperature.

The low-temperature data were collected at 180 (2) K. The high-pressure data were collected at 11.2 (2) kbar.

6.2.3 Results and Discussion

Isopropyl alcohol was found to form distinct phases at low-temperature and high-pressure. The low-temperature data were determined to be monoclinic with space group $P2_1/c$, with $Z' = 3$. The asymmetric unit of the low-temperature phase is shown in figure 6.1.

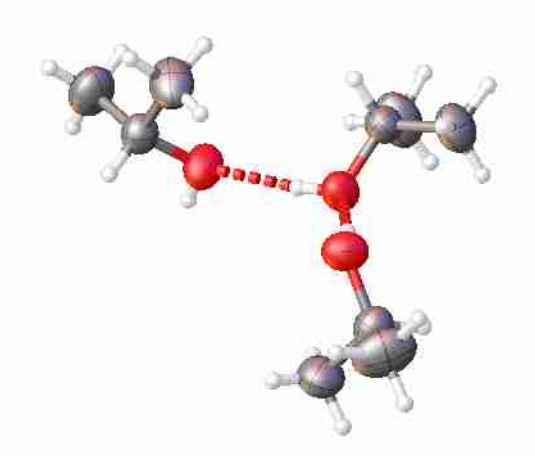

Figure 6.1 Asymmetric unit of cryo-crystallised isopropyl alcohol (polymorph I).

1-dimensional helical chains of O-H···O hydrogen bonds dictate the packing of the low-temperature phase of isopropyl alcohol, as shown below in figure 6.2.

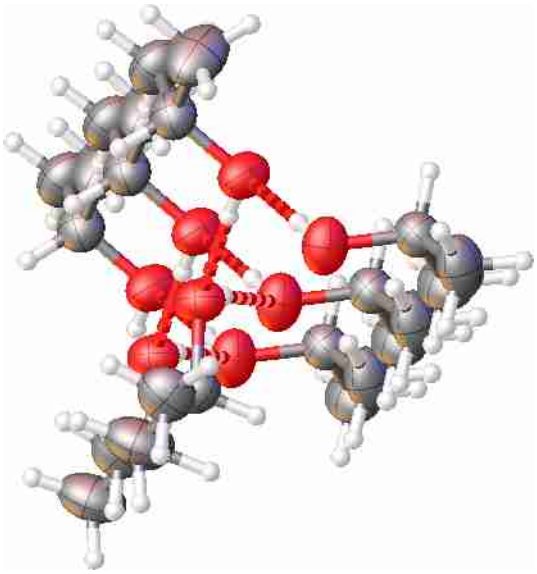

Figure 6.2 One-dimensional helical chain of hydrogen-bonding in the low-temperature polymorph of isopropyl alcohol (polymorph I).

The crystal structure of the cryo-crystallised structure of isopropyl alcohol in figure 6.3.

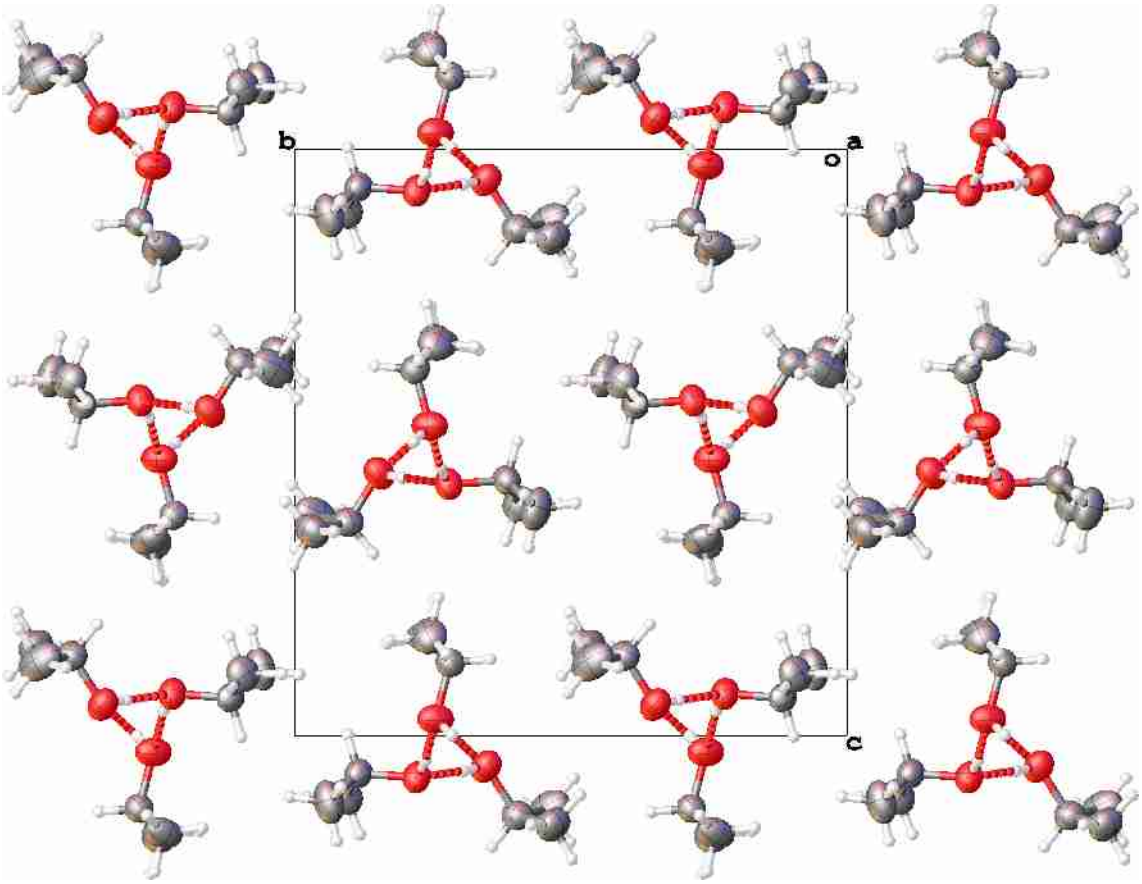

Figure 6.3 Crystal structure of isopropyl alcohol obtained through cryo-crystallisation (polymorph I).

The high *Z′* value in this structure is unsurprising, as it is known that monoalcohols have a tendency to crystallise with a *Z*' value greater than 1.[232] *Z′* = 3 is known as being particularly common, as it allows for the formation of a helix where the side-chains do not have to be linked by symmetry.

The high-pressure polymorph was also found to have a high *Z*' structure, (*Z*' = 4) in space group $P2_1/c$. The asymmetric unit of the high-pressure polymorph is shown below in figure 6.4.

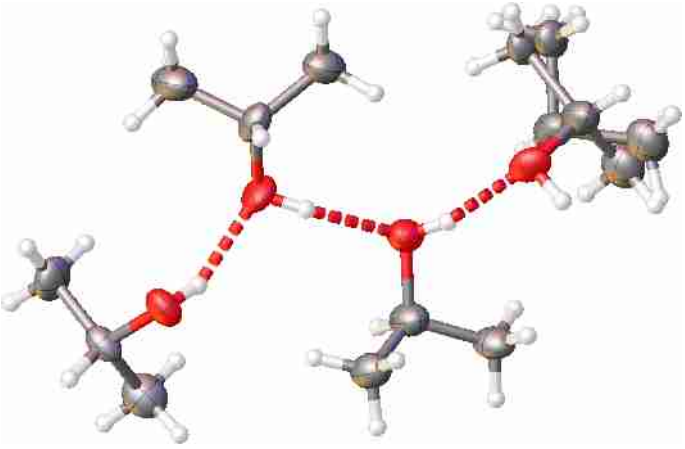

Figure 6.4 Asymmetric unit of high-pressure crystallised isopropyl alcohol (polymorph II).

The hydrogen-bonding motif is very different to that seen in the low-temperature structure, with isolated eight-membered rings being formed in preference to infinite helices. Having very different packing motifs is not entirely unexpected, as secondary alcohols are known to form ring- and chain- type structures with approximately equal propensity.[233] The hydrogen-bonding motif in the high-pressure polymorph is shown below in figure 6.5.

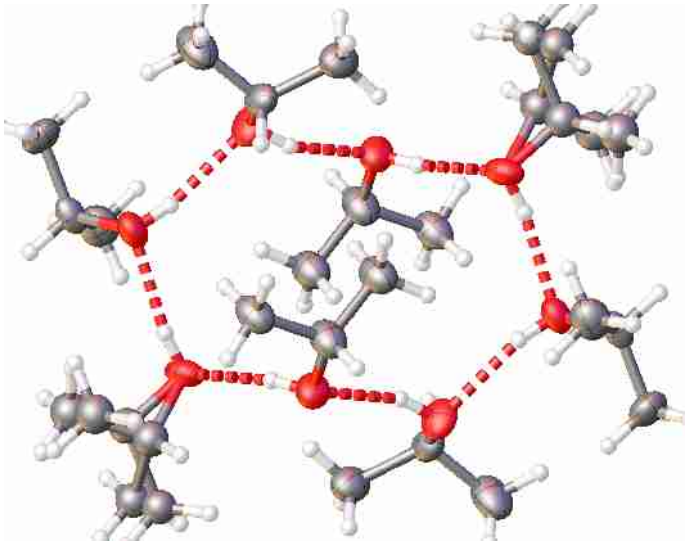

Figure 6.5 Hydrogen-bonding motif found in high-pressure crystallised isopropyl alcohol (polymorph II).

One of the four molecules in the asymmetric unit was found to have disorder of the carbon side-chain over two sites, with each position approximately equally occupied. The disorder is shown below in figure 6.6.

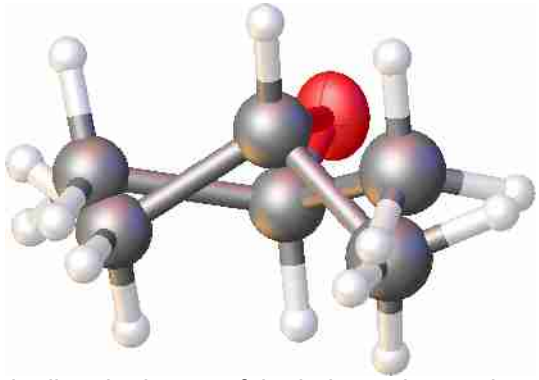

Figure 6.6 Side-chain disorder in one of the independent molecules in high-pressure crystallised isopropyl alcohol (polymorph II). The 50% probability ellipsoids of the carbon atoms are not shown for purposes of clarity.

The crystal structure of the high-pressure polymorph (polymorph II) is shown below in figure 6.7.

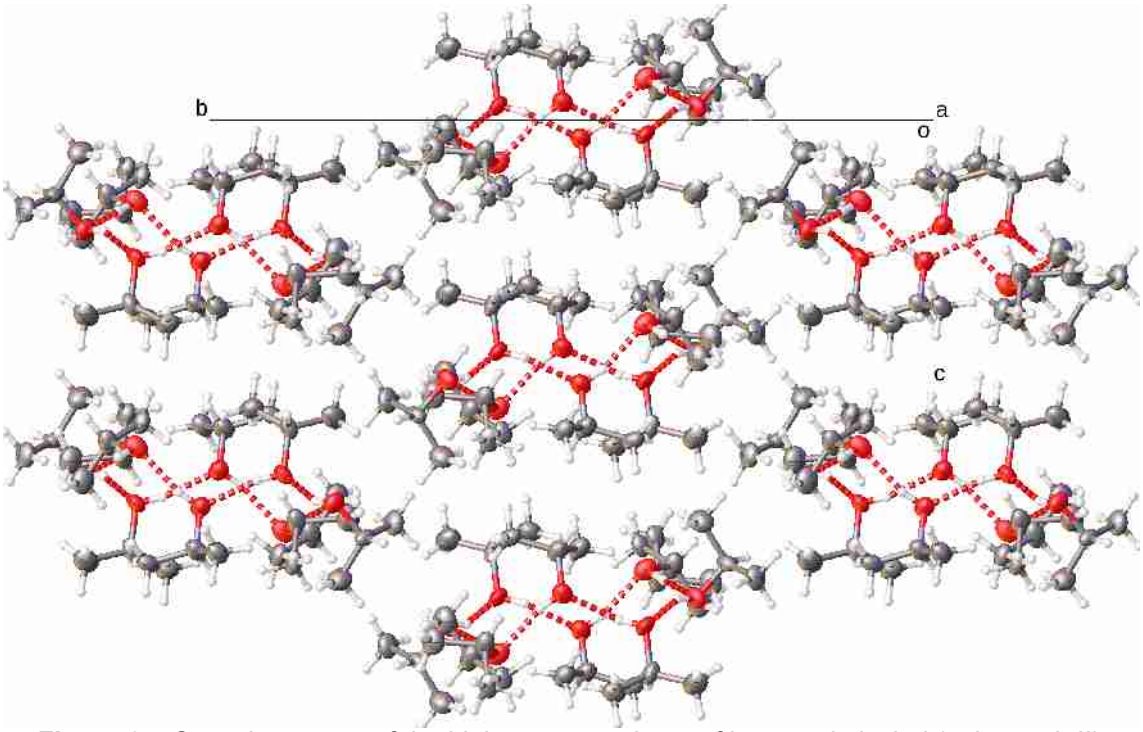

Figure 6.7 Crystal structure of the high-pressure phase of isopropyl alcohol (polymorph II).

The lengths of the hydrogen bonds in the two polymorphs and the densities are shown below in table 6.1.

	O···O Distance / Å	**Density / gcm^{-3}**
Low-Temperature (Polymorph I)	2.7191 (12)	0.958
	2.7222 (12)	
	2.7290 (14)	
High-Pressure (Polymorph II)	2.6812 (6)	1.131
	2.7081 (6)	
	2.7112 (5)	
	2.7335 (5)	

Table 6.1 Table showing the density and hydrogen bond lengths and angles in the two polymorphs of isopropyl alcohol.

The densities of the two polymorphs are very different, with the high-pressure polymorph being 18.3% more dense than the low-temperature polymorph. On the other hand, the lengths of the hydrogen bonds in the two polymorphs are similar. The C-O and C-C bond lengths and angles are not significantly distorted by the application of pressure. This is in contrast to the high-pressure polymorph of methanol, where the molecular geometry is distorted in order to form shorter, more linear hydrogen bonds.[234]

The crystallographic data for the two polymorphs of isopropyl alcohol are shown in table 6.2 below.

Compound	**Isopropyl alcohol (LT)**	**Isopropyl alcohol (HP)**
empirical formula	C_3H_8O	
formula weight	60.09	
T/K	180 (2)	ambient
P/kbar	ambient	11.2 (2)
crystal system	monoclinic	monoclinic
space group	$P2_1/c$	$P2_1/c$
a (Å)	6.542 (3)	8.7267 (18)
b (Å)	13.415 (14)	21.838 (6)
c (Å)	14.469 (11)	8.408 (3)
β (°)	99.79 (2)	118.243 (8)
Z	12	16
V/Å^3	1251.3 (17)	1441.6 (7)
D_{calc}/g cm^{-3}	0.958	1.131
μ/mm^{-1}	0.069	0.052
unique reflns	1487	1234
observed reflns	1369	743
θ_{max}	21.770	15.340
completeness/%	92.1	60.2
R_1 [I > 2σ]	0.0468	0.0585
wR_2 [all]	0.1231	0.1429
goodness-of-fit	1.002	1.100

Table 6.2 Crystallographic data from the two polymorphs of isopropyl alcohol.

6.3 Diethyl Ether

6.3.1 Introduction

Diethyl ether is a very common stock chemical, used as a highly volatile solvent and in solvent extractions (due to its immiscibility in water). The low-temperature polymorph was previously reported in 1972 by Andre *et al*.[235]. No high-pressure polymorphs have previously been reported.

6.3.2 Experimental

Due to the improvement in source and detector technology since the low-temperature was characterised in 1972,[235] it was decided to recollect this data. The standard cryo-crystallographic technique, as detailed in section 1.2 was used to form suitable single crystals of the low-temperature polymorph. The standard crystallisation protocol described in section 1.1 was used to grow a single crystal of the high-pressure polymorph. The pressure approximately 24 hours after the crystal was grown to fill the gasket was measured at 10.5 (2) kbar.

6.3.3 Results and Discussion

Diethyl ether was found to crystallise in the same phase as previously reported. In this polymorph the molecules are packed in a herringbone motif with the two symmetrically inequivalent molecules orientated approximately perpendicular to one another, as shown below in figure 6.8.

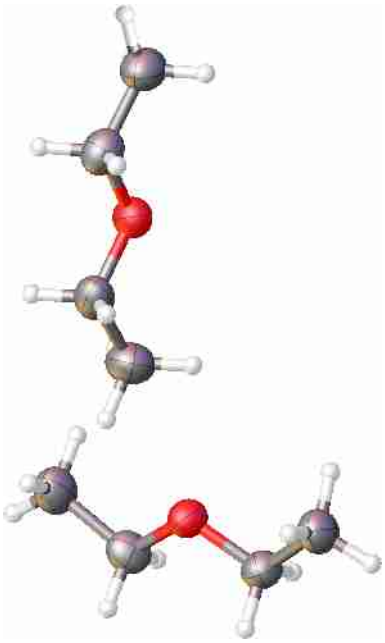

Figure 6.8 Asymmetric unit of the low-temperature polymorph of diethyl ether.

The crystal structure of the low-temperature polymorph is shown below in figure 6.9.

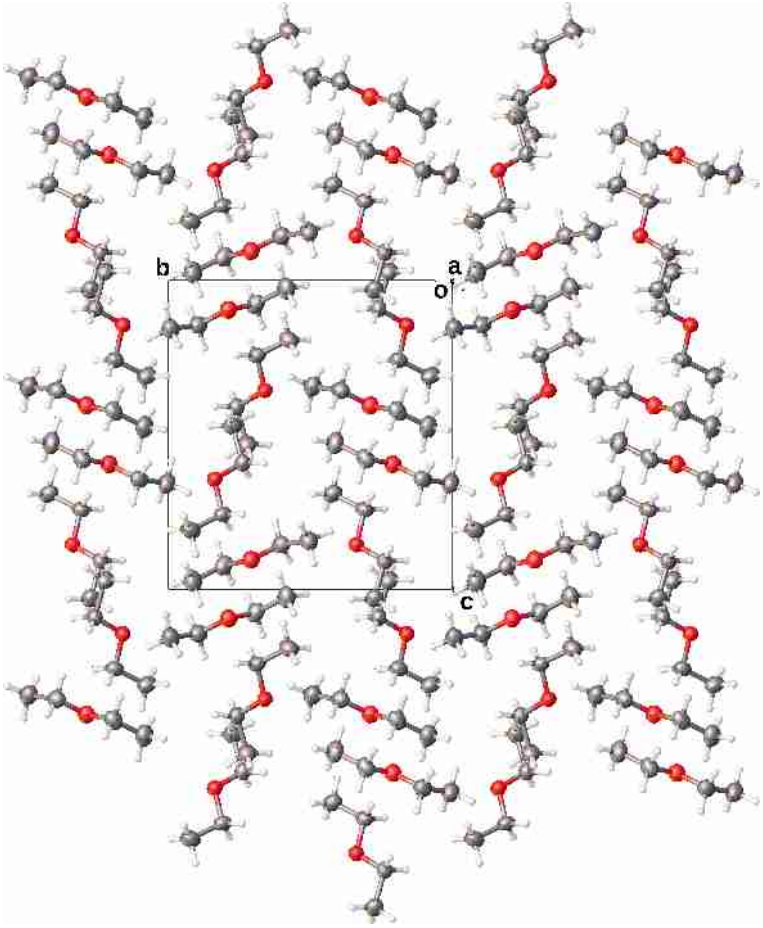

Figure 6.9 Crystal structure of the low-temperature polymorph of diethyl ether.

High-pressure crystallisation resulted in the formation of a different polymorph of diethyl ether. The reflections were assigned to the space group $P2_1/c$, (Z' = 1). The crystal structure of the high-pressure polymorph of diethyl ether is shown in figures 6.10 and 6.11.

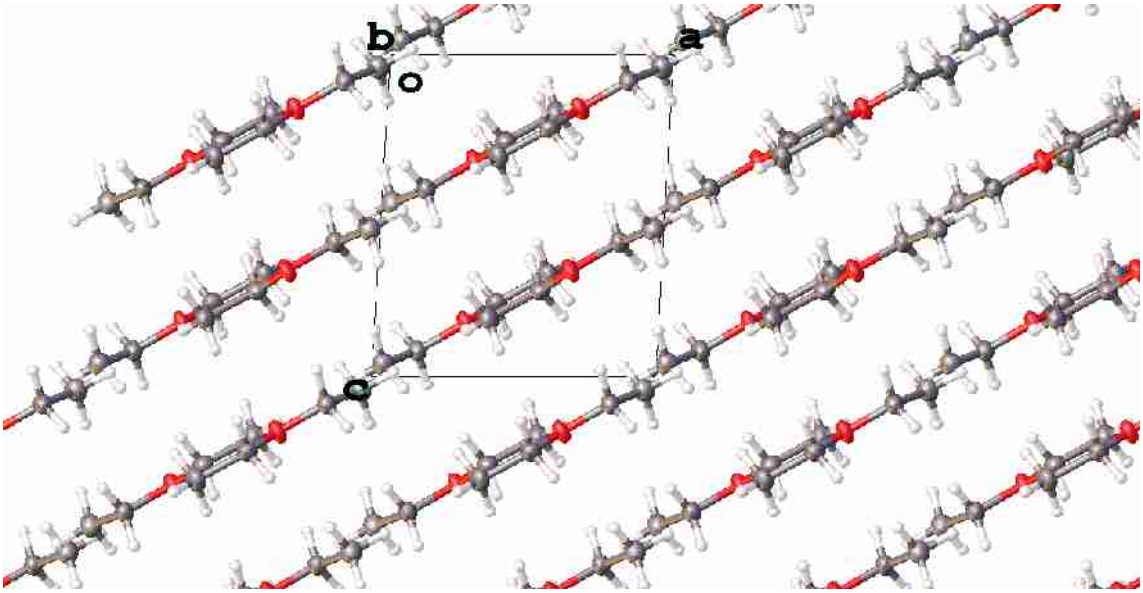

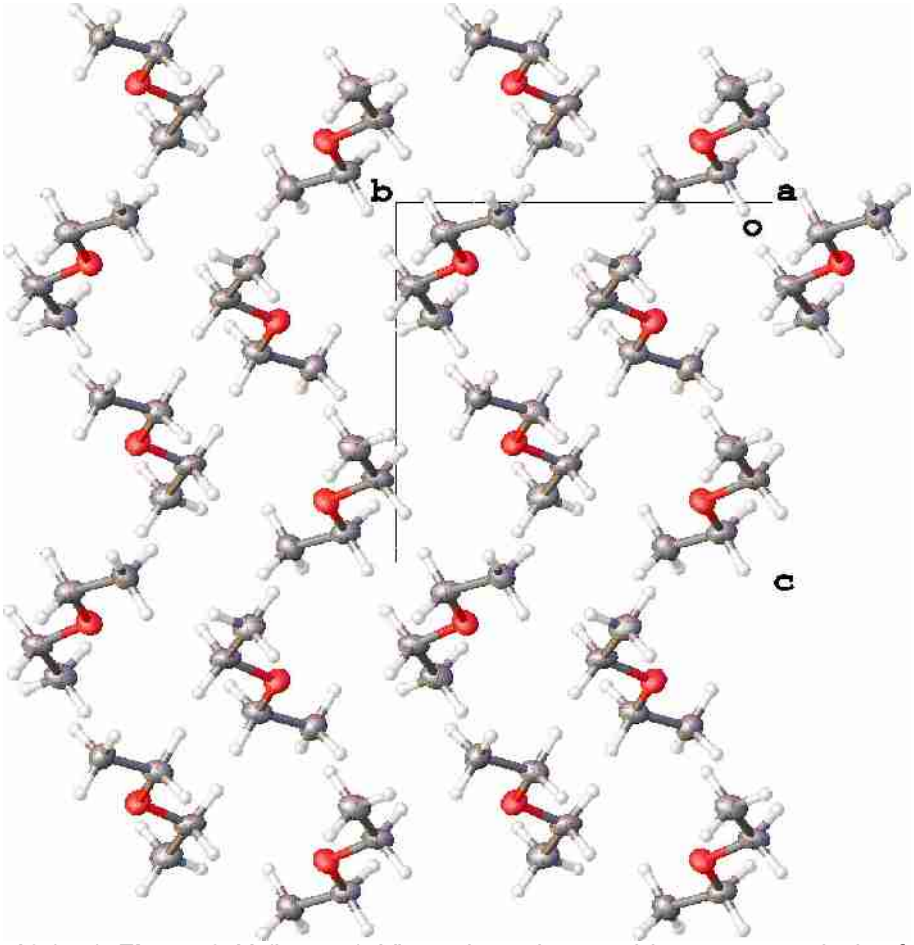

Figure 6.10 (top), **Figure 6.11** (bottom), Views down the *a* and *b* axes respectively of the high-pressure polymorph of diethyl ether.

In contrast to the herringbone motif seen in the low-temperature phase, the high-pressure phase has a layered structure, with significantly shorter intermolecular contact distances than the low-temperature polymorph. The shortest intermolecular contact distance in the high-pressure structure is an H···H contact (which are typically repulsive in nature) of 2.2014 (11) Å. This is approximately 10% lower than the sum of the Van der Waal's radii of the two atoms. In contrast, the closest H···H interaction in the low-temperature structure has a contact distance of 2.5770 (5) Å - considerably greater than the sum of the Van der Waal's radii. Accordingly, the high-pressure polymorph has a much greater density (1.120 g cm^{-3}) than the low-temperature polymorph (0.943 gcm^{-3}).

Crystallographic data for the two polymorphs is shown below in table 6.3.

Compound	**Diethyl Ether (LT)**	**Diethyl Ether (HP)**
empirical formula	$C_4H_{10}O$	
formula weight	74.12	
T/K	150 (2)	ambient
P/kbar	ambient	12.5 (2)
crystal system	orthorhombic	monoclinic
space group	$P2_12_12_1$	$P2_1/c$
a (Å)	8.1117 (18)	6.863 (3)
b (Å)	10.870 (3)	8.185 (4)
c (Å)	11.844 (3)	7.834 (4)
β (°)	90	93.231 (14)
Z	8	4
V/Å^3	1044.3 (4)	439.4 (4)
D_{calc}/g cm^{-3}	0.943	1.120
μ/mm^{-1}	0.065	0.049
unique reflns	2156	633
observed reflns	1201	314
θ_{max}	26.480	18.140
completeness/%	55.7	49.6
R_1 [I > 2σ]	0.0354	0.0683
wR_2 [all]	0.0993	0.1413
goodness-of-fit	1.043	1.230

Table 6.3 Crystallographic data of the two polymorphs of diethyl ether.

6.4 Anisole

6.4.1 Introduction

Anisole is a simple aromatic compound that is used both as a starting reagent and a solvent in organic chemistry. No solid-state structural studies of this compound have previously been reported.

6.4.2 Experimental

Anisole was crystallised using low-temperature and high-pressure using the standard crystallisation protocols detailed in sections 1.2 and 1.1 respectively.

6.4.3 Results and Discussion

Anisole was found to crystallise in two different polymorphs, one from cryo-crystallisation and the other from high-pressure crystallisation. Figures 6.12 and 6.13 show the asymmetric unit and packing diagram of the cryo-crystallised polymorph respectively.

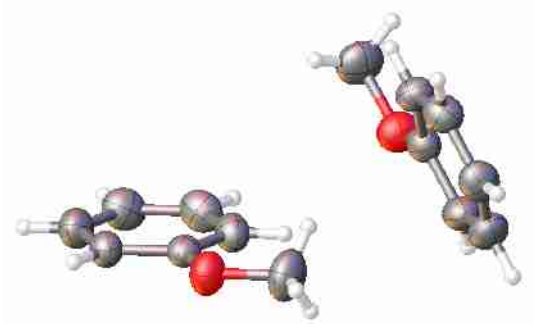

Figure 6.12 Asymmetric unit of cryo-crystallised anisole

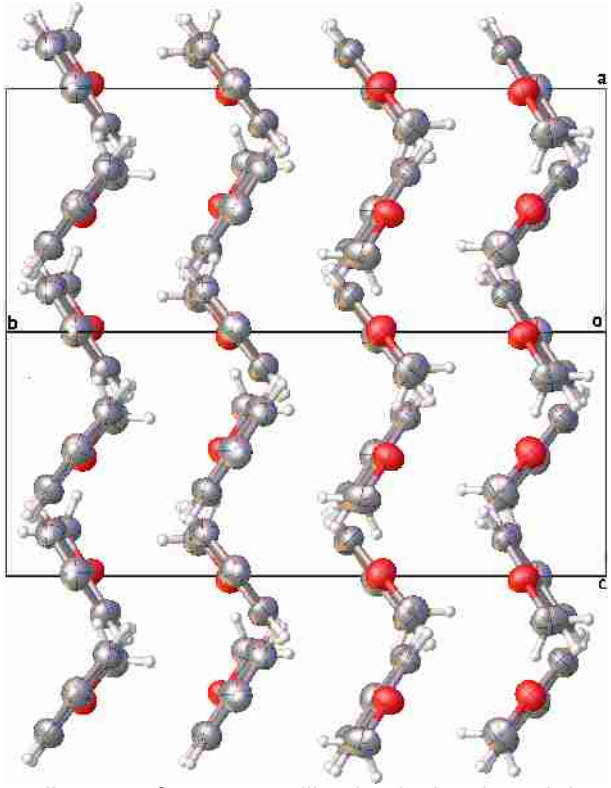

Figure 6.13 Packing diagram of cryo-crystallised anisole, viewed down (101), showing a herringbone packing motif.

One can see from figure 6.13 that this polymorph has two molecules in the asymmetric unit. The OMe group of one molecule is orientated directly above aromatic ring of the other molecule. This moiety repeats in an infinite chain down the *b* axis to form a herringbone motif.

Figures 6.14 and 6.15 show the asymmetric unit and packing diagram respectively of the high-pressure crystallised polymorph.

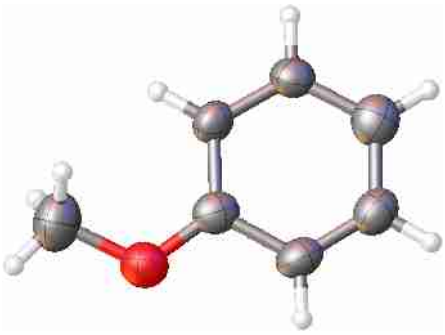

Figure 6.14 Asymmetric unit of high-pressure crystallised anisole

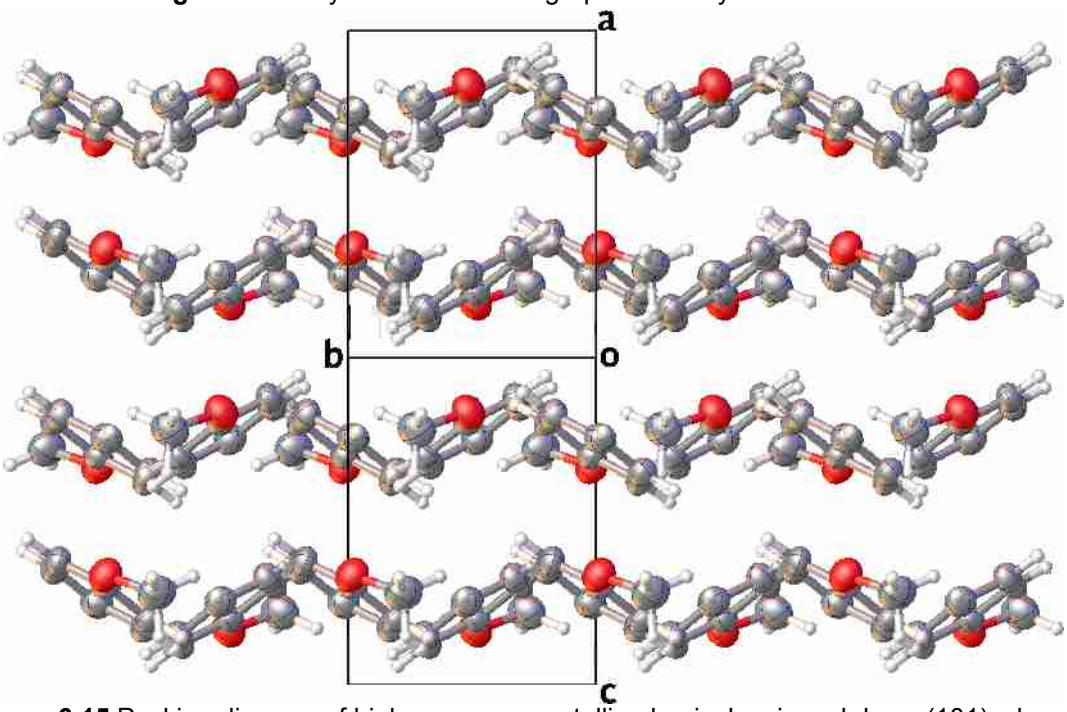

Figure 6.15 Packing diagram of high-pressure crystallised anisole, viewed down (101), showing a herringbone packing motif.

The molecules in the low-temperature phase are all orientated such that the plane of the aromatic rings are aligned approximately down the (101) axis with little overlap between each “bone” in the motif. The high-pressure motif differs in that the anisole molecules are skewed out of plane in an up-down-up-down motif such that they are no longer aligned down the (101) axis. This allows the “bones” to significantly overlap with one another.

The skew of the herringbone layers allows the high-pressure polymorph to have a much greater packing efficiency than the low-temperature form. *V*/*Z* was found to be 164.0 (2) Å^3 in the low-temperature polymorph and 144.3 (2) Å^3 in the high-pressure polymorph.

Table 6.4 lists the distances intermolecular interactions in the two polymorphs.

Polymorph	**Interaction**	**Distance / Å**	**Angle / °**
Low-Temperature	C-H···O	2.7937 (18)	125.98 (7)
		2.7956 (12)	151.74 (6)
	C-H···π	2.8969 (14)	139.94 (3)
High-Pressure	C-H···O	2.7386 (12)	148.663 (17)
		2.7809 (11)	122.36 (3)
	C-H···π	2.7845 (11)	146.54 (2)

Table 6.4 Distance and angles of intermolecular interactions in anisole. The distance given for for C-H···π interactions is that from the hydrogen atom to the nearest point on the aromatic ring.

As in other systems studied in this thesis, it appears that the polymorphism is driven by the higher density of the high-pressure phase. Table 6.5 shows crystallographic data from the two polymorphs of anisole.

Compound	**Anisole (LT)**	**Anisole (HP)**
empirical formula	C_7H_8O	
formula weight	1.095	
T/K	233 (2)	ambient
P/kbar	ambient	4.1 (2)
crystal system	monoclinic	monoclinic
space group	$P2_1/c$	$P2_1/c$
a (Å)	13.905 (9)	13.681 (10)
b (Å)	14.840 (8)	5.434 (3)
c (Å)	6.392 (4)	7.846 (5)
β (°)	95.908 (11)	98.44 (2)
Z	8	4
V/Å^3	1312.0 (14)	577.0 (6)
D_{calc}/g cm^{-3}	1.095	1.245
μ/mm^{-1}	0.072	0.052
unique reflns	3253	836
observed reflns	2331	338
θ_{max}	28.279	18.180
completeness/%	71.6	40.4
R_1 [I > 2σ]	0.0548	0.0262
wR_2 [all]	0.1638	0.0555
goodness-of-fit	1.042	1.188

Table 6.5 Crystallographic data of cryo- and high-pressure crystallised anisole.

6.5 Dimethylacetamide

6.5.1 Introduction

Dimethylacetamide is commonly used as a high-boiling (438 K) polar protic solvent in organic synthesis. No structures of this compound have been reported.

6.5.2 Experimental

Dimethylacetamide was crystallised using low-temperature and high-pressure using the standard crystallisation protocols detailed in sections 1.2 and 1.1 respectively.

6.5.3 Results and Discussion

Dimethylacetamide was found to form two distinct polymorphs, one from cryo-crystallisation and the other from high-pressure crystallisation. Figure 6.16 shows the asymmetric unit and figure 6.17 the crystal structure of cryo-crystallised dimethylacetamide.

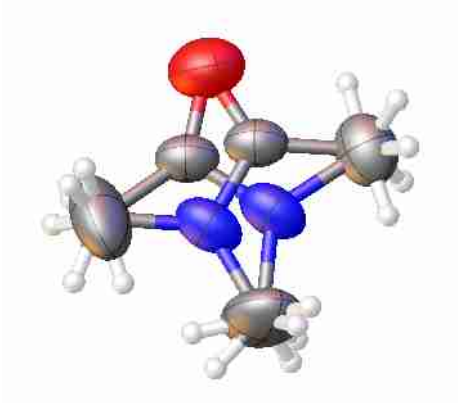

Figure 6.16 Asymmetric unit of cryo-crystallised dimethylacetamide.

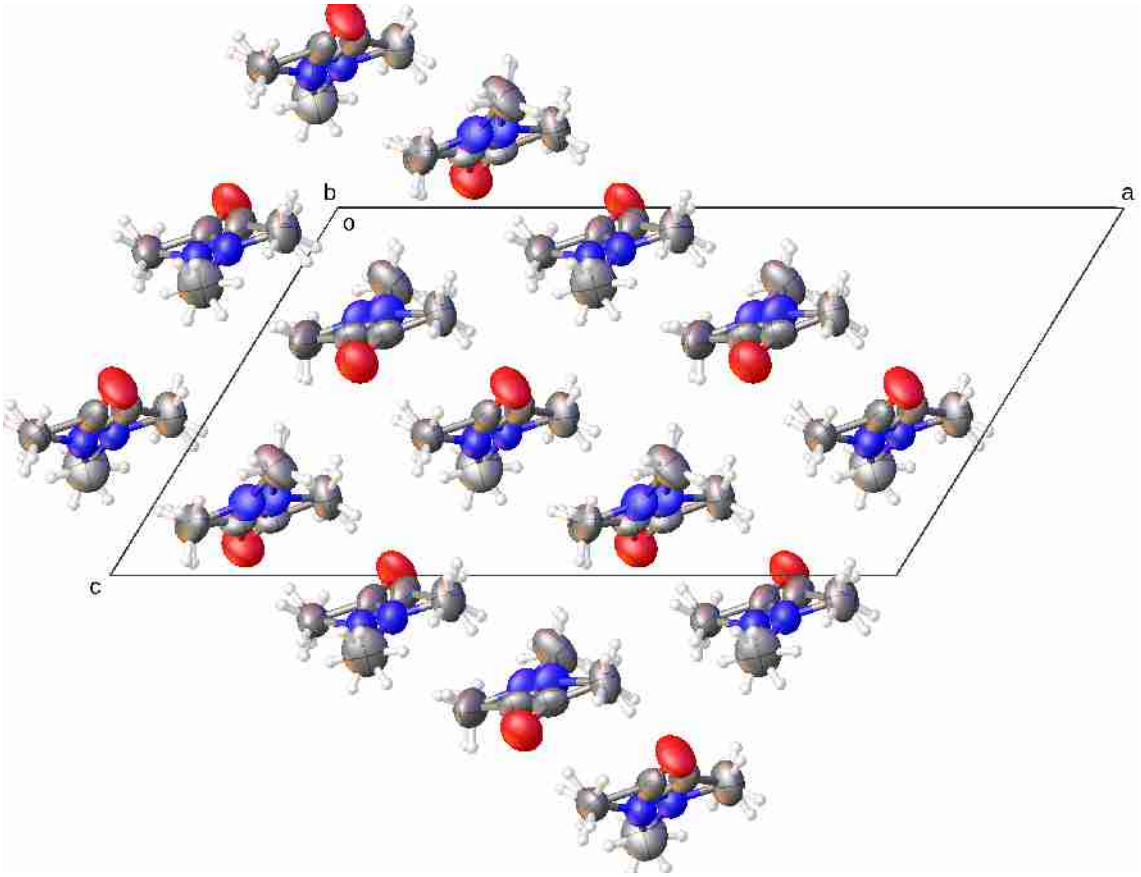

Figure 6.17 Crystal structure of cryo-crystallised dimethylacetamide.

The dimethylacetamide molecule was found to be disordered over two sites, with an occupancy ratio of approximately 0.75 : 0.25. This disorder is not surprising given that it does not affect the position of the outer carbon and oxygen atoms and as such does not greatly alter the intermolecular interactions in the structure.

The high-pressure polymorph exhibited similar disorder. The asymmetric unit and crystal structure of the high-pressure phase are shown below in figures 6.18 and 6.19.

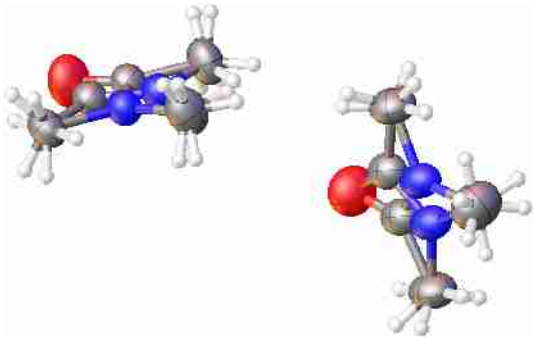

Figure 6.18 Asymmetric unit of high-pressure crystallised dimethylacetamide.

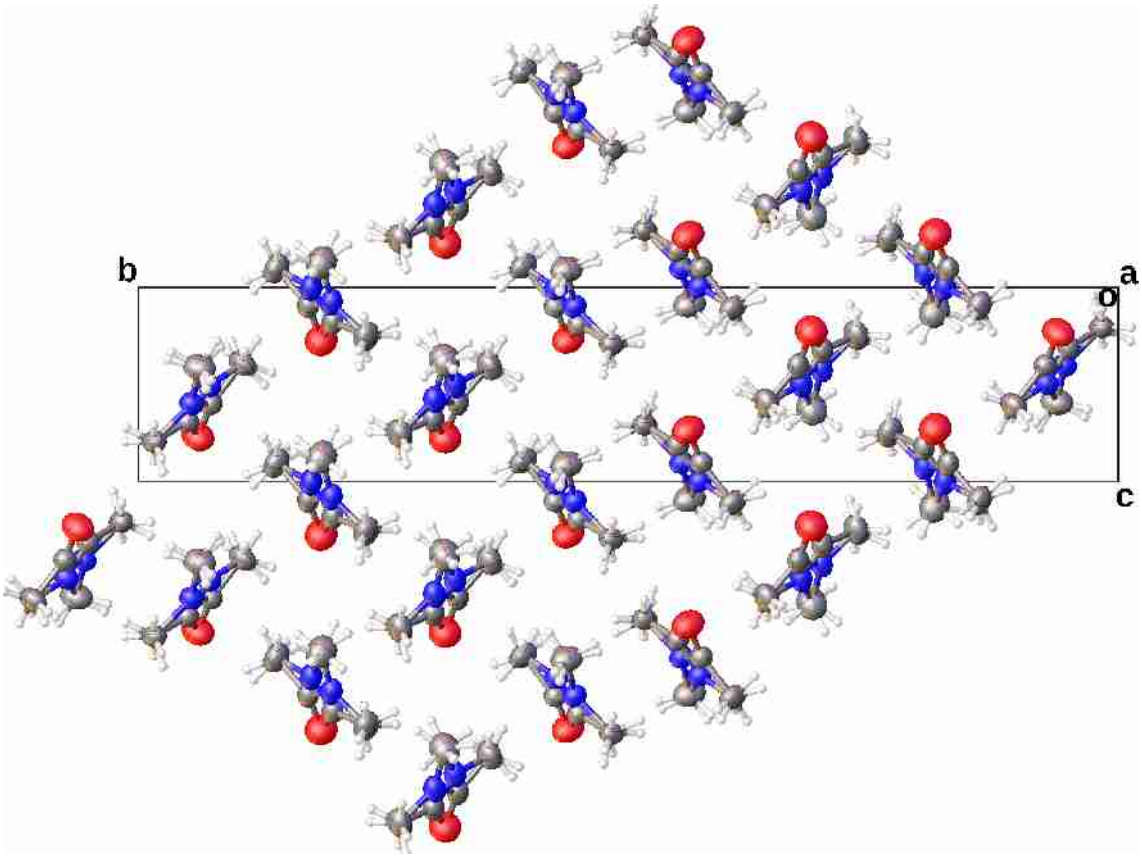

Figure 6.19 Crystal structure of high-pressure crystallised dimethylacetamide.

The high-pressure phase is rather complicated, with a very long unit cell axis (*b*) for such a small molecule, 29.430 (8) Å. Along this axis there is a ABCDEFGH ordering.

In one of the two molecules in the asymmetric unit, the occupancies of the two positions were found to be approximately 0.75 : 0.25. In the other molecule they were found to be approximately 0.5 : 0.5.

Table 6.6 below shows crystallographic data for the two data collections.

Compound	**Dimethylacetamide (LT)**	**Dimethylacetamide (HP)**
empirical formula	C_4H_9NO	
formula weight	173.97	
T/K	250 (2)	ambient
P/kbar	ambient	1.1 (2)
crystal system	Monoclinic	Monoclinic
space group	*C*2/*c*	$P2_1/c$
a (Å)	19.39 (4)	5.8329 (11)
b (Å)	6.076 (8)	29.430 (8)
c (Å)	10.82 (2)	5.9467 (16)
B (°)	121.75 (4)	100.416 (140)
Z	8	8
V/Å^3	1084 (3)	1004.0 (4)
D_{calc}/g cm^{-3}	1.068	1.153
μ/mm^{-1}	0.077	0.052
unique reflns	485	892
observed reflns	318	533
θ_{max}	21.959	15.340
completeness/%	65.6	59.8
R_1 [I > 2σ]	0.0844	0.0871
wR_2 [all]	0.2449	0.2937
goodness-of-fit	1.069	1.050

Table 6.6 Crystallographic data from cryo- and high-pressure crystallised dimethylacetamide.

6.6 Acetic Anhydride

6.6.1 Introduction

Acetic anhydride is widely used in synthetic chemistry, both in acetylation reactions and as a solvent. It is the simplest acid anhydride that can be easily isolated (formic anhydride is known, but is highly unstable). VSEPR theory predicts the molecule to be planar. There are three possible rotamers that have a planar geometry, shown below in figure 6.20.

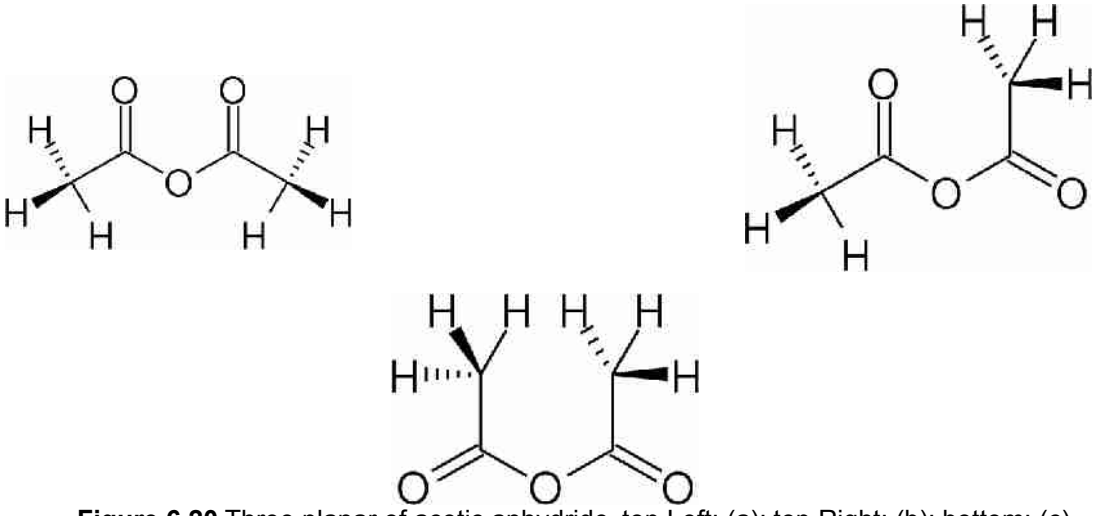

Figure 6.20 Three planar of acetic anhydride. top Left: (a); top Right: (b); bottom: (c)

A significant drive to planarity arises through the conjugation between the central oxygen and the carbonyl group. This conjugation is strongest when the molecule has a planar geometry and makes a significant contribution to the free energy (up to 30 $kJmol^{-1}$).[236]

All three planar rotamers shown above do not represent local energy minima. Rotamer (a) has an unfavourable dipole-dipole repulsion due to having two orientationally aligned carbonyl groups. There is clearly an unacceptably large steric hindrance in (c) due to the steric hindrance between the methyl hydrogens. There is also considerable steric hindrance in (b) between the carbonyl oxygen and a neighbouring hydrogen atom. As such, rotamers (a) and (b) are more energetically favourable than the (c). As a result, one would expect the lowest energy molecular structure to be a distorted form of either rotamer (a) or (b). The molecular geometry of acetic anhydride may be defined in terms of a combination of two torsion angles. φ_1 and φ_2 as shown in figure 6.21 below.

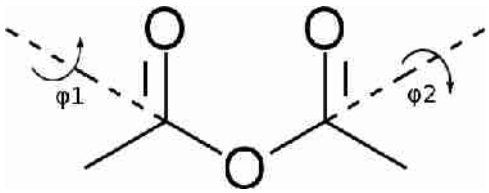

Figure 6.21 Torsional angles in acetic anhydride

In this scheme rotamer (a) may be defined as $\varphi_1 = 0°$, $\varphi_2 = 0°$. Rotamer (b) defined as $\varphi_1 = 0°$, $\varphi_2 = 180°$ and rotamer (c) as $\varphi_1 = 180°$, $\varphi_2 = 180°$.

Mirone *et al* found that the molecular geometry of acetic anhydride in solution is non-planar, with C_2 symmetry. This was determined on the basis of the number of polarized Raman lines and the intensity ratio between the absorption bands due to carbonyl stretchings.[228] Vledder *et al* confirmed that the molecular structure in the gaseous state is non-planar on the basis of the radial distribution function from electron diffraction data, but they were unable to confirm the exact structure. Analysis of vibrational spectra data revealed that there is a distribution of torsional angles around the C-O bonds, indicating that there is a large degree of flexibility in the liquid state.[229]

Colthup calculated the 1-dimensional potential energy as a function of the dihedral angles around both C-O single bonds (i.e. where φ_1, as defined in figure 6.18, is equal to φ_2) in 1985.[237] Wu *et al* calculated the 2-dimensional potential energy landscape in 2000.[238] They found that are two local energy minima, corresponding to distorted forms of (a) and (b). The distorted (a) form was found to be slightly lower in energy (0.71 to 5.40 $kJmol^{-1}$ dependant on the level of theory used).

Although there is significant interest in the geometry of acetic anhydride, no crystallographic study had previously been carried out. It is interesting to see how the various factors (pressure, temperature and solid-state intermolecular forces) alter the molecular geometry, as molecules with low torsional barriers may have hugely different geometries in the crystal and gas phases.[239,240]

6.6.2 Experimental Methods

Acetic anhydride was crystallised using the standard high-pressure and cryo-crystallisation techniques described in sections 1.1 and 1.2 respectively.

6.6.2.1 Complementary Computational Calculations

As computational methods have improved considerably in the fourteen years since the publication by Wu *et al*,[238] largely as a result of the enormous increase in computational power, we collaborated with Dr. D. Zaleski (Newcastle University) (to recalculate a potential energy map. Given the weak nature of the interactions involved, using a level of theory that takes into account long range non-covalent interactions is important. The dispersion-corrected DFT method, M06-2X/6-31G(d,p), was therefore used to generate the energy landscape as it models these interactions accurately. The minima were optimized at the MP2-Aug-cc-pVTZ level of theory in a program written by Zaleski.

6.6.3 Results and Discussion

6.6.3.1 Computational Results

The energy landscape calculated by Zaleski at the M062X/6-31G(d,p) level of theory is shown below in figure 6.22.

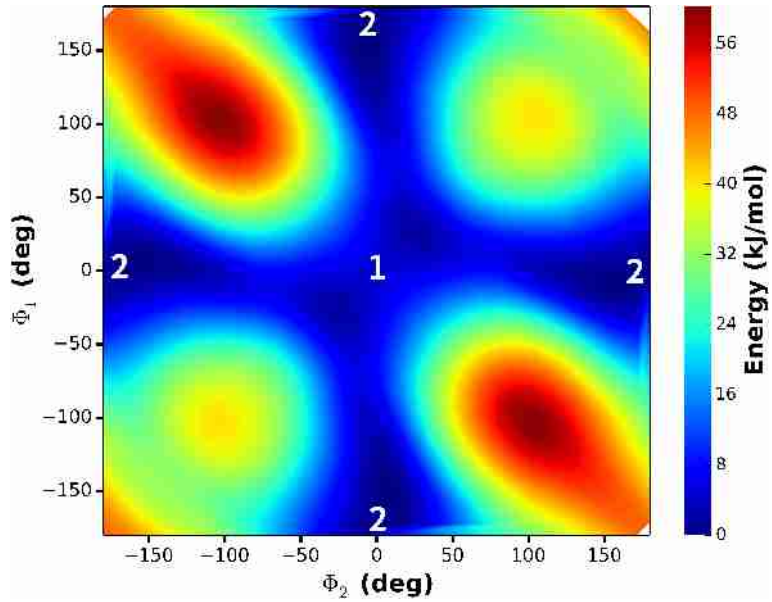

Figure 6.22 Potential Energy Landscape of Acetic Anhydride.

The two low energy conformations (a) and (b) were found to be very close in energy. The barrier to rotation at $\varphi_1 = \varphi_2 = 0°$ was found to be 2.4 kJmol^{-1}. A slice from the above plot where $\varphi_1 = \varphi_2$ is shown below in figure 6.23.

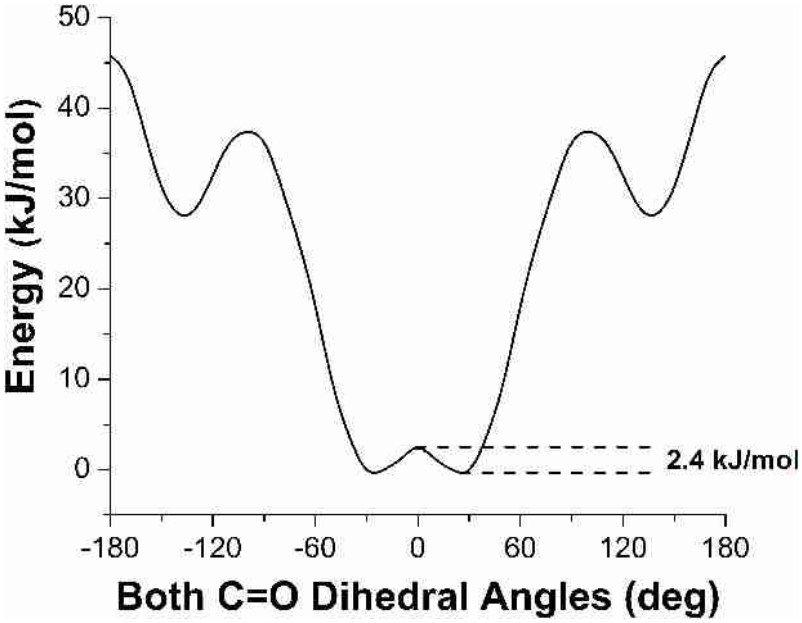

Figure 6.23 Potential energy profile taken from figure 6.19, where $\varphi_1 = \varphi_2$ (lower-left to upper-right diagonal)

The minima was optimized at the MP2-Aug-cc-pVTZ level of theory, φ was found to be 30.09° at the minima.

6.6.3.2 Experimental Results

The low-temperature diffraction pattern was assigned to the space group *Pbcn*, with the high-pressure pattern being assigned to *C2/c*. Both forms were found to have a *Z*' value of 0.5, (meaning that φ_1 must be equal to φ_2). The low-temperature data were collected at 195 (2) K and the high-pressure data at 9.1 (5) kbar. The molecular geometry of the two forms is shown below in figures 6.24 and 6.25.

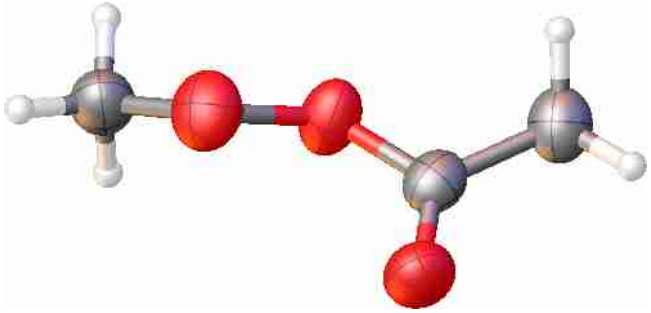

Figure 6.24 Molecular geometry in cryo-crystallised acetic anhydride.

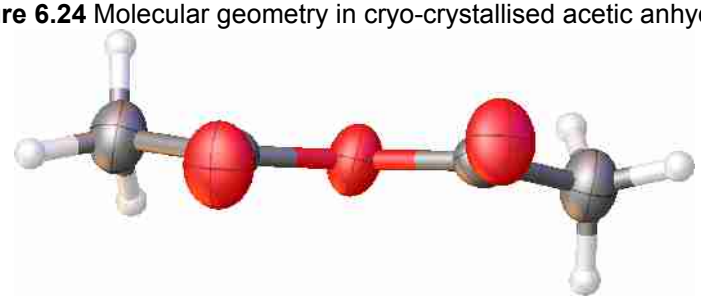

Figure 6.25 Molecular geometry in acetic anhydride crystallised through high-pressure.

As is apparent from figures 6.21 and 6.22, the molecular geometries in the two structures are very different. The value of φ determined from least-squares refinement was 27.75 (15)° in the cryo-crystallised form and 9.634 (8)° in the high-pressure form. The molecular geometry in the low-temperature form closely matches the optimized molecular geometry at the MP2-Aug-cc-pVTZ level of theory. The molecular geometry of the high-pressure form is clearly far more planar than the optimized geometry. The crystal structures of the two polymorphs are shown below in figures 6.26 and 6.27.

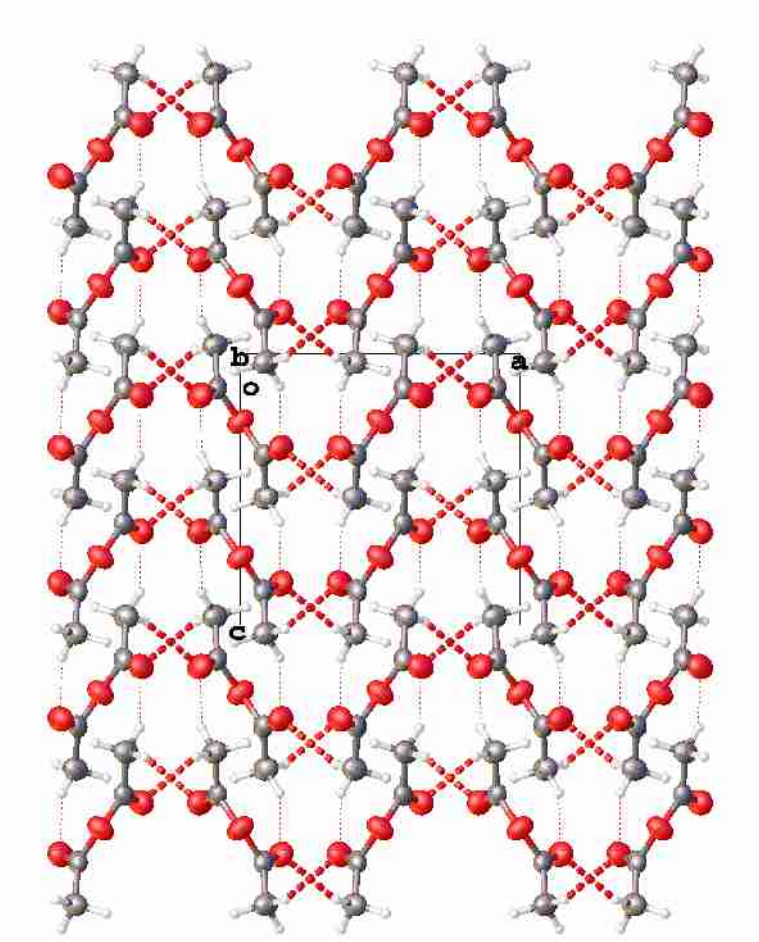

Figure 6.26 Packing diagram of the low-temperature polymorph of acetic anhydride. The heavier dashed line refers to shorter C-H···O contacts. The lighter dashed line refers longer C-H···O contacts.

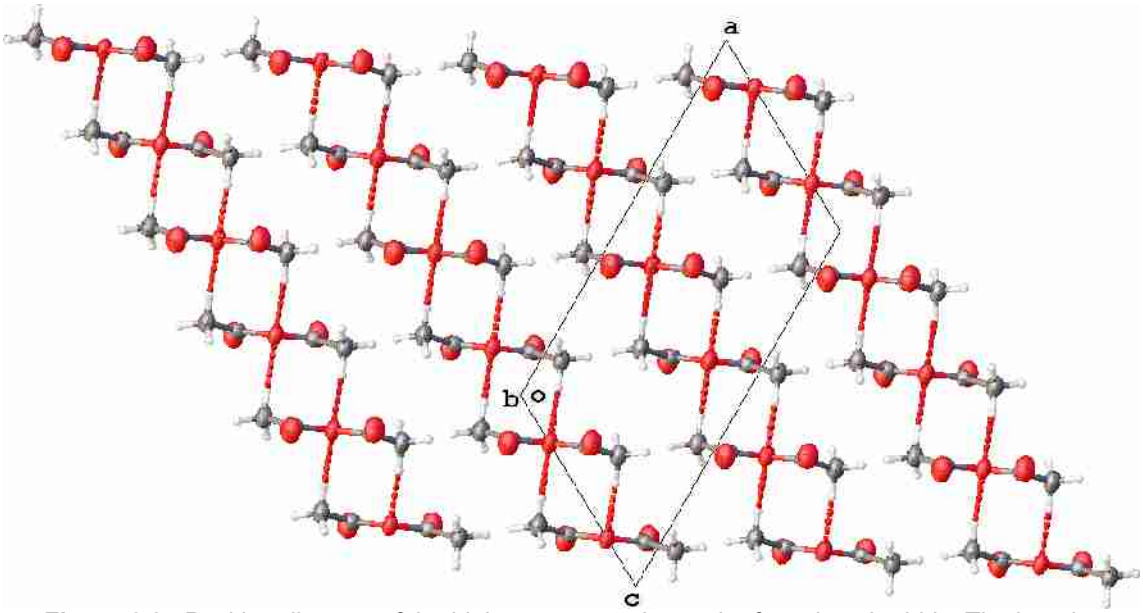

Figure 6.27 Packing diagram of the high-pressure polymorph of acetic anhydride. The heavier dashed line refers to shorter C-H···O contacts. The lighter dashed line refers longer C-H···O contacts.

The high-pressure phase has a layered structure, while the cryo-crystallised form has a herringbone structure. The high-pressure layered structure clearly requires that the molecular geometry is relatively planar in order for the structure to be closely packed while the low-temperature herringbone structure requires a twisted molecular geometry.

The lengths and angles of the intermolecular C-H···O lengths in the two polymorphs are shown below in table 6.7.

Polymorph	**C···O Distance / Å**	**H···O Distance / Å**	**C-H···O Angle / °**
Low-temperature	3.3731 (10)	2.4795 (7)	151.468 (8)
	3.5814 (11)	2.6673 (9)	155.351 (11)
High-pressure	3.4791 (12)	2.6141 (10)	153.059 (9)
	3.483 (2)	2.7253 (18)	136.34 (3)
	3.5295 (13)	2.7849 (10)	134.98 (3)

Table 6.7 Distances and angles of C-H···O interactions in the two polymorphs of acetic anhydride.

The C-H···O intermolecular interactions are of similar length in the two polymorphs.

After acetic anhydride was crystallised at high-pressure and a diffraction

pattern collected at the crystallisation pressure, data were collected at higher pressure [26.5 (5) and 48.0 (5) kbar). As the pressure increased, the resolution declined, mosaicity increased and the spot shape became increasingly elongated. As such the errors in the determination of φ increase with increasing pressure.

Table 6.8 shows the values of φ determined at different experimental conditions.

Polymorph	**Temperature / K**	**Pressure / kbar**	Φ / °
Low-temperature	195 (2)	ambient	27.75 (2)
High-pressure	ambient	9.1 (5)	9.5 (2)
		26.5 (5)	8.0 (2)
		48.0 (5)	6.3 (6)

Table 6.8. Values of φ at low-temperature and various high-pressures.

Increasing the pressure results in a further decrease in φ. Unfortunately, increasing the pressure further also results in the destruction of the crystal.

Crystallographic data are shown below in table 6.9.

Compound	**Acetic Anhydride (LT)**	**Acetic Anhydride (HP)**	**Acetic Anhydride (HP)**	**Acetic Anhydride (HP)**
empirical formula	$C_4O_3H_6$			
formula weight	102.09			
T/K	180 (2)	ambient		
P/kbar	ambient	9.1 (5)	26.5 (5)	48.0 (5)
crystal system	orthorhombic	monoclinic		
space group	*Pbcn*	*C*2/*c*		
a (Å)	8.189 (4)	13.416 (7)	12.719 (9)	12.468 (18)
b (Å)	7.875 (4)	5.5133 (18)	5.371 (3)	5.342 (5)
c (Å)	7.947 (3)	7.276 (3)	7.017 (4)	6.942 (8)
β (°)	90	118.933 (13)	117.09 (2)	116.47 (4)
Z	4	4		
V/Å^3	512.5 (4)	471.0 (4)	426.8 (5)	413.9 (9)
D_{calc}/g cm^{-3}	1.323	1.440	1.589	1.638
μ/mm^{-1}	0.115	0.075	0.083	0.085
unique reflns	637	575	428	346
observed reflns	553	243	132	130
θ_{max}	28.252	21.798	20.288	19.155
completeness/%	86.8	42.3	30.8	37.6
R_1 [I > 2σ]	0.0327	0.0389	0.0197	0.0557
wR_2 [all]	0.0906	0.1097	0.0395	0.1480
goodness-of-fit	1.059	1.087	0.993	1.147

Table 6.9 Crystallographic data from acetic anhydride

6.7 Conclusions

Two polymorphs of isopropyl alcohol were crystallised, one through cryo-crystallisation and the other through a modified high-pressure crystallisation protocol involving flash freezing and subsequent application of pressure. The two polymorphs were found to have significantly structural differences, with very different packing motifs. The high-pressure polymorph is far more dense and has isolated 8-membered rings linked by O-H···O hydrogen bonds. The cryo-crystallised form has isolated infinite chains with molecules in each chain linked by O-H···O hydrogen bonds.

Diethyl ether, anisole and dimethylacetamide were all found to have two polymorphs, one accessible through cryo-crystallisation, the other through high-pressure crystallisation. Diethyl ether also has a very large difference in density between the cryo-crystallised and high-pressure polymorphs. The high-pressure polymorph has a layered structure, with the low-temperature polymorph adopts a loosely packed zig-zag structure. The low-temperature polymorph of anisole was found to have OMe···π interactions in a Z' = 2 structure, while the high-pressure polymorph was considerably more dense but lacked these interactions.

Two polymorphs of acetic anhydride were crystallised, one through cryo-crystallisation, the other through high-pressure crystallisation. The molecules in the low-temperature polymorph pack in a herringbone motif, while a layered structure is adopted at high-pressure. The molecular geometry in the two polymorphs is very different. The molecules in the low-temperature polymorph have a twisted geometry that resembles the relaxed geometry in the gas phase. The molecules in the high-pressure polymorph have a far more planar geometry. Further application of pressure results in the molecular geometry in the high-pressure phase becoming even more planar, i.e. the drive towards close packing overcomes the energy barrier to the planar conformation.

Chapter 7: The structural response of a Ag (I) metal-organic framework to high-pressure

7.1 Introduction

Metal-organic frameworks (MOFs) are commonly used in applications such as gas storage, sensing and catalysis because the size of pores in the structure may be manipulated by changing the identity of the metal or the organic linker.[241] The self-assembly of $AgNO_3$ and N-N'-bis-(pyridin-3-ylmethylene)benzene-1,4-diamine in dichloromethane and acetonitrile using liquid-liquid diffusion was found to form a novel metal-organic framework comprising three distinct frameworks. The synthesis of the MOF was carried out by Lamming *et al*.[242] The molecular structure of the ligand is shown below in figure 7.1.

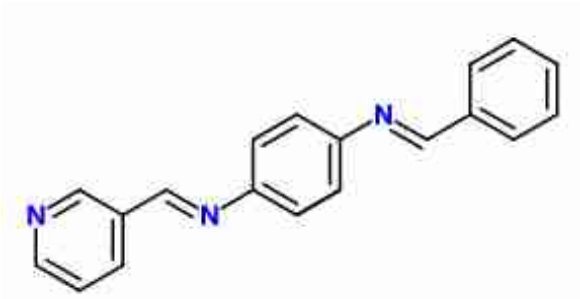

Figure 7.1 Molecular structure of the ligand, N-N'-bis-(pyridin-3-ylmethylene)benzene-1,4-diamine

Ambient pressure single-crystal diffraction showed that each framework comprises silver ions in a octahedral environment, co-ordinated by the pyridyl nitrogen atoms. This is a rather unusual co-ordination environment for Ag (I), which typically forms 2-, 3- or 4- co-ordination geometries.[243] One framework forms two-dimensional sheets, while the other forms two extended 3-dimensional motifs. The three frameworks are interpenetrating, with no ionic or covalent bonding linking the frameworks. Only five reports of interpenetrating 2-dimensional and 3-dimensional frameworks have been reported thus far, and as such this structure is rather interesting.[244,245,246,247,248] It was thought that the unusual co-ordination geometry of Ag (I) and packing arrangement may result in intriguing structural behaviour under the application of pressure.

7.2 Experimental

A single-crystal of the MOF and a ruby chip were loaded into the sample chamber. Paraffin oil was used as the hydrostatic medium. Sets of diffraction images were collected between ambient pressure up to near the hydrostatic limit (the maximum pressure at which the liquid provides a hydrostatically pressurise to the sample) of paraffin oil (30 kbar).[249] It was found that the crystal shattered as the pressure was increased beyond approximately 28 kbar. As the structure above this pressure was of interest, the experiment was repeated using a 1 : 1 mixture of pentane and isopentane as the pressure transmitting medium. This mixture has a hydrostatic limit of 70 kbar.[249]

7.3 Results and Discussion

The reflections from the ambient-pressure dataset were assigned to the rhombohedral space group *R*-3. The asymmetric unit is shown below in figure 7.2.

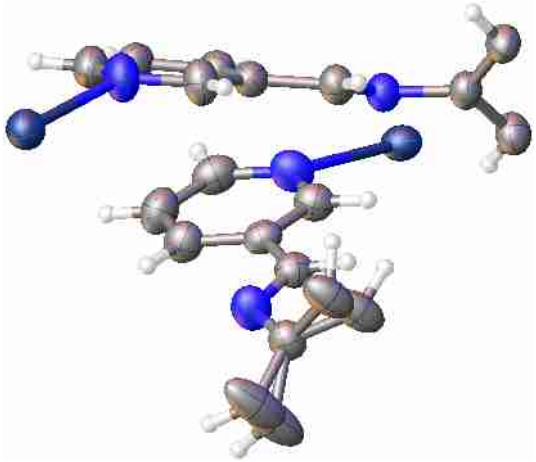

Figure 7.2 Asymmetric unit showing the 3-dimensional structure (top) and 2-dimensional sheets (bottom). The nitrate counter ions have been removed from the image to aid clarity.

Due to a limited data-to-parameter ratio, the RIGU restraint was applied to all atoms. As shown above, a phenyl ring is disordered across two positions. All atoms in the two positions of this phenyl ring were constrained to have the same anisotropic displacement parameters as the corresponding atom in the other disordered position through use of the EADP constraint. All bonds in the two rings were restrained to have similar bond lengths through use of the SADI restraint.

A diagram to show how the 3-dimensional networks interweave through the 2-dimensional layers and a schematic representing the crystal packing are shown below in figures 7.3 and 7.4.

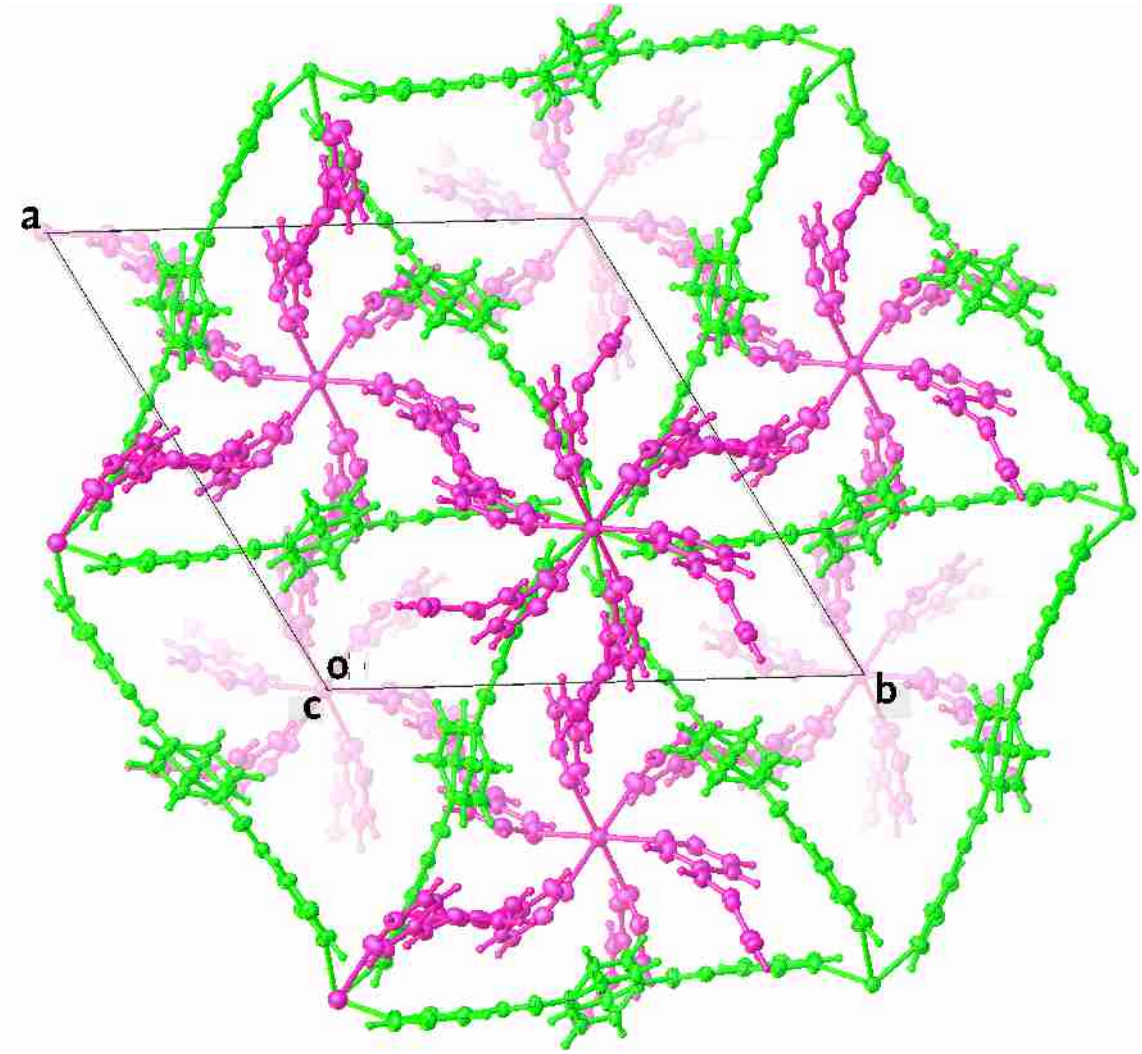

Figure 7.3 Packing diagram showing the 3-dimensional networks (pink) interweaving through the 2-dimensional sheets (green)

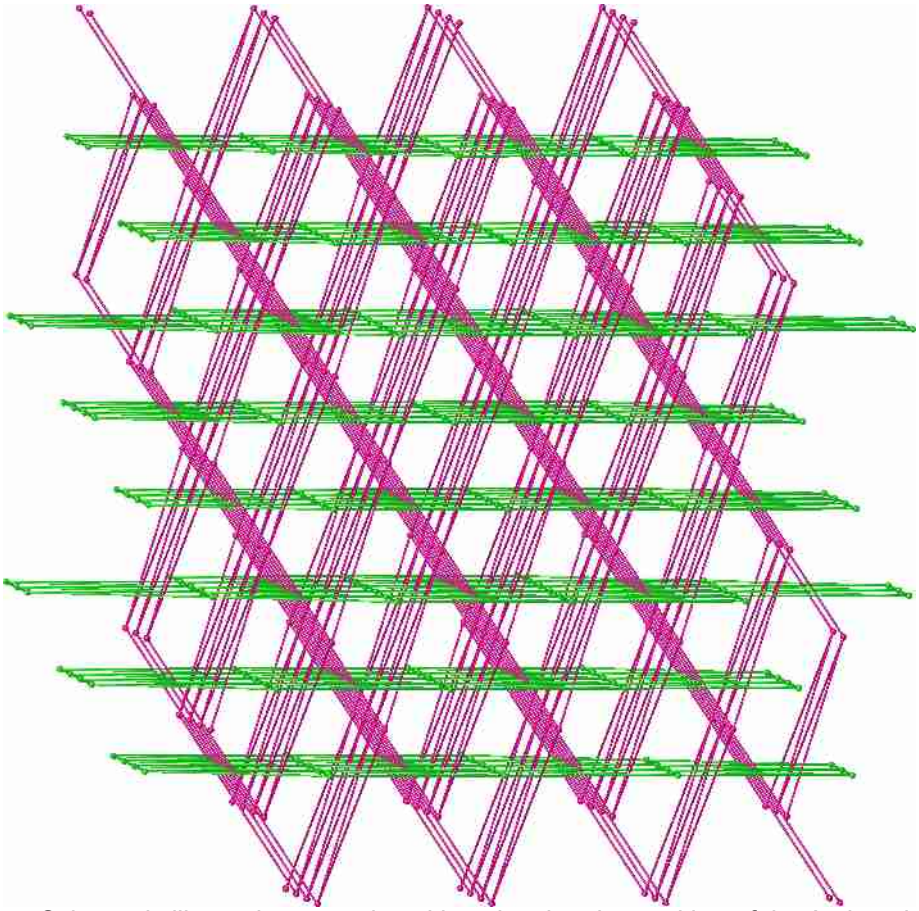

Figure 7.4 Schematic illustrating crystal packing showing the position of the Ag ions in the 3-dimensional (pink) networks and the 2-dimensional sheets (green). Reproduced with permission © Glenn Lamming.

The packing efficiency at ambient-pressure is 71.57 %. Calculations made in PLATON[250] found that there are no solvent accessible voids in the crystal structure. The void spaces at a given distance from the occupied areas of the crystal structure calculated in Olex2[37] are shown in table 7.1 below.

Distance From Surface / Å	**Volume / Å^3**
0	1942.612
0.2	1383.990
0.4	505.917
0.6	88.614
0.8	2.919

Table 7.1 Table showing volume of void space at or greater than a given distance from the surface of occupied space in the crystal structure (structure occupies 4889.80 Å^3).

When the crystal was compressed in paraffin oil, a phase-transition was found to occur between 11.6 (5) and 14.5 (5) kbar, with a decrease in symmetry from *R*-3 to *P*-1.[i]

When a 1 : 1 mixture of pentane and isopentane as a pressure transmitting medium it was found that when the pressure was increased, the rhombohedral symmetry was not lost, even at pressures above 30 kbar.

Figure 7.5 below shows the change in the length of the reduced unit cell axes with increasing pressure.

iThe unit cell dimensions at 11.6 (5) kbar were a, b= 17.811 (3)**; c= 23.285 (5) Å; α, β= 90; γ= 120°.**

The unit cell dimensions at 14.5 (5) kbar were a= 12.636 (3); b= 12.8361 (18); c=12.837 (2) Å; α= 87.392 (10); β= 87.233 (10); γ= 87.255 (11)°.

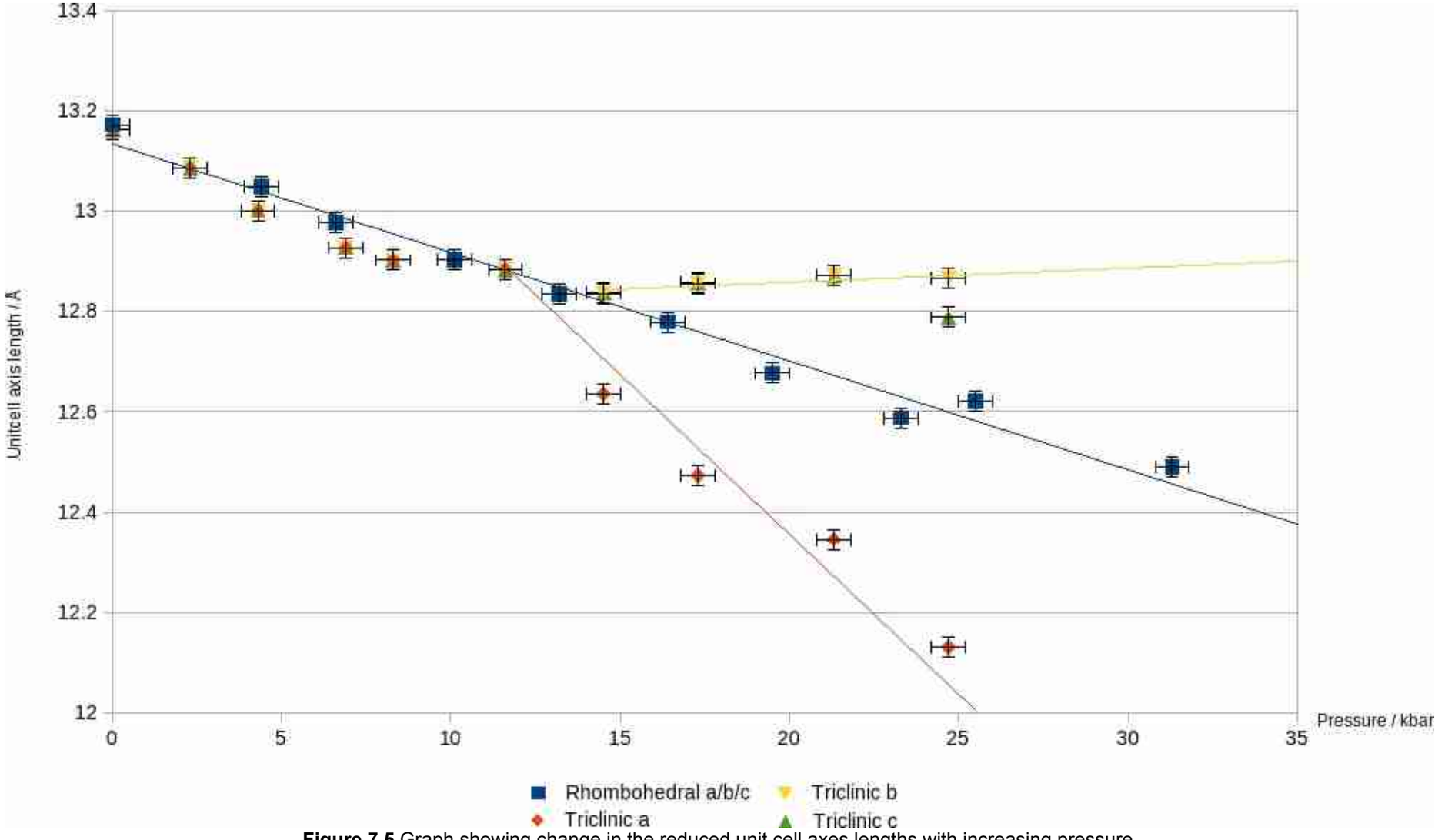

Figure 7.5 Graph showing change in the reduced unit cell axes lengths with increasing pressure

When a 1 : 1 mixture of pentane and isopentane is used as the pressure transmitting medium the length of the reduced unit cell axes decrease linearly with increasing pressure. When paraffin oil is used as the pressure transmitting medium the unit cell axes decrease linearly at a similar rate until a phase transition occurs between 11.6 (5) and 14.5 (5) kbar. Above 14.5 (5) kbar the *a* axis was found to decrease at a much greater rate than below 14.5 (5) kbar with increasing pressure. In contrast, the *b* and *c* axes both increased in length slightly from 14.5 (5) to 21.3 (5) kbar. From 21.3 (5) to 24.7 (5) kbar the *c* axis compressed significantly whereas the *b* axis did not.

Figure 7.6 below shows the change in the unit cell volume with increasing pressure.

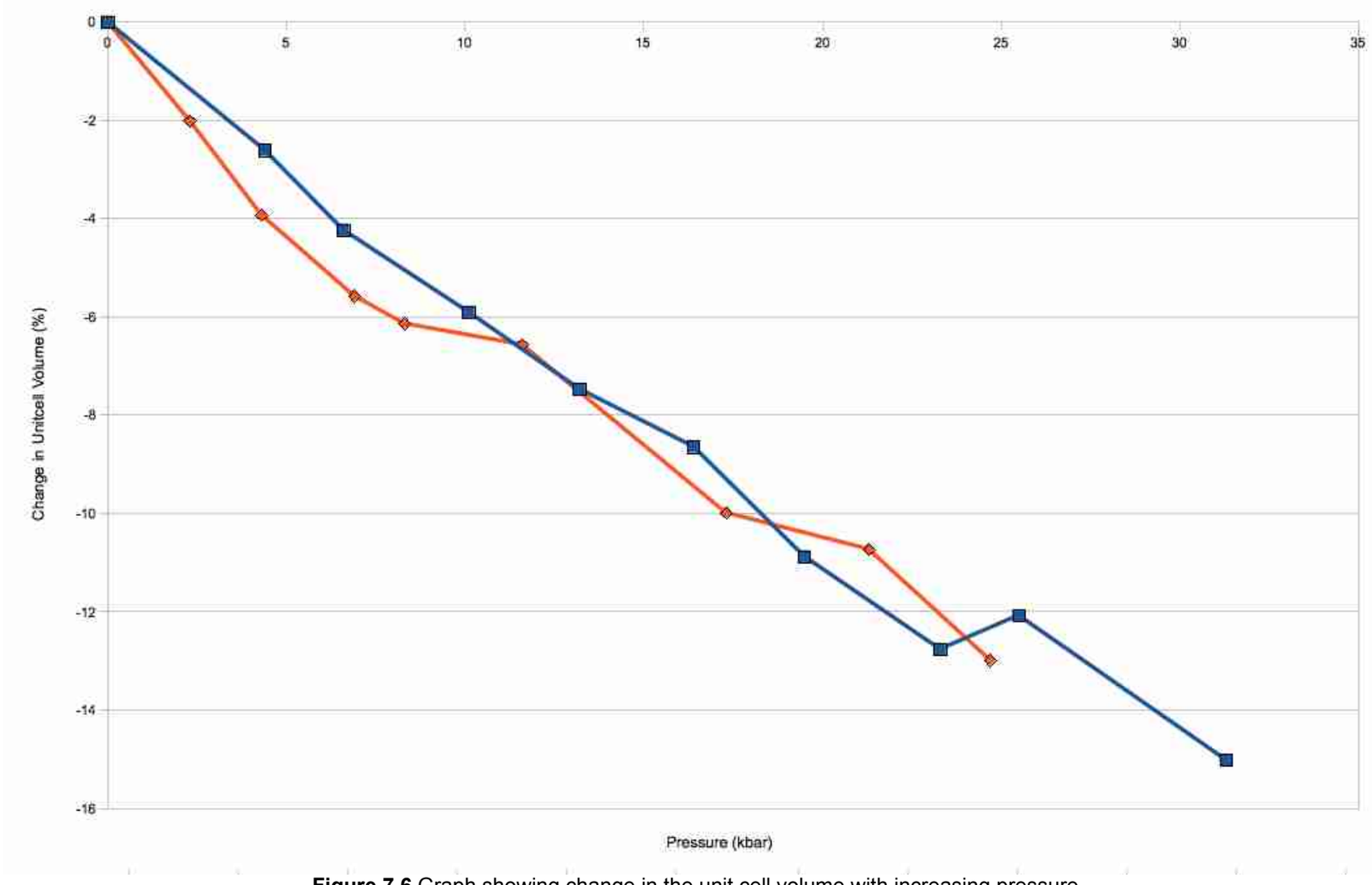

Figure 7.6 Graph showing change in the unit cell volume with increasing pressure

There is clearly no significant difference in the unit cell volumes of the two samples at any pressure. Figure 7.7 below shows the change in the angles of the reduced unit cell with increasing pressure

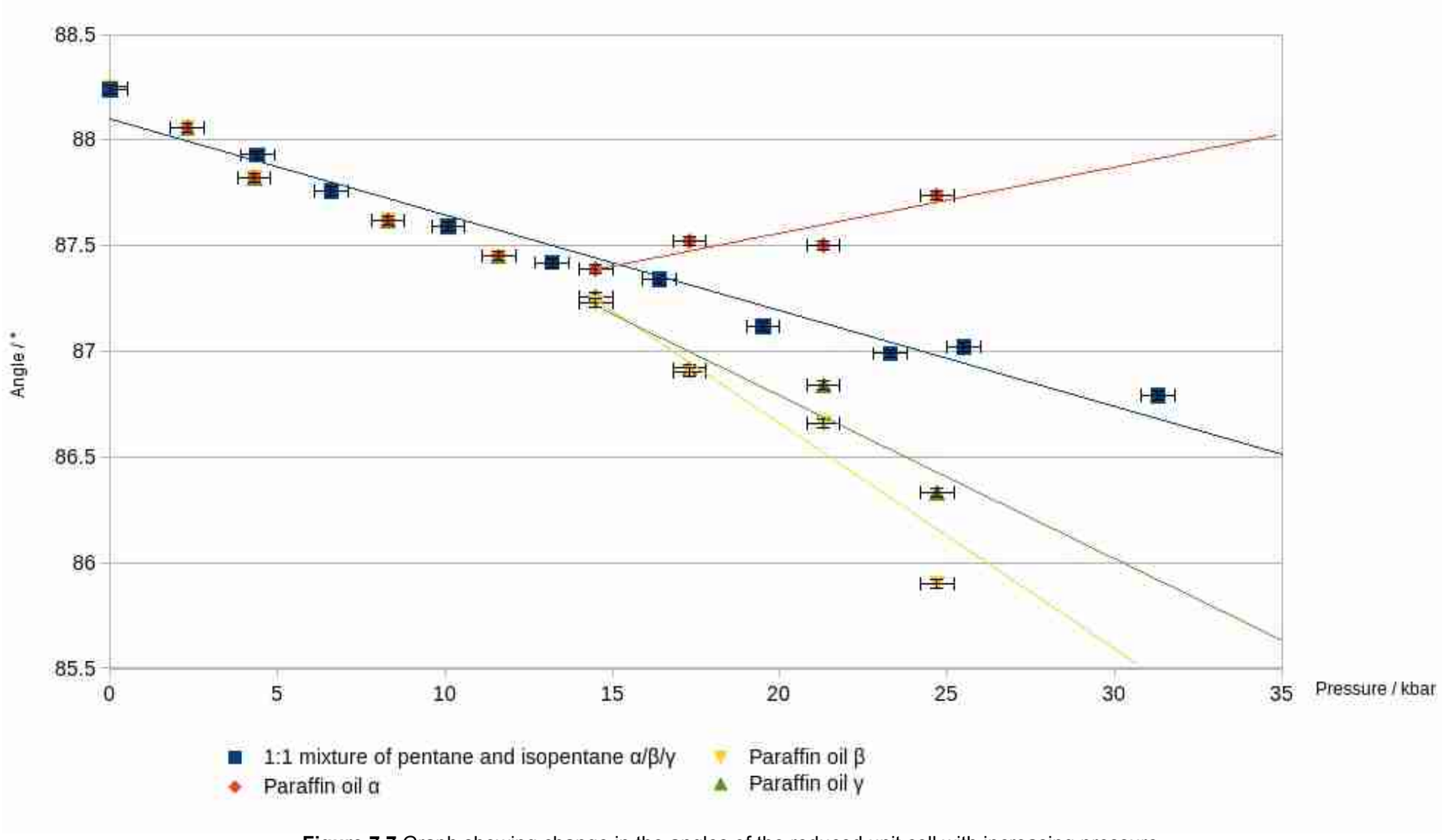

Figure 7.7 Graph showing change in the angles of the reduced unit cell with increasing pressure

When a 1 : 1 mixture of pentane and isopentane is used as the pressure transmitting medium, the reduced unit cell angles decrease linearly with increasing pressure. When paraffin oil is used as the pressure transmitting medium, the reduced unit cell angles decrease linearly at a similar rate until a phase transition occurs between 11.6 (5) and 14.5 (5) kbar. Above 14.5 (5) kbar α increases with increasing pressure, while β and γ both decrease with increasing pressure at a greater rate than below 14.5 (5) kbar.

The disorder in the orientation of an aromatic ring in the 2-dimensional sheets (shown above in figures 7.2 and 7.3) is eliminated with increasing pressure in both pressure transmitting media. When a 1 : 1 mixture of pentane and isopentane is used as the pressure transmitting phase (rhombohedral phase) the disorder is eliminated between 23.3 (5) and 25.5 (5) kbar, shown in figure 7.8 below. When paraffin oil is used, the disorder is eliminated following the phase transition from a rhombohedral to triclinic setting between 11.6 (5) and 14.5 (5) kbar, shown in figure 7.9 below.

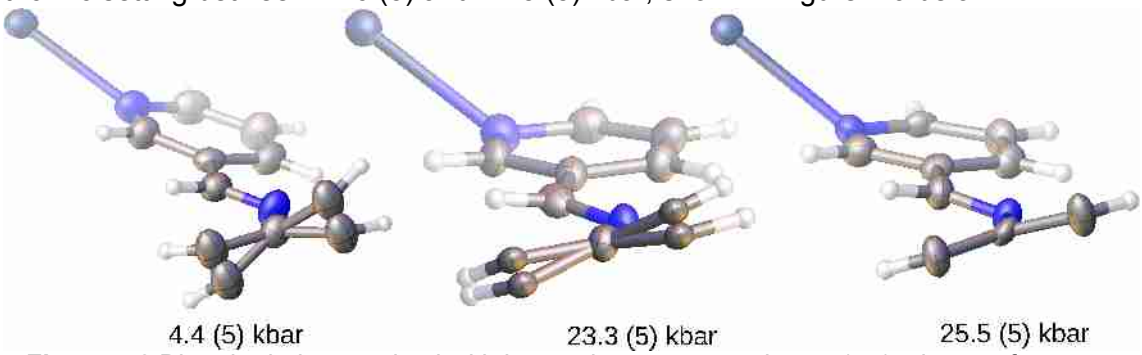

Figure 7.8 Disorder being resolved with increasing pressure when a 1 : 1 mixture of pentane and isopentane is used as the pressure transmitting medium.

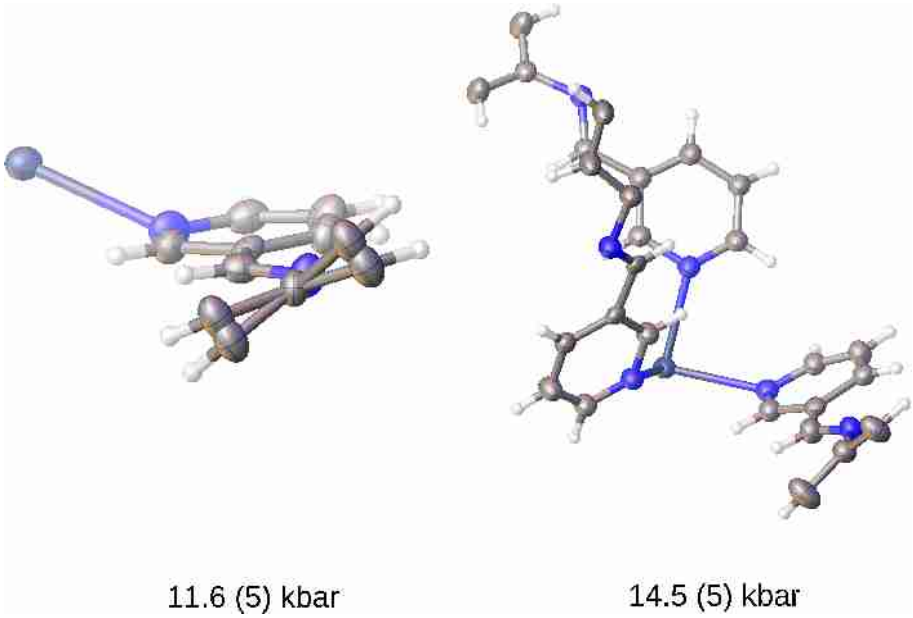

Figure 7.9 Disorder being resolved with increasing pressure when paraffin oil is used as the pressure transmitting medium.

The silver-nitrogen bond lengths and angles in the ambient structure, the structure at 23.3 (5) kbar in a 1 : 1 mixture of pentane and isopentane and the structure at 24.7 (5) kbar in paraffin oil are shown below in table 7.2.

		Ambient	**23.3 (5) kbar Pentane/Isopentane**	**24.7 (5) kbar Paraffin Oil**
2-d framework	Ag-N bond length / Å	2.574 (2)	2.475 (4)	2.59 (2)
				2.51 (2)
				2.37 (2)
	N-Ag-N bond angle / °	91.78 (7)	93.79 (16)	97.5 (8)
				95.7 (6)
				90.2 (6)
3-d framework	Ag-N bond length / Å	2.548 (2)	2.477 (4)	2.49 (3)
				2.47 (3)
				2.43 (2)
	N-Ag-N bond angle / °	96.89 (7)	98.03 (14)	99.2 (7)
				98.8 (6)
				95.0 (8)

Table 7.2 Table showing Ag-N bond lengths and N-Ag-N bond angles in the ambient structure, the structure at 23.3 (5) kbar in a 1 : 1 mixture of pentane and isopentane and the structure at 24.7 (5) kbar in paraffin oil

In the ambient structure, the Ag-N bond lengths were found to be of similar length in the 2-dimensional and 3-dimensional frameworks. However, the N-Ag-N bond angle in the 3-dimensional frameworks is more distorted from 90° [96.89 (7)°] than that in the 2-dimensional framework [91.78 (7)°].

The application of pressure to the crystal using a pentane : isopentane pressure transmitting medium causes the Ag-N bond lengths in the 2 and 3-dimensional frameworks to compress by approximately the same magnitude. The N-Ag-N bond angles were slightly further from 90° than at ambient conditions in both frameworks.

When paraffin oil was used as the pressure transmitting medium the reduction in symmetry from *R*-3 to *P*-1 resulted in there being three times as many independent Ag-N bond lengths and N-Ag-N bond angles. The three Ag-N bond lengths in the 2-dimensional framework at high-pressure in paraffin oil were found to be of a very different length to one another. One of the symmetrically independent bonds was found

to be within error of the Ag-N bond length at ambient conditions, one was slightly compressed relative to the ambient Ag-N bond length and the third was compressed by over 0.2 Å. All three Ag-N bond lengths in the 3-dimensional frameworks at high-pressure in paraffin oil are significantly lower than the Ag-N bond length at ambient conditions.

The N-Ag-N bond angles in the 2-dimensional framework at high-pressure in paraffin oil differed considerably, with one of the three angles being closer to 90° than the bond angle under ambient conditions, one being approximately 4° further from 90° and the final one being approximately 6° further from 90° than the ambient pressure bond angle. The N-Ag-N bond angles in the 3-dimensional frameworks were found to be less distorted from the bond angles seen at ambient conditions than those in the 2-dimensional framework.

It is clear from the bond angles and lengths discussed above that the structural response of the 2-dimensional framework to the application of pressure is greater than that of the 3-dimensional frameworks.

An overlay of the 2-dimensional framework at ambient conditions and at high-pressure is shown below in figures 7.10 and 7.11.

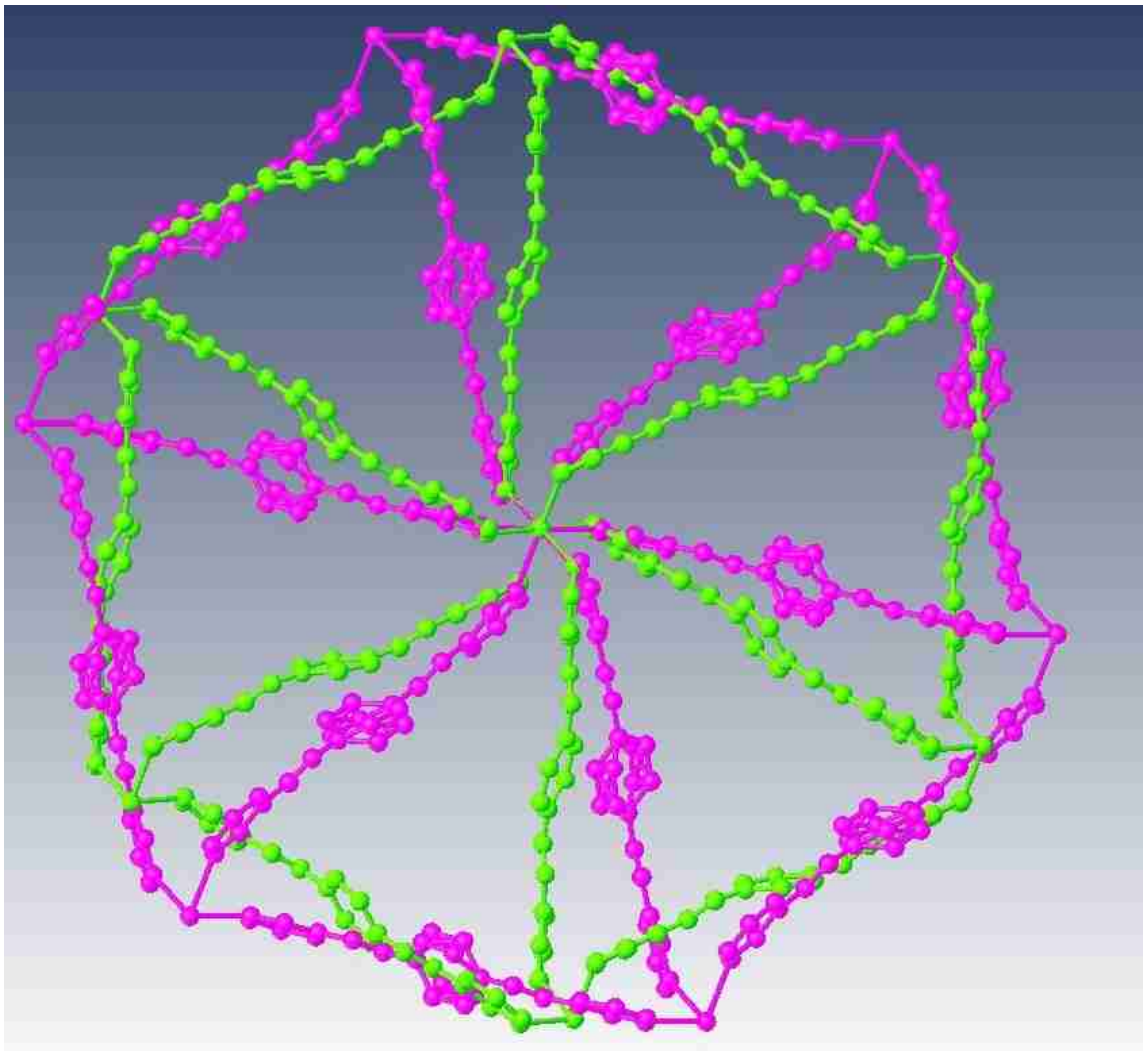

Figure 7.10 Overlay of the MOF structure at ambient conditions [**Pink**] with the structure at 23.3 (5) kbar in a 1 : 1 mixture of pentane and isopentane [**Green**] viewed down the 111 axis. The overlay has been generated by positioning the central Ag ions and co-ordinating nitrogen atoms to be in the same position.

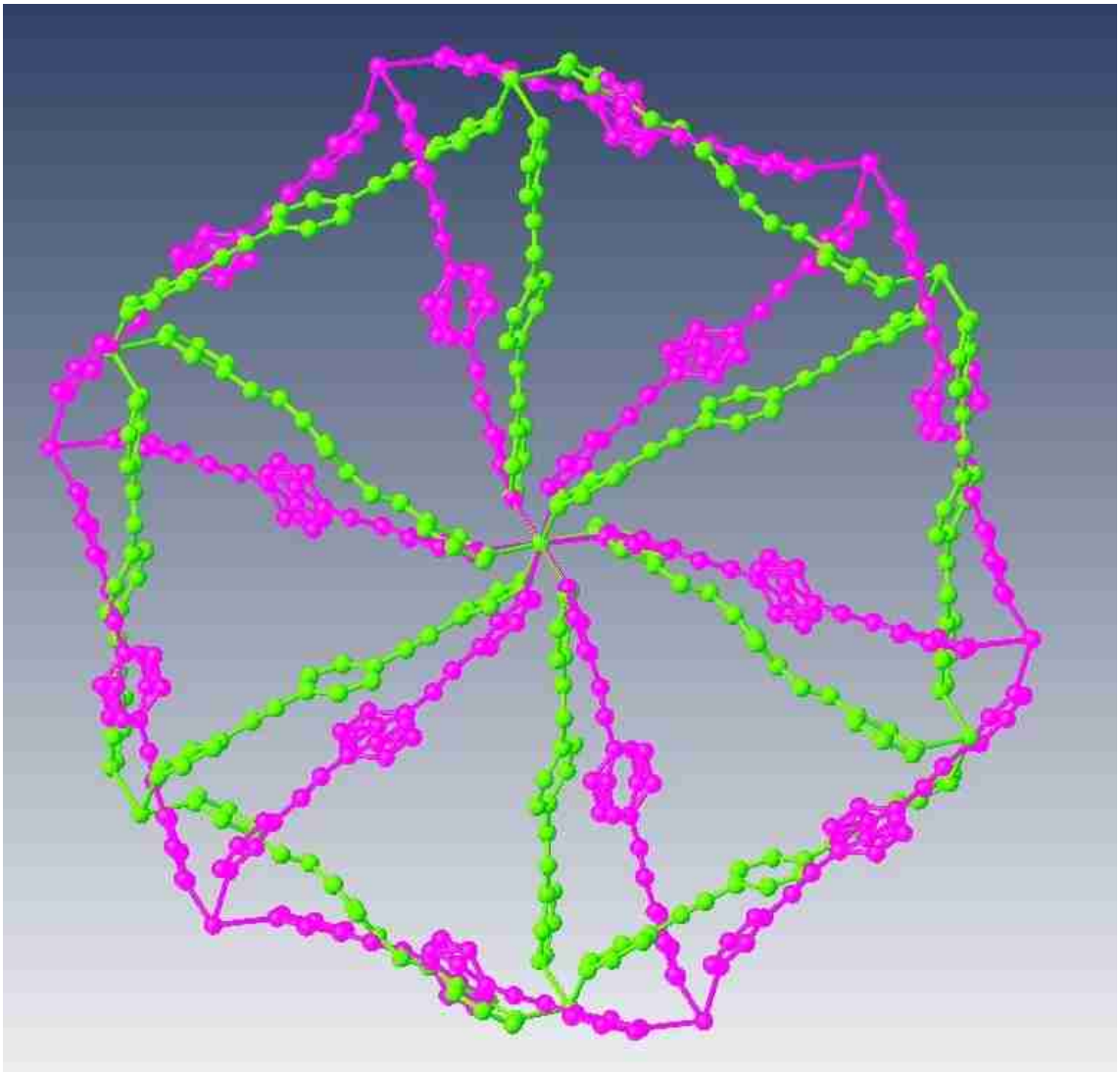

Figure 7.11 Overlay of the MOF structure at ambient conditions [**Pink**] with the structure at 24.7 (5) kbar in paraffin oil [**Green**] viewed down the 111 axis. The overlay has been generated by positioning the central Ag ions and co-ordinating nitrogen atoms to be in the same position.

Figures 7.9 and 7.10 show that when pressure is applied to the MOF the wheel-like structure of the 2-dimensional framework rotates and contracts, with the ligands approaching the Ag ion from a very different orientation under ambient and high-pressure conditions.

An overlay of the structure of the 2-dimensional framework at high-pressure in paraffin oil and in a 1 : 1 mixture of pentane and isopentane is shown below in figure 7.12.

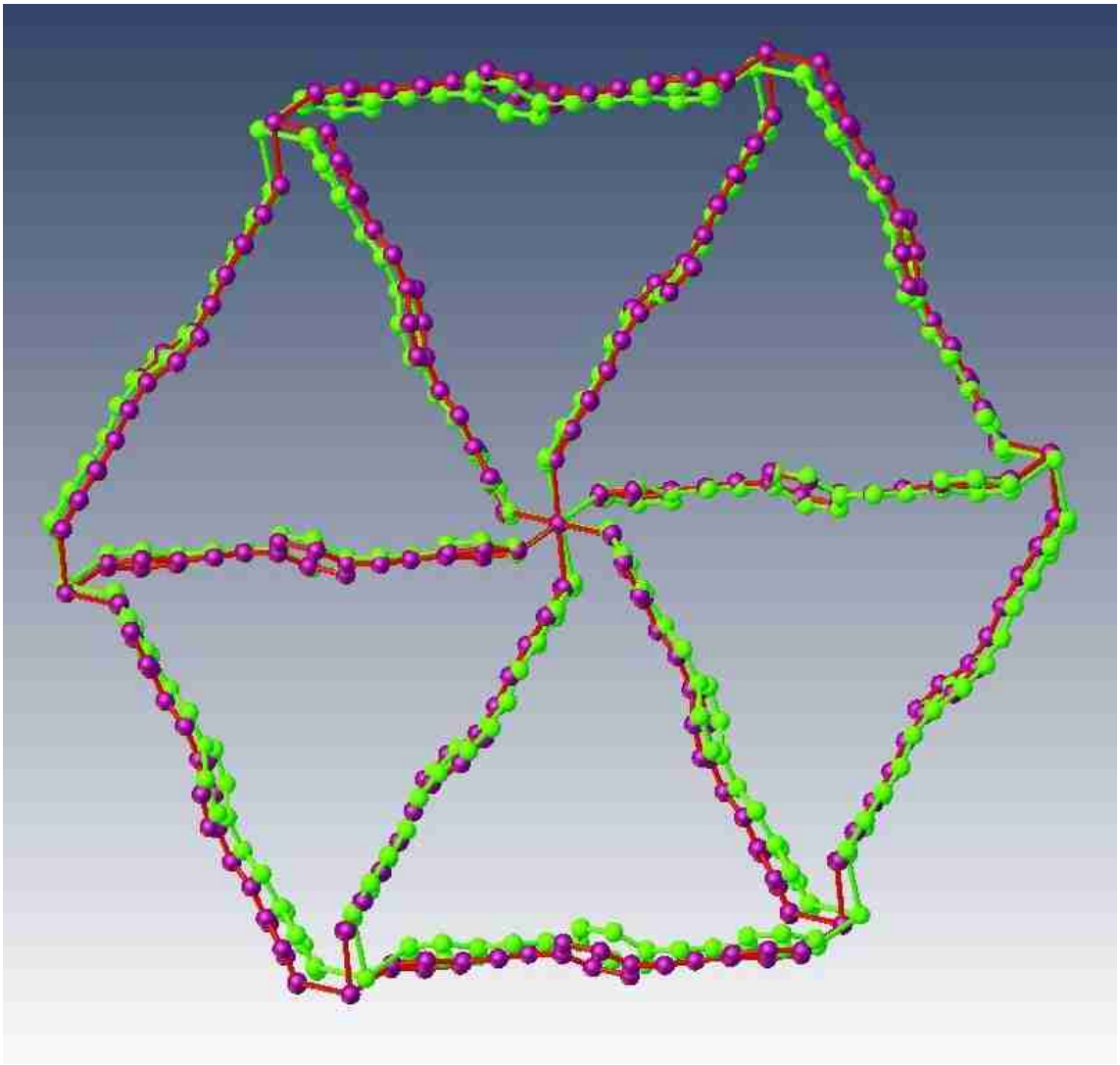

Figure 7.12 Overlay of the MOF structure at 24.7 (5) kbar in paraffin oil [**Purple**] with the structure at 23.3 (5) kbar in a 1 : 1 mixture of pentane and isopentane [**Green**] viewed down the 111 axis. The overlay has been generated by positioning the central Ag ions and co-ordinating nitrogen atoms to be in the same position.

It is apparent from figure 7.12 that the rhombohedral and triclinic high-pressure forms have a very similar structure, with only a slight distortion in the Ag "wheel". The "wheel" in the triclinic phase is slightly elongated along the (-*x*, -*y*, 0.5-*z*) vector (bottom left to top right in figure 7.12) and slightly compressed along the (*x*, *y*, *z*+0.5) vector (bottom right to top left in figure 7.12).

7.4 Conclusions

In this chapter, we have described the differing response of a Ag (I) based MOF to pressure in paraffin oil and a 1 : 1 mixture of pentane and isopentane. When paraffin oil was used to apply pressure to the MOF, there was a considerable distortion from rhombohedral to triclinic symmetry between 11.6 (5) and 14.5 (5) kbar, with the length and angles of the reduced unit cell axes diverging considerably from one-another at pressures above the phase transition. However, in a 1 : 1 mixture of pentane and isopentane rhombohedral symmetry was found to be preserved until the crystal breaks at approximately 40 kbar. The disorder in the 2-dimensional sheets observed at ambient conditions is slowly eliminated by increasing the pressure to 25.5 (5) kbar in the rhombohedral phase in the pentane/isopentane mixture, but instantaneously eliminated on the phase transformation to the triclinic phase at pressures in paraffin oil. The Ag-N bond lengths (constrained by symmetry to be the same in a rhombohedral setting) diverge considerably following the phase change in paraffin oil, particularly in the 2-dimensional framework.

To the best of our knowledge, this is only the second report where a single crystal has exhibited significantly different behaviour under the application of pressure in two different pressure transmitting media. Moggach *et al* previously noted that the transformation of L-cysteine I to L-cysteine III occurs at different pressures in a 4:1 mixture of MeOH and EtOH and a 1:1 mixture of pentane and isopentane.[251] This phenomena has also been reported in a powder sample - Boldyreva *et al* previously observed that $[Co(NH_3)_5NO_2]I_2$ powder undergoes a phase transition from polymorph I (*Pnma*) to II (*C*2/*m*) in an ethanol-methanol-water mixture between 0.45 and 0.65 GPa but no phase transition was observed at pressures up to 1.8 GPa in poly(chlor-trifluor-ethylen)-oil.[74] As single crystal samples often behave rather differently from powders on the application of pressure,[73] the observation of this phenomena occurring in a single crystal sample is significant.

One possible cause of unusual behaviour on the application of pressure to a MOF is due to solvent accessing pore spaces in the crystal. For example, Moggach *et al* found that increasing the pressure applied to ZIF-8 ($Zn(MeIM)_2$, MeIM = 2-methylimidazolate) from ambient conditions to 0.18 GPa resulted in an increase in the unit cell volume from 4900.5 (8) to 4999.6 (2) $Å^3$.[252] However, in this case it was clear that there was no pore large enough for solvent to enter. As such, the choice of

pressure transmitting medium must influence the phase transition through edge effects, with the phase transition then propagating through the crystal. Why this occurs is difficult to rationalise, but is nonetheless an interesting and unique discovery.

Chapter 8: Thesis Summary

Herein we have investigated the effect of high-pressure on the solid-state and the crystallisation process in several systems. The initial focus of the investigation was centred on the high-pressure crystallisation of weakly interacting compounds. We hypothesised that these molecules would be able to pack very efficiently in order to minimise the *PV* term in the free energy equation $\Delta G = \Delta H - T\Delta S + P\Delta V$. This is due to the lack of strong directing interactions between molecules limiting the arrays of possible orientation between molecules. Therefore, we proposed that molecules that do not possess any potential for strong intermolecular hydrogen-bonding may be more prone to low-temperature/high-pressure polymorphism.

The structures of cryo- and high-pressure crystallised fluoro-aromatics compounds are discussed in Chapter 2. We found that all three monofluorotoluenes have polymorphs that are only observed at high-pressure. Most notably, polymorph II of 2-fluorotoluene was only accessible through high-pressure crystallisation of a 1 : 1 mixture of 2-fluorotoluene and 3-fluorotoluene. This is the first report of the formation of more than one polymorph of a compound that is a liquid at ambient conditions through the isothermal application of pressure to the liquid in question.

We also studied a range of fluorobenzenes that had previously been cryo-crystallised by Thalladi *et al* through high-pressure crystallisation.[160] This group of compounds behaved very differently to the fluorotoluenes, with only one of the nine (4-fluoroiodobenzene) having a different polymorph formed through high-pressure crystallisation. The structure of the high-pressure polymorph of 4-fluoroiodobenzene was found to be very different from its low-temperature counterpart, with totally distinct supramolecular synthons in the two structures. The low-temperature polymorph contains type II I···I interhalogen interactions and C-F···H-C hydrogen bonds, with the high-pressure phase containing type I I···F halogen bonds.

It had previously been shown that structures with weaker intermolecular interactions may be adopted at high-pressure if these structures allows the molecules to pack more efficiently.[168] Given this, it was somewhat surprising to see C-F···H-C hydrogen bonds of lengths similar to or lower than the combined Van der Waal's radii present in all but one of the high-pressure structures studied in Chapter 3. However,

this is still a small dataset, and more fluorohydrocarbons (particularly aliphatic systems) need to be studied.

It had previously been hypothesised that kinetic factors such as the rate of compression or the presence of impurities (which may hinder nucleation) may cause polymorphism at high-pressure.[77] We therefore set about demonstrating the importance of the rate of compression. The crystallisation of 2-fluorophenylacetylene was studied at varying rates of compression. This compound was selected for investigation because it forms two distinct polymorphs form under different rates of cooling. Polymorph I forms through rapid cooling (quenching of the hot liquid in liquid N_2), polymorph II through slower cooling rates. The two polymorphs observed through cryo-crystallisation by Dikundwar *et al*[159] were both crystallised through the application of pressure. Polymorph I was formed under rapid compression and polymorph II under slow compression – analogous to the behaviour seen at low-temperature. Additionally, a new third polymorph not seen through cryo-crystallisation was formed through rapid compression. There are three potential supramolecular synthons in 2-fluorophenylacetylene, namely C-F···H-C hydrogen bonds, C-F···π interactions and π···π stacking forces. However, these interactions are not all present in each of the polymorphs. For example, π···π stacking forces are observed in polymorphs I and III but not in polymorph II. This indicates that the weak intermolecular interactions are in competition with one-another, allowing very different structures to have similar lattice energies. It is rather interesting that phenylacetylene and 2-fluorophenylacetylene both have three polymorphs; one that may be obtained through slow cooling, one through rapid cooling and one through high-pressure crystallisation. 3-fluorophenylacetylene also has two polymorphs accessible through cryo-crystallisation. Given that it is rather rare to observe multiple polymorphs of a compound that is liquid at ambient conditions at the same thermodynamic conditions, this family seems rather polymorphically rich.

The formation of low-melting molecular complexes from liquid mixtures was investigated in Chapter 5. It was believed that the requirement for close-packing at high-pressure might result in the formation of different ratios of co-crystal at high-pressure. Although this phenomenon was not observed, several liquid mixtures that were found to form molecular complexes through cryo-crystallisation form a single-component crystal under pressure. The first examples of low-temperature/high-pressure polymorphism in a low-melting molecular complex have also been reported herein. Both pyridine 1 : 2 butanoic acid and pyridine 2 : 1 suberic acid form different

polymorphs at low-temperature and high-pressure. In pyridine 1 : 2 butanoic acid the two polymorphs differ in the way trimers are packed. A layered structure is adopted at low-temperature, while at high-pressure the molecules pack in a herringbone motif. The suberic acid molecule in the cryo-crystallised polymorph of pyridine 2 : 1 suberic acid has a bent chain, while there are two acid molecules in the asymmetric unit in the high-pressure structure, one with a straight chain and the other with a bent chain.

We prepared a series of liquid mixtures of ratio pyridine 2 : 1 di-carboxylic acid. A wide range of different ratio of crystals were formed on crystallisation of this mixture, as shown in table 5.10. It was found that C5 dicarboxylic acid did not form a complex with pyridine, despite all other di-carboxylic acids doing so. The structure of the C4 complex is perhaps useful in explaining this behaviour. In this structure, one of the two pyridine molecules is only weakly bonded to the rest of the structure and is disordered across two positions. O-H···O hydrogen bonds are thus formed at the expense of O-H···N hydrogen bonds (which are typically stronger due to N being more basic than O) in this structure. On this basis, we speculated that the failure of C4 dicarboxylic acid and pyridine to form a complex can be explained on the basis of there being difficulties in packing pyridine molecules with acid molecules of this size.

In chapter 6, we described the structures of cryo- and high-pressure crystallised solvent molecules. Isopropyl alcohol forms two different polymorphs at low-temperature and high-pressure, with the packing of molecules being very different in the two polymorphs. The high-pressure polymorph has isolated eight-membered rings of molecules linked by hydrogen bonding. The low-temperature polymorph has infinite chains down the *a* axis. The high-pressure polymorph of acetic anhydride has a layered structure, with the low-temperature polymorph forming a herringbone motif. The molecule was far more planar in the high-pressure polymorph than both the low-temperature form and the relaxed geometry in the gas phase (a distortion of 9° rather than 27-30° from planarity). Increasing the pressure further results in the molecule becoming increasingly planar.

The structural response of a Ag (I) MOF was studied at various high-pressures in two pressure transmitting media, paraffin oil and a 1 : 1 mixture of pentane and isopentane. In paraffin oil, there was found to be a distortion from *R*-3 to *P*-1 between 11.6 (5) and 14.5 (5) kbar. However, in the pentane/isopentane mixture, the *R*-3 symmetry was preserved until the crystal broke through the excessive application of

pressure at approximately 40 kbar. Following the phase transition from rhombohedral to triclinic symmetry in paraffin oil, the Ag-N bond lengths and angles were found to diverge considerably. There are no prior reports of phase transitions under the application of pressure that are dependant on the choice of pressure-transmitting medium occurring in a single-crystal sample. Furthermore, it is clear that this behaviour cannot be attributed to the solvent accessing the pores of the MOF, as there are no solvent accessible voids present in the crystal structure.

There are several variables that can affect high-pressure crystallisation and variable-pressure diffraction experiments. Clearly, thermodynamics drives the formation of densely packed structures at high-pressure, with pressure even being able to drive the molecular geometry towards the local energy maxima in order to pack efficiently. However, we have shown that kinetics is clearly important. Altering the purity and rate of compression applied to the liquid as well as the choice of pressure transmitting medium used have all resulted in the formation of different structures.

A Appendices

A.1 Additional Crystal Structures

A.1.1 N,N-Dimethyl Formamide (High Pressure)

High-pressure crystallisation resulted in the generation of the same (*Z*'=2) polymorph that was observed through cryo-crystallisation.[253] Figure A.1 shows this structure refined with the high-pressure data.

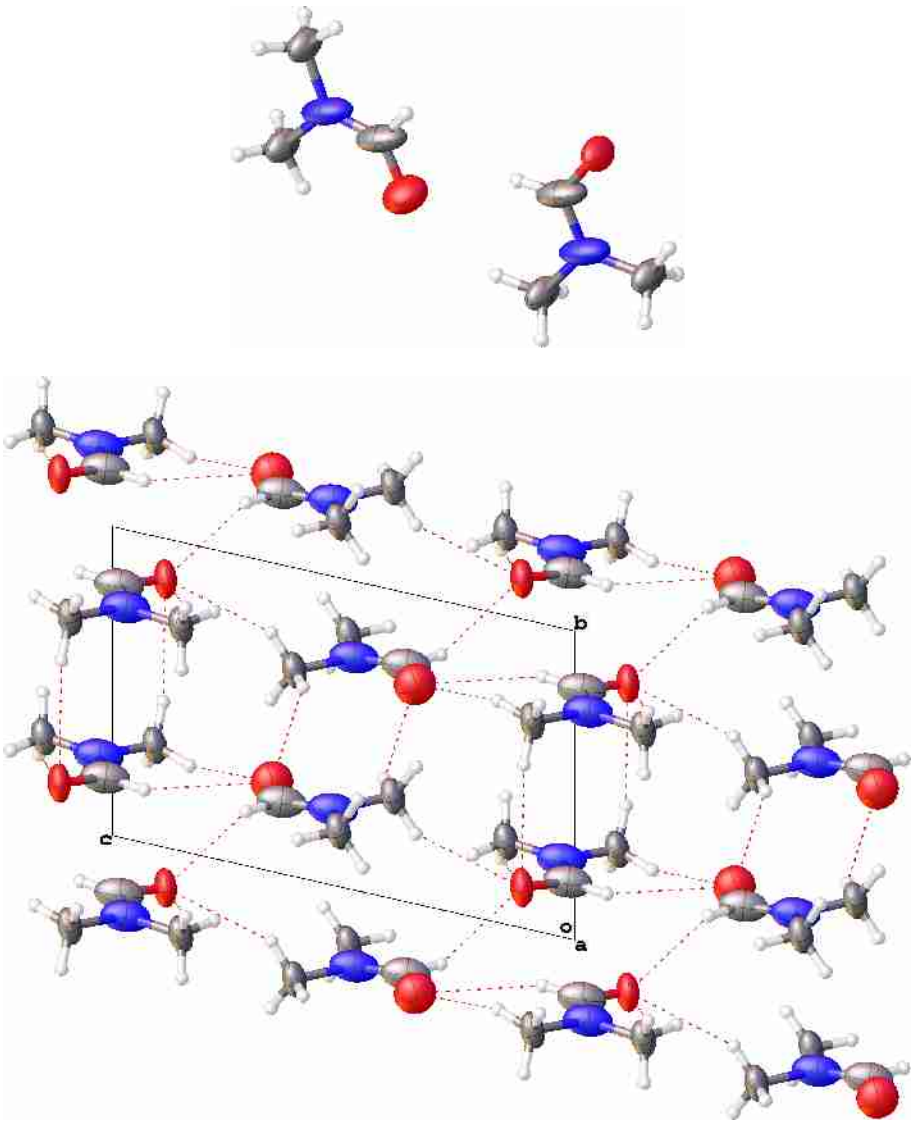

Figure A.1 (Top) Asymmetric Unit **(Bottom)**Packing diagram of N,N-Dimethyl Formamide at high-pressure

Table A.1 shows the crystallographic data from this data collection.

Compound	Dimethylformamide (HP)
empirical formula	C_3H_7NO
formula weight	73.09
T/K	ambient
P/kbar	3.2 (2) kbar
crystal system	triclinic
space group	*P-1*
a (Å)	5.904 (5)
b (Å)	6.928 (6)
c (Å)	10.275 (14)
α (°)	77.23 (4)
β (°)	88.15 (4)
γ (°)	75.13 (4)
Z	4
V/Å^3	396.0 (7)
D_{calc}/g cm^{-3}	1.226
μ/mm^{-1}	0.057
unique reflns	819
observed reflns	229
θ_{max}	16.280
completeness/%	28.0
R1 [I > 2σ]	0.0579
*w*R2 [all]	0.1685
goodness-of-fit	1.083

Table A.1 Crystallographic Data from the high-pressure crystallised N,N-Dimethylformamide

A.1.2 4-Fluorophenylacetylene (High Pressure)

Figure A.2 shows the structure of 4-fluorophenylacetylene at high-pressure data.

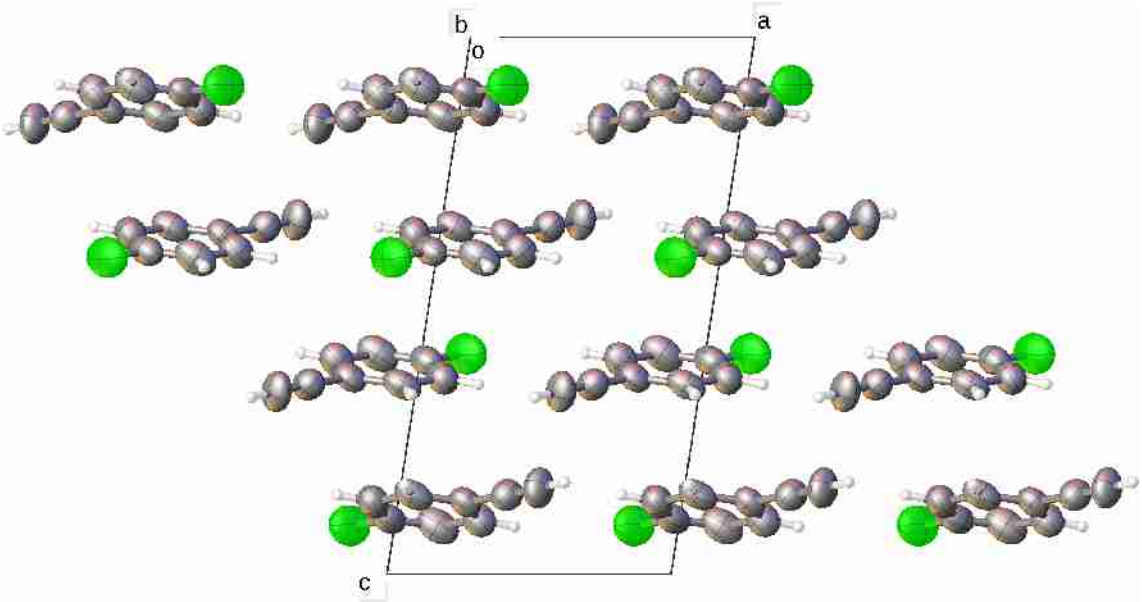

Figure A.2 Packing diagram of 4-fluorophenylacetylene at high-pressure.

Table A.2 shows the crystallographic data from this data collection.

Compound	**4-Fluorophenylacetylene (HP)**
empirical formula	C_8H_5F
formula weight	120.12
T/K	ambient
P/kbar	0.6 (2)
crystal system	monoclinic
space group	$P2_1/c$
a (Å)	7.122 (5)
b (Å)	6.675 (3)
c (Å)	13.624 (7)
β (°)	98.85 (3)
Z	4
V/Å^3	639.9 (7)
D_{calc}/g cm^{-3}	1.247
μ/mm^{-1}	0.056
unique reflns	780
observed reflns	332
θ_{max}	17.155
completeness/%	42.6
R_1 [I > 2σ]	0.0421
wR_2 [all]	0.0999
goodness-of-fit	1.240

Table A.2 Crystallographic Data from the high-pressure crystallised 4-fluorophenylacetylene.

A.1.3 2-Methylfuran

Figure A.3 shows the structure of the cryo-crystallised polymorph and figure A.4 shows that of the high-pressure crystallised polymorph.

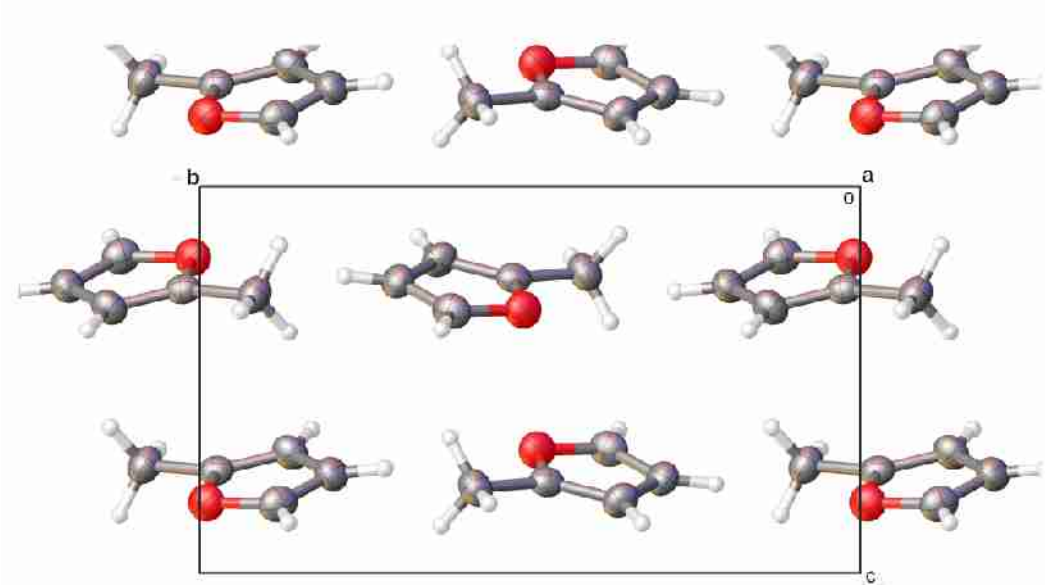

Figure A.3 Packing diagram of cryo-crystallised 2-methylfuran.

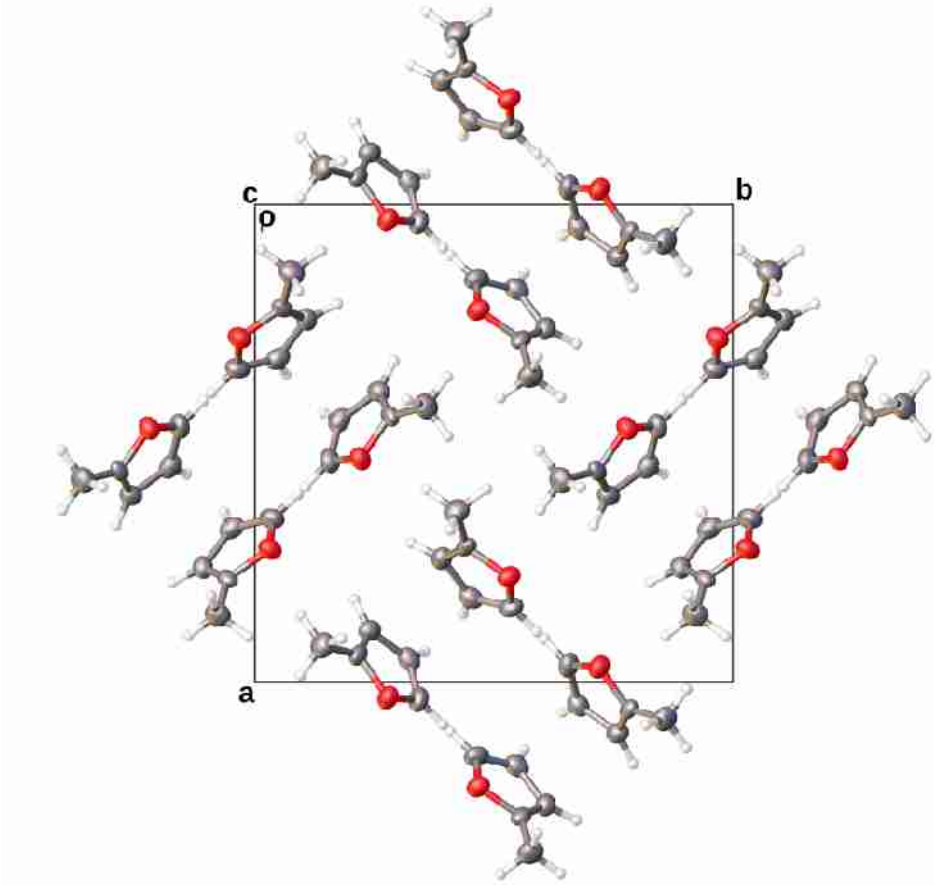

Figure A.4 Packing diagram of high-pressure crystallised 2-methylfuran.

Table A.3 shows the crystallographic data from this data collection.

Compound	**2-Methylfuran (LT)**	**2-Methylfuran (HP)**
empirical formula	C_8OH_6	
formula weight	82.10	
T/K	180 (2)	ambient
P/kbar	ambient	10.2 (2)
crystal system	tetragonal	monoclinic
space group	$P4_2bc$	$P2_1/n$
a (Å)	12.501 (6)	5.4921 (15)
b (Å)	12.501 (6)	11.381 (4)
c (Å)	6.096 (2)	7.113 (2)
β (°)	90	110.049 (8)
Z	8	4
V/Å^3	952.7 (10)	417.7 (2)
D_{calc}/g cm^{-3}	1.145	1.306
μ/mm^{-1}	0.079	0.057
unique reflns	689	694
observed reflns	675	378
θ_{max}	23.261	19.003
completeness/%	98.0	54.5
R_1 [I > 2σ]	0.0431	0.0286
wR_2 [all]	0.0882	0.0788
goodness-of-fit	1.017	1.111

Table A.3 Crystallographic Data from cryo- and high-pressure crystallised 2-methylfuran.

A.1.4 O-Xylene

O-Xylene was found to give the same polymorph from cryo-crystallisation and high-pressure crystallisation. Figure A.5 shows the packing arrangement of o-xylene.

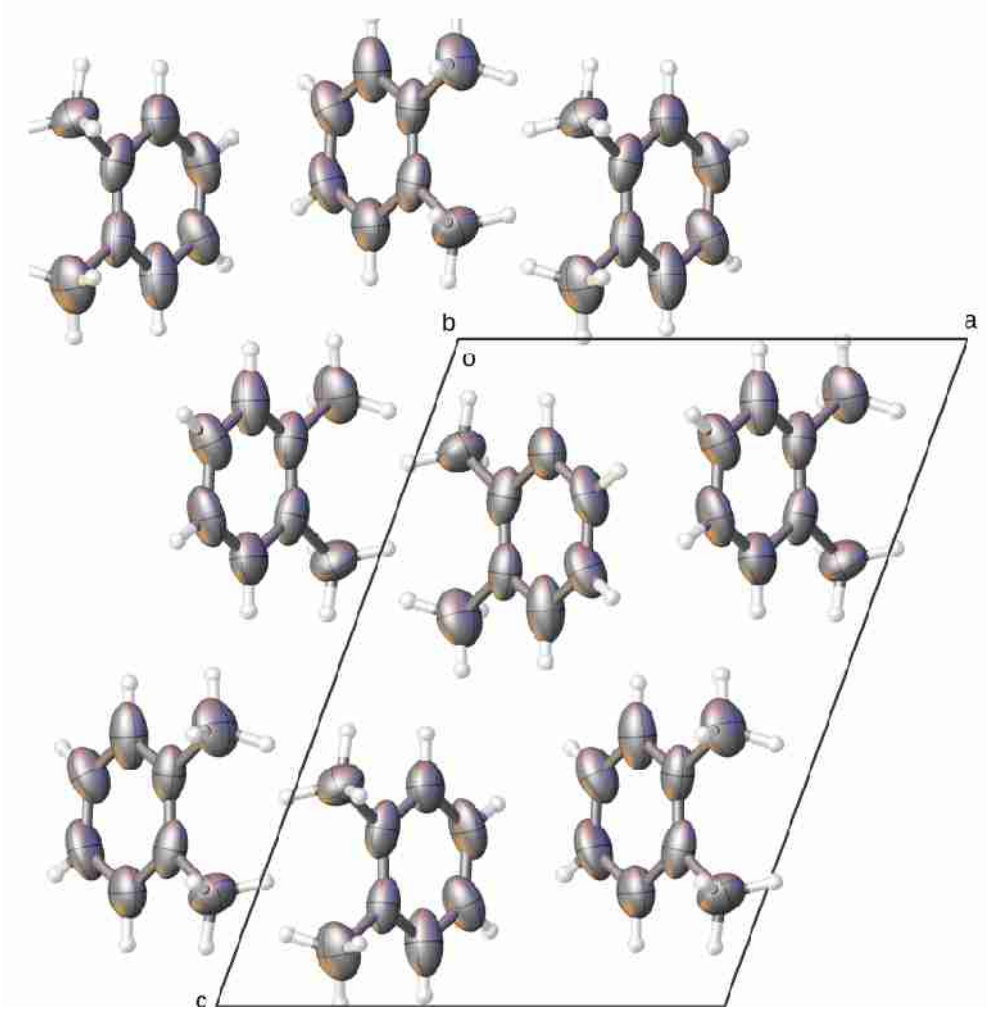

Figure A.5 Packing diagram of high-pressure crystallised o-xylene.

Table A.4 shows the crystallographic data from this data collection.

Compound	**O-Xylene (LT)**	**O-Xylene (HP)**
empirical formula	C_8H_{10}	
formula weight	1.125	
T/K	245 (2)	ambient
P/kbar	ambient	1.2 (2)
crystal system	monoclinic	
space group	$P2_1/c$	
a (Å)	9.020 (7)	9.00 (3)
b (Å)	6.173 (3)	6.00 (2)
c (Å)	12.807 (10)	12.56 (8)
β (°)	109.40 (2)	110.00 (17)
Z	4	
V/Å^3	672.6 (8)	637 (5)
D_{calc}/g cm^{-3}	1.048	1.107
μ/mm^{-1}	0.058	0.041
unique reflns	1672	705
observed reflns	1540	351
θ_{max}	28.280	16.620
completeness/%	92.1	49.8
R_1 [I > 2σ]	0.0627	0.0450
wR_2 [all]	0.1709	0.1454
goodness-of-fit	1.030	1.121

Table A.4 Crystallographic Data from the high-pressure crystallised o-xylene.

A.1.5 M-Xylene

M-xylene had previously been reported through cryo-crystallisation. High-pressure crystallisation was carried out, producing the same polymorph as previously reported.[254] Figure A.6 shows the crystal structure of m-xylene.

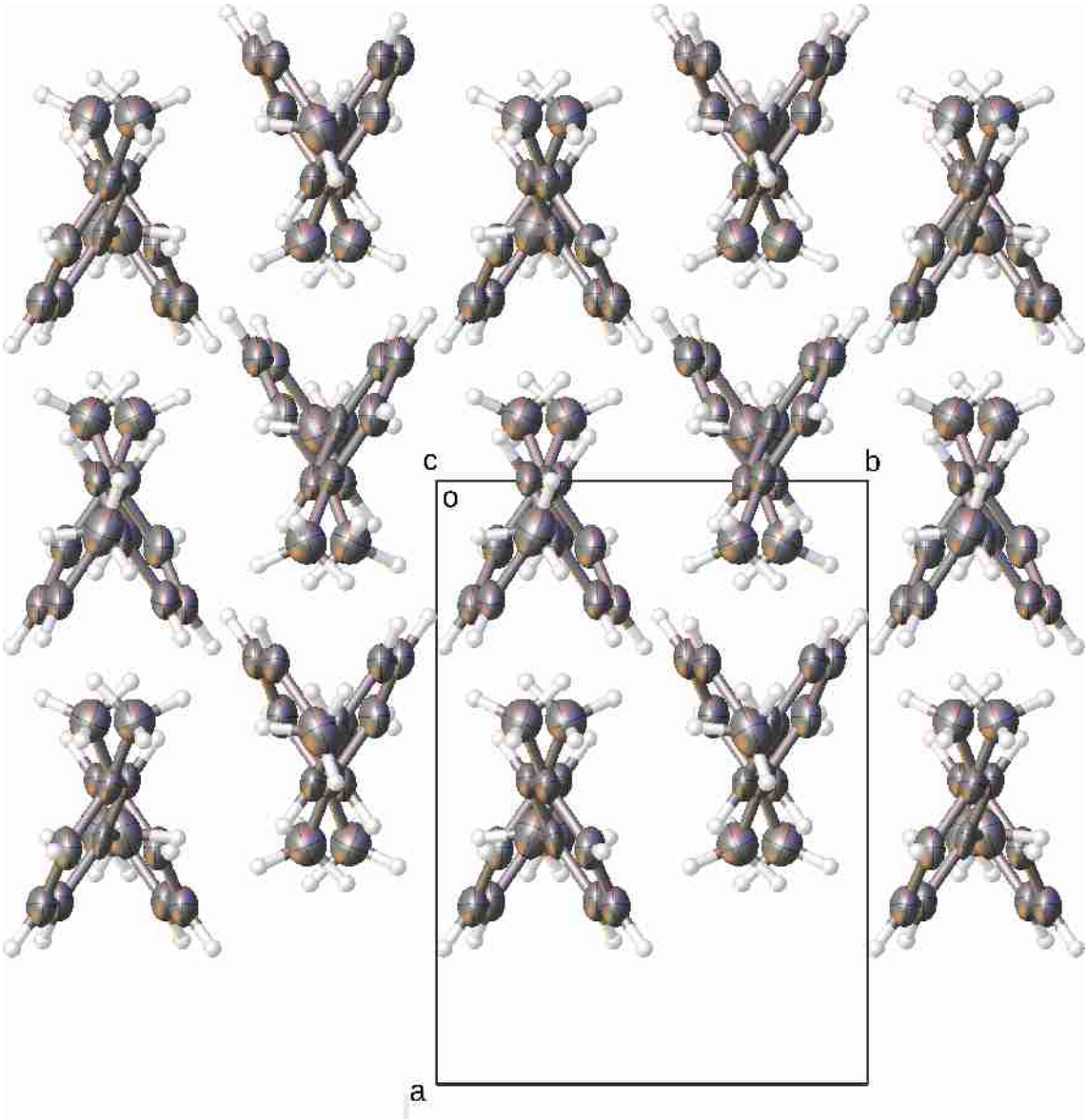

Figure A.6 Packing diagram of high-pressure crystallised m-xylene.

Table A.5 shows the crystallographic data from this data collection.

Compound	**M-Xylene (HP)**
empirical formula	C_8H_{10}
formula weight	1.125
T/K	ambient
P/kbar	1.2 (2)
crystal system	orthorhombic
space group	*Pbca*
a (Å)	10.340 (4)
b (Å)	7.389 (3)
c (Å)	16.415 (10)
Z	8
V/Å^3	1254.1 (10)
D_{calc}/g cm^{-3}	1.125
μ/mm^{-1}	0.042
unique reflns	491
observed reflns	219
θ_{max}	14.747
completeness/%	44.6
R_1 [I > 2σ]	0.0457
wR_2 [all]	0.1402
goodness-of-fit	1.150

Table A.5 Crystallographic Data from the high-pressure crystallised m-xylene.

A.1.6 P-Xylene

P-xylene had previously been reported through cryo-crystallisation. High-pressure crystallisation was carried out, producing the same polymorph as previously reported.[255] Figure A.7 shows the crystal structure of p-xylene.

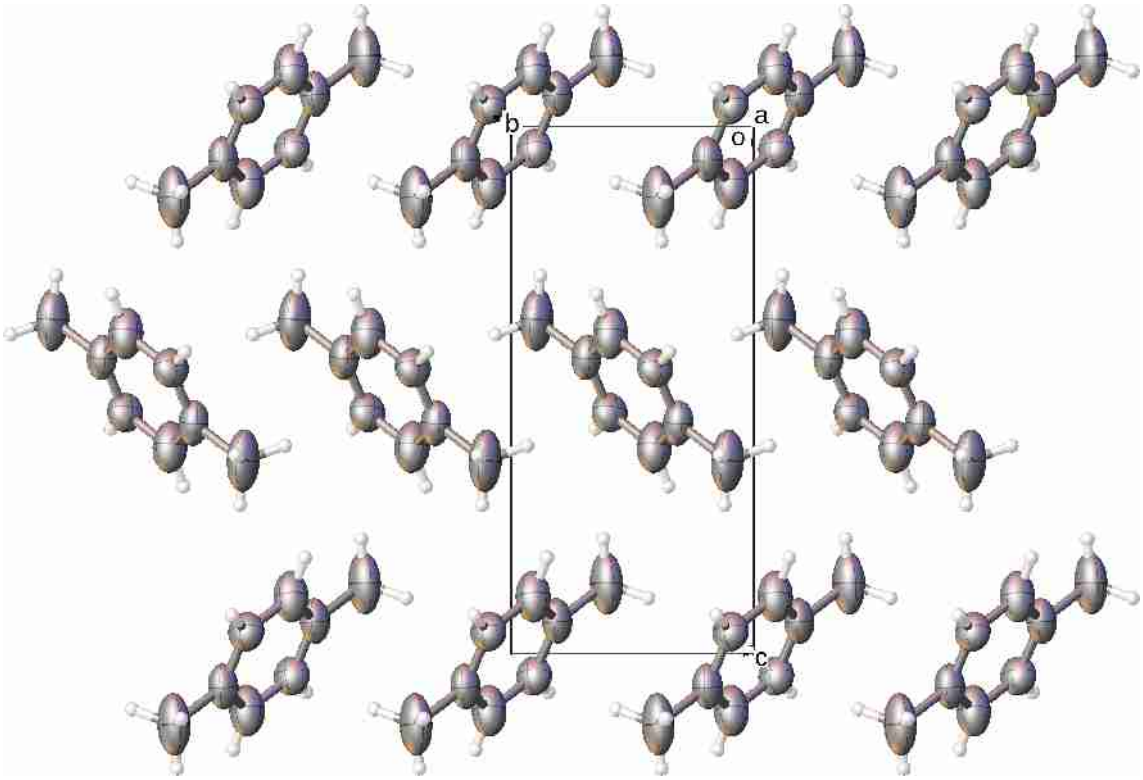

Figure A.7 Packing diagram of high-pressure crystallised p-xylene.

Table A.6 shows the crystallographic data from this data collection.

Compound	**P-Xylene (HP)**
empirical formula	C_8H_{10}
formula weight	106.16
T/K	ambient
P/kbar	0.4 (2)
crystal system	monoclinic
space group	$P2_1/c$
a (Å)	5.8551 (19)
b (Å)	5.1124 (16)
c (Å)	11.786 (7)
β (°)	109.15 (3)
Z	2
V/Å^3	333.3 (3)
D_{calc}/g cm^{-3}	1.058
μ/mm^{-1}	0.039
unique reflns	577
observed reflns	217
θ_{max}	19.451
completeness/%	37.6
R_1 [I > 2σ]	0.0360
wR_2 [all]	0.1002
goodness-of-fit	1.146

Table A.6 Crystallographic Data from the high-pressure crystallised p-xylene.

A.1.7 2-Methylanisole

2-Methylanisole was found to give the same polymorph from cryo-crystallisation and high-pressure crystallisation. There was found to be whole molecule disorder, with occupancies of the two sites refined to roughly the same occupancies (0.55953 : 0.44047) Figure A.8 shows the packing arrangement of 2-methylanisole.

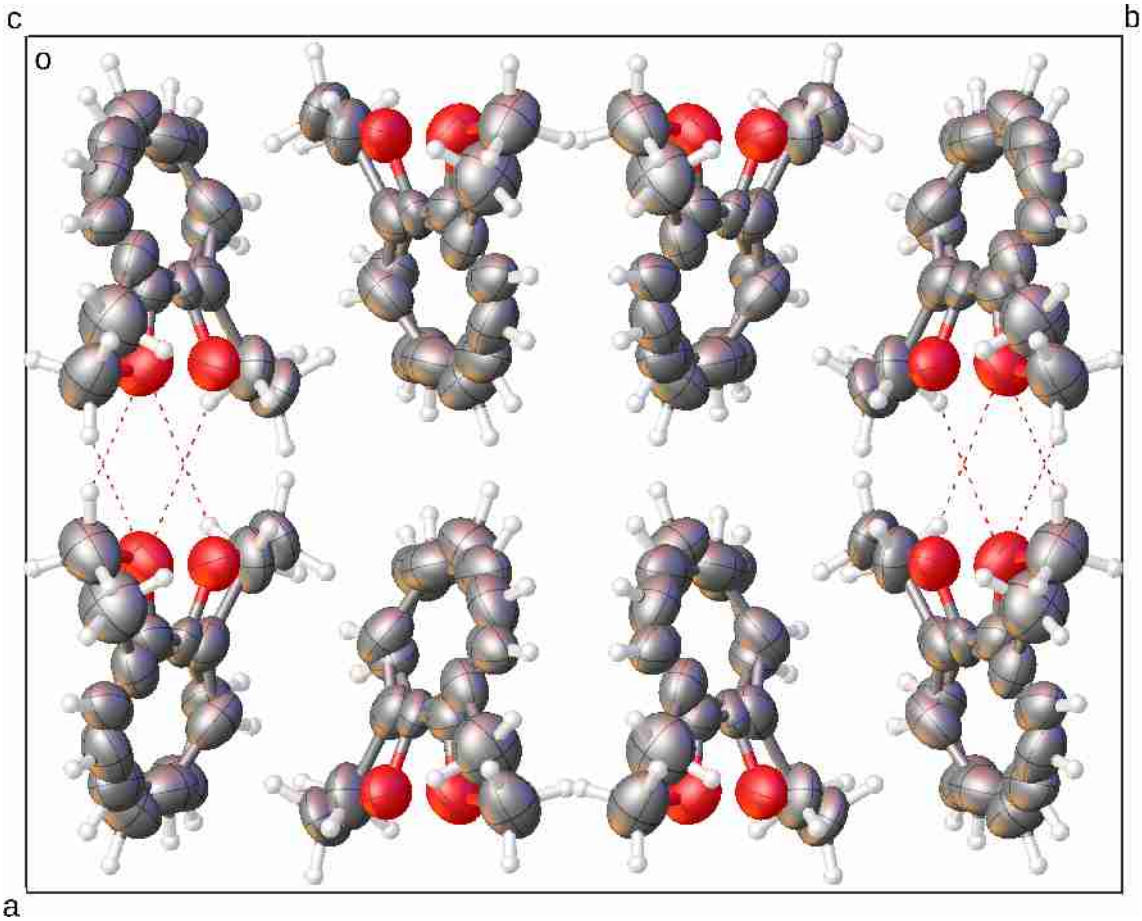

Figure A.8 Packing diagram of high-pressure crystallised 2-methylanisole.

Table A.7 shows the crystallographic data collected.

Compound	**2-Methylanisole (LT)**
empirical formula	$C_8H_{10}O$
formula weight	122.16
T/K	235 (2)
P/kbar	ambient
crystal system	orthorhombic
space group	*Iba*2
a (Å)	13.532 (7)
b (Å)	17.317 (6)
c (Å)	6.264 (3)
Z	8
V/Å^3	1467.9 (12)
D_{calc}/g cm^{-3}	1.105
μ/mm^{-1}	0.071
unique reflns	590
observed reflns	587
θ_{max}	23.280
completeness/%	99.5
R_1 [I > 2σ]	0.0345
wR_2 [all]	0.1003
goodness-of-fit	1.075

Table A.7 Crystallographic Data from cryo-crystallised 2-methylanisole. Diffraction at high-pressure was too weak for stable least-squares refinement.

A.1.8 2-Chlorotoluene

2-Chlorotoluene was found the same polymorph through cryo-crystallisation and and high-pressure crystallisation. Figure A.9 shows the asymmetric unit and crystal structure of 2-chlorotoluene.

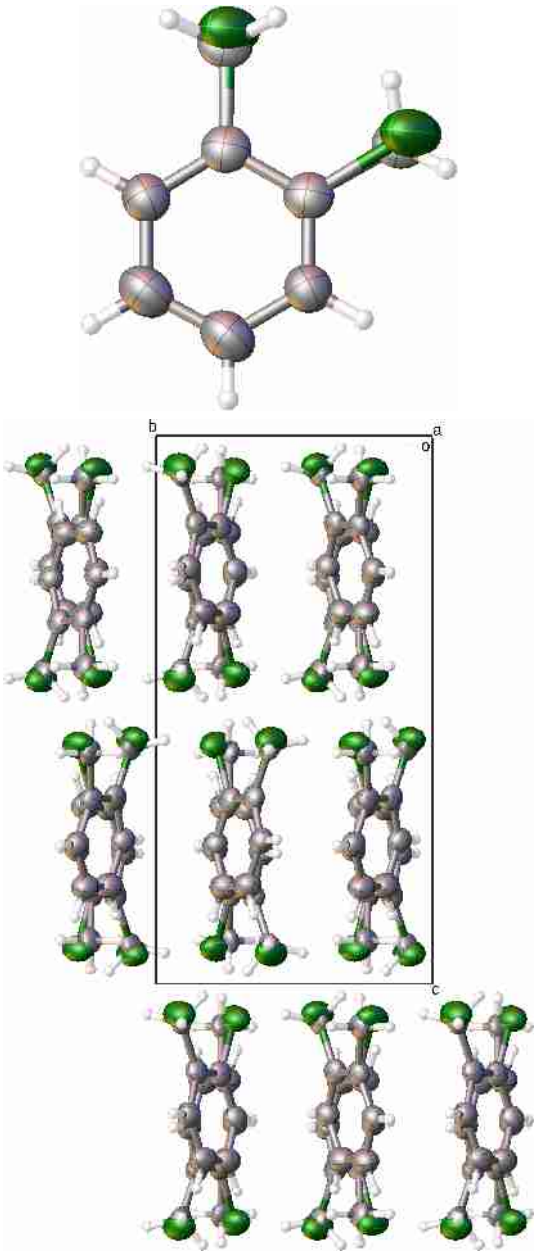

Figure A.9 Asymmetric Unit (**Top**) and Packing diagram (**Bottom**) of high-pressure crystallised 2-chlorotoluene.

Table A.8 shows crystallographic data for the high-pressure data collection. A suitable single crystal could not be isolated through cryo-crystallisation, although a unit cell matching that seen through high-pressure crystallisation was observed.

Compound	**2-Chlorotoluene (HP)**
empirical formula	C_7H_7Cl
formula weight	126.58
T/K	ambient
P/kbar	8.5 (2)
crystal system	orthorhombic
space group	*Pbca*
a (Å)	11.557 (17)
b (Å)	7.480 (7)
c (Å)	14.84 (3)
Z	8
V/Å^3	1283 (3)
D_{calc}/g cm^{-3}	1.311
μ/mm^{-1}	0.248
unique reflns	504
observed reflns	258
θ_{max}	14.754
completeness/%	56.5
R_1 [I > 2σ]	0.0666
wR_2 [all]	0.1623
goodness-of-fit	1.09

Table A.8 Crystallographic Data from the high-pressure crystallised 2-chlorotoluene. Diffraction at low-temperature was too weak for stable least-squares refinement.

A.1.9 3-Chlorotoluene

3-Chlorotoluene was found to give two different polymorphs, one from cryo-crystallisation and the other from high-pressure crystallisation, although the quality of the cryo-crystallised data was found to be quite poor, it was sufficient to solve the phase problem. Figure A.10 shows the asymmetric unit and structure of the cryo-crystallised polymorph.

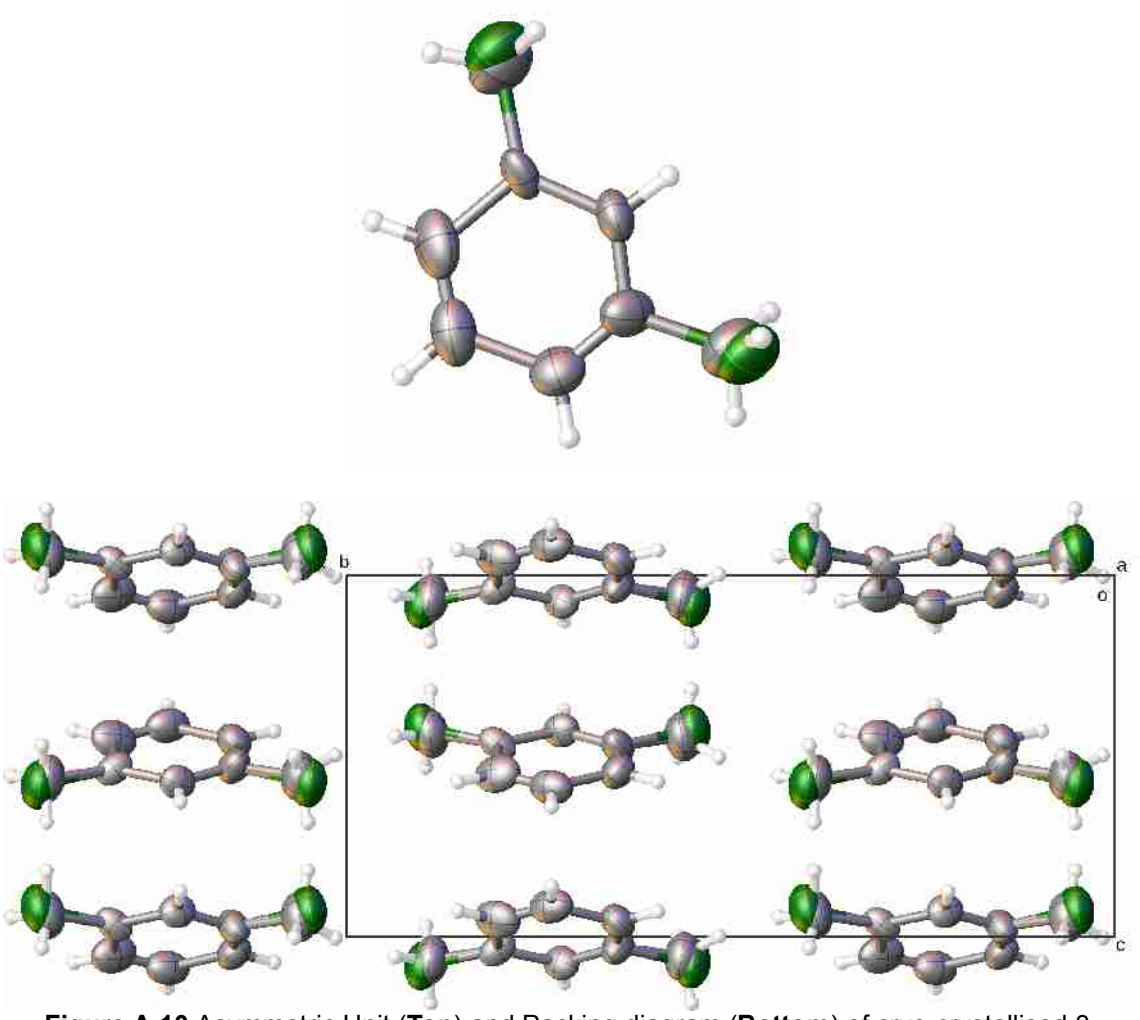

Figure A.10 Asymmetric Unit (**Top**) and Packing diagram (**Bottom**) of cryo-crystallised 3-chlorotoluene.

The high-pressure structure is shown below in figure A.11.

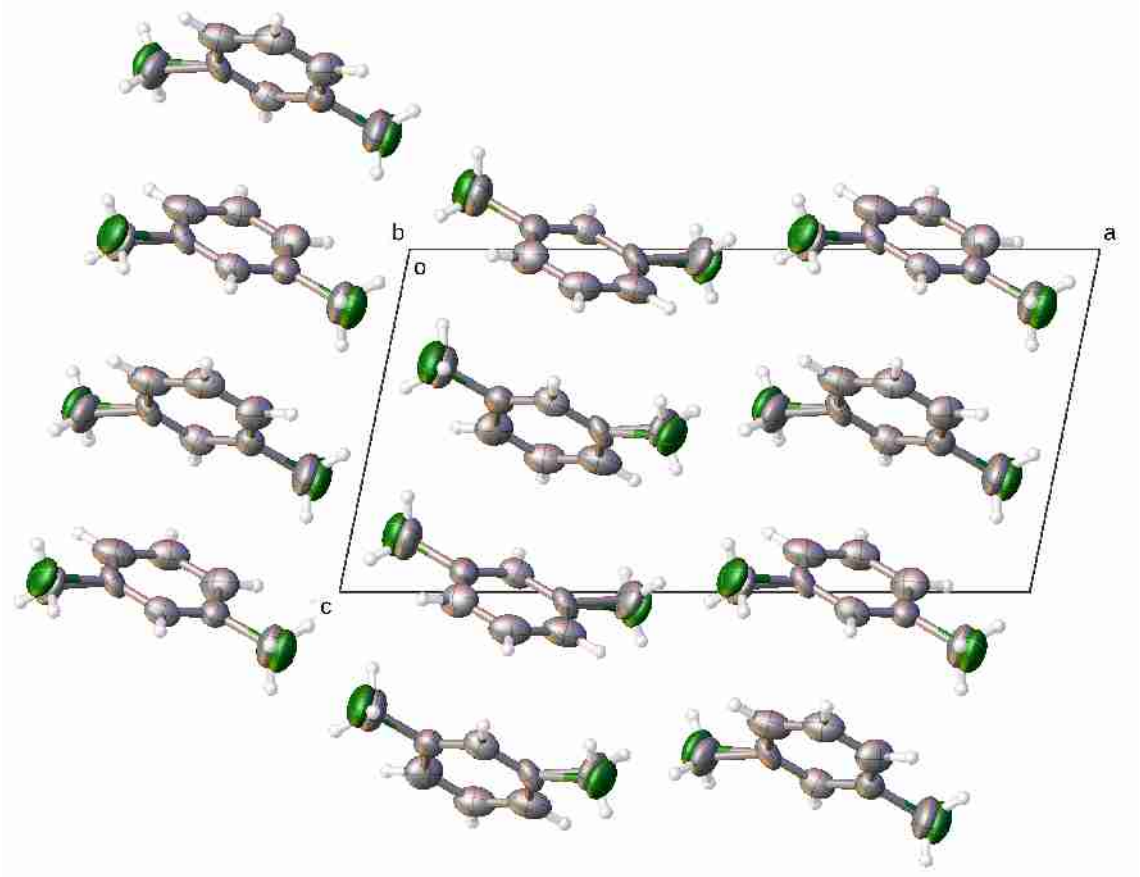

Figure A.11 Packing diagram of high-pressure crystallised 3-chlorotoluene.

Table A.9 shows crystallographic data for the two data collections.

Compound	**3-Chlorotoluene (LT)**	**3-Chlorotoluene (HP)**
empirical formula	C_7H_7Cl	
formula weight	126.58	
T/K	221 (2)	ambient
P/kbar	ambient	3.8 (2)
crystal system	orthorhombic	monoclinic
space group	$Pn2_1a$	$P2_1/c$
a (Å)	6.11 (1)	14.88 (3)
b (Å)	15.43 (3)	5.780 (9)
c (Å)	7.263 (13)	7.566 (8)
β (°)	90	101.58 (5)
Z	4	4
V/Å^3	685 (2)	637.5 (18)
D_{calc}/g cm^{-3}	1.227	1.319
μ/mm^{-1}	0.445	0.249
unique reflns	1400	663
observed reflns	1104	273
θ_{max}	26.370	16.280
completeness/%	78.9	41.2
R_1 [I > 2σ]	0.0912	0.0421
wR_2 [all]	0.2891	0.1058
goodness-of-fit	1.067	1.396

Table A.9 Crystallographic Data from the two polymorphs of 3-chlorotoluene.

A.1.10 4-Chlorotoluene

4-Chlorotoluene was found the same polymorph through cryo-crystallisation and and high-pressure crystallisation. Figure A.12 shows the asymmetric unit and crystal structure of 4-chlorotoluene.

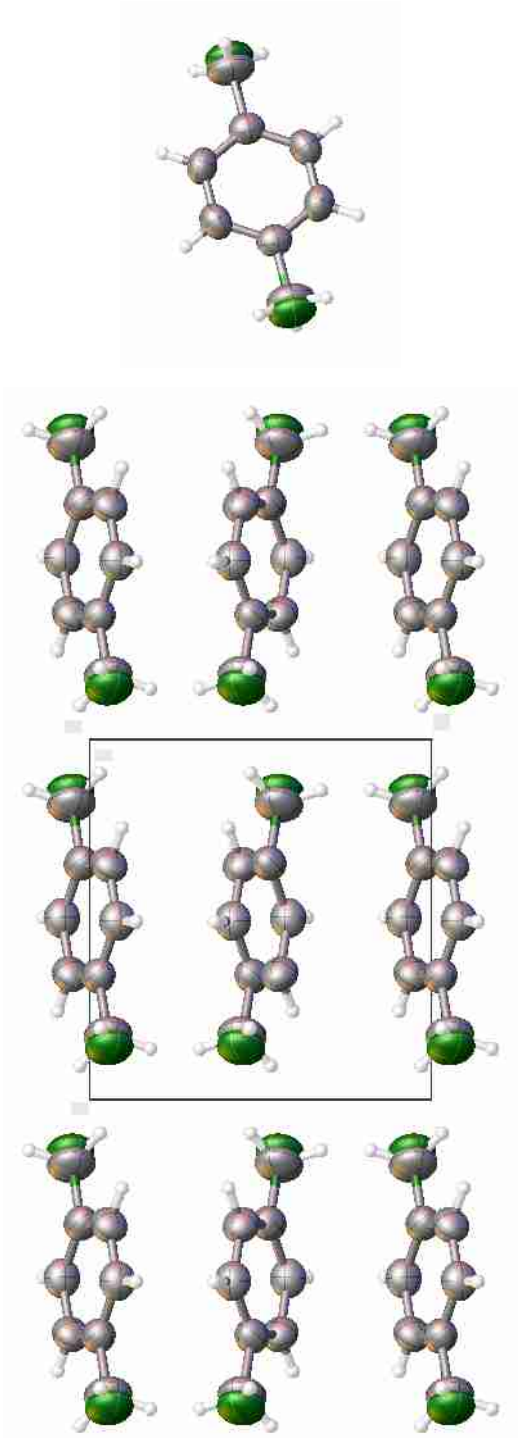

Figure A.12 Asymmetric Unit (**Top**) and Packing diagram (**Bottom**) of cryo-crystallised 4-chlorotoluene.

Table A.10 shows crystallographic data for the two data collections.

Compound	**4-Chlorotoluene (LT)**	**4-Chlorotoluene (HP)**
empirical formula	C_7H_7Cl	
formula weight	126.58	
T/K	275 (2)	ambient
P/kbar	ambient	0.3 (2)
crystal system	monoclinic	
space group	$P2_1/c$	
a (Å)	7.729 (9)	7.733 (12)
b (Å)	7.307 (8)	7.285 (6)
c (Å)	6.069 (7)	6.022 (7)
B (°)	94.903 (17)	94.62 (5)
Z	2	
V/Å^3	341.5 (7)	338.1 (7)
D_{calc}/g cm^{-3}	1.231	1.243
μ/mm^{-1}	0.447	0.232
unique reflns	846	286
observed reflns	619	141
θ_{max}	28.356	19.274
completeness/%	73.2	49.3
R_1 [I > 2σ]	0.0431	0.0334
wR_2 [all]	0.1116	0.0746
goodness-of-fit	1.062	1.090

Table A.10 Crystallographic Data from cryo- and high-pressure crystallised 4-chlorotoluene.

A.1.11 Diethylene Glycol

Diethylene glycol was found to found two distinct polymorphs at low-temperature and high-pressure. Figure A.13 shows the asymmetric unit and crystal structure of cryo-crystallised diethylene glycol.

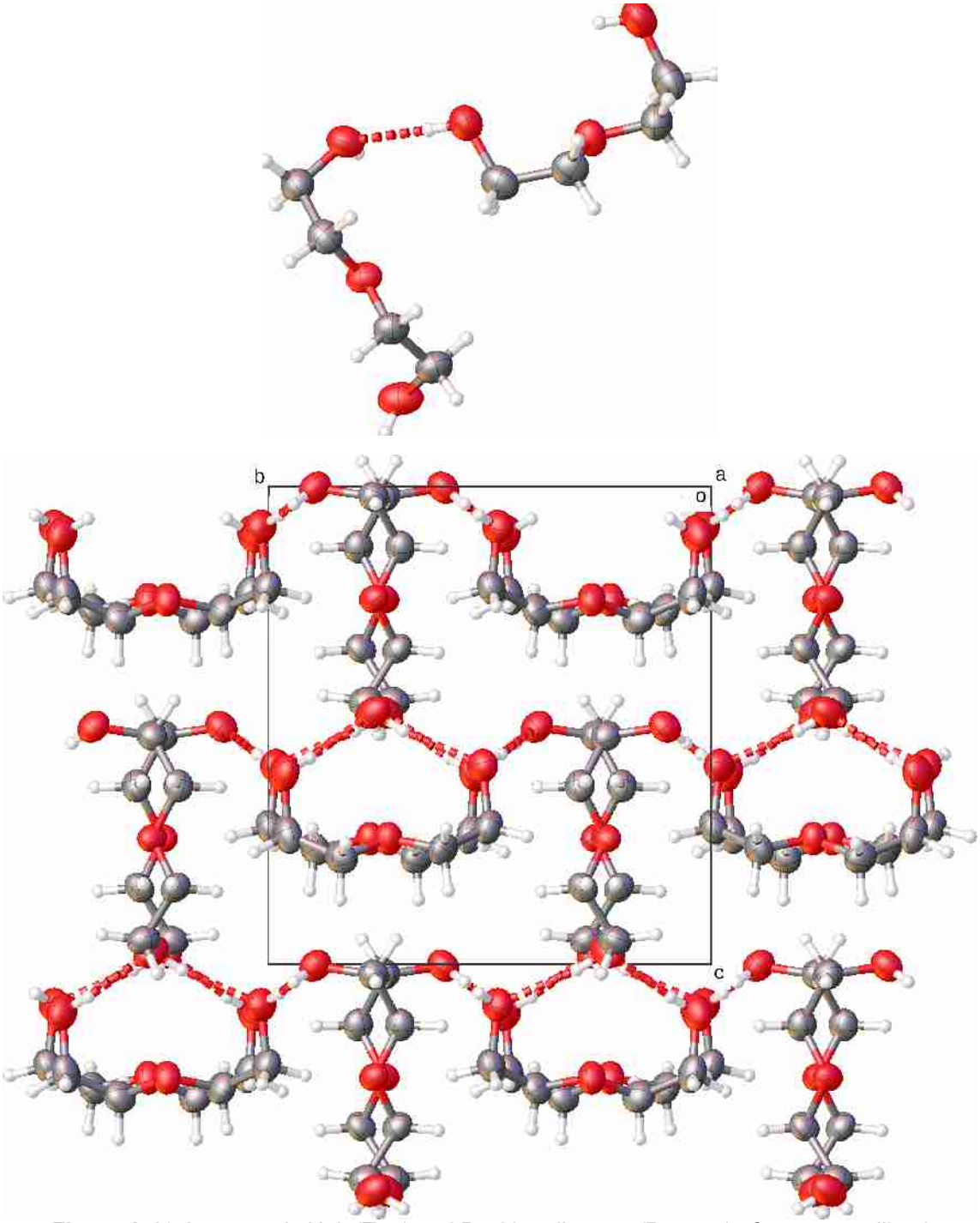

Figure A.13 Asymmetric Unit (**Top**) and Packing diagram (**Bottom**) of cryo-crystallised diethylene glycol.

Figure A.14 shows the crystal structure of high-pressure crystallised diethylene glycol.

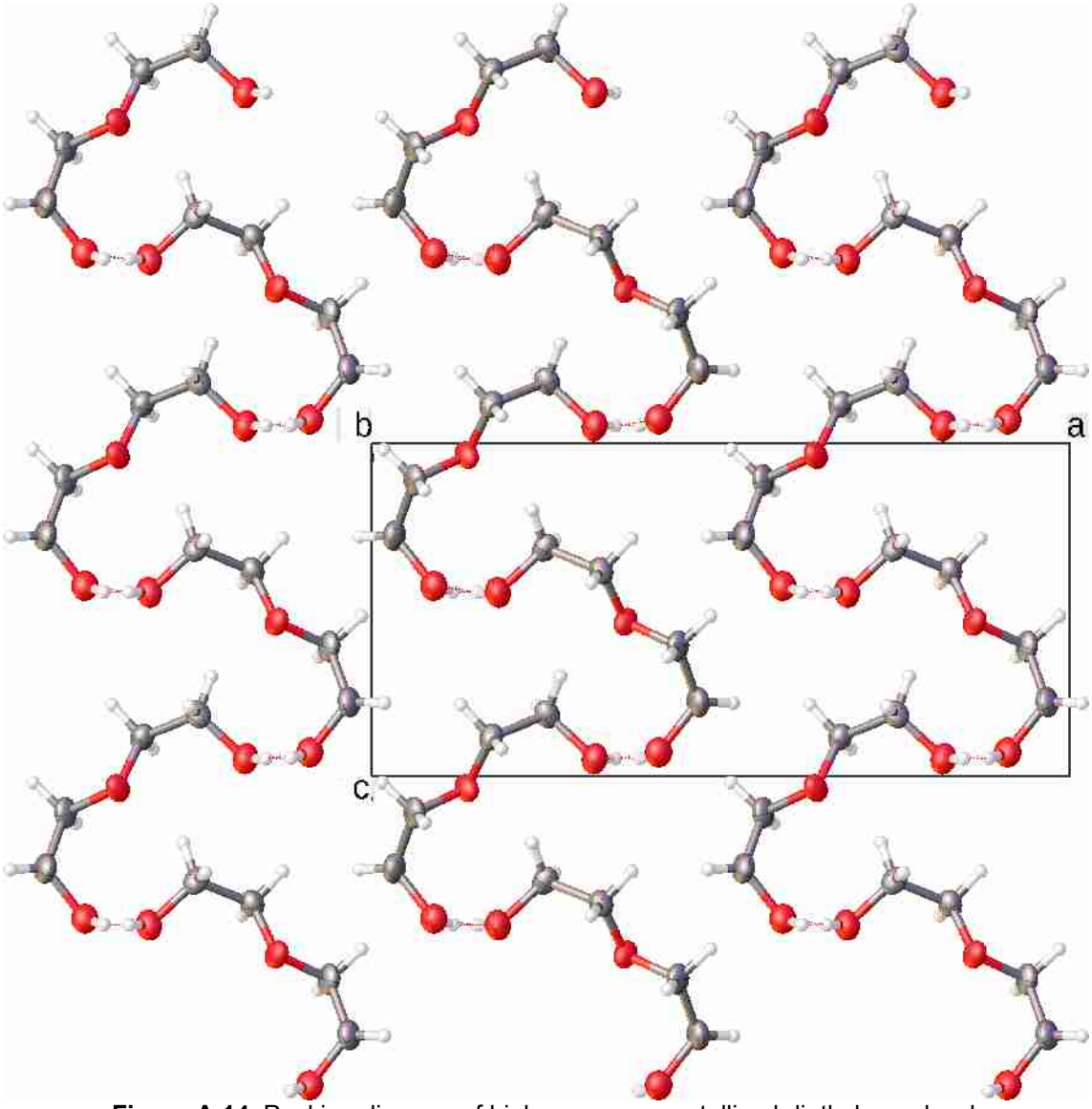

Figure A.14 Packing diagram of high-pressure crystallised diethylene glycol.

Table A.11 shows crystallographic data for the two data collections.

Compound	**Diethylene Glycol (LT)**	**Diethylene Glycol (HP)**
empirical formula	C_4H_9NO	
formula weight	1.256	
T/K	250 (2)	ambient
P/kbar	ambient	2.8 (2)
crystal system	orthorhombic	orthorhombic
space group	*Pna*2$_1$	*Pna*2$_1$
a (Å)	10.040 (7)	15.291 (9)
b (Å)	10.186 (7)	4.699 (3)
c (Å)	10.974 (5)	7.302 (4)
B (°)	90	90
Z	8	4
V/Å^3	1122.3 (12)	524.7 (5)
D_{calc}/g cm^{-3}	1.256	1.343
μ/mm^{-1}	0.107	0.069
unique reflns	1222	638
observed reflns	1116	456
θ_{max}	26.402	17.129
completeness/%	91.3	71.5
R_1 [I > 2σ]	0.0506	0.0455
wR_2 [all]	0.1232	0.0895
goodness-of-fit	1.154	1.081

Table A.11 Crystallographic Data from cryo- and high-pressure crystallised diethylene glycol.

A.1.12 2-Bromo-4-fluoropyridine

2-Bromo-4-fluoropyridine was found the same polymorph through cryo-crystallisation and and high-pressure crystallisation. Figure A.15 shows the crystal structure of 2-bromo-4-fluoropyridine.

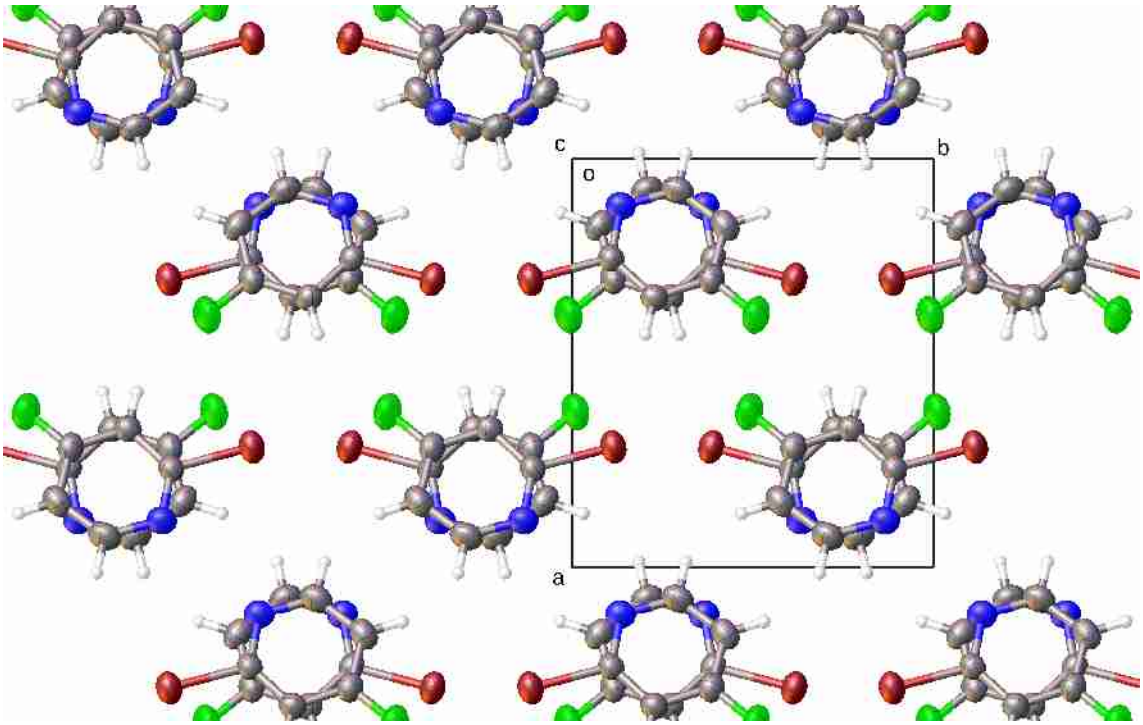

Figure A.15 Packing diagram of cryo-crystallised 2-bromo-4-fluoropyridine.

As expected, there is extensive π/π stacking, with a plane-to-plane distance of only 3.476 (6) Å (in the cryo-crystallised structure).

Table A.12 shows crystallographic data for the two data collections.

Compound	**2-Bromo-4-fluoropyridine (LT)**	**2-Bromo-4-fluoropyridine(HP)**
empirical formula	C_5H_3BrFN	
formula weight	175.98	
T/K	275 (2)	ambient
P/kbar	ambient	0.3 (2)
crystal system	monoclinic	
space group	$P2_1/c$	
a (Å)	9.521 (2)	9.4891 (18)
b (Å)	8.1595 (17)	8.1426 (18)
c (Å)	7.6531 (13)	7.6242 (17)
B (°)	104.147 (5)	104.035 (8)
Z	4	
V/Å^3	576.5 (2)	571.5 (2)
D_{calc}/g cm^{-3}	2.028	2.045
μ/mm^{-1}	7.029	3.799
unique reflns	1752	1035
observed reflns	1487	478
θ_{max}	30.488	19.688
completeness/%	84.9	46.2
R_1 [I > 2σ]	0.0348	0.0228
wR_2 [all]	0.0897	0.0543
goodness-of-fit	1.124	1.041

Table A.12 Crystallographic Data from cryo- and high-pressure crystallised 2-bromo-4-fluoropyridine.

A.1.13 2-Bromo-4-chloropyridine and 2-Chloro-4-bromopyridine

2-Bromo-4-chloropyridine and 2-chloro-4-bromopyridine were found to be isostructural to one another and the same polymorph was found through cryo-crystallisation and and high-pressure crystallisation for both compounds. Figure A.16 shows the crystal structure of 2-bromo-4-chloropyridine.

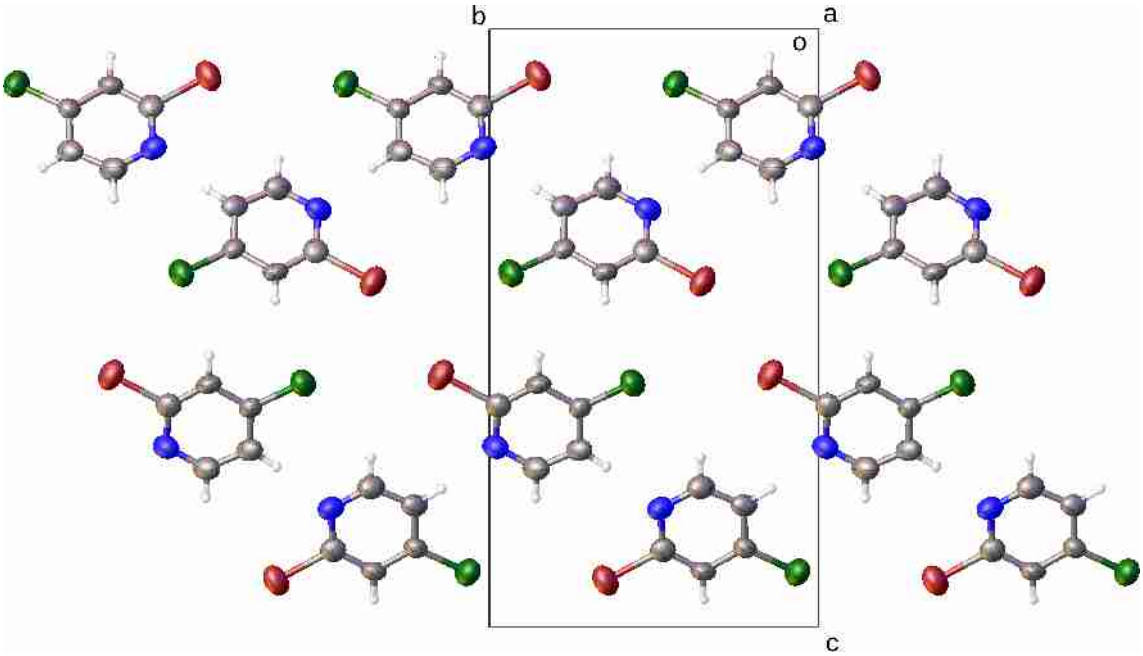

Figure A.16 Packing diagram of cryo-crystallised 2-chloro-4-bromopyridine (**Top**) and 2-bromo-4-chloropyridine (**bottom**).

Table A.13 shows crystallographic data for 2-bromo-4-chloropyridine, while table A.14 shows that for 2-chloro-4-bromopyridine.

Compound	**2-Bromo-4-chloropyridine (LT)**	**2-Bromo-4-chloropyridine (HP)**
empirical formula	C_5H_3BrClN	
formula weight	192.43	
T/K	285 (2)	ambient
P/kbar	ambient	0.3 (2)
crystal system	orthorhombic	
space group	$P2_12_12_1$	
a (Å)	4.027 (4)	3.9810 (16)
b (Å)	9.543 (11)	9.419 (4)
c (Å)	17.31 (2)	17.104 (9)
Z	4	
V/Å^3	665.2 (13)	641.4 (5)
D_{calc}/g cm^{-3}	1.922	1.993
μ/mm^{-1}	6.468	3.581
unique reflns	724	1569
observed reflns	589	939
θ_{max}	24.950	21.827
completeness/%	81.4	56.6
R_1 [I > 2σ]	0.0553	0.0468
wR_2 [all]	0.1545	0.1320
goodness-of-fit	1.090	1.068

Table A.13 Crystallographic Data from cryo- and high-pressure crystallised 2-bromo-4-chloropyridine.

Compound	**2-Chloro-4-bromopyridine (LT)**	**2-Chloro-4-bromopyridine (HP)**
empirical formula	C_5H_3BrClN	
formula weight	192.43	
T/K	296.5 (20)	ambient
P/kbar	ambient	0.5 (2)
crystal system	orthorhombic	
space group	$P2_12_12_1$	
a (Å)	3.985 (4)	3.936 (4)
b (Å)	9.586 (11)	9.447 (9)
c (Å)	17.23 (2)	16.91 (2)
Z	4	
V/Å^3	658.2 (13)	628.8 (11)
D_{calc}/g cm^{-3}	1.942	2.033
μ/mm^{-1}	6.547	3.653
unique reflns	511	573
observed reflns	471	348
θ_{max}	21.960	18.090
completeness/%	92.2	60.7
R_1 [I > 2σ]	0.0672	0.0380
wR_2 [all]	0.1916	0.0961
goodness-of-fit	1.083	1.196

Table A.14 Crystallographic Data from cryo- and high-pressure crystallised 2-chloro-4-bromopyridine.

A.1.14 2-Fluoro-5-bromopyridine

2-Fluoro-5-bromopyridine was found the same polymorph through cryo-crystallisation and and high-pressure crystallisation. Figure A.17 shows the asymmetric unit and crystal structure of 2-fluoro-5-bromopyridine.

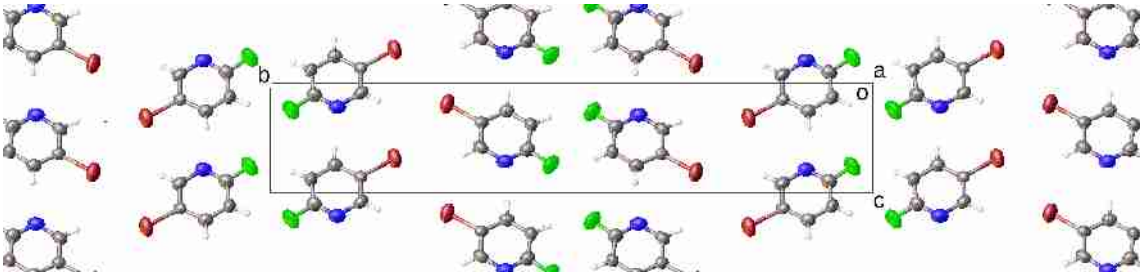

Figure A.17 Packing diagram of cryo-crystallised 2-fluoro-5-bromopyridine.

Table A.15 shows crystallographic data for the low-temperature data collection. A suitable single crystal could not be isolated through high-pressure crystallisation, although a unit cell matching that seen through cryo-crystallisation was observed.

Compound	**2-Fluoro-5-bromopyridine (LT)**
empirical formula	C_5H_3BrFN
formula weight	175.98
T/K	283 (2)
P/kbar	ambient
crystal system	monoclinic
space group	$P2_1/n$
a (Å)	4.046 (3)
b (Å)	28.93 (2)
c (Å)	5.262 (4)
B (°)	97.189 (13)
Z	4
V/Å^3	611.3 (8)
D_{calc}/g cm^{-3}	1.913
μ/mm^{-1}	6.630
unique reflns	1078
observed reflns	1033
θ_{max}	25.014
completeness/%	95.8
R_1 [I > 2σ]	0.0577
wR_2 [all]	0.1628
goodness-of-fit	1.083

Table A.15 Crystallographic Data from cryo-crystallised 2-fluoro-5-bromopyridine.

A.1.15 3-Bromopyridine

3-Bromopyridine was found the same polymorph through cryo-crystallisation and and high-pressure crystallisation. Figure A.18 shows the crystal structure of 3-bromopyridine (that observed through cryo-crystallisation).

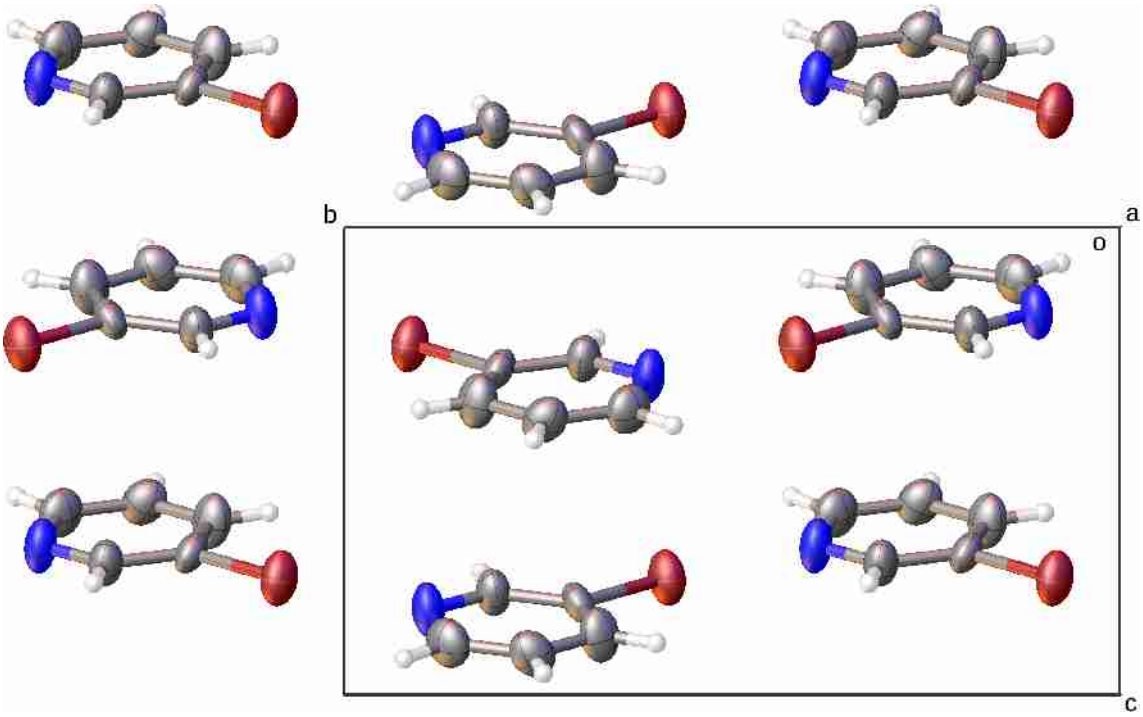

Figure A.18 Packing diagram of cryo-crystallised 3-bromopyridine.

Table A.16 shows crystallographic data for the two data collections.

Compound	**3-Bromopyridine (LT)**	**3-Bromopyridine (HP)**
empirical formula	C_5H_4NBr	
formula weight	157.99	
T/K	243 (2)	ambient
P/kbar	ambient	2.3 (2)
crystal system	monoclinic	
space group	$P2_1/c$	
a (Å)	6.448 (5)	6.216 (11)
b (Å)	12.046 (9)	11.735 (15)
*c (*Å*)*	7.345 (5)	7.130 (9)
B (°)	98.539 (13)	98.07 (6)
Z	4	
V/Å^3	564.2 (7)	515.0 (14)
D_{calc}/g cm^{-3}	1.860	2.038
μ/mm^{-1}	7.146	4.195
unique reflns	1302	1042
observed reflns	1051	379
θ_{max}	27.515	20.420
completeness/%	80.7	36.4
R_1 [I > 2σ]	0.0866	0.0193
wR_2 [all]	0.2545	0.0527
goodness-of-fit	1.059	1.046

Table A.16 Crystallographic Data from cryo- and high-pressure crystallised 3-bromopyridine.

A.1.16 2,4,6-Trimethylaniline

2,4,6-Trimethylaniline was found the same polymorph through cryo-crystallisation and and high-pressure crystallisation, although the high-pressure data were not of sufficient quality for least-squares refinement. Figure A.19 shows the asymmetric unit and crystal structure of 2,4,6-trimethylaniline.

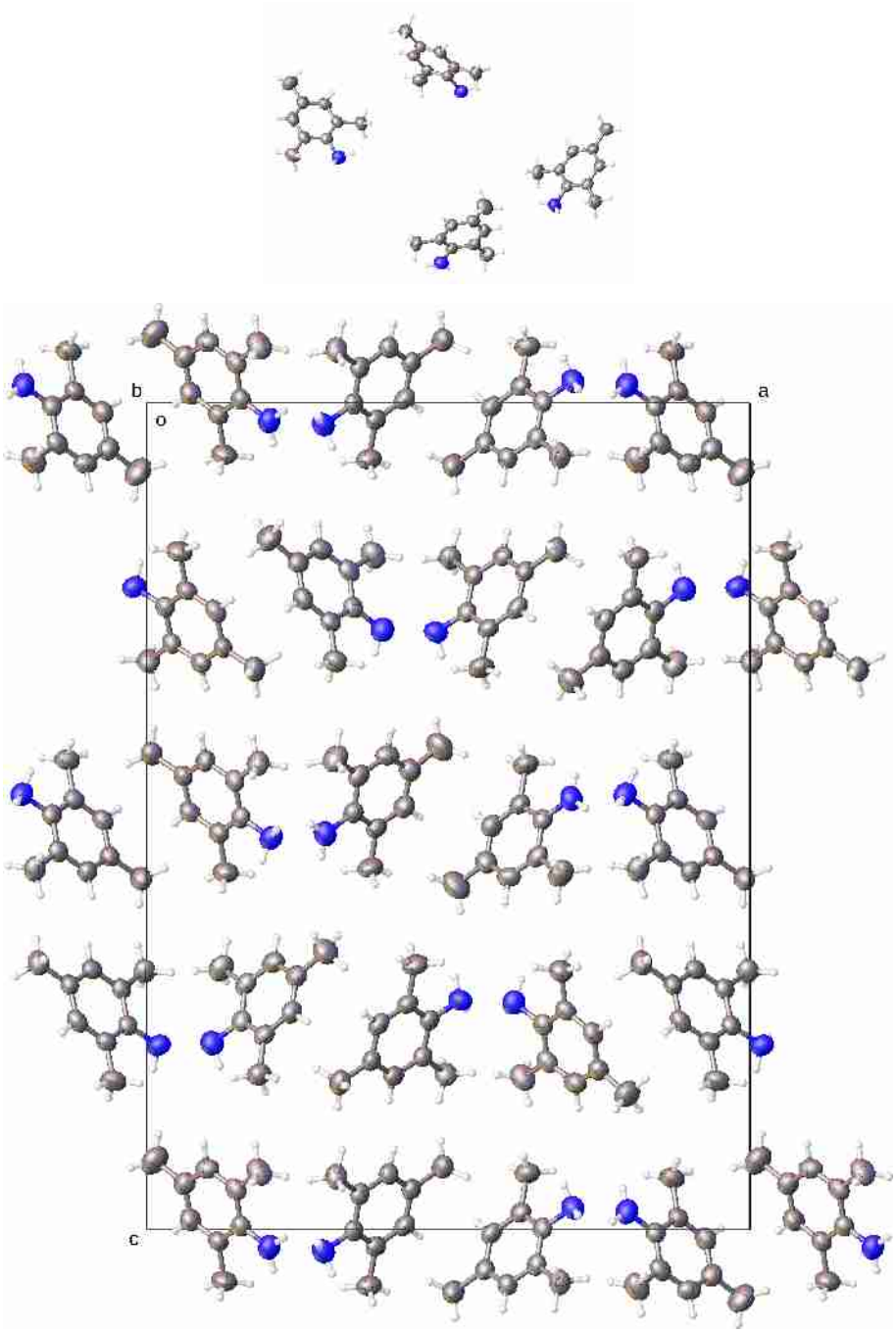

Figure A.19 Asymmetric Unit (**Top**) and packing diagram (**Bottom**) of cryo-crystallised 2,4,6-trimethylaniline.

Table A.17 shows the crystallographic data for the cryo-crystallised structure.

Compound	**2,4,6-Trimethylaniline (LT)**
empirical formula	$C_9H_{13}N$
formula weight	135.20
T/K	269 (2)
P/kbar	ambient
crystal system	orthorhombic
space group	$Pna2_1$
a (Å)	21.506 (6)
b (Å)	5.1829 (10)
c (Å)	29.497 (8)
Z	16
V/Å^3	3287.8 (14)
D_{calc}/g cm^{-3}	1.093
μ/mm^{-1}	0.064
unique reflns	5148
observed reflns	4438
θ_{max}	24.004
completeness/%	86.2
R_1 [I > 2σ]	0.0460
wR_2 [all]	0.1432
goodness-of-fit	0.990

Table A.17 Crystallographic Data from cryo-crystallised 2,4,6-trimethylaniline.

A.1.17 2,3-Dimethylaniline

2,3-Dimethylaniline was found to give two different polymorphs, one from cryo-crystallisation and the other from high-pressure crystallisation. Figure A.20 shows the crystal structure of 2,3-dimethylaniline (that observed through cryo-crystallisation).

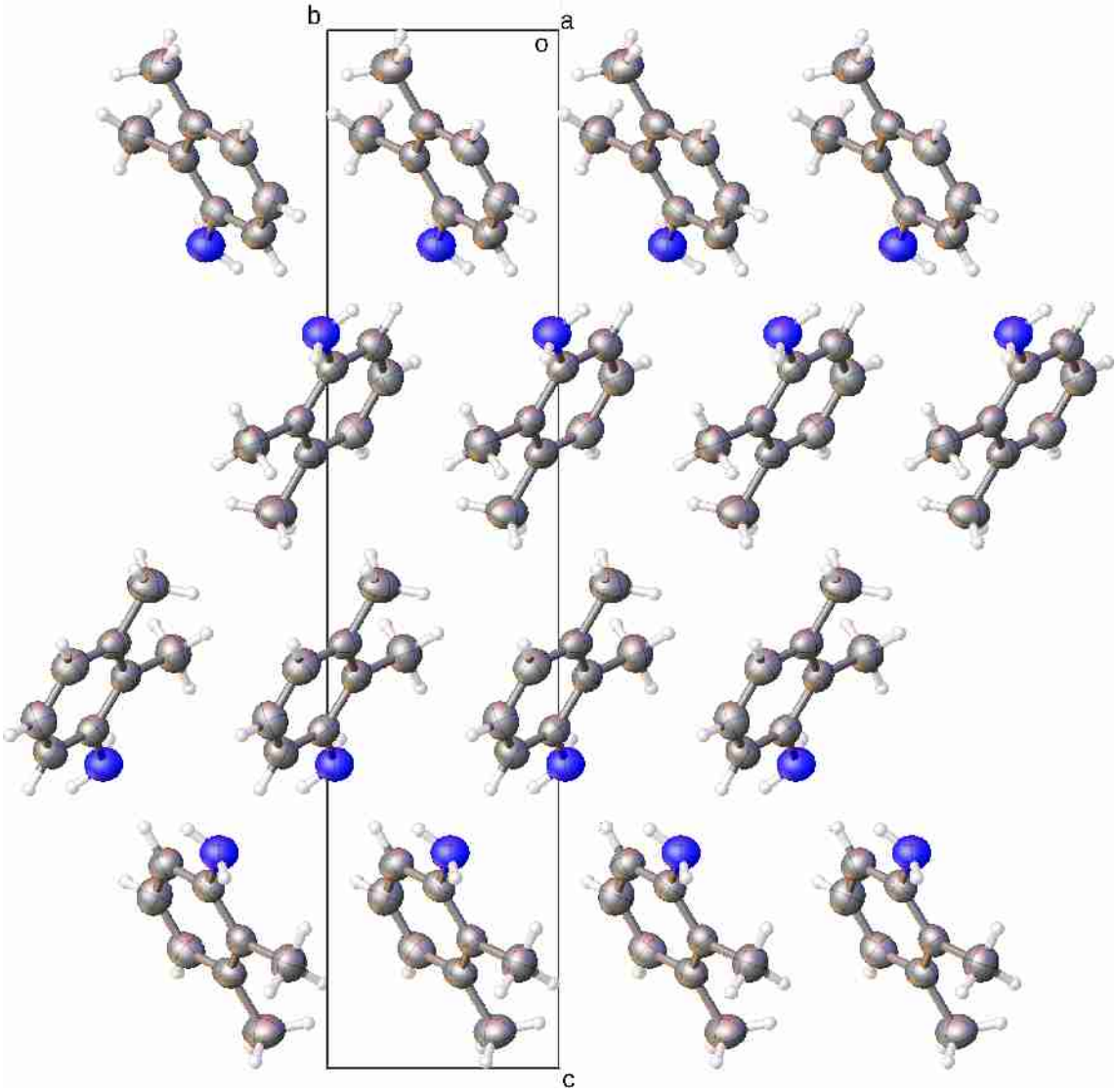

Figure A.20 Packing diagram of cryo-crystallised 2,3-dimethylaniline.

Figure A.21 shows the high-pressure structure.

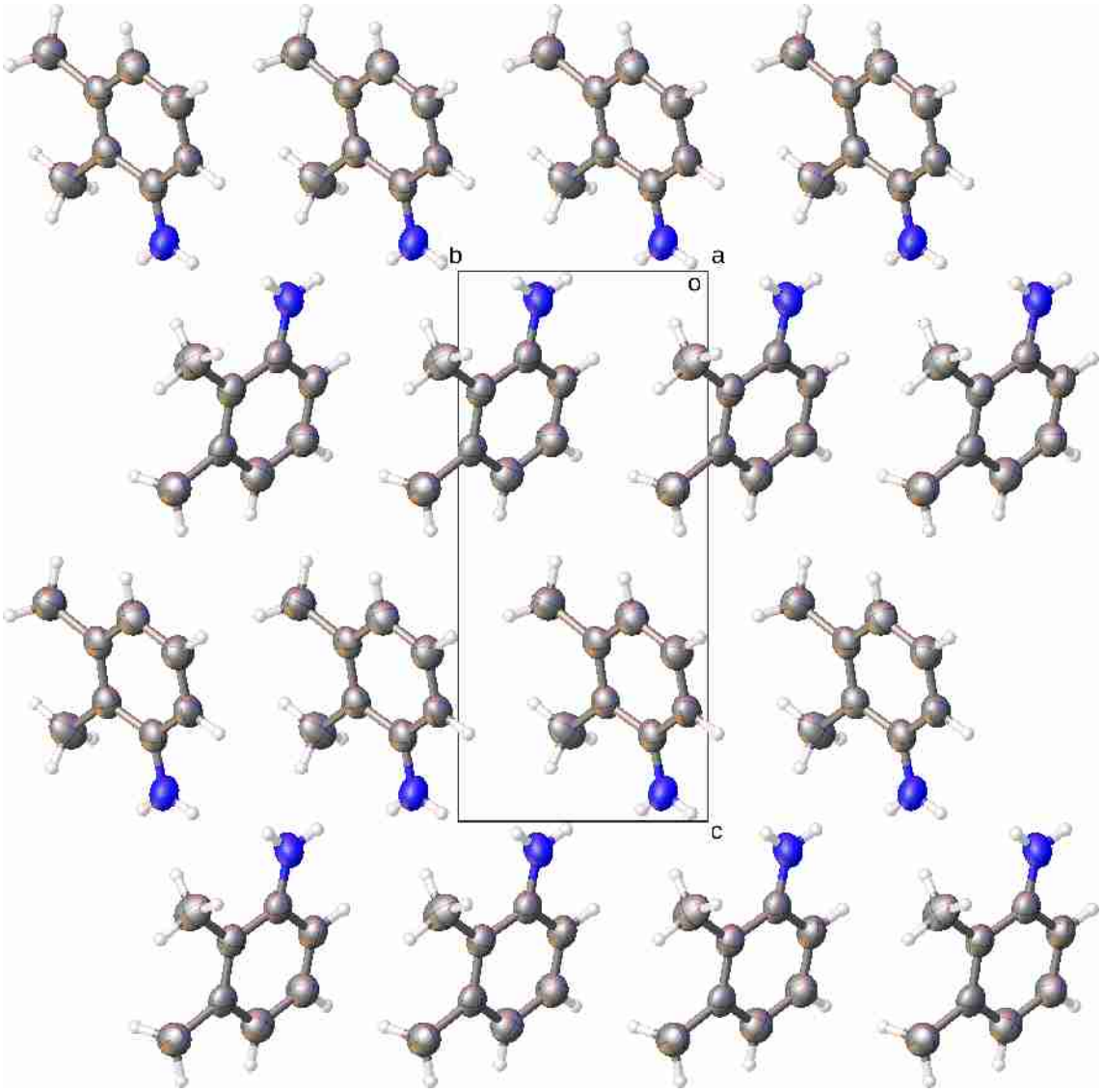

Figure A.21 Packing diagram of high-pressure crystallised 2,3-dimethylaniline.

Table A.18 shows crystallographic data for the two data collections.

Compound	**2,3-Dimethylaniline (LT)**	**2,3-Dimethylaniline (HP)**
empirical formula	$C_8H_{11}N$	
formula weight	121.18	
T/K	273 (2)	ambient
P/kbar	ambient	3.0 (2)
crystal system	monoclinic	monoclinic
space group	$P2_1/n$	$P2_1$
a (Å)	6.321 (8)	5.146 (4)
b (Å)	5.020 (4)	5.503 (4)
*c (*Å*)*	22.59 (3)	12.378 (12)
B (°)	91.10 (3)	100.83 (3)
Z	4	2
V/Å^3	716.7 (14)	344.3 (15)
D_{calc}/g cm^{-3}	1.123	1.169
μ/mm^{-1}	0.066	0.045
unique reflns	1031	979
observed reflns	953	364
θ_{max}	23.335	18.126
completeness/%	92.4	37.2
R_1 [I > 2σ]	0.0662	0.0531
wR_2 [all]	0.1962	0.1204
goodness-of-fit	1.045	1.078

Table A.18 Crystallographic Data from cryo- and high-pressure crystallised 2,3-dimethylaniline.

A.1.18 2,5-Dimethylaniline

2,5-Dimethylaniline was found the same polymorph through cryo-crystallisation and high-pressure crystallisation. Figure A.22 shows the asymmetric unit and crystal structure of 2,5-dimethylaniline.

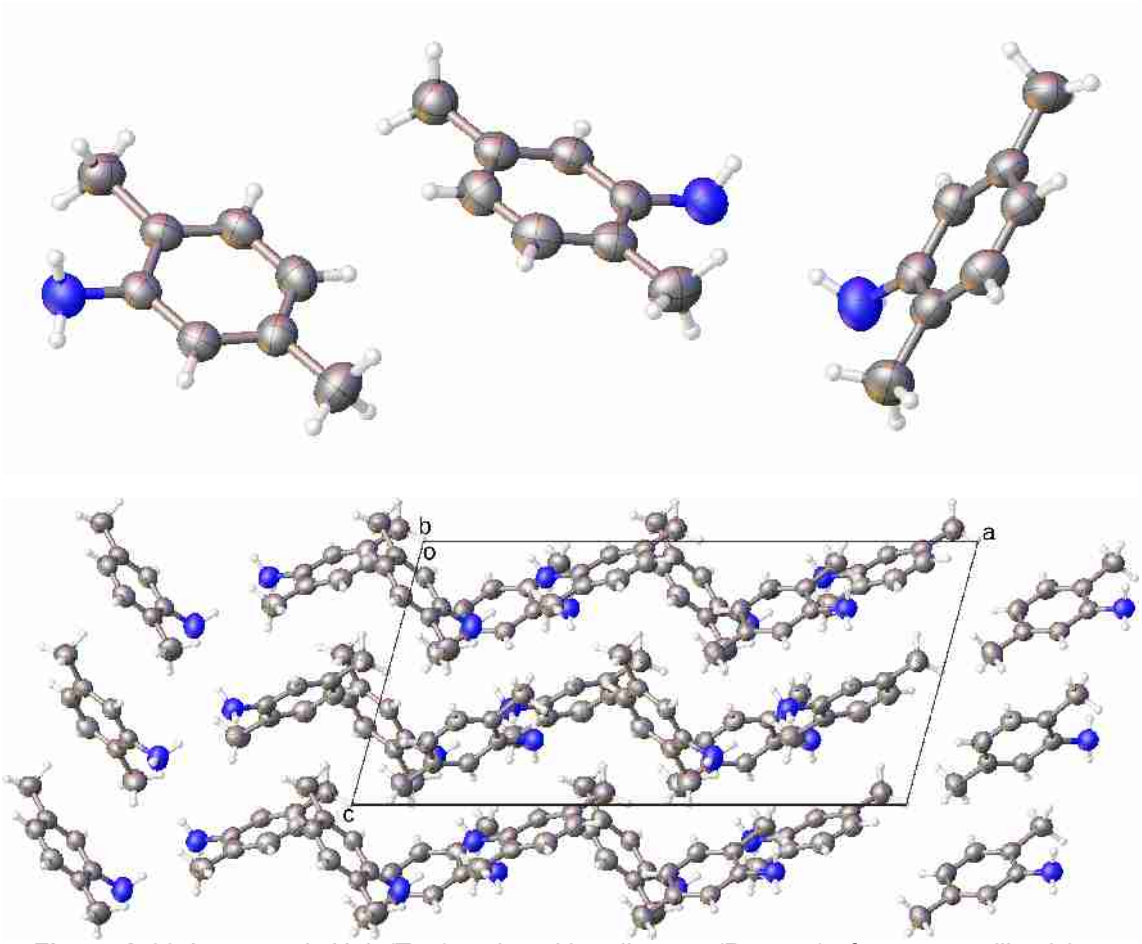

Figure A.22 Asymmetric Unit (**Top**) and **p**acking diagram (**Bottom**) of cryo-crystallised 2,5-dimethylaniline.

Table A.19 shows crystallographic data for the two data collections.

Compound	**2,5-Dimethylaniline (LT)**	**2,5-Dimethylaniline (HP)**
empirical formula	$C_8H_{11}N$	
formula weight	121.18	
T/K	277 (2)	ambient
P/kbar	ambient	0.8 (2)
crystal system	monoclinic	
space group	*Cc*	
a (Å)	19.677 (4)	19.433 (19)
b (Å)	11.795 (2)	11.736 (9)
*c (*Å*)*	9.684 (3)	9.639 (8)
B (°)	105.289 (10)	103.26 (4)
Z	12	12
V/Å^3	2168.2 (10)	2140 (3)
D_{calc}/g cm^{-3}	1.114	1.128
μ/mm^{-1}	0.066	0.044
unique reflns	5435	2367
observed reflns	3691	757
θ_{max}	28.389	16.580
completeness/%	67.9	32.0
R_1 [I > 2σ]	0.0550	0.0650
wR_2 [all]	0.1646	0.1665
goodness-of-fit	1.007	1.100

Table A.19 Crystallographic Data from cryo- and high-pressure crystallised 2,5-dimethylaniline.

A.1.19 2,6-Dimethylaniline

2,6-Dimethylaniline was found the same polymorph through cryo-crystallisation and and high-pressure crystallisation. The high-pressure data were of quite low quality (not surprising, given that the triclinic lattice and a Z' value of 3). Figure A.23 shows the asymmetric unit and crystal structure of 2,6-dimethylaniline (that observed through cryo-crystallisation).

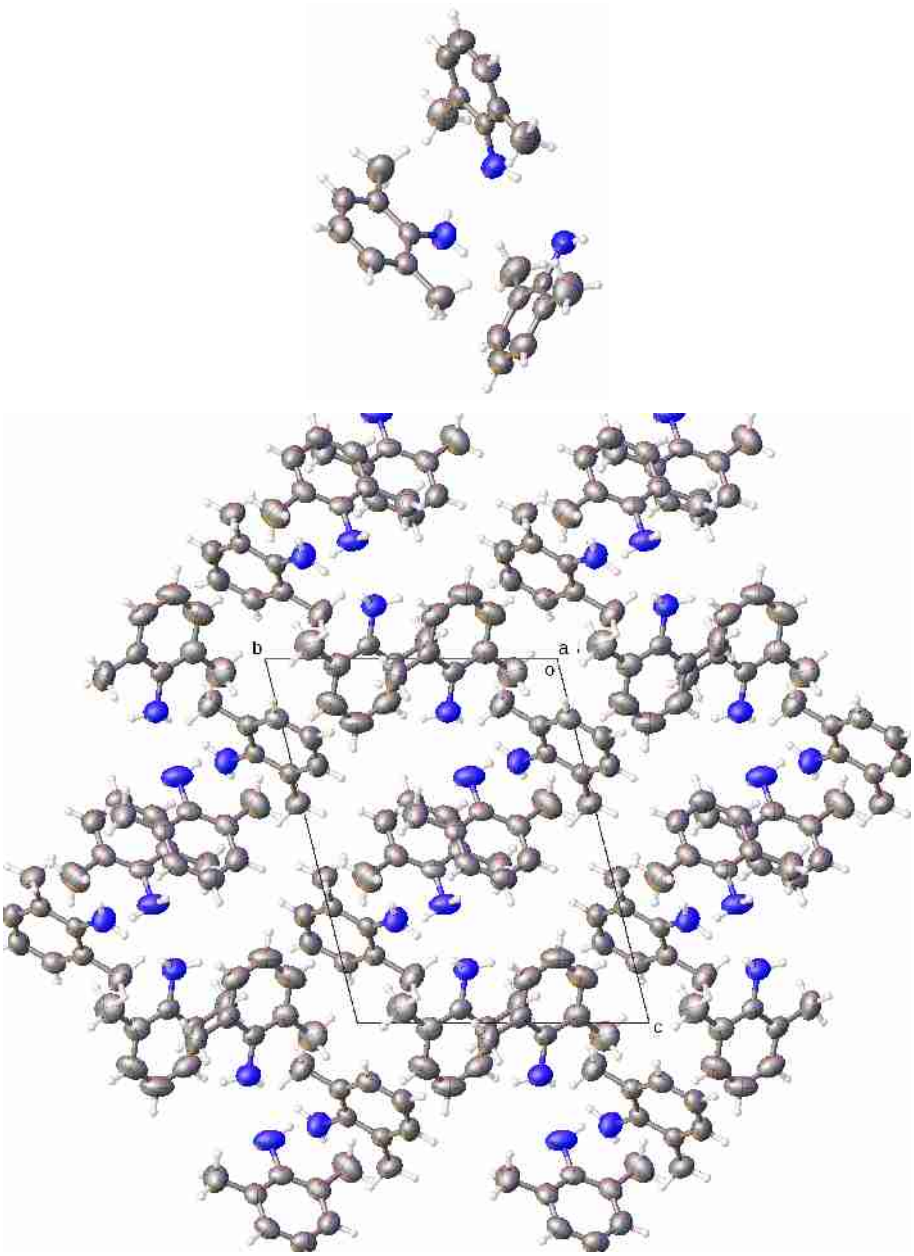

Figure A.23 Asymmetric Unit (**Top**) and packing diagram (**Bottom**) of cryo-crystallised 2,6-dimethylaniline.

Table A.20 shows crystallographic data for the two data collections.

Compound	**2,6-Dimethylaniline (LT)**	**2,6-Dimethylaniline (HP)**
empirical formula	$C_8H_{11}N$	
formula weight	121.18	
T/K	281 (2)	ambient
P/kbar	ambient	1.8 (2)
crystal system	triclinic	
space group	*P-1*	
a (Å)	8.895 (10)	8.7731 (10)
b (Å)	10.259 (12)	10.1409 (18)
*c (*Å*)*	13.618 (16)	13.430 (3)
α (°)	100.88 (2)	100.999 (9)
B (°)	106.88 (2)	106.915 (10)
γ (°)	98.63 (2)	99.011 (10)
Z	6	
V/Å^3	1140 (2)	1093.1 (3)
D_{calc}/g cm^{-3}	1.059	1.105
μ/mm^{-1}	0.062	0.043
unique reflns	4175	2292
observed reflns	4083	946
θ_{max}	25.349	16.273
completeness/%	97.8	41.3
R_1 [I > 2σ]	0.0553	0.0688
wR_2 [all]	0.1464	0.2413
goodness-of-fit	1.029	1.096

Table A.20 Crystallographic Data from cryo- and high-pressure crystallised 2,6-dimethylaniline.

A.1.20 N,N-dimethylaniline

N,N-dimethylaniline was found the same polymorph through cryo-crystallisation and and high-pressure crystallisation, although the high-pressure data were not of sufficient quality for least-squares refinement. Figure A.24 shows the crystal structure of N,N-dimethylaniline.

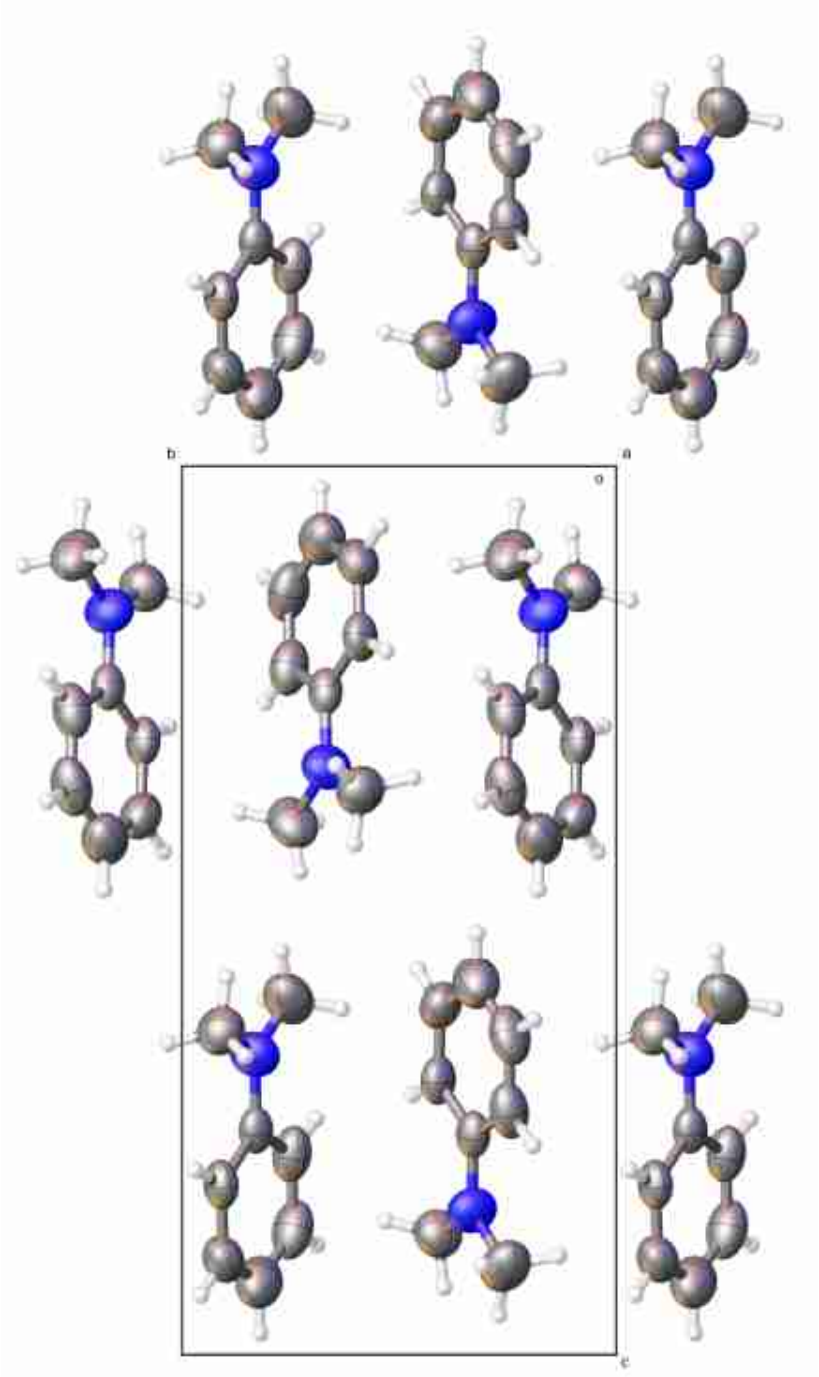

Figure A.24 Packing diagram of cryo-crystallised N,N-dimethylaniline.

Table A.21 shows crystallographic data for the cryo-crystallised data collection.

Compound	**N,N-dimethylaniline (LT)**
empirical formula	$C_8H_{11}N$
formula weight	121.18
T/K	274 (2)
P/kbar	ambient
crystal system	orthorhombic
space group	$P2_12_12_1$
a (Å)	6.091 (11)
b (Å)	7.684 (14)
c (Å)	15.75 (3)
Z	4
V/Å^3	737 (2)
D_{calc}/g cm^{-3}	1.092
μ/mm^{-1}	0.064
unique reflns	1069
observed reflns	976
θ_{max}	23.363
completeness/%	91.3
R_1 [I > 2σ]	0.0733
wR_2 [all]	0.2225
goodness-of-fit	1.085

Table A.21 Crystallographic Data from cryo- crystallised N,N-dimethylaniline.

A.1.21 1,3,5-Trimethylbenzene

1,3,5-Trimethylbenzene was found the same polymorph through cryo-crystallisation and and high-pressure crystallisation. Figure A.25 shows the crystal structure of 1,3,5-trimethylbenzene.

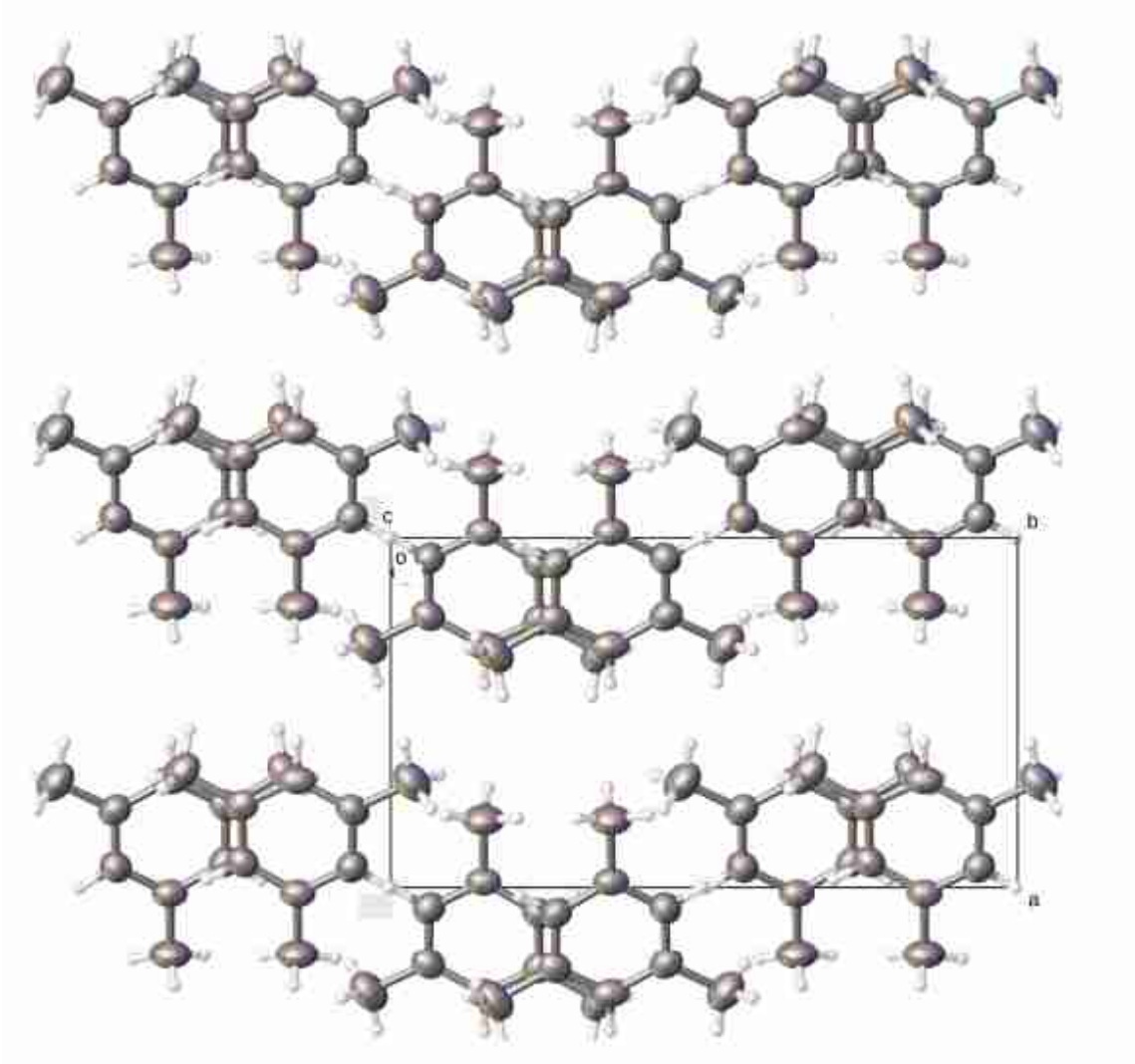

Figure A.25 Packing diagram of cryo-crystallised 1,3,5-trimethylbenzene.

Table A.22 shows crystallographic data for the two data collections.

Compound	**1,3,5-Trimethylbenzene (LT)**	**1,3,5-Trimethylbenzene (HP)**
empirical formula	C_9H_{12}	
formula weight	120.19	
T/K	218 (2)	ambient
P/kbar	ambient	5.4 (2)
crystal system	monoclinic	
space group	$P2_1/c$	
a (Å)	8.473 (7)	8.214 (2)
b (Å)	13.805 (11)	13.221 (5)
*c (*Å*)*	7.780 (6)	7.4510 (16)
B (°)	114.892 (9)	114.992 (11)
Z	4	
V/Å^3	825.5 (11)	733.4 (4)
D_{calc}/g cm^{-3}	0.967	1.089
μ/mm^{-1}	0.054	0.041
unique reflns	1622	677
observed reflns	1278	331
θ_{max}	26.021	15.633
completeness/%	78.8	48.9
R_1 [I > 2σ]	0.0636	0.0461
wR_2 [all]	0.2016	0.1203
goodness-of-fit	1.060	1.144

Table A.22 Crystallographic Data from cryo- and high-pressure crystallised 1,3,5-trimethylbenzene.

A.1.22 1,2,3,5-Tetramethylbenzene

1,2,3,5-Tetramethylbenzene was found the same polymorph through cryo-crystallisation and and high-pressure crystallisation, although the high-pressure data were of insufficient quality for least-squares refinement. Figure A.26 shows the crystal structure of 1,2,3,5-tetramethylbenzene.

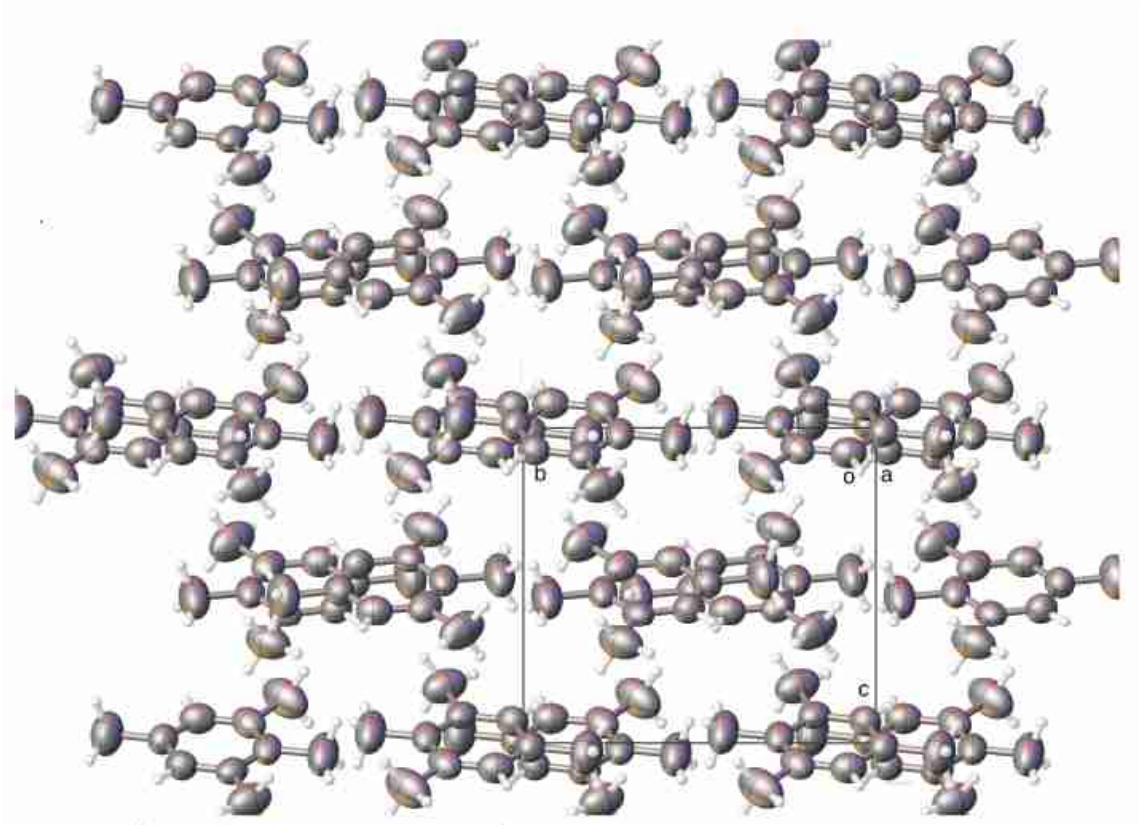

Figure A.26 Packing diagram of cryo-crystallised 1,2,3,5-tetramethylbenzene.

Table A.23 shows crystallographic data for the cryo-crystallised data collection.

Compound	**1,2,3,5-Tetramethylbenzene (LT)**
empirical formula	$C_{10}H_{14}$
formula weight	134.21
T/K	248 (2)
P/kbar	ambient
crystal system	monoclinic
space group	$P2_1/c$
a (Å)	11.495 (12)
b (Å)	9.372 (10)
*c (*Å*)*	8.414 (7)
B (°)	93.457 (16)
Z	4
V/Å^3	904
D_{calc}/g cm^{-3}	0.985
μ/mm^{-1}	0.055
unique reflns	1144
observed reflns	963
θ_{max}	22.222
completeness/%	84.2
R_1 [I > 2σ]	0.0828
wR_2 [all]	0.2409
goodness-of-fit	0.958

Table A.23 Crystallographic Data from cryo- and high-pressure crystallised 1,2,3,5-tetramethylbenzene.

A.2 Computational Results: 2-fluorophenylacetylene

Treatment of flexibility	Model potential Fit + DMA (φ)	a	b	c	β	Initial Energy	Final energy	Compack RMS15 / Å	Relative Energies / $kJmol^{-1}$
Form I major									
Experimental	-	7.577	13.024	6.17	90	-	-	-	**-**
ExpminExp	SCF	7.466	13.175	6.207	90	-67.128	-67.922	0.088	**0.00**
ExpminExp + P	SCF	7.313	13.042	6.114	90	-16.710	-18.584	0.116	**0.00**
ExpminOpt	SCF	7.461	13.136	6.353	90	-67.236	-68.582	0.201	**0.00**
ExpminOpt + P	SCF	7.286	12.996	6.272	90	-16.820	-18.441	0.185	**0.00**
ExpminExp	MP2	7.502	13.251	6.184	90	-63.574	-64.268	0.084	**0.00**
ExpminExp + P	MP2	7.343	13.099	6.093	90	-13.157	-14.701	0.109	**0.00**
ExpminOpt	MP2	7.463	13.196	6.356	90	-63.733	-64.944	0.199	**0.00**
ExpminOpt + P	MP2	7.289	13.043	6.272	90	-13.316	-14.543	0.179	**0.00**
Form I minor									
Experimental	-	7.578	13.024	6.171	90	-	-	-	**-**
ExpminExp	SCF	7.473	13.155	6.365	90	-60.301	-62.725	0.203	**5.20**
ExpminExp + P	SCF	7.270	13.019	6.295	90	-9.869	-12.445	0.193	**6.14**
ExpminOpt	SCF	7.486	13.111	6.444	90	-61.042	-63.917	0.246	**4.67**
ExpminOpt + P	SCF	7.273	12.984	6.378	90	-10.610	-13.110	0.231	**5.33**
ExpminExp	MP2	7.438	13.224	6.382	90	-58.345	-60.960	0.213	**3.31**
ExpminExp + P	MP2	7.245	13.071	6.307	90	-7.913	-10.501	0.198	**4.20**
ExpminOpt	MP2	7.437	13.199	6.472	90	-58.259	-61.317	0.262	**3.63**
ExpminOpt + P	MP2	7.238	13.049	6.398	90	-7.827	-10.282	0.241	**4.26**
Form II									
Experimental	-	7.031	5.924	7.441	103.563	-	-	-	**-**
ExpminExp	SCF	7.205	6.003	7.416	104.666	-65.875	-67.228	0.125	**0.69**

ExpminExp + P	SCF	7.121	5.969	7.205	105.148	-15.980	-17.279	0.168	**1.30**
ExpminOpt	SCF	7.249	6.009	7.455	104.832	-64.949	-67.011	0.151	**1.57**
ExpminOpt + P	SCF	7.161	5.980	7.238	105.346	-15.054	-16.479	0.172	**1.96**
ExpminExp	MP2	7.230	6.081	7.333	105.163	-61.863	-63.633	0.178	**0.63**
ExpminExp + P	MP2	7.140	6.041	7.130	105.987	-11.968	-12.564	0.226	**1.12**
ExpminOpt	MP2	7.272	6.103	7.358	105.382	-60.618	-63.701	0.200	**1.77**
ExpminOpt + P	MP2	7.181	6.073	7.143	105.987	-10.723	-13.529	0.243	**1.98**
Form III major									
Experimental	-	3.934	5.934	12.962	98.467	-	-	-	**-**
ExpminExp	SCF	3.851	6.206	13.120	96.489	-60.747	-62.900	0.253	**5.02**
ExpminExp + P	SCF	3.747	6.136	13.010	96.892	-11.181	-12.615	0.241	**5.97**
ExpminOpt	SCF	3.842	6.211	13.260	96.700	-60.663	-64.144	0.275	**4.44**
ExpminOpt + P	SCF	3.737	6.145	13.141	97.092	-11.098	-13.439	0.264	**5.00**
ExpminExp	MP2	3.822	6.237	13.210	96.627	-58.051	-60.876	0.285	**3.39**
ExpminExp + P	MP2	3.725	6.160	13.076	96.926	-8.486	-10.446	0.267	**4.25**
ExpminOpt	MP2	3.811	6.254	13.339	96.661	-56.929	-61.478	0.318	**3.47**
ExpminOpt + P	MP2	3.713	6.178	13.197	96.727	-7.364	-10.579	0.298	**3.96**
Form III minor									
Experimental	-	3.934	5.934	12.962	98.467	-	-	-	**-**
ExpminExp	SCF	3.891	6.043	13.351	96.213	-49.237	-58.318	0.221	**9.60**
ExpminExp + P	SCF	3.804	5.934	13.206	95.859	0.328	-8.162	0.213	**10.42**
ExpminOpt	SCF	3.895	6.055	13.508	95.871	-43.457	-56.933	0.265	**11.65**
ExpminOpt + P	SCF	3.800	0.000	13.360	95.373	6.109	-6.033	0.250	**12.41**
ExpminExp	MP2	3.871	6.036	13.410	95.688	-50.246	-59.280	0.242	**4.99**
ExpminExp + P	MP2	3.789	5.929	13.253	95.510	-0.681	-9.143	0.230	**5.56**
ExpminOpt	MP2	3.869	6.054	13.574	95.313	-44.918	-58.292	0.288	**6.65**
ExpminOpt + P	MP2	3.780	5.951	13.415	95.074	4.648	-7.460	0.268	**7.08**

Form III major									
Experimental	-	3.9343	5.9336	12.962	98.467	-	-	-	**-**
ExpminExp	SCF	3.851041	6.206210	13.120150	96.488680	-60.746686	-62.900376	0.253	**5.02**
ExpminExp + P	SCF	3.746877	6.136261	13.010029	96.892095	-11.181307	-12.614553	0.241	**5.97**
ExpminOpt	SCF	3.842136	6.211495	13.260312	96.700016	-60.662889	-64.143561	0.275	**4.44**
ExpminOpt + P	SCF	3.737341	6.145476	13.140814	97.091866	-11.097509	-13.438937	0.264	**5.00**
ExpminExp	MP2	3.822076	6.236740	13.209581	96.626570	-58.051106	-60.876314	0.285	**3.39**
ExpminExp + P	MP2	3.724777	6.159642	13.075552	96.926236	-8.485727	-10.445788	0.267	**4.25**
ExpminOpt	MP2	3.810906	6.254225	13.338722	96.661269	-56.929455	-61.477664	0.318	**3.47**
ExpminOpt + P	MP2	3.713040	6.178226	13.197442	96.726640	-7.364076	-10.578749	0.298	**3.96**
Form III minor									
Experimental	-	3.9343	5.9336	12.962	98.467	-	-	-	**-**
ExpminExp	SCF	3.891152	6.043138	13.350517	96.213366	-49.236912	-58.317956	0.221	**9.60**
ExpminExp + P	SCF	3.804236	5.933841	13.205521	95.859386	0.328467	-8.162000	0.213	**10.42**
ExpminOpt	SCF	3.895246	6.055175	13.508359	95.871397	-43.456649	-56.933033	0.265	**11.65**
ExpminOpt + P	SCF	3.800101	5.952423	13.360094	95.373432	6.108730	-6.033105	0.250	**12.41**
ExpminExp	MP2	3.871140	6.035862	13.410411	95.687762	-50.246476	-59.280476	0.242	**4.99**
ExpminExp + P	MP2	3.789077	5.929172	13.252905	95.510379	-0.681097	-9.143456	0.230	**5.56**
ExpminOpt	MP2	3.868503	6.053710	13.573982	95.312517	-44.917798	-58.292498	0.288	**6.65**
ExpminOpt + P	MP2	3.779977	5.951413	13.415305	95.073787	4.648	-7.460	0.268	**7.08**

Table B.1 Minimised and optimised energies and structures for the three experimentally observed polymorphs. P = 0.55 GPa

All calculations give unit cell dimensions that are not drastically different from the starting values (unsurprisingly the deviations for the minor components in I and III tend to be higher than for the major components). The two theory levels both give the stability ordering I(maj) > II > III(maj) ≈ I(min) > III(min). However, the gap between I(min) and III(min) is rather higher with SCF than MP2.

1 W. Friedrich, P. Kipping and M. Laue, *Ann. Phys*. **346**, 971-988.
2 W. L. Bragg, *Proc R. Soc. London Ser. A*, 1913, **89**, 248-277.
3 K. Lonsdale, *Proc. R. Soc. London Ser. A*, 1929, **123**, 494-515.
4 P. W. Bridgman, *Proc. R. Soc. London Ser. A*, 1950, **203**, 1-17.
5 P. W. Bridgman, *Proc. Am. Acad. Arts Aci.*, 1952, **71**, 167-251.
6 P. W. Bridgman, *Proc. Am. Acad. Arts Aci.*, **81**, 167-251.
7 P. W. Bridgman, *The Physics of High Pressure*, Bell and Sons: London, U. K., 1931.
8 P. W. Bridgman, *Rev. Mod. Phys.*, 1946, **18**, 1-93.
9 C. E. Weir, E. R. Lipincott, A. van Valkenburg and E. N. Bunting, *J. Res. Natl Bur. Stand. Technol.*, 1959, **63A**, 55-62.
10 J. C. Jamieson, A. W. Lawson, N. D. Nachtrieb, *Rev. Sci. Instrum.*, **30**, 1016-1019.
11 G. J. Piermarini, S. Block and J.D Barnett, *J. App;. Phys.*, 1973, **44**, 5377-5382.
12 A. Katrusiak, *Acta Crystallogr., Sect. A: Found. Crystallogr.*, 2008, **64**, 135-148.
13 G. J.Piermarini, S. Block, J. D. Barnett and R. A. Forman, *J. Appl. Phys*., 1975, **46**, 2774-2780.
14 *APEX2*, version 1.08, Bruker AXS Inc., Madison, WI, 2004.
15 S. Block, C. E. Weir and G. J. Piermarini, *Science*, 1965, **148**, 947-948.
16 R. J. Fourme, *J. Appl. Crystallogr.*, 1968, 1, 23-30.
17 R. J. Fourme, D. Andre and M. Renaud, *Acta Crystallogr. Sect. B: Struct. Sci.*, 1971, **27**, 1275-1276.
18 A. Dawson, D. R. Allan, S. Parsons and M. Ruf, *J. Appl. Cryst.*, 2004, **37**, 410-416.
19 A. Zajac, E. Hecht and E. Cummings, *Optics*. 4Th Edition. 2003, Pearson Higher Education.
20 P. Dera and A. Katrusiak, *J. Appl. Cryst.*, 1999, **32**, 510-515.
21 S. Parsons, *ECLIPSE*, The University of Edinburgh: Edinburgh, U.K., 2009.
22 M. R. Probert, J. A. Coome, A. E. Goeta and J. A. K. Howard, *Acta Crystallogr., Sect. A: Found. Crystallogr.*, 2011, **67**, 528.
23 M. R. Probert, C. M. Robertson, J. A. Coome, J. A. K. Howard, B. C. Mitchell and A. E. Goeta, *J. Appl. Cryst.*, 2010, **43**, 1415-1418.
24 T. Schulz, K. Meindl, D. Leusser, D. Stern, J. Graf, C. Michaelsen, M. Ruf, G. M. Sheldrick and D. Stalke, *J. Appl. Crystallogr.*, 2009, 42, 885-891.
25 A. Bravais, *J. Ecole Polytech.*, 1850, **19**, 1-128.
26 G. M. Sheldrick, CELL NOW, University of Göttingen & Bruker AXS Inc., Madison, WI, 2005.
27 RLATT, Bruker AXS Inc., Madison, WI, 2004.
28 *SADABS*, G. M. Sheldrick and Bruker AXS Inc., Madison, WI, 2001.
29 G. M. Sheldrick, Current Developments in SADABS and TWINABS, Presentation given at Bruker Nonius Users' Meeting, 2003.
30 S. C. Nyburg, *X-Ray Analysis of Organic Structures*, 1961, Academic Press.
31 J. P. Glusker and K. N. Trueblood, C*rystal Structure Analysis; A Primer*, 3rd Ed., 2010, Oxford University Press, Oxford, U.K.
32 D. Sayre, *Acta Crystallogr.,* 1952*,* **5***,* 60-65.
33 W. T. Cochran and M. M. Woolfson, *Acta Crystallogr.,* 1955*,* **8**, 1-12.
34 J. Karle and H. Hauptman, *Acta Crystallogr.,* 1956*,* **9**, 635-651.
35 *SAINT*, Bruker AXS Inc., Madison, WI, 2007.
36 G. M. Sheldrick, *Acta Crystallogr., Sect. A: Found. Crystallogr.*, 2008, **64**, 112.
37 O. V. Dolomanov, L. J. Bourhis, R. J. Gildea, J. A. K. Howard and H. Puschmann, *J. Appl. Crystallogr.*, 2009, **42**, 339-341.
38 R. J. Gildea, L. J. Bourhis, O. V. Dolomanov, R. W. Grosse-Kuntstleve, H. Puschmann, P.D Adams and J. A. K. Howard, *J. Appl. Cryst.*, 2011, **44**, 1259-1263.
39 M. A. Viswamitra and K. K. Kannan, *Nature*, 1996, **209**, 1016-1017.
40 E. B. Moore and V. Molinero, *Nature*, 2011, **479**, 506-508.
41 D. Chopra and T. N. Guru-Row, *J. Indian Inst. Sci.*, 2007, **87**, 167-211.
42 V. R. Thalladi, H.-C. Weiss and R. Boese, *Angew. Chem. Int. Ed. Engl.*, 2000, **39**, 918-922.
43 V. R. Thalladi, R. Boese, H.-C. Weiss *J. Am. Chem. Soc.*, 2000, **122**, 1186-1190.
44 M. Y. Antipin, R. Boese, D. Blaser and A. Maulitz, J. Am. Chem. Soc., 1997, 119, 326-333.
45 G. Frenking, A. J. Krapp, *J. Comp. Chem.*, 2007, **28**, 15-24.
46 R. Boese, N. Niederprum, D. Bläser, A. Maulitz, N. Y. Antipin and P. R. Mallinson, *J. Phys.*

Chem. B, 1997, **101**, 5794-5799.
47 I. D. H. Oswald, D. R. Allan, G. M. Day, W. D. S. Motherwell and S. Parsons, *Cryst. Growth Des*. 2005, **5**, 1055-1071.
48 I. D. H. Oswald, D. R. Allan, W. D. S. Motherwell, S. Parsons, *Acta Crystallogr., Sect. B: Struct. Sci.*, 2005, **61**, 69-79.
49 J. D. Dunitz and J. Bernstein, *J. Acc. Chem. Res.*, 1995, **28**, 193-200.
50 Y. Kobayashi, S. Ito, S. Itai and K. Yamamoto, *Int. J. Pharm.*, 2000, **193**, 137-146.
51 http://www.doitpoms.ac.uk/tlplib/anisotropy/electrical.php
52 W. C. McCrone, *Polymorphism in physics and chemistry of the organic solid state*. 1965, Vol 2. Interscience, New York. U.S.A.
53 M. J. Buerger and M. C. Bloom, *Zeit. Kristallogr.,* 1937, **96**, 182–200.
54 S. L. Price, *Acta Crystallogr. Sect. B: Struct. Sci*., 2013, **69**, 313-328
55 W. Z. Ostwald, *Phys. Chem.,* 1897, **22**, 289.
56 E. Boldyreva, *Cryst. Growth Des.*, 2007, **7**, 1662-1668.
57 A. Budzianowski, A. Olejniczak and A. Katrusiak, *Acta Crystallogr., Sect. B: Struct Sci*., 2006, **62**, 1078-1089.
58 E. V. Boldyreva, H. Ahsbahs, V. V. Chernyshev, S. N. Ivashevskaya, A. R. Oganov, *Z. Kristallogr.*, 2006, **221**, 186-197.
59 N. A. Tumanov, E. V. Boldyreva, B. A. Kolesov, A. V. Kurnosov, and R. Quesada Cabrera, *Acta Crystallogr., Sect. B: Struct Sci*., 2010, **66**, 458-471.
60 S. A. Moggach, D. R. Allan, S. J. Clark, M. J. Gutmann, S. Parsons, C. R. Pulham and L. Sawyer, *Acta Crystallogr., Sect. B: Struct Sci*., 2006, **62**, 296-309.
61 G. L. Perlovich, L. K. Hansen and A. Bauer-Brandl, *J. Therm. Anal. Calorim.*, 2001, **66**, 699-715.
62 E. V. Boldyreva, V. A. Drebushchak, T. N. Drebushchak, I. E. Paukov, Y. A. Kovalevskaya and E. S. Shutova, *J. Therm. Anal. Calorim.*, **73**, 409-418.
63 E. V. Boldyreva, V. A. Drebushchak, T. N. Drebushchak, I. E. Paukov, Y. A. Kovalevskaya and E. S. Shutova, *J. Therm. Anal. Calorim.*, **73**, 419-428.
64 V. A. Drebushchak, E. V. Boldyreva, Y. A. Kovalevskaya, I. E. Paukov and T. N. Drebushchak, *J. Therm. Anal. Calorim.*, **79**, 2005, 65-70.
65 C. Murli, S. M. Sharma, S. Karmakar and S. K. Sikka, *Physica B*, *Condens. Matter*, 2003, **339**, 23-30.
66 S. V. Goryainov, E. N. Kolesnik and E. V. Boldyreva, *Physica B, Condens. Matter*, 2005, **357**, 340-347.
67 A. Dawson, D. R. Allan, S. A. Belmonte, S. J. Clark, W. I. F. David, P. A. McGregor, S. Parsons, C. R. Pulham and L. Sawyer, *Cryst. Growth Des.*, 2005, **5**, 1415-1427.
68 E. V. Boldyreva, H. Ahsbahs and H. P. Weber, *Z. Kristallogr.*, 2003, **218**, 231-236.
69 E. V. Boldyreva, S. N. Ivashevskaya, H. Sowa, H. Ahsbahs and H.-P. Weber, *Dokl. Akad. Nauk*, 2004, **396**, 358-361.
70 E. V. Boldyreva, S. N. Ivashevskaya, H. Sowa, H. Ahsbahs and H.-P. Weber, *Z. Kristallogr.*, 2005, **220**, 50-57.
71 S. V. Goryainov, E. V. Boldyreva and E. N. Kolesnik, *Chem. Phys. Lett.*, 2006, **419**, 496-500.
72 E. V. Boldyreva, T. P. Shakhtsneider, M. A. Vasilchenko, H. Ahsbahs and H. Uchtmann, *Acta Crystallogr. Sect. B: Struct Sci*., 2000, **54**, 299-309.
73 E. V. Boldyreva, T. P. Shakhtsneider and H. Ahsbahs, *J. Therm. Anal. Calorim.*, 2002, **68**, 437-452.
74 E. V. Boldyreva, H. Ahsbahs, H. Uchtmann and N. E. Kashcheeva, *High Pressure Res.*, 2000, **17**, 79-99.
75 M. Podsiadlo and A. Katrusiak, *Acta Crystallogr.*, *Sect. A: Found. Crystallogr.*, 2005, **61**, C329; M. Podsiadlo, K. F. Dziubek and A. Katrusiak, *Acta Crystallogr., Sect. B: Struct. Sci.*, 2005, **61**, 595-600.
76 M. Bujak, K.Dziubek, A. Katrusiak, *Acta Crystallogr., Sect. B: Struct. Sci*., 2007, **63**, 124-131.
77 E. B. Boldyreva, *Acta Crystallogr., Sect. A: Found. Crystallogr.*, 2008, **64**, 218-231.
78 D. R. Allan, S. J. Clark, R. M. Ibberson, S. Parsons, C. R. Pulham and L. Sawyer, *Chem. Commun.*, 1999, 751-752.
79 D. R. Allan, S. J. Clark, A. Dawson, P. A. McGregor and S. Parsons, *Acta Crystallogr., Sect. B: Struct Sci.*, 2002, **58**, 1018-1024
80 M. Bujak, A. Budzianowski and A. Katrusiak, *Z. Kristallogr.*, 2004, **219**, 573-579.

81 R. Gajda, K. F. Dziubek and A. Katrusiak. *Acta Crystallogr. Sect. B: Struct. Sci.*, 2006, **62**, 86-93.
82 M. R. Probert, Y. H. P. Chung and J. A. K. Howard, *CrystEngComm*, 2010, **12**, 2584-2586.
83 I. D. H. Oswald, D. R. Allan, W. D. S. Motherwell and S. Parsons, *Acta Crystallogr., Sect. B: Struct. Sci.*, 2005, **61**, 69-79.
84 G. R. Desiraju, *The crystal as a supramolecular entity, Perspectives in supramolecular chemistry*; 1995, Vol. 2. John Wiley & Sons: Chichester, U.K.
85 E. J. Corey, *Pure Appl. Chem.*, 1967, **14**, 19-37.
86 E. Arunan, G. R. Desiraju, R. A. Klein, J. Sadlej, S. Scheiner, I. Alkorta, D. C. Clary, R. H. Crabtree, J. J. Dannenberg, P. Hobza, H. G. Kjaergaard, A. C. Legon, B. Mennucci, and D. J. Nesbitt, *Pure Appl. Chem.,* 2011, **83**, 1637–1641.
87 L. Turi and J. J. Dannenberg, *J. Phys. Chem.,* 1993, **97**, 7899-7909.
88 S. Gronert, *J. Am. Chem. Soc.,* 1993, **115**, 10258-10266.
89 K. Morokuma, *Acc. Chem. Res.,* 1997, **10**, 294-300.
90 G. R. Desiraju and T. Steiner, *The weak hydrogen bond: In structural chemistry and biology*, 2001, Oxford University Press, U.S.A.
91 L. Pauling, *The Nature of the Chemical Bond*, 1939, Oxford University Press, U. K.
92 A. Allerhand, and P. V. R. Schleyer, *J. Am. Chem. Soc.,* 1963, **85**, 1715-1723.
93 D. J. Sutor, *Nature*, 1962, **195**, 68-69.
94 D. J. Sutor, *J. Am. Chem. Soc.,* 1963, 1105-1110.
95 J. Donohue, *Selected topics in hydrogen bonding in Structural Chemistry and Molecular Biology*, 1968, Freeman U.S.A.
96 R. Taylor, and O. Kennard, *J. Am. Chem. Soc.*, 1982, **104**, 5063-5070.
97 F. H. Allen, *Acta Crystallogr. Sect. B: Struct. Sci.*, 2002**, 58**, 380-388.
98 I. J. Bruno, J. C. Cole, P. R. Edgington, M. Kessler, C. F. Macrae, P. McCabe, J. Pearson, and R. Taylor, *Acta Crystallogr. Sect. B: Struct. Sci.*, 2002, **58**, 389-397.
99 C. B. Aakeroy, T. A. Evans, K. R. Seddon and I. Palinko, *New J. Chem.,* 1999, **11**, 145-152.
100 T. Steiner, *New J. Chem.*, 1998, **10**, 1099-1103.
101 T. Steiner, and G. R. Desiraju, *Chem. Commun*. **1998**, 891-892.
102 F. H. Allen, J. A. K. Howard, V. J. Hoy, G. R. Desiraju, D. S. Reddy, and C. C. Wilson, *J. Am. Chem. Soc.,* 1996, **118**, 4081-4084.
103 J.-M. Dumas, M. Kern and J. L. Janier-Dubry, *Bull. Soc. Chim. Fr.*, 1976, 1785–1787.
104 P. Murray-Rust and W. D. S. Motherwell, *J. Am. Chem. Soc.*, 1979, **101**, 4374–4376.
105 P. Murray-Rust, W. C. Stallings, C. T. Monti, R. K. Preston and J. P. Glusker, *J. Am. Chem. Soc.*, 1983, **105**, 3206–3214.
106 P. Politzer, P. Lane, M. C. Concha, Y. Ma and J. S. Murray. *J. Mol. Model.*, 2007, **13**, 305-311
107 O. Hassel and C. Rømming, *Q. Rev., Chem. Soc.*, 1962, **16**, 1–18.
108 P. Politzer, J. S. Murray and T. Clark, *Phys. Chem. Chem. Phys.*, 2013, **15**, 11178-11189.
109 P. Metrangolo and G. Resnati, *Halogen Bonding: Fundamentals and Applications*, Springer-Verlage Berlin Heidelberg, Germany, 2008.
110 A. I. Kitaigorodskii, *Acta Crystallogr.* 1965, **18**, 585.
111 J. A. R. P. Sarma and G. R. Desiraju, *Acc. Chem. Res*. 1986, **19**, 222-228.
112 R. Boese, A. D. Boese, D. Blaser, M. Y. Antipin, A. Ellern and K. Seppelt, *Angew. Chem. Int. Ed.*, 1997, **36**, 1489-1492.
113 V. R. Hathwar, and T. N. Guru Row, *J. Phys. Chem. A,* 2010**, 114**, 13434–13441.
114 D. E. Williams, and L. Y. Hsu, *Acta Crystallogr., Sect. A: Found. Crystallogr.,* 1985, **41**, 296–301.
115 G. R. Desiraju, and R. Parthasarathy, *J. Am. Chem. Soc.* 1989, **111**, 8725–8726.
116 S. L. Price, A. J. Stone, J. Lucas, R. S. Rowland, and A. E. Thornley, *J. Am. Chem. Soc.,* 1994, **116**, 4910–4918.
117 P. Garca, S. Dahaoui, C. Katan, M. Souhassou, and C. Lecomte, *Faraday Discuss.,* 2007, **135**, 217–235.
118 T. T. T. Bui, S. Dahaoui, C. Lecomte, G. R. Desiraju, and E. Espinosa, *Angew. Chem., Int. Ed.,* 2009, **48**, 3838–3841.
119 S. C. Nyburg, and W. Wong-Ng, *Inorg. Chem.,* 1979, **18**, 2790–2791.
120 S. C. Nyburg, and W. Wong-Ng, *Proc. R. Soc. London, Ser. A,* 1979, **367**, 29–45.

121 V. R. Perdireddi, D. S. Reddy, B. S. Goud, D. C. Craig, A. D. Rae and G. R. Desiraju, *J. Chem. Soc. Perkin Trans.*, 1993, **2**, 2353-2360.
122 F. F. Awwadi, R. D. Willett, K. A. Peterson, and B. Twamley, *Chem. Eur. J.*, 2006, **12**, 8952–8960.
123 Figures from http://en.wikipedia.org/wiki/File:BenzeneDimerGeometries.png
124 C. A. Hunter and J. K. M. Hunterm *J. Am. Chem. Soc.*, 1990, **112,** 5525–5534.
125 S. Tsuzuki, K. Honda, T. Uchimaru, M. Mikami and K. Tanabe, *J. Am. Chem. Soc.*, 2002, **124**, 104-112.
126 S. Tsuzuki, K. Honda, T. Uchimaru and M. J. Mikami, *J. Chem. Phys.*, 2005, **122**, 144323.
127 S. E. Wheeler, and K. N. Houk, *J. Am. Chem. Soc.*, 2008, **130**, 10854–10855.
128 A. L. Ringer, and C. D. Sherrill, *J. Am. Chem. Soc.*, 2009, **131**, 4574–4575.
129 M. Watt, L. K. E. Hardebeck, L. C. C. Kirkpatrick, and M. Lewis, *J. Am. Chem. Soc.,* 2011, **133**, 3854–3862.
130 M. O. Sinnokrot and C. D. Sherrill, J. Am. Chem. Soc., 2004, 126, 7690–7697.
131 E. G. Hohenstein, J. Duan and C. D. Sherrill, *J. Am. Chem. Soc.*, 2011, **133**, 13244-13247.
132 J.-I. Seo, I. Kim and Y. S. Lee, Chem. Phys. Lett., 2009, **474**, 101–106.
133 M. Tamres, *J. Am. Chem. Soc.*, 1952, **74**, 3375-3378.
134 M. Muraki, *Protein Peptide Lett.*, **9**, 195-209.
135 K. Kobayashi, Y. Asakawa, Y. Kikuchi, H. Toi, Y. Aoyama, *J. Am. Chem. Soc.*, 1993, **115**, 2648-2654.
136 M. Hirota, Y. Takahashi, M. Nishio and K. Nishihata, *Bull. Chem. Soc. Jpn.*, 1978, **51**, 2358-2360.
137 Y. Iitaka, Y. Kodama, K. Nishihata and M. Nishio, *J. C. S. Chem. Comm.*, 1974, 389-390.
138 Y. Kodama, K. Nishihata, M. Nishio and N. Nakagawa, *Tetrahedron Lett.*, 1977, 2105.
139 Y. Umezawa, S. Tsuboyama, K. Honda, J. Uzawa, and M. Nishio, *Bull. Chem. Soc. Jpn.*, 1998, **71**, 1207-1213.
140 Y. Umezawa, S. Tsuboyama, K. Honda, J. Uzawa, and M. Nishio, *Tetrahedron*, 1999, **55**, 10047-10056.
141 F. London, *Trans. Faraday Soc.,* 1937, 8-26.
142 A. J. Stone, *The Theory of Intermolecular Forces,* 1996, 1st. Ed, Oxford University Press, Oxford, U.K.
143 Figure From: http://en.wikipedia.org/wiki/File:Argon_dimer_potential.png
144 J. N. Isrealachvili, *Intermolecular & Surface Forces,* 3rd Ed. Elsevier Academic Press, London, U.K., 2011.
145 CrystalExplorer (Version 3.0), S. K. Wolff, D. J. Grimwood, J. J. McKinnon, M. J. Turner, D. Jayatilaka and M. A. Spackman, University of Western Australia, 2012.
146 M. A. Spackman and D. Jayatilaka, *CrystEngComm*, 2009, **11**, 19-32.
147 J. J. McKinnon, D. Jayatilaka and M. A. Spackman, *Chem. Commun.*, 2007, **37**, 3814-3816.
148 http://ra.bcs.uwa.edu.au/CrystalExplorer/wiki/index.php/Surface_Properties
149 M. A. Spackman and J. J. McKinnon, *CrystEngComm*, 2002, **4**, 378-392.
150 **CrystalExplorer (Version 3.1)**, *S.K. Wolff, D.J. Grimwood, J.J. McKinnon, M.J. Turner, D. Jayatilaka, M.A. Spackman*, University of Western Australia, 2012.
151 J. D. Dunitz, A. Gavezzotti and W. B. Schweizer, *Helv. Chem. Acta*, 2003, **86**, 4073.
152 Y. Gu, T. Kar and S. Scheiner, *J. Am. Chem. Soc.*, 1999, **121**, 9411-9422.
153 S. Gronert, *J. Am. Chem. Soc.*, 1993, **115**, 10258-10266.
154 J. D. Dunitz, and R. Taylor, *Chem. Eur. J.*, 1997, **3**, 89-98.
155 J.E. Huheey, E.A. Keiter, and R.L. Keiter, *Inorganic Chemistry: Principles of Structure and Reactivity*, 4th edition, HarperCollins, New York, USA, 1993.
156 K. Müller, C. Faeh and F. Diederich, *Science*, 2007, **317**, 1881.
157 J. A. K. Howard, V. J. Hoy, D. O'Hagan and G. T. Smith, *Tetrahedron*, 1996, **52**, 12613-12622.
158 H.-C. Weiss, R. Boese, H. L. Smith and M. M. Haley, *Chem. Commun.*, 1997, **24**, 2403-2404.
159 A. G. Dikundwar, R. Sathishkumar, T. N. Guru Row and G. R. Desiraju, *Cryst. Growth Des.*, 2011, **11**, 3954-3963.
160 V. R. Thalladi, H.-C. Weiss, D. Blaser, R. Boese, A. Nangia and G. R. Desiraju, *J. Am. Chem. Soc.*, 1998, **120**, 8702-8720.

161 D. Lentz, *J. Chem. Cryst.*, 2003, **33**, 977-981.
162 F. Akkerman, J. Buschmann, D. Lentz, P. Luger and E. Rodel, *J. Chem. Cryst.*, 2003, **33**, 969-975.
163 A. J. Durie, A. M. Z. Slawin, T. Lebl, P. Kirsch and D. O' Hagan, *Chem. Commun.*, 2011, **47**, 8265-8267.
164 J. Ridout and M. R. Probert, *Cryst. Growth Des.*, 2013, **13**, 1943-1948.
165 S. L. Masters, I. D. Mackie, D. A. Wann, H. E. Robertson, D. W. H. Rankin and S. Parsons, *Struct. Chem.*, 2011, **22**, 279.
166 J. Benet-Buchholz, T. Haumann and R. Boese, *Chem. Commun.*, 1998, **18**, 2003.
167 R. Gajda and A. Katrusiak, *Acta Crystallogr., Sect. B: Struct. Sci.*, 2007, **63**, 111-117.
168 G. J. Piermarini, A. B. Braun, J. Chem. Phys., 1973, **58**, 1974.
169 F. P. A. Fabbiani, D. R. Allan, W. I. F. David, S. A. Moggach, S. Parsons and C. R. Pulham, *CrystEngComm*, 2004, **6**, 505-511.
170 F. P. A. Fabbiani, D. R. Allan, W. G. Marshall, S. Parsons, C. R. Pulham and R. I. Smith, *J. Cryst. Growth*, **275**, 185-192.
171 F. P. A Fabbiani, D. R. Allan, S. Parsons and C. R. Pulham, *CrystEngComm*, 2005, **7**, 179-186.
172 F. P. A. Fabbiani, D. R. Allan, W. I. F. David, A. J. Davidson, A. R. Lennie, S. Parsons, C. R. Pulham and J. E. Warren, *Cryst. Growth Des.*, **7**, 1115-1124.
173 M. Podsiadlo and A. Katrusiak, *J. Phys. Chem. B*, 2008, **112**, 5355-5362.
174 T. Koyano, I. Hachiya, T. Arishimo, K. Sato and N. Sagi, *J. Am. Oil Chem. Soc.*, 1989, **66**, 675-679.
175 K. Sato and T. Kuroda, *J. Am. Oil Chem. Soc.*, 1987, **64**, 124-127.
176 R. Tripathi, S.V. Biradar, B. Mishra and A. R. Paradkar, *AAPS PharmSciTech*, 2010, **11**, 1493-1498.
177 A. R. Chodhury, K. Islam, M. T. Kirchner, G. Mehta and T. N. Guru Row, *J. Am. Chem. Soc.*, 2004, **126**, 12274-12275.
178 J. Ridout, L. S. Price, J. A. K. Howard and M. R. Probert, *Cryst. Growth Des.*, 2014, **14**. 3391.
179 C. Ouvard and S. L. Price, *Cryst. Growth Des.*, 2004, **4**, 1119–1127.
180 W. T. M. Mooij, B. P. Van Eijck, S. L. Price, P. Verwer and J. Kroon, *J. Comput. Chem.*, 1998, **19**, 459-474.
181 J. P. M. Lommerse, W. D. S. Motherwell, H. L. Ammon, J. D. Dunitz, A. Gavezzotti, D. W. M. Hofmann, F. J. J. Leusen, W. T. M. Mooij, S. L. Price, S. L. B. Schweizer, M. U. Schmidt, B. P. van Eijck, P. Verwer and D. E. Williams, *Acta Crystallogr. Sect. B: Struct. Sci.*, 2000, **56**, 697-714.
182 W. D. S. Motherwell, H. L. Ammon, J. D. Dunitz, A. Dzyabchenko, P. Erk, A. Gavezzotti, D. W. M. Hofmann, F. J. J. Leusen, J. P. M. Lommerse, W. T. M. Mooij, S. L. Price, H. Scheraga, B. Schweizer, M. U. Schmidt, B. P. van Eijck, P. Verwer and D. E. Williams, *Acta Crystallogr. Sect. B: Struct. Sci.*, 2002, **58**, 647-661.
183 G. M. Day, W. D. S. Motherwell, H. L. Ammon, S. X. M. Boerrigter, R. G. Della Valle, E. Venuti, A. Dzyabchenko, J. D. Dunitz, B. Schweizer, B. P. van Eijck, P. Erk, J. C. Facelli, V. E. Bazterra, M. B. Ferraro, D. W. M. Hofmann, F. J. J. Leusen, C. Liang, C. C. Pantelides, P. G. Karamertzanis, S. L. Price, T. C. Lewis, H. Nowell, A. Torrisi, H. A. Scheraga, Y. A. Arnautova, M. U. Schmidt and P. Verwer, *Acta Crystallogr. Sect. B: Struct. Sci.*, 2005, **61**, 511-527.
184 G. M. Day, T. G. Cooper, A. J. Cruz-Cabeza, K. E. Hejczyk, H. L. Ammon, S. X. M. Boerrigter, J. S. Tan, R. G. Della Valle, E. Venuti, K. V. J. Jose, S. R. Gadre, G. R. Desiraju, T. S. Thakur, B. P. van Eijck, J. C. Facelli, V. E. Bazterra, M. B. Ferraro, D. W. M. Hofmann, M. A. Neumann, F. J. J. Leusen, J. Kendrick, S. L. Price, A. J. Misquitta, P. G. Karamertzanis, G. W. A. Welch, H. A. Scheraga, Y. A. Arnautova, M. U. Schmidt, J. van de Streek, A. K. Wolf and B. Schweizer, *Acta Crystallogr. Sect. B: Struct. Sci.,* 2009, **65**, 107-125.
185 D. A. Bardwell, C. S. Adjiman, Y. A. Arnautova, E. Bartashevich, S. X. M. Boerrigter, D. E. Braun, A. J. Cruz-Cabeza, G. M. Day, R. G. Della Valle, G. R. Desiraju, B. P. van Eijck, J. C. Facelli, M. B. Ferraro, D. Grillo, M. Habgood, D. W. M. Hofmann, F. Hofmann, K. V. J. Jose, P. G. Karamertzanis, A. V. Kazantsev, J. Kendrick, L. N. Kuleshova, F. J. J. Leusen, A. V. Maleev, A. J. Misquitta, S. Mohamed, R. J. Needs, M. A. Neumann, D. Nikylov, A. M. Orendt, R. Pal, C. C. Pantelides, C. J. Pickard, L. S. Price, S. L. Price, H. A. Scheraga, J. van de Streek, T. S. Thakur, S. Tiwari, E. Venuti and I. K. Zhitkov, *Acta Crystallogr. Sect. B: Struct. Sci.,* 2011. **67**, 535-551.

186 W. Mooij, B. P. van Eijck, S. L. Price, P. Verwer and J. Kroon, *J. Comput. Chem.*, 1998, **19**, 459-474.
187 A. Asmadi, M. A. Neumann, J. Kendrick, P. Girard, F. M. A. Perrin and J. J. Leusen, *J. Phys. Chem. B.*, 2009, **113**, 16303–16313.
188 J. Spencer, H. Patel, J. J. Deadman, R. A. Palmer, L. Male, S. J. Coles, O. G. Uzoh and S. L. Price, *CrystEngComm*, 2012, **14**, 6441–6446.
189 O. G. Uzoh, A. J. Cruz-Cabeza and S. L. Price, *Cryst. Growth Des.*, 2012, **12**, 4230–4239.
190 S. L. Price, *CrystEngComm*, 2004, **61**, 344-353.
191 A. J. Stone and M. Alderton, *Mol. Phys.*, 1985, **56**, 1047.
192 S. L. Price, *Acc. Chem. Res.*, 2009, **42**, 117–126.
193 A. L. Misquitta, G. W. A. Welch, A. J. Stone and S. L. Price, *Chem. Phys. Lett.*, 2008. **456,** 105-109.
194 Gaussian 03, M. J. Frisch, G. W. Trucks, H. B. Schlegel, G. E. Scuseria, M. A. Robb, J. R. Cheeseman, J. A. Montgomery, Jr., T. Vreven, K. N. Kudin, J. C. Burant, J. M. Millam, S. S. Iyengar, J. Tomasi, V. Barone, B. Mennucci, M. Cossi, G. Scalmani, N. Rega, G. A. Petersson, H. Nakatsuji, M. Hada, M. Ehara, K. Toyota, R. Fukuda, J. Hasegawa, M. Ishida, T. Nakajima, Y. Honda, O. Kitao, H. Nakai, M. Klene, X. Li, J. E. Knox, H. P. Hratchian, J. B. Cross, V. Bakken, C. Adamo, J. Jaramillo, R. Gomperts, R. E. Stratmann, O. Yazyev, A. J. Austin, R. Cammi, C. Pomelli, J. W. Ochterski, P. Y. Ayala, K. Morokuma, G. A. Voth, P. Salvador, J. J. Dannenberg, V. G. Zakrzewski, S. Dapprich, A. D. Daniels, M. C. Strain, O. Farkas, D. K. Malick, A. D. Rabuck, K. Raghavachari, J. B. Foresman, J. V. Ortiz, Q. Cui, A. G. Baboul, S. Clifford, J. Cioslowski, B. B. Stefanov, G. Liu, A. Liashenko, P. Piskorz, I. Komaromi, R. L. Martin, D. J. Fox, T. Keith, M. A. Al-Laham, C. Y. Peng, A. Nanayakkara, M. Challacombe, P. M. W. Gill, B. Johnson, W. Chen, M. W. Wong, C. Gonzalez, and J. A. Pople, Gaussian, Inc., Wallingford CT, 2004.
195 J. R. Holden, Z. Du and H. L. Ammon, *J. Comput. Chem.*, 1993, **14**, 422-437.
196 D. J. Willock, S. L. Price, M. Leslie, et al., J. Comput. Chem. 16, 628 (1995).
197 GDMA: A Program for Performing Distributed Multipole Analysis of Wave Functions Calculated Using the Gaussian Program System; A. J. Stone, University of Cambridge, 2010.
198 S. L. Price, M. Leslie, G. W. A. Welch, M. Habgood, L. S. Price, P. G. Karamertzanis and G. M. Day, *Phys. Chem. Chem. Phys.*, 2010, **12**, 8478-8490.
199 D. E. Williams and S. R. Cox, *Acta Crystallogr. Sect. B: Struct. Sci.*, 1984, **40**, 404-417.
200 D. E. Williams and D. J. Hopt, *Acta Crystallogr. Sect. B: Struct. Sci.*, 1986, **42**, 286.
201 NEIGHCRYS, S. L. Price *et al*, University College London, 2010.
202 C. F. Macrae, I. J. Bruno, J. A. Chisholm, P. R. Edgington, P. McCabe, E. Pidcock, L. Rodriguez-Monge, R. Taylor, J. van de Streek and P. A. Wood, *J. Appl. Cryst.*, 2008, **41**, 466-470.
203 M. D. Segall, P. L. D. Lindan, M. J. Probert, C. J. Pickard, P. J. Hasnip, S. J. Clark and M. C. Payne, *J. Phys. Cond. Matt.*, 2002, **14**, 2717-2743.
204 H.-C. Weiss, D. Blaser, R. Boese, B. M. Doughan and M. M. Haley, *Chem. Commun.*, 1997, 1703.
205 K. Dziubek, M. Podsiadlo and A. Katrusiak, *J. Am. Chem. Soc.*, 2007, **129**, 12620.
206 T. S. Thakur, R. Sathishkumar, A. G. Dikundwar, T. N. Guru Row and G. R. Desiraju, *Cryst. Growth Des.*, 2011, **11**, 3954-3963.
207 G. R. Desiraju, *CrystEngComm*, 2003, **5**, 466-467.
208 P. Vishweshwar, J. A. McMahon, M. L. Peterson, M. B. Hickey, T. R. Shattock and M. J. Zaworotko, M. J. *Chem. Commun.*, 2005, **36**, 4601-4603.
209 N. Shan, A. D. Bond and W. Jones. *Cryst. Eng.*, 2002, **5**, 9-24.
210 A. V. Trask and W. Jones, Crystal engineering of organic cocrystals by the solid-state grinding approach. In *Organic Solid State Reactions* (pp. 41-70). Springer Berlin Heidelberg, Germany, 2005.
211 S. Tothadi and G. R. Desiraju, G. *Phil. Trans. R. Soc. A*, 2012, **370**, 2900-2915.
212 D. S. Yufit and J. A. K. Howard, *Acta Crystallogr. Sect C: Cryst. Struct. Commun.*, 2012, **68**, 37–40.
213 D. S. Yufit, R. Zubatyuk, O. V. Shishkin and J. A. K. Howard, *CrystEngComm*, 2012, **14**, 8222–8227.
214 D. S. Yufit and J. A. K. Howard, *CrystEngComm*, 2012, **14**, 2003-2008.
215 A. D. Bond, *Chem. Commun.*, 2003, 250-251.

216 A. D. Bond, *CrystEngComm*, 2006, **8**, 333-337.
217 D. Wiechert and D. Mootz, *Angew. Chem., Int. Ed.*, 1999, **38**, 1974–1976.
218 M. T. Kirchner, D. Blaser and R. Boese, *Chem.-Eur. J.*, 2010, **16**, 2131-2146.
219 M. T. Kirchner, R. Boese, W. E. Billups and L. R. Norman, *J. Am. Chem. Soc.*, 2004, **126**, 9407-9412.
220 M. T. Kirchner, D. Blaser, R. Boese and G. R. Desiraju, *CrystEngComm*, 2009, **11**, 229-231.
221 D. S. Yufit and J. A. K. Howard, *CrystEngComm*, 2010, **12**, 737–741.
222 D. S. Yufit and J. A. K. Howard, *CrystEngComm*, 2010, **12**, 737-741.
223 H. A. Shallard Brow, D. J. Watkin and A. R. Cowley, *Acta Crystallogr., Sect. E: Struct. Rep. Online*, 2005, **61**, 2424.
224 R. Gajda and A. Katrusiak, *J. Phys. Chem. B.*, 2009, **113**, 2436-2442.
225 K. F. Dziubek and A. Katrusiak, *J. Phys. Chem. B.*, 2008, **112**, 12001.
226 S. K. Nayak, S. J. Prathapa and T. N. Guru Row, *J. Mol. Struct.*, 2009, **935**, 156-160.
227 D. Chopra, V. Thiruvenkatam, S. G. Manjunath and T. N. Guru Row, *Cryst. Growth Des.*, 2007, **7**, 868-876.
228 P. Mirone, B. Fortunato and P. Canziani, *J. Mol. Struct.*, 1970, **5**, 283-295.
229 H. J. Vledder, F. C. Mijlhoff, J. C. Leyte and C. Romers, *J. Mol. Struct.*, 1971, **7**, 421-429.
230 A. Cirkel and R. Boese, *Acta Crystallogr., Sect. A: Found. Crystallogr.,* 2004, **60**, s205.
231 I. M. Shmyt'ko, R. J. Jimenez-Rioboo, M. Hassaine and M. A. Ramos, *J. Phys. Condens. Matter*, 2010, 22, 195102.
232 J. W. Steed, *CrystEngComm*, 2003, **5**, 169-179.
233 R. Taylor and C. F. Macrae, *Acta Crystallogr. Sect. B: Struct. Sci.*, 2001, **57**, 815-827.
234 D. R. Allan, S. J. Clark, M. J. P. Brugmans, G. L. Ackland and W. L. Vos, *Phys. Rev. B: Condens. Matter Mater. Phys.*, 1998, **58**, 11809.
235 D. Andre, R. Fourme and K. Zechmeister, *Acta Crystallogr., Sect. B: Struct. Sci.*, 1972, **28**, 2389.
236 G. W. Wheland, *Resonance in Organic Chemistry*, Wiley, New York, 1955, 100-110.
237 N. B. Colthup, *Appl. Spectrosc.*, 1985, **39**, 1030-1032.
238 G. Wu, C. Van Alsenoy and H. J. Gelse, *J. Phys. Chem. A*, 2000, **104**, 1576-1587.
239 M. P. Johansson and J. Olsen, *J. Chem. Theory Comput.*, 2008, **4**, 1460-1471.
240 J. Trotter, *Acta Crystallogr*. 1961, **14**, 1135.
241 J. An, O. K. Farha, J. T. Hupp, E. Pohl, J. I. Yeh and N. L. Rosi, *Nat. Commun.*, 2011, **3**, 1-6.
242 G. Lamming, C. McGurk and A. Houlton. Yet to be published
243 A. G. Young and L. R. Hanton, *Coord. Chem. Rev.*, 2008, **252**, 1346-1386.
244 a) D. M. Shin, I. S. Lee, D. Cho and Y. K. Chung, *Inorg. Chem.*, 2003, **42**, 7722-7724.
b) D. M. Shin, I. S. Lee, Y. K. Chung and M. S. Lah, *Chem. Commun.*, 2003, **2**, 1036-1037.
245 J. Y. Lu and A. M. Babb, *Chem. Commun.*, 2001, 821-822.
246 H. J. M. Lee, P. Y. Cheng, C. Y. Chen, J. S. Shen and D. Nandi, *CrystEngComm*, 2011, **13**, 4814-4816.
247 C. Y. Jiang, Y. C. Lai, S. L. Wang and K. H. Lii, *Inorg. Chem.*, 2001, **40**, 5320-5321.
248 L. Hou, J. Zhang and X. Chen, *Cryst. Growth Des.*, 2009, 2-6.
249 R. Lee, J. A. K. Howard, M. R. Probert and J. W. Steed, *Chem. Soc. Rev.*, 2014, **43**, 4300=4311.
250 PLATON, A Multipurpose Crystallographic Tool, A. L. Spek. Utrecht, the Netherlands, 1998.; A. Spek, J. Appl. Cryst. (2003), 36, 7-13.
251 S. A. Moggach, D. R. Allan, S. J. Clark, M. J. Gutmann, S. Parsons, C. R. Pulham and L. Sawyer, *Acta Crystallogr., Sect. B: Struct. Sci.*, 2006, **62**, 296-309.
252 S. A. Moggach, T. D. Bennett and A. K. Cheetham, *Angew. Chem. Int. Ed.* 2009, **121**, 7221-7223.
253 H. Borrmann, I. Persson, M. Sandstrin, C. M. V. Stalhandske, *J. Chem. Soc., Perkin Trans. 2*, 2000, **2**, 393-402.
254 R. M. Ibberson, W. I. F. David, S. Parsons, M. Prager, K. Shankland, *J. Mol. Struct.*, 2000, 524, 121-128.
255 H. van Konigsveld, A. J. Van der Berg, J. C. Jansen, R. De Goede, *Acta Crystallogr. Sect. B: Struct. Sci.*, 1986, **42**, 491-497.